TAILORING EXTRACELLULAR MATRIX MECHANICS

Federica Burla

This thesis was reviewed by:

dr. Wouter G. Ellenbroek	Technische Universiteit Eindhoven
prof. dr. Martin L. van Hecke	AMOLF/Universiteit Leiden
prof. dr. Paul A. Janmey	University of Pennsylvania
prof. dr. ir. Erwin J.G. Peterman	Vrije Universiteit Amsterdam
dr. ir. Tina Vermonden	Universiteit Utrecht

The work described in this thesis was performed at AMOLF, Science Park 104, 1098 XG, Amsterdam, The Netherlands. This work is part of an Industrial Partnership Program between the Dutch Research Council (NWO) and Unilever research and development B.V..

Thesis design cover by Jerom Langeveld. This thesis was printed by Ipskamp.

ISBN 978-94-028-2027-0

A digital version of this thesis can be obtained from www.amolf.nl and www.ub.vu.nl. Printed copies can be obtained by request via library@amolf.nl.

VRIJE UNIVERSITEIT

TAILORING EXTRACELLULAR MATRIX MECHANICS

ACADEMISCH PROEFSCHRIFT

ter verkrijging van de graad Doctor of Philosophy
aan de Vrije Universiteit Amsterdam,
op gezag van de rector magnificus
prof.dr. V. Subramaniam,
in het openbaar te verdedigen
ten overstaan van de promotiecommissie
van de Faculteit der Bètawetenschappen
op vrijdag 19 juni 2020 om 11.45 uur
in de aula van de universiteit,
De Boelelaan 1105

door

Federica Burla

geboren te Como, Italië

promotor: prof.dr. G.H. Koenderink

Contents

1

Introduction

1.1 The architecture of the human body

From the beginning of history, man has drawn inspiration from nature to devise functional objects and solutions to practical problems. This resulted in a powerful synergy between art, architecture, engineering and natural sciences. Examples include the flying machine from Leonardo da Vinci [1], who looked at the flight of birds to create the ancestors of an airplane, as well as the architect Antoni Gaudi, who employed the load bearing concept of tree branches in the canopy tree-like pillar supporting the vault of the Sagrada Familia [2, 3]. Millions of years of evolution have allowed natural systems to fine-tune their structural organization to their function in the most efficient way, making them a prime source of inspiration.

Arguably, two of the most functionally adapted masterpieces of nature are the mechanical scaffolds that support the human body, the cell cytoskeleton and the extracellular matrix. The cytoskeleton (Figure 1a) comprises a highly dynamic skeletal structure, which continuously rearranges in order to allow the movement of cells. The extracellular matrix (Figure 1b) is a much more static structure, which provides stability and mechanical support to tissues. Even though these structures are made of very tiny filaments, they are able to provide us with mechanical support by assembling in space-spanning networks that can bear large mechanical loads.

Parts of this chapter are from Burla, F.*, Mulla, Y.*, Vos, B., Aufderhorst-Roberts, A., Koenderink, G.H. *From mechanical resilience to active material properties in biopolymer networks.* Nat. Phys. Rev. **1**, 249-263, 2019.

Our daily life imposes constant mechanical challenges to these structures, as for example high shear deformations exerted by blood flow on the wall of a pulsating vein, or the mechanical loads our joints and bones bear when we walk or sport. A further challenge that our body faces is that every tissue needs to have the right mechanical properties to provide the proper cues to cells. Cells (Figure 1c) actively measure the stiffness of their surroundings by means of integrin receptor proteins in the cell membrane, which then convert the mechanical information into biochemical signaling that triggers a cellular response such as cell migration, division or differentiation [4, 5].

Living tissues developed strategies to cope with these mechanical challenges despite having access to just a limited number of building blocks. Perhaps counterintuitively, networks of biopolymers can withstand large loads because they operate at the edge of mechanical stability. Cytoskeletal and extracellular networks are subisostatic, meaning that each node of the network is only connected to a small number of neighbors. The low connectivity makes the networks relatively soft, but it provides them with the ability to accommodate large deformations by having additional degrees of freedom. Thus, firstly the topology of these networks is crucial to determine the way they respond to deformation. Secondly, tissues achieve properties tailored to their function by combining different building polymeric blocks with distinct structural and mechanical properties. The interplay of these building blocks can give rise to new mechanical properties that surpass those of the individual components.

Understanding how the combination of network topology and synergy between different components give rise to the mechanical tunability of tissues can provide us with a better insight in the way tissues achieve their mechanical adaptability. Eventually, we can use this knowledge to engineer new materials that could for instance replace damaged tissues.

1.2 The building blocks of the extracellular matrix

The main component of the extracellular matrix (ECM) is the fibrous protein collagen, which is produced inside cells and then secreted in the extracellular environment in a monomeric form. This molecule consists of a triple helix of polypeptide chains wound around each other that is terminated on both ends by protective regions called propeptides [7]. Enzymatic removal of the propeptides triggers precise quarter-staggered assembly of collagen molecules into a fibril characterized by an axial periodicity called the D-period. The fibrils subsequently assemble in large networks with typical pore sizes on the order of 1-10 μm and fibril diameters on the order of 100 nm. These fibrillar networks provide an adhesive scaffold to cells and at the same time confer shape and mechanical stability to tissues.

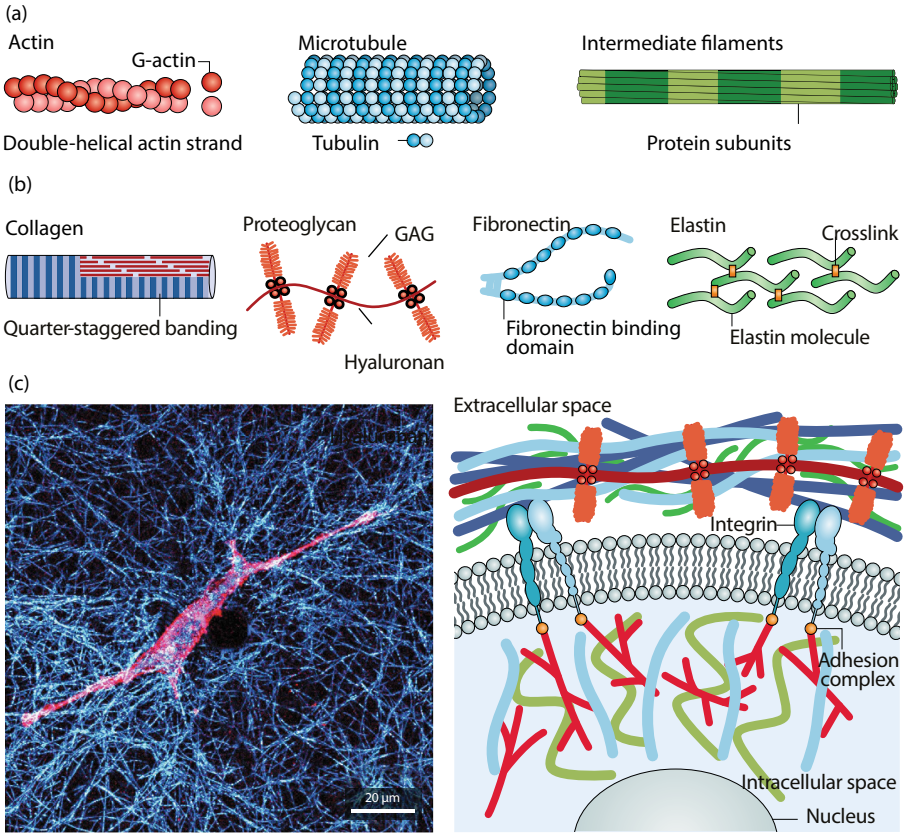

Figure 1.1: The building blocks of biopolymer networks. Cells and tissues are mechanically supported by biopolymer networks known as the cytoskeleton and extracellular matrix, respectively. (a) Illustration of the three filaments that constitute the cytoskeleton of a cell. (b) Illustration of the most prevalent biopolymers in the extracellular matrix. (c) The left panel shows a confocal microscopy image of a cell (actin is shown in red) adhered to a collagen matrix (blue fibres). The right panel shows a schematic of the cytoskeleton and extracellular matrix connected across the cell membrane by integrin adhesion proteins. Note that the extracellular matrix is three-dimensional in some tissues, such as skin, but forms a two-dimensional sheet in other tissues, such as epithelia. GAG, glycosaminoglycan. Image from Ref. [6].

Other important polymers of the extracellular matrix are proteoglycans [8], bottlebrush proteins linked to long carbohydrate chains. The highly charged nature of these molecules enables them to bind water molecules and thereby hydrate tissues. In addition, they play essential roles in cell-cell communication, for instance in the brain [9]. One of these carbohydrate chains is hyaluronan, a highly charged polysaccharide with a thickness of only a few nanometers and a length of several micrometers [10], prominent in tissues such as cartilage and vitreous humor. Hyaluronan is also present in the pericellular matrix [11], a coating that covers the cell and plays an important role in cell-cell communication [12].

While collagen, proteoglycans and hyaluronan form fibrous networks in the extracellular matrix, there are also other components that confer tissue-specific properties. Elastin for instance contributes to the high elasticity of arteries [13], and fibronectin makes the extracellular matrix adhesive for cells [14].

Finally, another extracellular protein which we consider in this thesis is fibrinogen, which is normally not present in the extracellular matrix but in blood. Upon tissue injury, this protein can rapidly assemble into a fibrillar network that forms the backbone of blood clots. Fibrin has extraordinary mechanical requirements, as it needs to withstand large deformations such as the tensile forces exerted by blood flow. At the same time, it also needs to rapidly disappear once the wound is healed, to prevent thrombosis [15].

1.3 Architecture and hybrid composition in tissues

Bones are the stiffest material in the body, composed by aligned collagen fibrils providing a certain degree of flexibility intertwined with inorganic crystals of hydroxyapatite conferring stiffness [16, 17] (see Figure 2a). Tendons are likewise highly hierarchical structures [18], where collagen fibrils are arranged into long cables by fibroblast cells known as 'tenoblasts', interspersed with proteoglycans which provide a high resistance to compressive loads [19] (see Figure 2b). An example of a disordered (isotropic) collagen network is the vitreous humor of the eye, composed mainly by water and supported by collagen fibers intertwined with space-filling hyaluronan [20] (see Figure 2c). Composites of collagen and hyaluronan can be found also in the soft extracellular matrix of the brain [21, 22] (see Figure 2d).

Abnormalities in the organization of the extracellular matrix generate pathological situations. The erroneous mineralization of bones causes defects resulting in inferior mechanical properties of the bone [24], while the lack of precise organization in tendons generates tendinopathy [25]. The tight mechanical balance that extracellular brain networks need to maintain is breached in pathological situations such as multiple sclerosis, where the excessive deposition of extracellular components impairs remyelination [26], the process of axon repair [27].

Understanding how the architectural organization and the interplay between ECM components each contributes to the mechanical properties of tissues is therefore of crucial importance. However, this is a complicated question to address because of the simultaneous presence of many components in tissues, whose effects are challenging to disentangle. Reductionist approaches employing model systems of purified extracellular matrix components have been widely used to deal with this

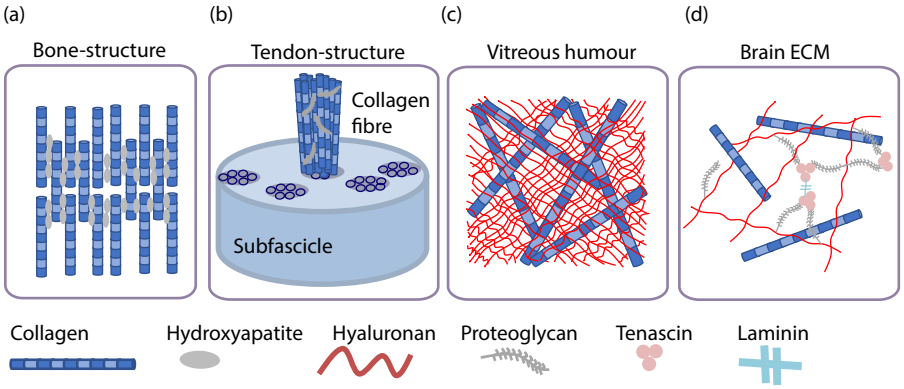

Figure 1.2: Architecturally and compositionally distinct tissues of the body. (a) The bone ECM is composed by aligned collagen fibrils interspersed with hydroxyapatite minerals, which confer rigidity. Redrawn from Ref. [16]. (b) Tendons are highly hierarchical structures composed by tertiary fibre bundles, bundles of fascicles, in turn resulting from the assembly of subfascicles, bundles of collagen fibres composed of aligned collagen fibrils and proteoglycans for compressive strain resistance. Redrawn from Ref. [23]. (c) The vitreous humour of the eye is composed by a collagen network interspersed with hyaluronic acid. Redrawn from Ref. [20]. (d) The brain ECM is composed mainly of hyaluronan and proteoglycans, with some inclusions of collagen. Redrawn from Ref. [21].

complexity, and indeed a great body of work has been produced to understand the mechanical properties of networks composed by single-proteins in terms of polymer physics models, which we introduce here.

1.4 Mechanics of biopolymer networks

Mechanical models of cytoskeletal and extracellular matrix polymers usually coarse–grain the filaments as smooth linear rods that resist bending with a modulus κ and stretching with a modulus μ. At finite temperatures, thermal fluctuations cause the filaments to bend as a function of their persistence length (l_p), which is defined as the decay length of angular correlations along the polymer contour. The persistence length is related to the bending modulus by $\kappa = k_B T l_p$, where k_B is Boltzmann's constant and T is the absolute temperature. Biopolymers are categorized on the basis of the ratio between the persistence length and total (or contour) length (L) as flexible ($l_p \ll$ L), semiflexible ($l_p \sim$ L) or stiff ($l_p \gg$ L). Collagen fibres and microtubules have persistence lengths in the range of a few millimetres and contour lengths on the order of several micrometres, and are thus examples of stiff filaments. By contrast, actin filaments and intermediate filaments have persistence and contour lengths in the micrometre range and are therefore semiflexible [28–30]. Hyaluronan is an example of a flexible polysaccharide, with a persistence length of ~4–8 nm and contour length of several micrometres [31].

Biopolymers are assembled into load bearing networks by a variety of mechanisms. The simplest mechanism is by entanglements that naturally arise from steric interactions (Fig. 3a). At sufficiently high densities, polymers constrain each other's motions to snakelike paths along their contour, as conceptualized by the reptation model [32, 33] (Fig. 3a). In this model, each filament is considered to be constrained in its motion to a narrow tube formed by contacts with the surrounding filaments [32]. As cytoskeletal filaments have lengths of hundreds of nanometres up to several micrometres, it has been possible to directly observe filament reptation by fluorescence microscopy [34]. Entangled biopolymer solutions can store elastic energy only on short timescales, because on longer timescales, the filaments escape the constraints imposed by entanglements [35]. Long-term mechanical stability is therefore possible only in the presence of long–lived filament interactions, which can occur by branching or crosslinking (Fig. 3b). In the cytoskeleton, actin filaments and microtubules are branched and crosslinked by a large set of specialized proteins [36, 37], whereas intermediate filaments are crosslinked through a combination of accessory proteins and cation–mediated interactions [38]. The transient nature of these filament connections turns cytoskeletal networks into viscoelastic materials. By contrast, the extracellular matrix has a more elastic character owing to covalent crosslinking. For example, the collagen framework is covalently crosslinked by lysyl oxidase [39]. When polymerised on its own, purified collagen tends to form networks through a combination of branching and crosslinking [40, 41], whereas in the body, collagen assembly and mechanics are tightly regulated in a tissue–specific manner by cells and accessory matrix molecules [7]. In order to recreate the complex regulation of collagen mechanics in vitro, artificial methods of collagen crosslinking have been used. Examples of crosslinking agents include ribose [42], threose [43] and transglutaminase [44].

An instrument often used to investigate biopolymer mechanics is rheology, where a sample is polymerised between two parallel plates that can be rotated with respect to each other, measuring the torque needed to rotate the sample by a certain angle, and thereby probing its stiffness (Fig. 4a). Rheological measurements on reconstituted biopolymer networks have revealed that these materials exhibit a general tendency to stress-stiffen in response to shear or uniaxial tensile loads and to stress-soften under compressive loads [45–48] (Fig. 4a). Theoretical modelling has shown that these nonlinear elastic properties are an intrinsic feature of filamentous networks. Compression induced network softening involves a competition between softening due to polymer buckling and stiffening due to polymer densification upon solvent efflux [46–48].

Much more is known about the stiffening response upon tensile or shear loading. Interestingly, the mechanisms that govern stiffening are fundamentally different for semiflexible and rigid polymer networks. Semiflexible polymer networks stiffen

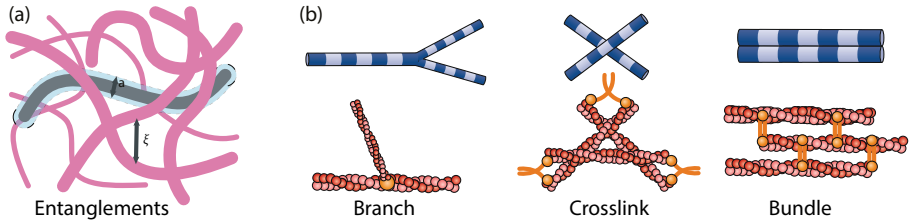

Figure 1.3: Mechanisms of biopolymer network formation. (a) Biopolymers entangle when their density is sufficiently high such that they sterically hinder each other's transverse motion. The cylinder indicates the snake-like path along which each polymer is forced to reptate. The arrows indicate the tube width (a) and network mesh size (ξ). (b) Branches, crosslinks and bundles are key components of filament networks and form through intermolecular interactions between the filaments, as in the case of collagen (top panels), or with the aid of accessory proteins, as in the case of actin (bottom panels). Image is taken from Ref. [6]

because the conformational entropy of the polymers decreases as they are pulled taut along the direction of principal strain [49] (Fig. 4b). The elastic modulus can be calculated by averaging over the entropic force-extension response of the constituent filaments [49], provided that the network is densely crosslinked so that it deforms uniformly (that is, affinely) down to length scales on the order of the crosslink distance [50]. The elastic modulus is expected to increase with applied (shear) stress according to a power law with an exponent of 3/2, which is indeed observed for actin and intermediate filaments [38, 51]. The onset strain at which stiffening sets in is governed by the amount of excess length stored in thermal fluctuations of polymer segments between adjacent crosslinks and is therefore a function of the persistence length and crosslink density. Networks of actin and intermediate filaments are highly strain-sensitive because stiffening sets in at strains of just a few per cent, and the stiffness can easily increase by a factor of 10–100 before rupture. This strain sensitivity is believed to mechanically protect cells because it prevents large deformations. Moreover, the strain sensitivity enables cells to tune their stiffness by molecular motor activity [52]. Given these advantages, there is a growing interest in mimicking strain sensitivity in synthetic polymer gels. Although synthetic polymers are typically flexible [45], several groups have successfully created synthetic polymers that are sufficiently stiff to exhibit strain sensitivity [53–55].

Networks of stiff (that is, athermal) filaments such as collagen also strain-stiffen, but in this case, the nonlinearity is an emergent phenomenon that arises at the network level (Fig. 4c). This form of nonlinearity is related to the network connectivity. As biopolymers form networks through a combination of bundling, branching and crosslinking, the average coordination number (that is, the number of fibrils meeting at a junction) is in the range of three to four [40, 41]. As

mentioned earlier in this chapter, these networks are referred to as subisostatic because the coordination number is below the Maxwell criterion of six required for the mechanical stability of networks of springs [56]. Nevertheless, unlike springs, fibres can form stable subisostatic networks because of their large bending rigidity [57]. Filamentous networks are soft at low strains because they deform in a non-affine manner dominated by fibre bending [58, 59]. However, shear or tensile strains drive a transition to a rigid state dominated by fibre stretching, owing to the alignment of fibres along the principal direction of strain. This transition occurs at a critical strain determined by the network connectivity [41, 59, 60]. Collagen networks are highly strain-sensitive, given that nonlinearity usually sets in at strains of only ~10% and the stiffness can increase by 100-fold before network rupture. Strain stiffening is thought to help prevent tissue rupture while also promoting long-range mechanical communication between cells [61].

1.5 Mechanical enhancement in composite networks

Composite biopolymer networks have only recently begun to be investigated by quantitative rheological measurements and theoretical modelling. The focus so far has been on two-component systems, but even these simplified systems have a large parameter space in which the network mechanics can be tuned by variations in the persistence lengths of the two polymers, their relative and absolute densities and the interconnectivity between the two components. In theoretical studies, this complex phase space has been mainly explored in the limit of permanently crosslinked networks that combine rigid with either flexible or semiflexible polymers.

When both polymers form percolating networks, the linear elastic modulus of the composite can become substantially larger than the sum of the moduli of the separate networks [62]. In such systems, the biopolymer with a lower rigidity forms a denser elastic background owing to its smaller mesh size, which in turn increases the effective bending rigidity of the more rigid biopolymer [62, 63]. Networks of flexible or semiflexible polymers have also been predicted to reinforce rigid polymers against compressive loads [64], an effect that has indeed been observed in actin-microtubule composites [65] and is thought to be important for cells crawling through soft matrices [66]. Recently, active superelasticity (that is, the ability to undergo large and reversible deformation by accommodating strain in an inhomogeneous manner) was observed in epithelial cells and attributed to the synergistic behaviour of actin and intermediate filament networks [67]. In the context of the extracellular matrix, collagen-hyaluronan composites were also reported to exhibit an enhanced resistance to compressive loading compared with collagen alone [68]. However, in this case, the mechanism was not elastic but viscous in origin: hyaluronan increases the viscosity of the fluid in the interstices of the collagen matrix and thus increases the hydraulic resistance to fluid outflow. Glycosaminoglycans tend to swell in hypotonic

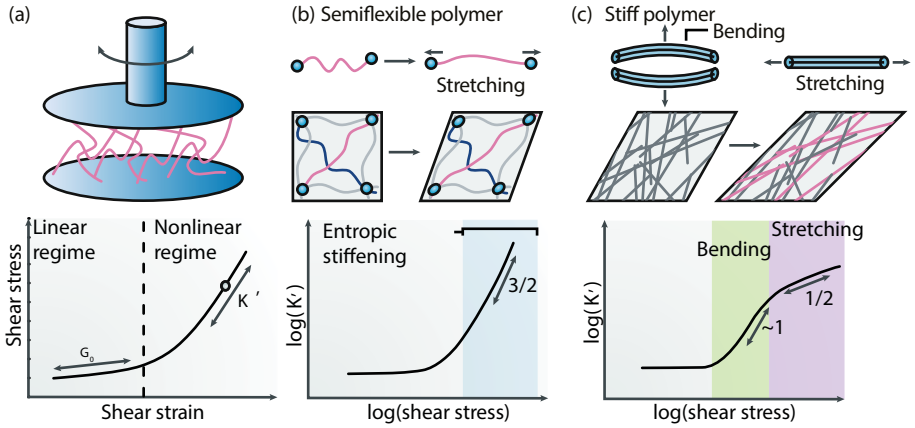

Figure 1.4: Nonlinear elasticity in biopolymer networks. (a) The nonlinear elastic response of biopolymer networks to strain can be probed by subjecting networks polymerised between two plates to an oscillatory or steady shear deformation (shown in the top panel). The stress-strain response (shown in the bottom panel) is linear at low strain, where the slope gives the linear modulus (G_0), but becomes nonlinear at high strain. In this nonlinear regime, the derivative of the stress-strain curve gives the differential modulus (K'). (b) Semiflexible polymer networks strain-stiffen owing to the entropic resistance of the thermally undulating filaments against stretching (shown in the top panel). Filaments under tension (pink, middle panel) extend by stretching out thermal fluctuations, while filaments in the opposite direction (blue) are compressed. The pulling-out of thermal fluctuations gives rise to a characteristic 3/2 power-law stiffening. (c) Stiff polymer networks strain-stiffen by undergoing a transition from a soft, bending-dominated state to a stiff, stretching-dominated state (shown in the top panel), in which filaments are aligned along the direction of strain (pink, middle panel). This gives rise to a power-law stiffening regime with an exponent close to 1 at moderate stress and a regime with an exponent of 1/2 at high stress. Image from Ref. [6].

solutions so they can also induce prestress when interpenetrated with a collagen network [69]. As we will show in this thesis, this prestress can change the nonlinear elastic response of collagen owing to its stress sensitivity [70].

Mechanical enhancement can also be achieved for composites in which only one of the two polymers forms a percolating network. In this case, the percolated component determines the linear elastic modulus, whereas the non-percolated one influences the nonlinear elastic response [71]. Rigid polymer inclusions are expected to lower the threshold shear strain required to induce strain stiffening of semiflexible polymers by making the strain field more affine [63, 71–73]. This effect has been confirmed experimentally for composite networks of actin and microtubules [74, 75]. Furthermore, rigid polymer inclusions are predicted to induce compressibility in an otherwise almost incompressible matrix because they constrain the displacement field [76], a phenomenon observed in co-entangled actin and microtubule composites [77].

A challenge in experimental studies of composite networks is that the constituent polymers can influence each other's organization through steric constraints, direct interactions or depletion effects. Structural changes caused by mutual interactions have been reported in, for example, composites of actin and intermediate filaments [78] and composites of collagen and glycosaminoglycans [79].

1.6 Scope of this thesis

The overarching question of this thesis is how the interplay between network topology and the composite nature of tissues can give rise to the tunable mechanical properties of the extracellular matrix. To address this question, we study reconstituted extracellular matrix model systems with rheology combined with imaging techniques, such as microscopy, particle tracking and differential dynamic microscopy, and SAXS (small-angle x-ray scattering).

In **chapter 2**, we first investigate how the assembly of collagen into structures with different connectivity determines their resistance against shear-induced rupture. We find that networks that are less connected can endure larger deformations. While this finding can be largely explained by a simple elastic model that treats collagen networks as networks of elastic beams, we find that the detailed molecular structure does influence the network strength by means of plastic effects. Collagen networks therefore exploit both their network topology and hierarchical structure to delay fracture.

We then move on to explore the mechanical properties of a collagen-hyaluronan composite, in **chapter 3**. This hybrid composition is the base of tissues like cartilage, where a fibrillar matrix of collagen is intertwined with a flexible hyaluronan matrix. Here, we reveal that the polyelectrolyte nature of hyaluronan induces internal stresses on the collagen matrix that delays its strain-stiffening response. We complement these experimental findings with a computational model that allows us to predict the strain-stiffening behaviour in terms of the stiffness of the collagen fibrils and the amount of hyaluronan-driven internal stress.

Combining different extracellular matrix polymers generates not only mechanical changes, but also changes in the transport and diffusion of nutrients, drugs and pathogens through the tissue. We therefore investigate, in **chapter 4**, the diffusion of probe particles in a composite system of collagen and hyaluronan, and compare it to particle diffusion in single component networks. While in the two single-component systems we report simple diffusion, in the composite system the dynamics are characterized by cage-hopping, typical of systems presenting spatial heterogeneities, such as glassy-systems.

We then consider another composite system, that of fibrin and collagen, in **chapter 5**. This composite occurs during wound healing, where a provisional fibrin matrix is replaced in time by collagen. We first measure structural rearrangements induced by strain in the single-component systems by performing SAXS experiments complemented by rheology, and then extend these measurements to the composite system. We find that, for both networks, deformation is accompanied by fibre alignment. However, while for collagen network deformation is accompanied by fibril densification, for fibrin we could not detect any change in the fibrin packing order. We furthermore show that the composite system is mechanically weaker than the single component networks of collagen and fibrin, because collagen causes bundling of fibrin fibres.

In **chapter 6**, we focus on a peculiar state of matter of hyaluronic acid, obtained by inducing pH-triggered gelation, and characterized by a large increase in elasticity in a narrow range of pH. We quantify in detail the activation energy required for flow as a function of pH, temperature and molecular weight, and conclude that the acid-induced gel state can be described by a model whereby the entangled hyaluronan chains experience enhanced friction from hydrogen bonding association.

Finally, in **chapter 7** we conclude by providing a summary and brief discussion of the results we obtained in this thesis, and we propose potential future lines of research.

Acknowledgments

The sections “Mechanics of biopolymer networks”and “Mechanical enhancement in composite networks”are based on Ref. [6], written in collaboration with Y.Mulla (AMOLF), B.Vos (AMOLF) and A. Aufderhorst-Roberts (AMOLF).

2

Connectivity and plasticity determine collagen network fracture

Collagen forms the scaffold of connective tissues and is responsible for their mechanical strength. Tissues are remarkably resistant against mechanical deformations because collagen molecules hierarchically self-assemble in fibrous networks that stiffen with increasing strain. Nevertheless, collagen networks do fracture when tissues are overloaded or subject to pathological conditions such as aneurysms. Prior studies of the role of collagen in tissue fracture have mainly focussed on tendons, which contain highly aligned bundles of collagen. By contrast, little is known about fracture of the more disordered, isotropic collagen networks present in many other tissues such as skin and cartilage. Here, we combine experimental shear rheology and computer simulations of collagen networks to investigate the primary determinants of their fracture. We show that the fracture strain is controlled by the coordination number of the network junctions, with less connected networks fracturing at larger strains. We find, however, that plastic effects at the network and fibre level can fine-tune the fracture strain. Our findings imply that structural disorder provides a protective mechanism against network fracture that can optimize the strength of biological tissues.

Chapter based on: Burla, F.*, Dussi, S.*, Martinez-Torres, C., Tauber, J., van der Gucht, J., Koenderink, G.H. *Connectivity and plasticity determine collagen network fracture.* PNAS 117 (15), 2020.

2.1 Introduction

Collagen is the most abundant protein in the human body. Secreted in the extracellular space by cells, it assembles in networks of thick rope-like fibrils that shape and reinforce tissues and provide a scaffold for cell growth and movement [23]. The spatial organisation of these networks varies widely among tissues, from aligned bundles in tendons to randomly oriented (isotropic) networks in skin. Isotropic collagen networks tend to assemble through branching and crosslinking, where the number of fibres meeting at a junction is, respectively, three and four. As a result, the network connectivity is below the Maxwell criterion of six required for mechanical stability of random networks of springs [41, 56]. It was recently shown that the subisostatic architecture offers a great mechanical advantage for collagen networks, because it causes them to be soft at small deformations, which primarily cause fibril bending, yet stiff at large deformations, due to alignment and a transition from fibril bending to stretching [40, 41, 70]. Nevertheless, tissues still fracture when exposed to large deformations, especially in pathological conditions such as injuries [80], surgical interventions [81], aneurysms [82, 83] and hydraulic fracture of tumors [84, 85].

Fracture of collagen has so far mainly been investigated in tendons [86, 87], where collagen fibrils organize in long cable-like structures optimized to withstand large axial loads [88, 89]. Because of the unidirectional fibre orientations, the fracture of tendons is mainly governed by molecular properties of the fibrils, which vary among functionally distinct tendons [87] and change upon age-related enzymatic crosslinking reactions [90, 91] and during diseases [92]. However, collagen in many other connective tissues assembles in disordered networks that lack a preferential orientation. Examples are skin [93], cartilage [94], vitreous humour [95], and the aortae [96]. Interestingly, studies on aortae fracture in the context of aneurysms [83], as well as studied using tissue models [97–100], have revealed that isotropic tissues fracture at higher strain than aligned materials, because the propagation of cracks is contained. This observation suggests that isotropic networks might be optimized to withstand larger strains. However, a mechanistic understanding of the role of network architecture in tissue fracture is lacking, due to the complexity of living tissues.

Here, we investigate the mechanisms that govern fracture of collagen networks by performing quantitative measurements of shear-induced fracture of reconstituted collagen networks, both experimentally and computationally. Experimentally, we control the collagen structure from the network level (mesh-size and connectivity) down to the fibre level (diameter and intrafibrillar crosslinking) by reconstituting networks of collagen purified from different animal and tissue sources and by exploiting the known sensitivity of collagen self-assembly to the polymerisation temperature [101, 102]. By comparing our results against a computational model of

network fracture, we find that the connectivity of the network is the main determinant of collagen fracture. We can explain almost all of our findings by using a threshold strain for fibre fracture in the range of 10-20%, a range consistent with prior tensile tests on single collagen fibrils [103, 104]. Furthermore, the computational model enables us to assess the contributions of system size and detailed network and fibre properties on the fracture behaviour. We find that molecular effects, such as intrafibrillar crosslinking, and network properties, such as branching, modulate the fracture strain by setting the degree of plasticity. Our results are important not only for understanding how disorder protects collagen networks -and therefore, living tissues- from fracture, but also for the rational design of synthetic fibrillar materials resistant to strain-induced breakage.

2.2 Materials and methods

2.2.1 Sample preparation

Collagen networks were reconstituted from commercially available collagen purified from different animal species (cow, rat, human) and from different tissues (dermis, tendon) (see Supplementary Table 1). Moreover, we compared collagens obtained by two different extraction methods: telocollagen obtained by acid solubilisation, which has intact telopeptide end sequences necessary for interfibrillar crosslinking, and atelocollagen obtained by pepsin solubilisation, which lacks these telopeptides [101, 102]. Finally, we also compared two different fibril-forming collagen types: type I, which is ubiquitous in all tissues except cartilage, and type II, which is characteristic of cartilage [105]. All samples were prepared on ice, to prevent early collagen polymerisation, by first weighing collagen in an Eppendorf tube and subsequently adding water, 10x-concentrated PBS (Phosphate Buffered Saline, NaCl 0.138 M; KCl 0.0027 M, pH 7.4, Sigma Aldrich), and an adequate amount of 0.1 M NaOH (sodium hydroxide, Sigma Aldrich) in order to obtain the final desired concentration of collagen (0.5 or 1 mg/mL) in a solution of PBS and at a pH of 7.4. Each sample was subsequently vortexed for a few seconds and then quickly placed in the measurement cell (cone-plate geometry or plate-plate geometry for rheometry, glass flow cell for microscopy, Eppendorf tube for electron microscopy) to start polymerisation at the desired temperature. For the confocal rheometer experiments, we used a fluorescently tagged bacterial protein (CNA35-eGFP) that specifically binds to collagen fibrils[106] at a CNA/collagen molar ratio of 1:10.

2.2.2 Rheological measurements

Strain-stiffening and fracture experiments were performed using an Anton Paar Physica MCR501 rheometer, with a stainless steel, cone-plate geometry where the cone had a 40 mm diameter and 1°cone angle. We verified the absence of wall

slippage by repeating experiments with steel cone-plate cells with diameters of 20 and 30 mm. To test for gap size effects, we used plate-plate geometries with a gap of 100 μm, 250 μm, 500 μm or 750 μm and a diameter of 40 mm. Collagen solutions were allowed to polymerise for two hours between the rheometer plates at a constant temperature (27, 30, 34 or 37°C) maintained by a Peltier plate. During polymerisation, the evolution of the linear shear moduli was monitored with a small amplitude oscillatory strain (γ=0.5%, f=0.5 Hz) protocol. The steady-state values of the linear viscoelastic moduli reached after two hours were calculated as an average over the last ten data points of the polymerisation curve. We report averages of at least 3 independent measurements, while the error bars represent the standard error of the mean. After polymerisation, the nonlinear elastic response was measured using a well-established prestress protocol [107]. Briefly, a constant shear stress σ was applied for 30 s, to probe for network creep, and then an oscillatory stress $\delta\sigma$ was superposed with an amplitude of σ/10 and frequency of 0.5 Hz. The resulting differential strain $\delta\gamma$ was then used to calculate the differential (or tangent) modulus K'= $\delta\sigma/\delta\gamma$. To evaluate network fracture, we applied a linear strain ramp (with a loading rate of 0.5%/s) to the samples after polymerisation. The fracture strain of each network was calculated as the strain where the stress reached its peak value. To verify that fracture occurred inside the network rather than at the plates, we performed measurements at different strain rates (0.125 %/s, 1 %/s, 4 %/s) and we compared measurements for bare rheometer plates and for the rheometer plates coated with an adhesive layer by depositing, spreading and drying 30 μL of a solution of fibrinogen (10 mg/mL, Human plasma fibrinogen, Plasminogen, Enzyme Research Laboratories, UK) or poly-L-lysine (Poly-L-lysine solution, 0.1% w/v in H2O, Sigma Aldrich) before depositing the collagen gels. We assessed the degree of plasticity of the collagen networks by performing repeated strain ramps and measuring the hysteresis during each stress-strain cycle. Each strain ramp was performed for strains up to γ_p/2, where γ_p represents the fracture strain, previously determined for each type of collagen.

2.2.3 Confocal rheology measurements

Confocal rheology measurements were performed on a custom-built confocal rheometer consisting of a rheometer head (DSR 301, Anton Paar) mounted in a metal rack on top of an inverted microscope (DMIRB, Leica Microsystems) equipped with a confocal spinning disk (CSU22, Yokogawa Electric Corp.). The collagen networks were imaged using a 488 nm laser (Sapphire 488-30 CHRH, Coherent Inc., Utrecht, Netherlands) for excitation and a back-illuminated cooled EM-CCD camera (C9100, Hamamatsu Photonics, Germany) for detection. As a bottom plate, we used a circular glass coverslip (Menzel Glaeser, 40 mm), which was coated beforehand with poly-L-lysine (Sigma Aldrich) to promote attachment of the collagen network to the surface. To determine the gap size, the confocal head was manually lowered towards the glass bottom plate using a micrometer screw until the normal force

increased from 0 to 0.02 N, signalling contact with the surface. Subsequently, the rheometer head was raised again from this reference point, the sample was loaded and the gap manually closed to the desired gap size. The experiments were performed at a gap of 0.5 mm and with an upper steel plate with a diameter of 20 mm. Samples were polymerised in situ at 22°C and solvent evaporation was prevented by placing a thin layer of mineral oil (Sigma Aldrich) around the measuring geometry. The samples were allowed to polymerise for at least two hours, while the elastic and viscous moduli were monitored by applying small oscillations with a strain amplitude of 0.5% and frequency of 0.5 Hz. Afterwards, a linear strain ramp was applied, analogous to the standard rheology protocol described above, while the network was imaged at a confocal plane located 20 μm above the bottom surface. Time-lapse videos were collected during the strain ramp at a frame rate of 2 fps and exposure time of 500 ms. After fracture (as evident from a drop of the shear stress), we verified that the network had not detached from the lower plate by acquiring a z-stack from the bottom plate upwards, up till a height of 20 μm into the sample, and inspecting the z-stack projection from the side.

2.2.4 Confocal microscopy imaging

Confocal data for quantification of the network mesh size were obtained with an inverted Eclipse Ti microscope (Nikon, Tokyo, Japan) using 40x and 100x oil immersion objectives with numerical apertures of 1.30 and 1.49, respectively (Nikon, Tokyo, Japan). The networks were imaged in confocal reflectance mode with a 488 nm Argon laser for illumination (Melles Griot, Albuquerque, NM). The networks were prepared in dedicated sample holders composed of two coverslips (Menzel Microscope Coverslips 24x60mm, #1, Thermo Scientific) separated by a silicon chamber (Grace Bio-Labs CultureWell chambered coverglass, Sigma Aldrich). The sample holders were subsequently placed in a petri dish wrapped with humidified tissues and closed by parafilm, in order to prevent sample dehydration, and then placed in a warm room (37°C) or in a temperature-controlled oven (for polymerisation at 34°C-30°C-27°C) to allow collagen polymerisation for at least two hours before observation. The data are shown as maximum intensity projections obtained with ImageJ [108]. Image stacks were acquired starting at a height of 10 μm above the coverslip to avoid surface effects, over a total depth of 20 μm, and with a step size of 0.5 μm.

2.2.5 Mesh size analysis

The mesh size of the collagen networks was determined with a custom-written Python code, according to a previously published protocol [109]. Briefly, a z-stack of images was background subtracted, thresholded and binarised with the Otsu method in ImageJ [108] and the Python program was used to count the distance between on and off pixels in each image, for each row and column. The distance distributions

were fitted to an exponential function. The characteristic $1/e$ distance was converted from pixel to micron and taken as the average mesh size.

2.2.6 Scanning Electron Microscopy

The samples for scanning electron microscopy were prepared following a previously established protocol [110]. Collagen networks were formed overnight in Eppendorf tubes at 0.5 or 1 mg/mL. The samples were washed three times for 60 minutes each with sodium cacodylate buffer (50 mM cacodylate, 150 mM NaCl, pH 7.4) obtained by mixing Cacodylic acid sodium salt (Sigma Aldrich), 0.2 M HCl and milliQ water. The samples were fixed with 2.5% glutaraldehyde in sodium cacodylate for at least two hours, washed again three times with cacodylate buffer at room temperature, and dehydrated with a stepwise increasing percentage of ethanol in milliQ water by sequential 10-20 min incubations (30, 50, 70, 80, 90, 95%). Finally, the samples were washed with 50% HMDS (hexamethyldisilazane, Sigma Aldrich) in ethanol and 100% HMDS. HMDS was pipetted out and the Eppendorf tubes were left open overnight in order to dry. Subsequently, the samples were mounted on a support with carbon tape and covered with a 11-14 nm layer of palladium gold with a sputtercoater (Leica EM ACE600). The samples were then imaged with a Scanning Electron Microscope (Verios 460, FEI, Eindhoven, the Netherlands). To determine the fibril diameters, we manually analysed images taken at a magnification of 80000x, by drawing segments perpendicular to a collagen fibril and then measuring the distance between the edges. To prevent bias, we overlaid a grid of 500x500 nm onto each image through the ImageJ grid plugin, and measured the fibrils at the intersections of the crosses. We note that the measured fibril diameters are semi-quantitative because the sample preparation for electron microscopy introduces fibril shrinkage from drying but also fibril thickening due to metal deposition, while imaging in vacuum also introduces fibril shrinkage. This does not influence our conclusions, because the diameter data are only used as a relative measure between different collagen networks.

2.2.7 Determination of onset and critical strain for collagen

The non-linear rheology data (differential elastic modulus as a function of shear stress) were evaluated using a custom-written Python routine. We determined the onset strain where strain-stiffening first sets in by plotting K'/σ as a function of σ, performing a cubic spline interpolation, and determining the stress where K'/σ reached a minimum. We called this the onset stress σ_o, and the associated strain, onset strain γ_o. The critical strain γ_c was the strain at which the derivative of log K' as a function of log γ attained its maximum value . The characteristic strain values reported are averages with standard error of the mean of at least three independent measurements.

2.2.8 Determination of structural and mechanical properties of collagen from rheology data

It was previously shown that the nonlinear elastic response of collagen networks is quantitatively described by a theoretical model of athermal networks of rigid beams [41, 60]. Specifically, the increase of the differential modulus K' with increasing shear strain γ obeys the following equation of state:

$$\frac{\tilde{\kappa}}{|\Delta\gamma|^{\Phi}} = \frac{K'}{|\Delta\gamma|^{f}} \left(\pm 1 + \frac{K'^{\frac{1}{f}}}{\Delta\gamma} \right)^{(\phi - f)} \tag{2.1}$$

where $\tilde{\kappa}$ represents the dimensionless bending rigidity, defined as the ratio between the fibril bending modulus κ and stretch modulus μ, $|\Delta\gamma|$ is the distance between the measured strain and the critical strain γ_c, and ϕ and f are critical exponents controlling the transition from the bend-dominated to the stretch-dominated regime. The critical strain and the critical exponents depend on the network architecture through its average connectivity z and can be determined from computer simulations of 2D random lattice networks [60]. From this same comparison between experiments and simulations, we could also obtain the corresponding values of f and ϕ. Next, we used these parameters as input to fit the experimental strain-stiffening curves to Eq. 1, using the dimensionless bending rigidity of the fibrils $\tilde{\kappa}$ as the fitting parameter (see Supplementary Table 2).

2.2.9 Computer simulations of fibril networks

We performed athermal and quasistatic shear simulations of elastic networks composed of L by L nodes (or L_x by L_y nodes in cases where the simulation box was asymmetric). In line with previous studies [40, 41, 60, 70], we chose a phantom network architecture that has been proven to capture the essential coarse-grained features controlling the mechanics of collagen networks. The phantomisation procedure is as follows: (i) starting from a triangular lattice with unit spacing, only two of the three fibrils meeting at the same node are cross-linked; (ii) for each fibril at least one segment is randomly removed to avoid unphysical system-spanning bonds; (iii) the desired average connectivity z is achieved by diluting the network, i.e. by randomly removing a fraction 1-p of bonds, yielding z=4p. In the simplest model considered in this study, each bond was modelled as an elastic linear (Hookean) spring with unit stiffness and rest length equal to the lattice spacing (set to unity). All springs have the same rupture threshold λ and break irreversibly when their deformation exceeds λ. To test for the influence of fibril plasticity, we finally performed simulations where we allowed for spring lengthening: as soon as the spring length reaches l_m, its rest length increases to r_2. The relation $l_m + r_2 - 2r_1 < \lambda$ must hold, otherwise spring lengthening would occur after bond rupture (inaccessible region above the line in Fig. 4d). In all cases, networks were subjected to a shear

deformation. Bonds were broken one at a time (if any), starting from the weakest (the one that exceeded λ the most) and performing energy minimization in between fracture events. The mechanical response was quantified via the shear stress σ calculated using the xy-component of the virial stress tensor. Quantities (σ and K') were expressed in reduced units and averaged over a sufficiently large number of configurations, ranging from 500 for L=24 to 20 for L=256.

2.3 Results

To test the mechanical resistance of collagen networks against fracture, we perform rheology experiments on reconstituted collagen networks polymerised between the plates of a custom-built confocal rheometer. The bottom plate of the rheometer is stationary and optically transparent, to allow direct visualization of changes in network structure in response to mechanical deformation using an inverted confocal microscope (Figure 1a). In order to assess collagen fracture, we apply a linear strain ramp γ on the networks by rotating the top plate and measuring the resulting shear stress σ. As illustrated in Figure 1b, the stress initially increases linearly with strain, as expected in the linear elastic regime. However, above a threshold strain, the stress starts to deviate from this linear behaviour and shows an upturn indicative of network stiffening, eventually reaching a maximum value, which we call the peak stress σ_p, associated to a peak strain γ_p. Beyond the stress peak, the shear stress decreases, which is symptomatic of fracture. Images taken during the strain ramp at a fixed height of 20 μm above the bottom plate of the rheometer indeed reveal network fracture (Fig. 1c). However, fracture is always first observed at strains beyond γ_p (see Supplementary Figs. S1-S2), as signalled also from the decrease in intensity of the sample. This may be partly explained from the fact that the macroscopic strain we report here corresponds to the strain at the edge of the sample, while our imaging area is located at a radial distance of 1/2 of the plate radius from the centre so the local strain is only 50% of the macroscopic strain. Additionally, it is possible that cracks first form in areas outside the field of view and are observable only once they propagate to the field of view. In some cases, the plane of fracture is localized above the imaging plane and we cannot observe network fracture at all. Imaging of the post-fracture samples over an extended height range confirms that fracture always occurred in the middle of the sample rather than at the bottom plate (Supplementary Fig. S3).

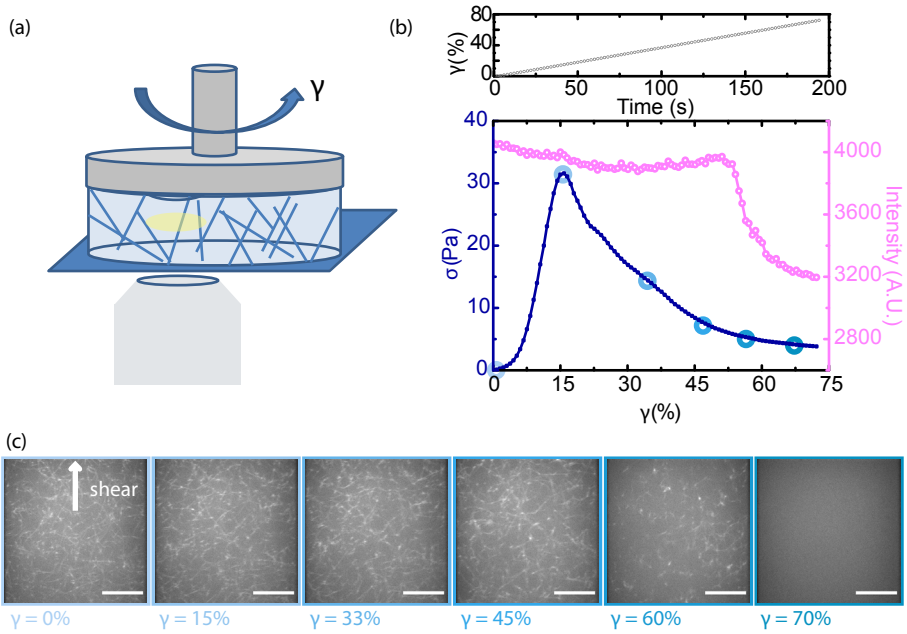

Figure 2.1: Fracture of reconstituted collagen networks under a shear deformation. (a) Schematic of the experimental setup, which combines a parallel plate rheometer with a steel top plate to apply a shear strain γ and a transparent bottom plate to allow for imaging of the collagen network with an inverted spinning disc confocal microscope. We image a horizontal (xy) plane at a fixed distance (20 μm) away from the bottom surface (yellow-shaded region) and shifted by 1/2 of the plate radius from the centre of the sample where the local strain is 50% of the strain at the edge that is reported by the rheometer. (b) Imposed linear strain ramp (top) and example measurement of the shear stress σ (blue, left-hand y-axis) as a function of shear strain γ for a 1 mg/mL network of bovine dermal telocollagen polymerised at 25°C. The total fluorescence intensity of the confocal plane is also shown (pink, right-hand y-axis). (c) Confocal fluorescence images of the network labelled with eGFP-CNA35, at various strain levels (see legend) that correspond to the circles in panel (b). Scale bar is 10 μm. The arrow labelled 'shear' indicates the direction of flow.

In order to understand which structural parameters are predictive of collagen network fracture, we prepare networks with a wide range of architectures by using collagen extracted from different animal and tissue sources and by polymerising the networks at different temperatures [60] (Figure 2a). We are thus able to control the structure both at the network level (mesh size and coordination number) and at the single-fibre level (diameter) (see Figure 2b and quantification in Supplementary Fig. S4). Furthermore, we vary the bending rigidity of the fibrils by comparing collagen molecules with and without telopeptide end sequences, disordered extension of the collagen triple helix which favours intrafibrillar crosslinking [111]. When we subject collagen networks to the strain ramp protocol, we measure peak strains γ_p over a remarkably large range, from 20% all the way up to nearly 90% (see Figure 2c).

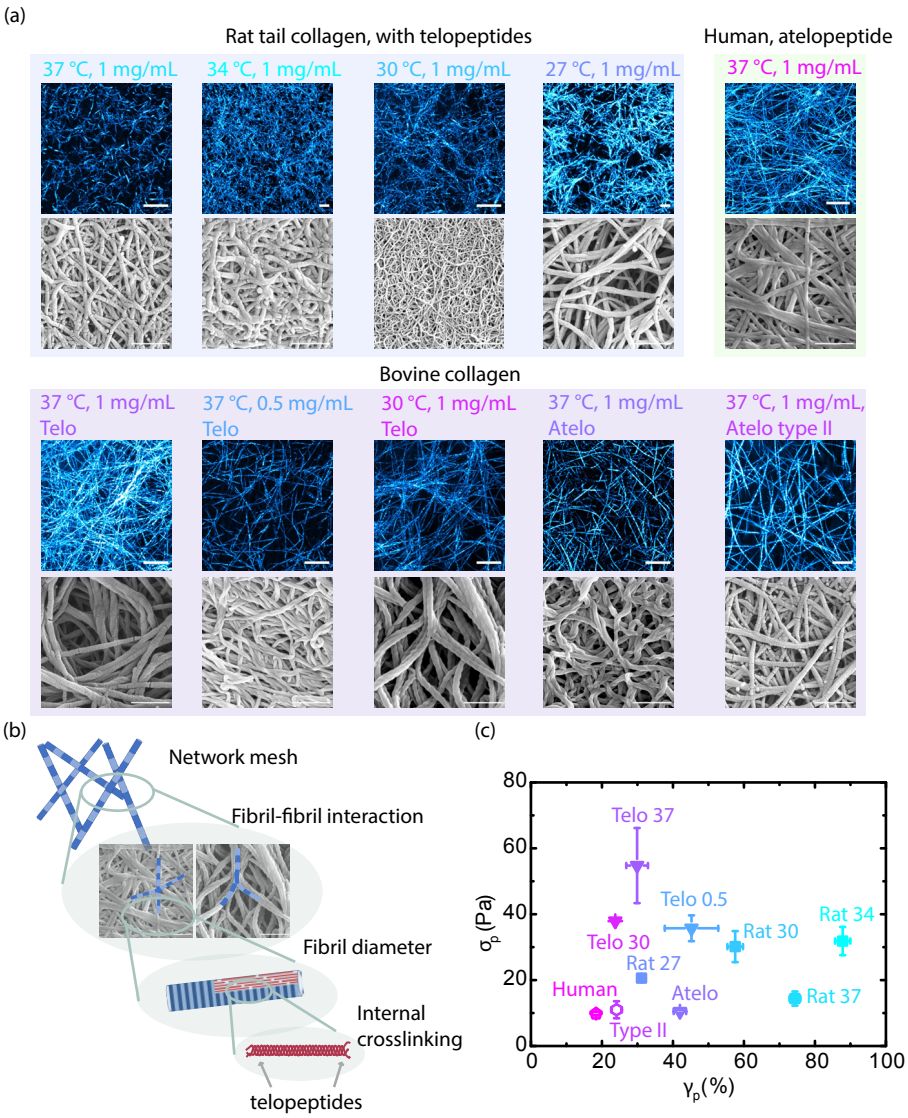

Figure 2.2: The strain where collagen networks fracture varies with network structure. (a) Top rows: confocal reflectance images of collagen networks (scale bar: 10 μm); bottom rows: corresponding scanning electron microscopy images (scale bar: 1 μm). The networks were assembled from collagens from different animals, tissues, and at different temperatures (see Supplementary Table 1). (b) Collagen networks possess a hierarchical structure that can differ at the network level (mesh size), fibril-fibril interaction level (junctions formed either by branching or fibril-fibril crossings), fibril properties (diameter) and intrafibrillar crosslinking via telopeptide end regions. (c) Overview of peak strains and stresses at rupture for the entire range of collagen networks. Same symbol shapes indicate same animal and tissues, open symbols refer to collagens without telopeptides (uncrosslinked fibrils) while closed symbols refer to telocollagens (crosslinked fibrils).

The peak strains are independent of strain rate and plate diameter (Supplementary

Figs. S5-S6), suggesting that the networks fail cohesively and not at the interface with the rheometer plate. We notice a slight dependence on the surface chemistry (Supplementary Figure S7) which is, anyway, small compared to the range over which the strain varies.

We do find a strong correlation between the rupture strain and the critical strain, the strain at which the networks transition from the soft bend-dominated regime to the rigid stretch dominated regime (Figure 3a inset). A potential explanation for this correlation could be that the rupture strain, like the critical strain, is controlled by the collagen networks' average connectivity [40, 41, 60]. By mapping the nonlinear elastic response and in particular the critical strain measured by shear rheology onto computational predictions for fibrillar networks, we can extract the network average connectivity. This mapping method was recently validated for collagen networks over a wide range of connectivities [60]. We find that our collagen networks have average connectivities ranging between 2.9 and 3.7, spanning the range between mostly branched (z=3) and mostly crosslinked (z=4) (see Supplementary Fig. S8), and the fracture strain monotonically decreases from ~90% for z=2.9 to ~20% for z=3.7 (see Figure 3a and Supplementary Fig. S9). By contrast, we observe no correlation of the fracture strain with the parameters characterizing the fibres themselves, such as the fibres' diameter and bending rigidity, nor with the network mesh size (Supplementary Fig. S10). Our experimental findings therefore strongly suggest that the network connectivity is the dominant factor in setting the rupture strain.

This observation is consistent with recent simulations and experiments on other disordered systems, including elastic spring networks and metamaterials, whose fracture is governed by connectivity [112–115]. We therefore compare our results to fracture simulations of coarse-grained fibre networks composed of L by L nodes, where each bond is modelled as an elastic spring that fractures irreversibly when its axial deformation exceeds a certain rupture threshold strain λ. When we apply a shear deformation to the simulated networks, bonds align along the direction of the deformation and the network strain-stiffens (Fig. 3b), consistent with earlier findings [40, 41]. In the strain-stiffening regime, the stress is heterogeneously distributed, concentrating in regions of aligned load-bearing bonds referred to as force chains. The lower the average network connectivity, the more heterogeneous is the stress distribution (see Supplementary Fig. S11). Above a threshold shear strain, bonds first start fracturing in an uncorrelated fashion and some force chains disappear, while new ones appear. When the strain reaches γ_p, an individual fracturing event triggers the formation of a large crack (see middle and right snapshots in Fig. 3b). Although this crack has not yet propagated through the entire sample, it does cause a large and abrupt stress drop. After the peak, the stress has not completely vanished and small drops are observed, indicative of the breakage of the remaining few force chains.

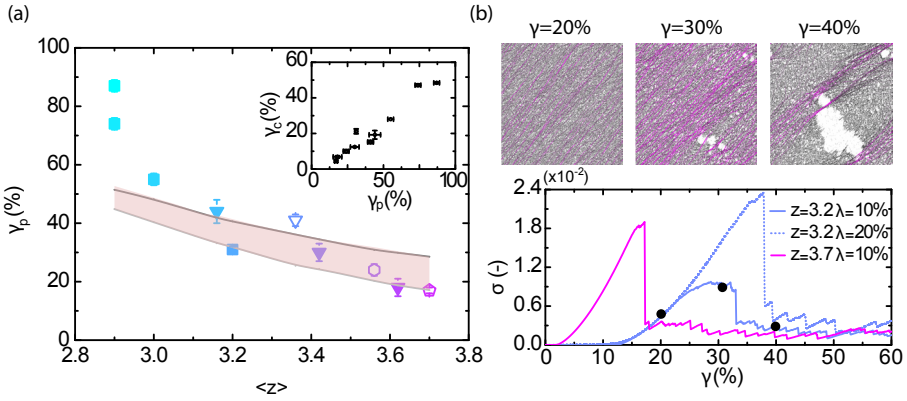

Figure 2.3: Rupture experiments on collagen networks and simulations on subisostatic spring networks both show that the average network connectivity governs the rupture strain. (a) Experimentally measured (same symbols as in Figure 2c) and simulated (lines) peak strain as a function of the average connectivity z. The simulations were performed for two fibril rupture thresholds (λ=10 and 20%, see legend) that bracket the physiologically relevant range. The inset shows the correlation between the measured critical strain γ_c and the peak strain γ_p. Experimentally, z is inferred from γ_c by mapping the strain-stiffening response on simulations. (b) Example simulations of network fracture. Upper panels: simulation snapshots for a network with z=3.2 and λ=10% at shear strains of 10% (before fracture), 20% (peak stress) and 30% (post-rupture). Springs are coloured according to their axial deformation (grey to pink, low to high). Lower panel: stress-strain curves for large networks (L=256) with z=3.7 and λ=10% (pink), z=3.2 and λ=10% (solid blue), and z=3.2 and λ=20% (dashed blue). Black circles correspond to the snapshots in the upper panel.

To test whether this simple model can account for the connectivity-dependent fracture of collagen network, we performed a series of simulations for networks with different connectivity within the experimental range. We assume a rupture threshold λ of either 10 or 20%, bracketing the range observed in single-fibril rupture experiments [103, 104]. As shown in Fig. 3a, the simulations indeed captured the experimentally measured dependence of the fracture strain on connectivity rather well. Although collagen fibres have a finite bending rigidity, additional simulations show that bending plays a negligible role in fracture, as fracture always occurs at large enough strains, where the networks have already undergone the transition from the bending- to the stretching-dominated regime (data not shown). We note that the post-peak behaviour in experiments and simulations is different: the stress-strain curves show an abrupt post-peak behaviour indicative of brittle fracture for the simulations (Figure 3b), while the experimental stress-strain curves exhibit a more gentle, ductile fracture (Supplementary Fig. S9). We ascribe this difference to the different system sizes in experiments and simulations. To prove this point, we first verify that simulations of sheared networks reveal more brittle fracture with increasing system size (see Supplementary Fig. S12), in accordance with recent simulations of networks under tension [115]. We then perform fracture

experiments for varying gap sizes and again observe a size-dependent change in ductility (see Supplementary Figure S12), even though the peak strain shows no gap size dependence for gaps larger than 200 μm (Supplementary Figure S13), in accordance with a previous study [116]. Finally, to further close the gap between the system sizes in simulations and experiments, we perform simulations keeping the vertical dimension L_y fixed while increasing the lateral size L_x, in order to mimic the experimental conditions, where the lateral dimensions (4 cm) are almost two orders of magnitude larger than the gap size. We find that the post-peak stress-strain response indeed becomes smoother with increasing L_x (Supplementary Fig. S12), capturing the experimental response.

Interestingly, we notice that for low connectivity (between 2.9 and 3.0) the experimentally measured peak strain is systematically higher than the predictions. The model we use here consider perfectly elastic networks, while collagen has been shown to present plastic behaviour. Plastic mechanisms can occur either at the network level, with opening up of branches, or at the fibre level, where fibril lengthening can occur via monomer sliding [117–119](See Figure 4a). We expect sliding to be particularly prominent in case of the non-crosslinked fibrils formed from collagen molecules that lack telopeptides. To experimentally test fibril plasticity, we perform cyclic strain ramp tests (with a maximum strain equal to $\gamma_p/2$ to prevent fracture), comparing two bovine collagen molecules that gave networks with a similar connectivity (z~3.4) but where one collagen lacked telopeptides ('atelo'), while the other had intact telopeptides ('telo'). To test for network plasticity, we instead compared collagens that were both crosslinked via telopeptides but had different connectivities: telocollagen from bovine dermal skin (z=3.42) and rat tail collagen (z=2.9). As shown in Fig. 4b, we observe a larger hysteresis between the loading and unloading curves for the non-crosslinked collagen compared to the crosslinked variant, and a higher hysteresis for the z=2.9 (rat tail) collagen as compared to the z=3.42 (bovine) collagen, consistent with more pronounced plasticity for networks with lower connectivity. We furthermore observe that non-crosslinked collagen is softer than the crosslinked one, and exhibits a larger softening interval before fracture, consistent with a higher degree of plasticity (see Supplementary Figure S14).

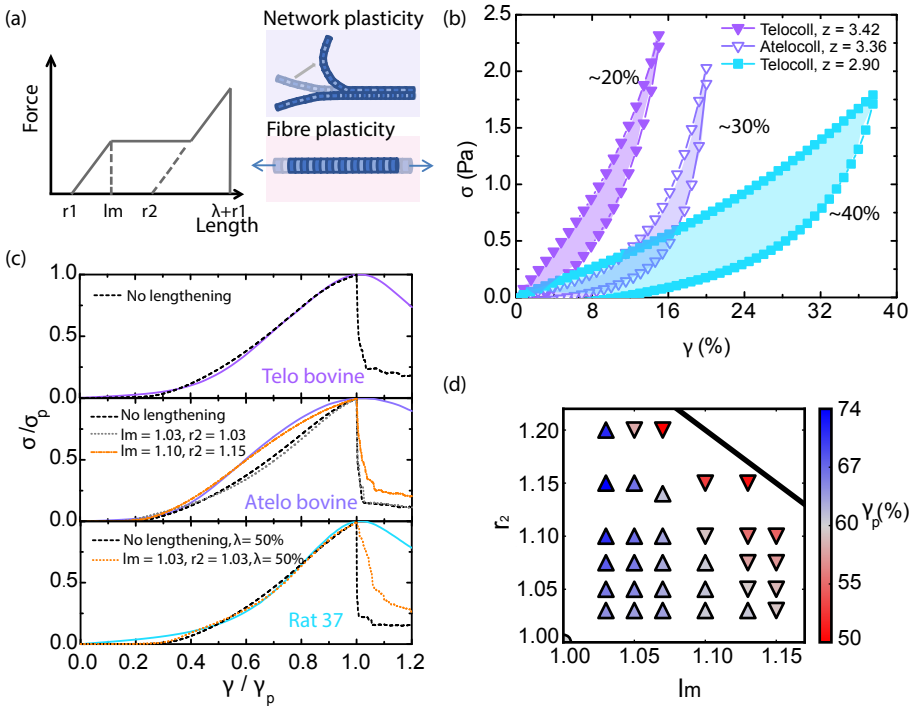

Figure 2.4: The influence of plasticity on the fracture of collagen networks. (a) Plasticity effects are implemented in the model by allowing spring lengthening based on two control parameters: the onset axial strain for fibril lengthening l_m and the increase in length r_2. Plasticity can occur at the network-level due to branch/bundle opening (top schematic) and at the fibril-level due to fibril lengthening (bottom schematic). (b) Experimental shear rheology cycles measured for three different collagen networks (see legend). The normalised dissipated work W calculated from the areas under the loading and unloading curves according to $W = (A_{load} - A_{unload})/(A_{load} + A_{unload})$ is indicated next to each curve. Larger values indicate larger dissipation, meaning larger plasticity. (c) Direct comparison of normalized stress-strain curves from experiments (averaged over 3 samples) and from simulations (averaged over 20 configurations with L=256). Top: the response of telocollagen (Telo bovine) networks agrees with simulations of fibrils that do not lengthen (top). Middle: the response of atelocollagen (Atelo bovine) networks reveals significant lengthening. Bottom: for telocollagen networks with low connectivity (Rat 37, bottom), the experimental curve matches with simulations only if we assume either an unrealistically large fibril rupture threshold λ or fibre plasticity. (d) Phase space for the network peak strain γ_p of simulated networks (L=256, z=2.9, λ=30%, representative of Rat 37) as a function of l_m and r_2. Symbols are color-coded according to the value of γ_p (see color bar). Up triangles indicate enhanced γ_p compared to the elastic limit (no lengthening) while down triangles indicate reduced γ_p.

In order to get more insight in the influence of branch and fibre plasticity on network fracture, we finally consider the shape of the stress-strain curves. We compare simulations and experiments by normalizing the curves with respect to

the peak strain γ_p and stress σ_p (Fig. 4c), focussing on the interval $0.6 < \gamma/\gamma_p < 0.9$ (see Supplementary Figure S15). For crosslinked (telocollagen) networks, we find that the experiments agree well with simulations of networks that do not consider any plastic effects (Fig. 4c (top)). By contrast, the stress-strain curves of low-connectivity and uncrosslinked networks can only be mapped onto the simulations if we allow for bond lengthening before fracture. We implement bond lengthening in the simulations by allowing the elastic springs to extend above a lengthening threshold l_m. For simplicity, we assume that when the spring length reaches l_m, the rest length permanently changes from its initial value r_1=1 to a value $r_2 > r_1$. As before, we assume that the springs furthermore irreversibly break as soon as their deformation exceeds λ (i.e. their length is $r_1+\lambda$), as shown in Fig. 4a. For comparison with the experiments, we scan different combinations of l_m and r_2 and, as shown in Fig. 5c (middle), we obtain a good match between measurements on (bovine) atelocollagen networks and simulations only for $l_m \sim 1.10$. An onset strain of 10% for fibre lengthening is consistent with previous tensile measurements on isolated collagen fibrils [120–122]. By contrast, for the telocollagen (rat-tail) networks (Rat 37, z=2.9) we only find reasonable agreement with simulations for values of $l_m \sim 1.03$ (Fig. 4c, bottom). This small value of l_m suggests that network-level plasticity, rather than fibril lengthening, modulates the fracture of these loosely connected (z∼3) networks.

The two parameters l_m and r_2 control the onset and degree of plastic effects due to bond lengthening in the simulations. As shown in Fig. 4d (where we fixed the rupture threshold λ=30%), networks with bond lengthening (blue up-pointing triangles) only have an enhanced peak strain γ_p compared to the elastic limit (no lengthening) in case of small l_m. By contrast, networks with larger l_m fracture earlier (red down-pointing triangles) than in the absence of lengthening. Apparently, lengthening effects are not always beneficial for delaying fracture. This can be rationalised with the fact that the stress distribution is highly heterogeneous for networks with low connectivity, where very few bonds are highly stressed (Supplementary Fig. 11). Lengthening is beneficial for alleviating stress concentration in these few bonds only if it occurs at small deformation (small l_m). If the lengthening occurs at large l_m, the already high stress carried by the few bonds will not be efficiently redistributed in the network due to its low connectivity. As a consequence, these few bonds will lengthen without releasing enough stress to their neighbours and will subsequently fracture. These springs thus have an effective rupture threshold, determined by l_m, lower than their intrinsic threshold λ, and the entire network will fracture earlier than in the elastic limit. Future studies should employ less coarse-grained models, able to describe the mechanical response of bundles and branches, to further unveil the microscopic origin of these toughening mechanisms.

2.4 Conclusions

Collagen forms the scaffold of living tissues, where it is often present in the form of a network of disordered fibrils with random orientation. Large mechanical stress and pathological situations such as aneurysms can threaten the mechanical integrity of collagenous tissues. Prior studies showed that fracture of tendons, which feature a strongly anisotropic collagen structure, is governed by the molecular makeup of collagen fibers. Here, we show that fracture of isotropic collagen networks representative of tissues such as skin and cartilage is instead governed by the average connectivity z. Our findings imply that orientational disorder combined with subisostatic connectivity protect collagen networks against fracture. This correlation between network fracture strain and connectivity is similar to that found in simpler elastic networks, such as spring networks and metamaterials, which lack the hierarchical complexity of collagen. Plasticity in the form of branch opening or fiber lengthening can provide additional protection of collagen networks, delaying the onset of fracture to larger strains by introducing extra stored length. Our computational model provides a minimal yet powerful way to predict the fracture strain of collagenous tissues and other fibrillar materials from first principles. Our findings provide new routes to design strong fibrous materials based on the combination of a random subisostatic architecture with controlled plasticity at the network or fibril scale [123].

Acknowledgments

The work presented in this chapter was performed in close collaboration with S. Dussi (WUR), J. Tauber (WUR) and J. van der Gucht (WUR), who developed and performed all the simulations described in this chapter and C. Martinez-Torres (TUDelft) who helped with the acquisition of the SEM images. We gratefully acknowledge Fred C. MacKintosh for extensive scientific discussions and M. Dompé (WUR) for a critical reading of the manuscript. M. van Hecke (AMOLF/Leiden) for kindly lending us the confocal rheometer head and critically reading the manuscript; M. Verweij, J.B. Aans and D.-J. Spaanderman for help with building the confocal rheometer; and M. Vinkenoog for help with CNA35 protein purification. The work of F.B. and G.H.K. is part of the Industrial Partnership Programme Hybrid Soft Materials that is carried out under an agreement between Unilever Research and Development B.V. and the Netherlands Organisation for Scientific Research (NWO). The work of S.D, J.T. and J.v.d.G. is part of the SOFTBREAK project funded by the European Research Council (ERC Consolidator Grant).

2.5 Supplementary Figures

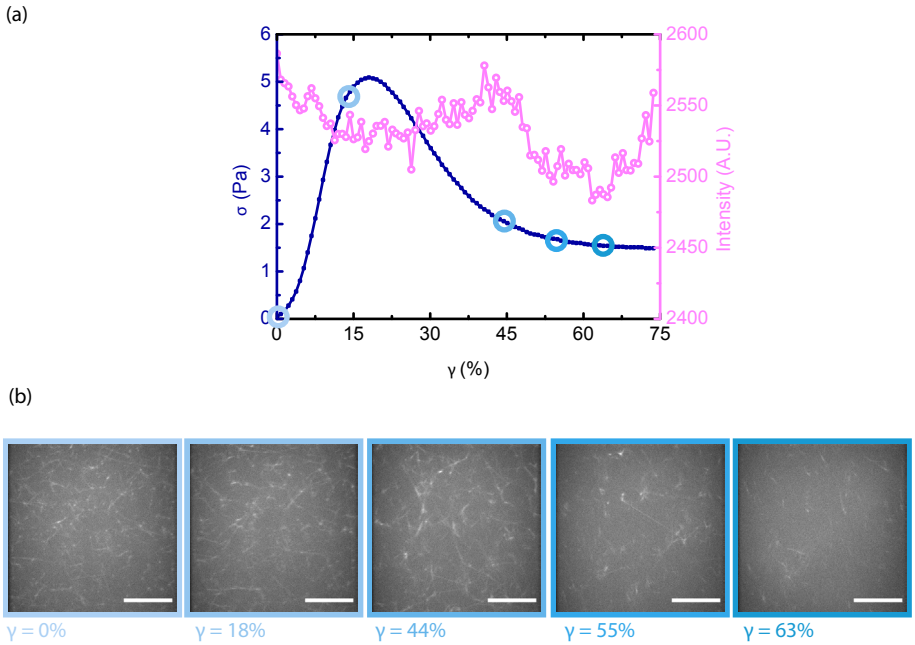

Supplementary Figure 1: Shear-induced rupture of a bovine telocollagen network visualized with confocal rheology. Analogously to Figure 1 in the main text, panel (a) shows the stress-strain curve recorded with the rheometer (blue, left-hand y-axis) and the total intensity of the confocal plane imaged by spinning disc confocal microscopy (purple, right-hand y-axis), while panel (b) shows selected snapshots of the network (single confocal slices) at different levels of applied shear strain (see legend). The measurement was performed for a 1 mg/mL bovine dermal telocollagen network polymerised at 22°C and fluorescently labelled with CNA35. Scale bar is 10 μm.

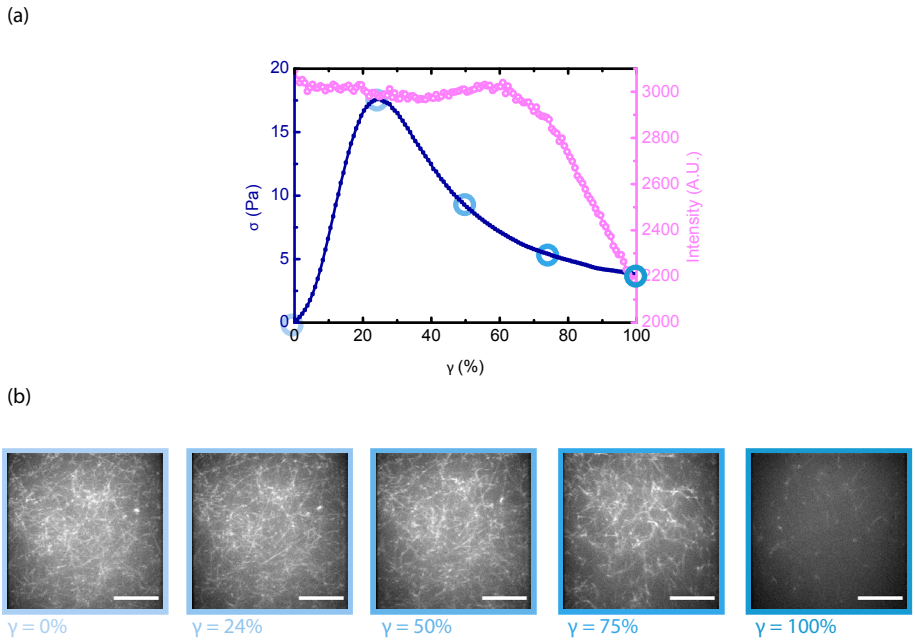

Supplementary Figure 2: Shear-induced rupture of a rat tail collagen network visualized with confocal rheology. (a) Stress-strain curve recorded with the rheometer (blue, left-hand y-axis) and total fluorescence intensity of a confocal slice recorded by spinning disc confocal microscopy (purple, right-hand y-axis). (b) Selected snapshots (single confocal slices) of the network obtained at a distance of 20 μm above the bottom surface at different levels of applied shear strain (see legend). The measurement was performed for a 1 mg/mL rat tail telocollagen network polymerised at 22°C and fluorescently labelled with CNA35. Scale bar is 10 μm.

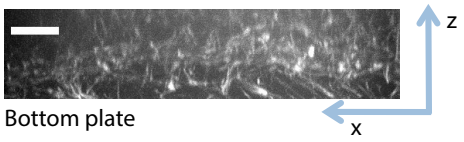

Supplementary Figure 3: Post-rupture confocal fluorescence z-stack of a collagen network. Y-projection of a confocal z-stack recorded by spinning disc confocal microscopy for a bovine telopeptide collagen network after shear-induced rupture. The scale bar is 5 μm in the x direction and the total z height is 20 μm. The presence of connected fibres on the bottom plate suggests that network failure is cohesive and not due to detachment from the lower surface.

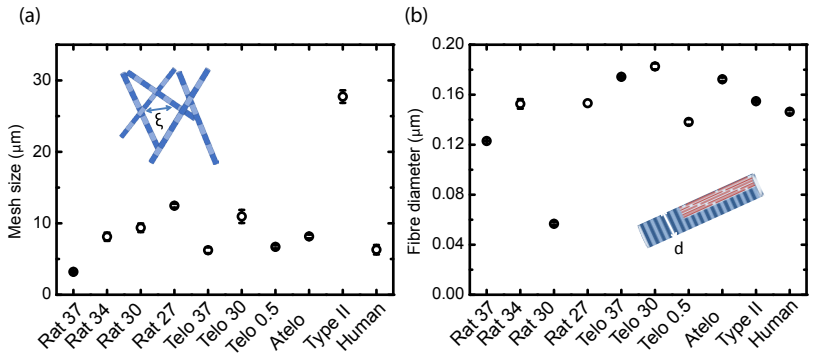

Supplementary Figure 4: Mesh size and fibre diameters of the collagen networks. (a) Mesh size ξ for the entire range of collagen networks obtained from confocal reflectance images. Data are averages over measurements on three independently prepared samples, and error bars represent the standard error of the mean. (b) Corresponding average fiber diameter d obtained from scanning electron microscopy images. Data are averages over at least 100 different fibres in different regions of each sample (one sample per condition), and error bars represent standard error of the mean.

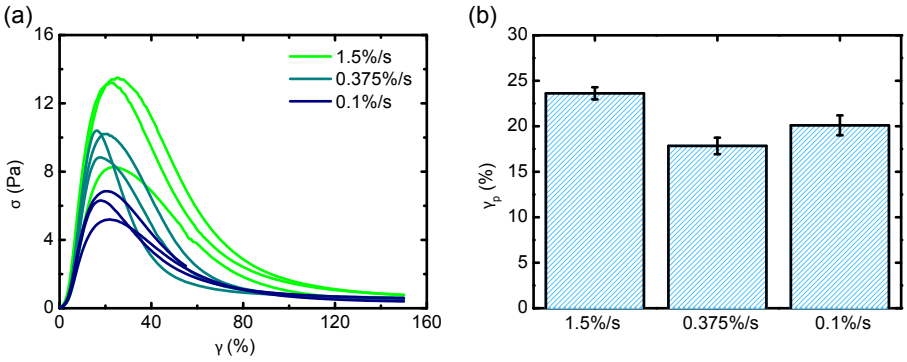

Supplementary Figure 5: The peak strain of collagen networks is independent of shear rate. (a) Stress-strain curves measured for 1 mg/mL human atelocollagen networks during strain ramps performed at different strain rates between 0.1%/s and 1.5 %/s (legend). The peak strain γ_p shows little variation with strain rate. Each curve represents a single experiment. (b) Peak strain γ_p for the three different strain rates, showing averages of three independent measurements ± S.E.M. Note that 0.375%/s is the strain rate used for the majority of our experiments.

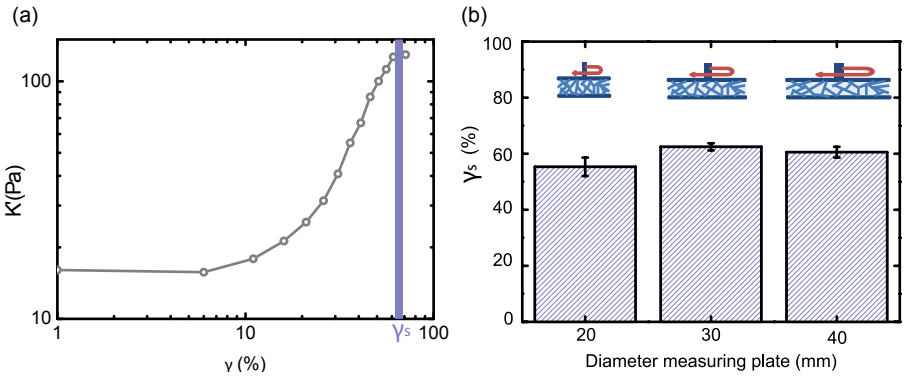

Supplementary Figure 6: Independence of the softening strain on the diameter of the cone-plate measuring geometry as measured with a stress-ramp (0.1 Pa/s). (a) Determination of softening strain from a stress-ramp for a rat tail collagen network at 37°C. The softening strain is defined as the strain where the differential elastic modulus K' is maximal. (b) Average softening strain for three different rheometer plate diameters (see legend). Data are averages of three independent measurements ± S.E.M.

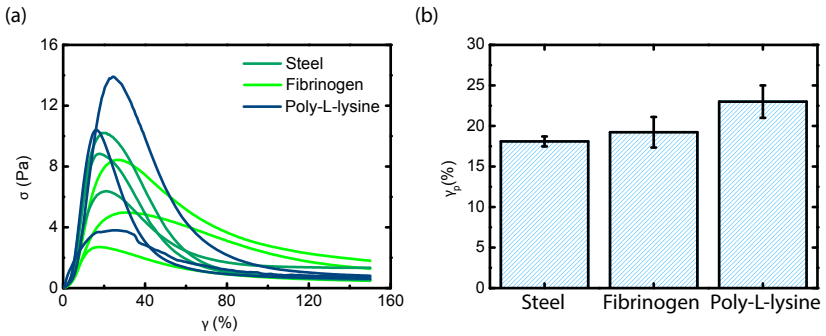

Supplementary Figure 7: The peak strain of collagen networks is roughly independent of the surface chemistry of the rheometer plates. (a) Stress-strain curves of 1 mg/ml human atelocollagen networks measured with uncoated steel plates (petrol) and for plates coated with either an adhesive fibrinogen-coating (green) or a poly-L-lysine coating (blue). While the peak strain is consistent, the peak stress varies because of intrinsic sample-to-sample variations in the elastic modulus of the networks. Each curve represents a single experiment. (b) Average peak strain for the different surface chemistry, shown as the average of three independent measurements ± S.E.M.

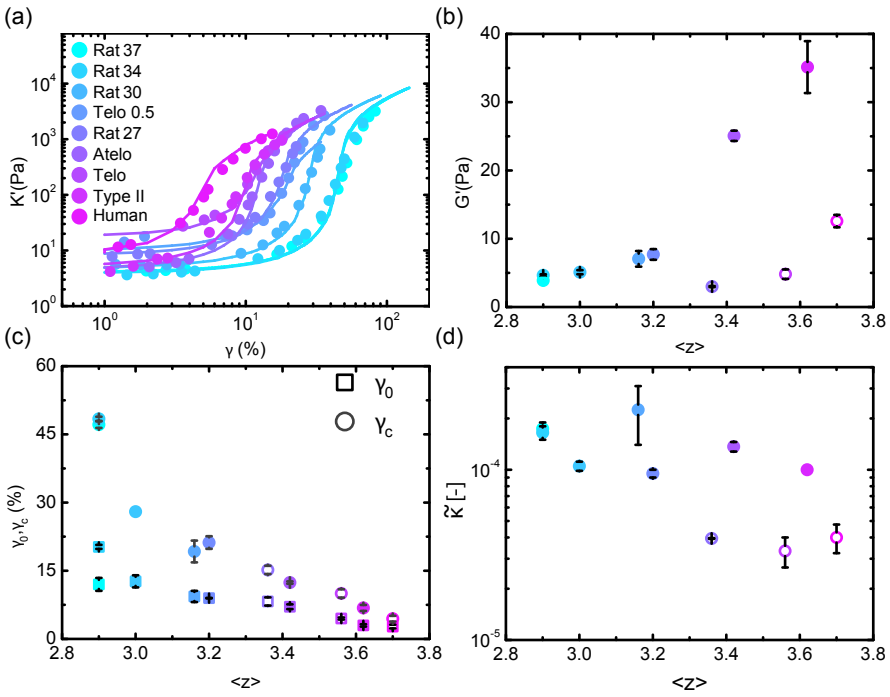

Supplementary Figure 8: Determination of the connectivity and dimensionless bending rigidity of the collagen networks by calibrating rheology data with simulations of disordered fibre networks. (a) Measured strain-stiffening curves (symbols) for the different collagen networks (legend) plotted together with fits (solid lines) to Eq.(1) in the main text. (b) The linear elastic modulus of the different collagen networks plotted as a function of connectivity. Solid symbols denote telocollagen (crosslinked) networks and open symbols denote atelocollagen (uncrosslinked) networks. (c) Onset strain for strain-stiffening and critical strain for the transition from soft (bend-dominated) to rigid (stretch-dominated) obtained from the stiffening curves. These data were calibrated against 2D network simulations reported in Ref. [60] in order to infer the average connectivity values z shown on the x-axis. (d) Dimensionless bending rigidity $\tilde{\kappa}$ of the collagen networks obtained from the fits shown in panel (a). Note that the telocollagens that possess intrafibrillar crosslinking (solid symbols) have a systematically larger $\tilde{\kappa}$ than the atelocollagens that lack intrafibrillar crosslinking (open symbols), indicating that crosslinking makes the collagen fibres behave as more rigid and tight bundles of collagen molecules. Colour code corresponds to the colours used in the main text. Note that in the fitting curves we do not report telocollagen at 30°C, as we could not reliably fit the stiffening curve.

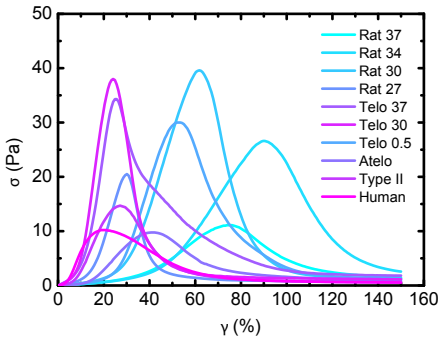

Supplementary Figure 9: Example stress-strain curves in response to an applied strain ramp for the entire range of collagen networks. Each curve represents a single experiment. The colour code represents the different collagen networks (legend) in the order of increasing connectivity z.

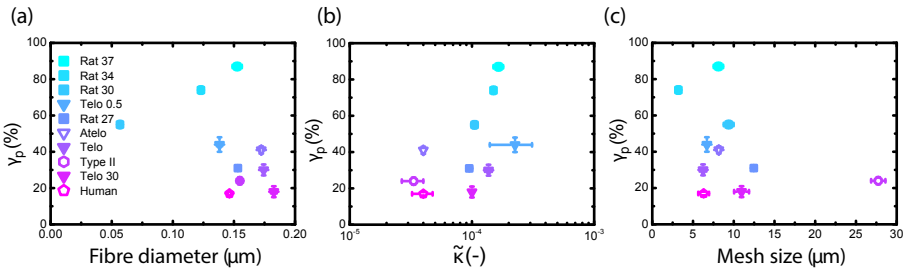

Supplementary Figure 10: The peak strain shows no correlation with the fibre diameter, nor bending rigidity, nor with the network mesh size. (a) Scatter plot of peak strain (averaged over at least 3 measurements) against fibre diameter (averaged over at least 100 measurements of fibre diameters in electron microscopy images). (b) Scatter plot of peak strain against network mesh size (averaged over confocal data from at least three different samples). (c) Scatter plot of peak strain against dimensionless bending rigidity (averaged over rheology data of at least three different samples). In all panels, error bars represent the standard error of the mean.

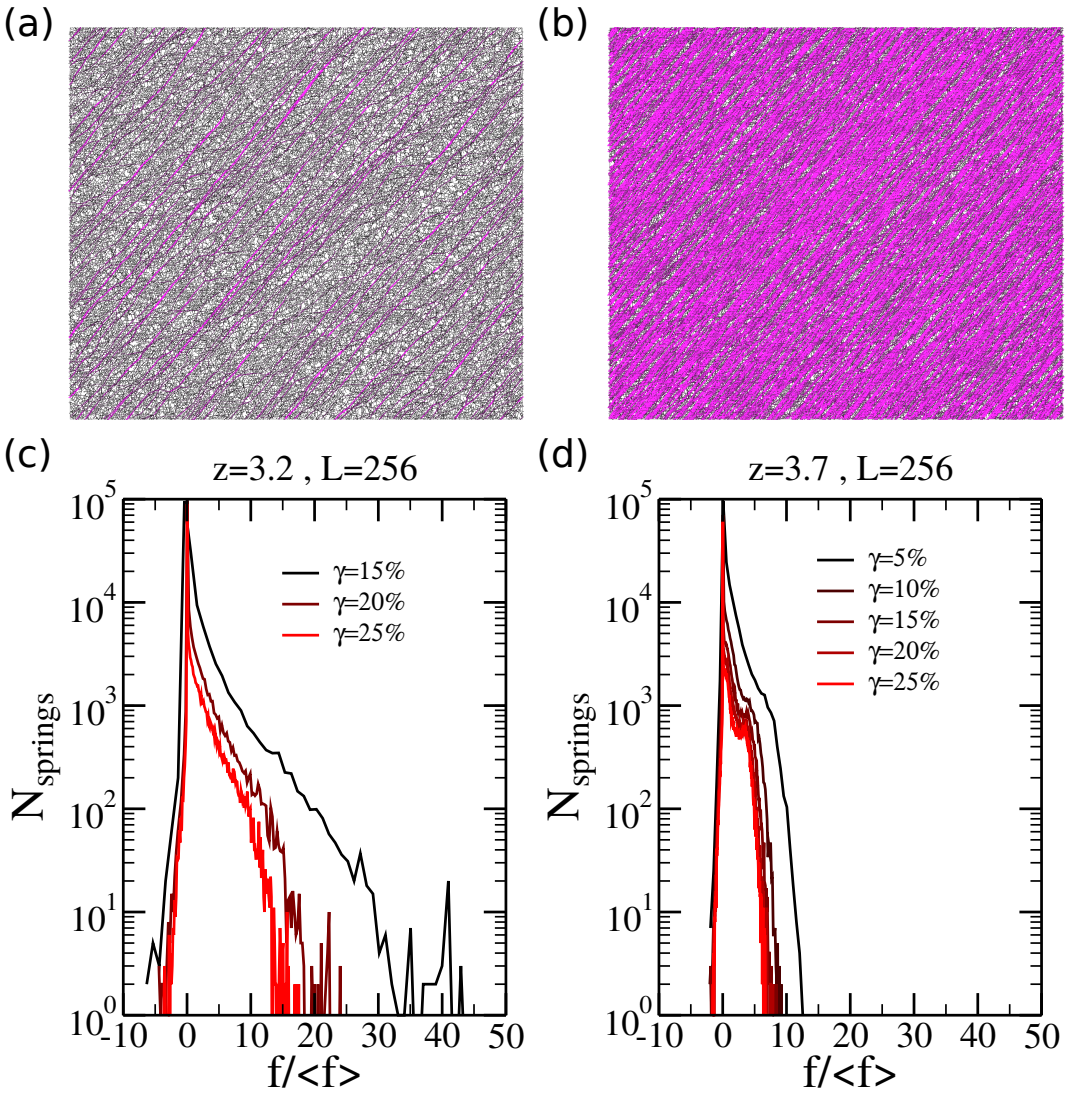

Supplementary Figure 11: Heterogeneous stress distribution in simulated networks. Top: Snapshots of networks composed of unbreakable springs under shear deformation with average connectivity (a) z=3.2 and (b) z=3.7 at a shear strain γ=20%. Both the colour of each spring and its thickness indicate its axial strain, or equivalently the tension it carries (colours range from black for low tension to pink for high tension). Bottom: Histograms of the number of springs carrying a (normalized) force f/<f>, where <f> is the instantaneous average force, for networks with (c) z=3.2 and (d) z=3.7, in both cases shown for different levels of shear strain γ (see legends). The distribution for the more sparsely connected network (z=3.2) has a longer tail than for the more highly connected network (z=3.7), indicating a more heterogeneous stress distribution (i.e., fewer bonds carry larger forces). The networks have sizes of LxL where L=256.

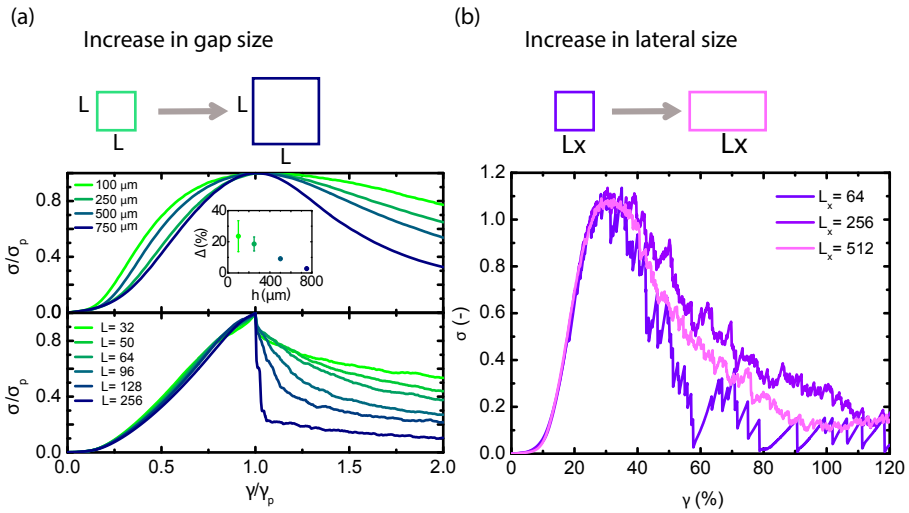

Supplementary Figure 12: Fracture brittleness is masked by large lateral dimensions in the experiments. (a) Upper panel: experimental stress-strain curves (human atelocollagen, polymerised at 37°C) measured for different gap sizes h, from 100 μm (black) to 750 μm (red). Each curve was normalised by the peak strain γ_p and peak stress σ_p and averaged over three samples. Inset shows that the asymmetry between the pre- and post-peak response (Δ), decreases with gap size, indicating a more brittle response for larger h. Lower panel: in simulations of networks composed of L by L nodes (see legend), it is evident that brittleness increases for larger L (z=3.7, λ=10%). (b) A more ductile (smooth) post-peak response is observed also in simulations when the lateral dimension L_x is increased while keeping L_y (the gap size) fixed, approaching the experimental conditions.

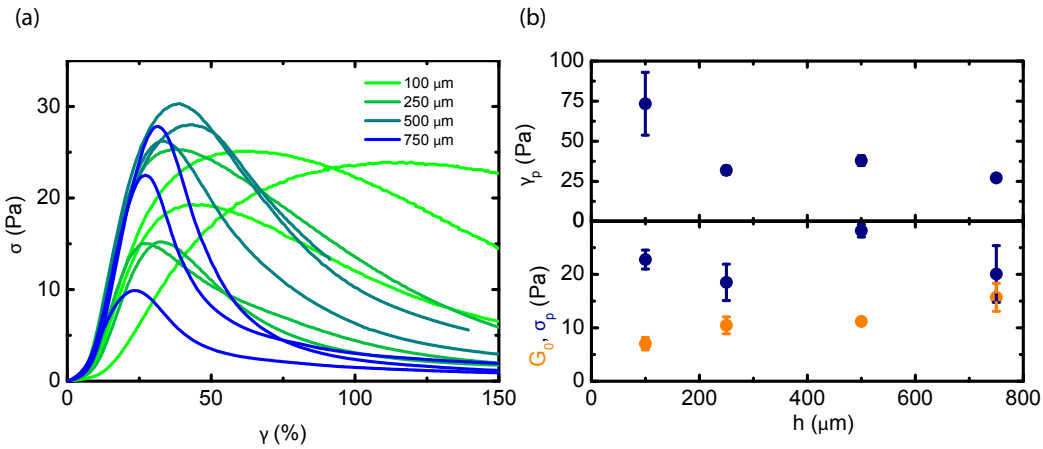

Supplementary Figure 13: Effect of gap size on fracture of collagen networks. (a) Individual stress-strain curves for networks of human atelocollagen measured in a plate-plate geometry with different gap sizes h, ranging from 100 to 750 μm (see legend). (b) Peak strain (top) and the linear elastic modulus (bottom, red squares) and peak stress (bottom, black circles) of the networks as a function of h. For gap sizes above 200 μm, no significant differences are observed, although the shape of the stress-strain curves still does change with h. Data are averages over three independent measurements ± S.E.M.

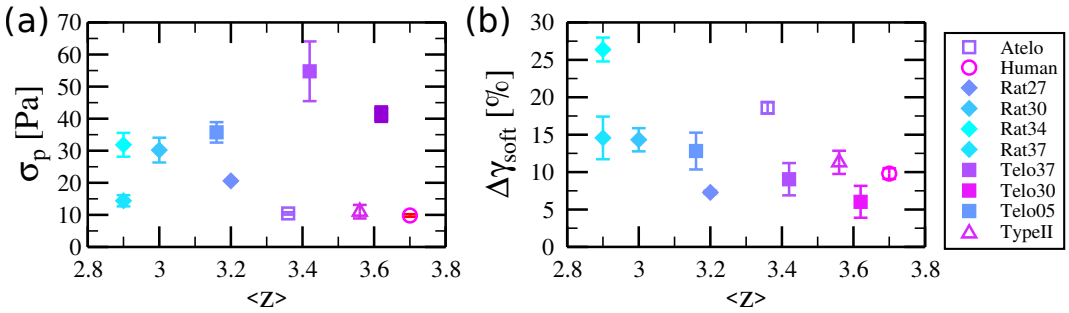

Supplementary Figure 14: Atelocollagen (uncrosslinked) networks are softer than telocollagen (crosslinked) networks and exhibit a larger softening interval (experiments). (a) Peak stress for different collagen networks as a function of their average connectivity. (b) Corresponding softening interval, defined as the strain interval between the strain where the differential elastic modulus is maximal and the peak strain γ_p where the modulus is zero. Note that, for the same connectivity, the atecollagen (uncrosslinked) networks (open symbols) tend to exhibit a smaller peak stress σ_p and larger softening interval than the telocollagen (crosslinked) networks (solid symbols), consistent with uncrosslinked collagen fibers being softer and more plastic than crosslinked fibers.

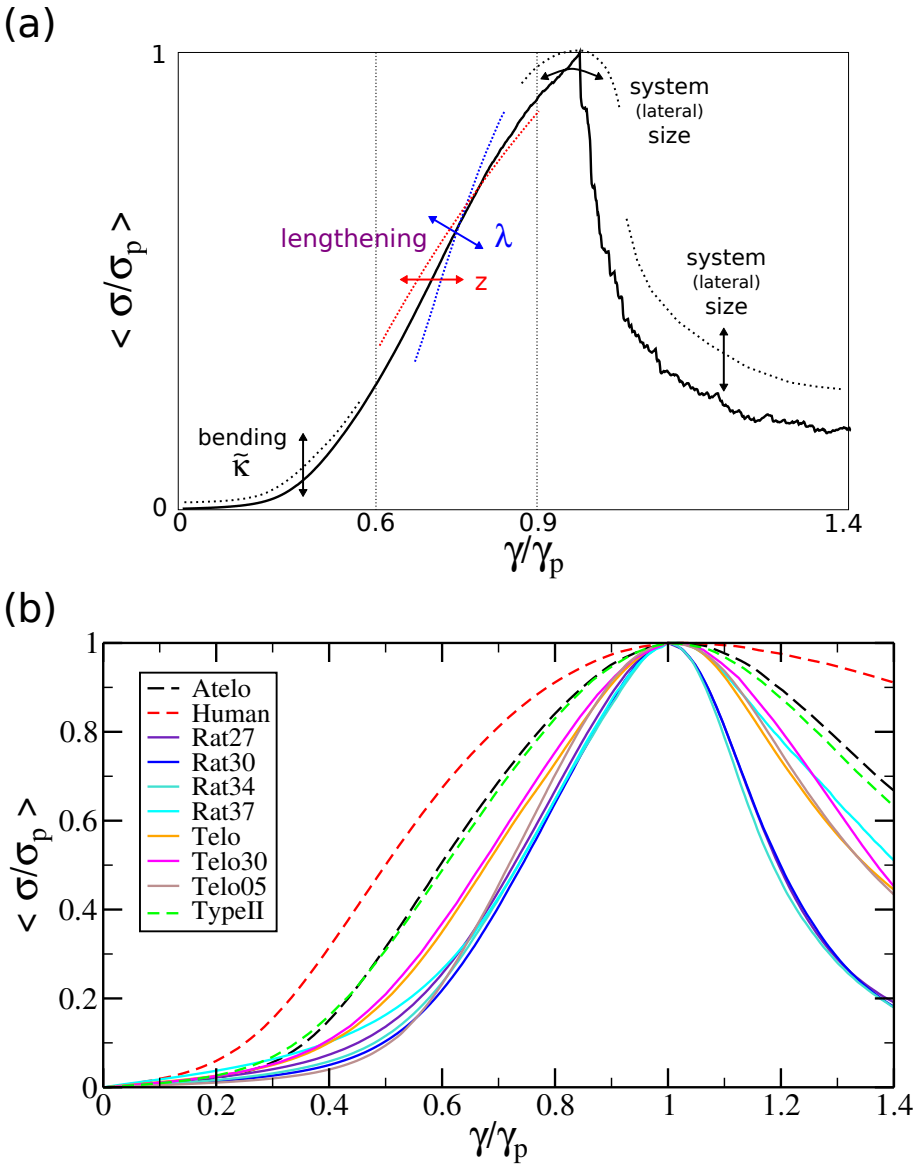

Supplementary Figure 15: The shape of the stress-strain response of collagen networks in simulations and experiments reveals differences in plasticity depending on network connectivity and intrafibrillar crosslinking. (a) Schematic summarizing the influence of the different parameters in the simulations on the shape of the normalized stress-strain curves. We match the middle region of the curves (the reduced strain interval $0.6 < \gamma/\gamma_p < 0.9$, indicated by the vertical dashed lines) measured experimentally against simulation results in order to assess the role of fibre lengthening in the network response. (b) Experimental normalized and averaged curves for all the collagen networks investigated in this study. Note that the curves associated with atelocollagen (uncrosslinked) networks (Atelo, Human, TypeII, shown with dashed lines) have a different shape from the curves obtained for telocollagen (crosslinked) networks, consistent with enhanced fibre plasticity.

Name	Animal source	Tissue origin	Type	Telopeptides (y/n)	Stock conc.	Buffer	Supplier
PureCol	Bovine	Dermis	I	n	3.2 (mg/mL)	0.01 M HCl	CellSystems
RatCol	Rat	Tail tendons	I	y	8.34 (mg/mL)	0.02 M acetic acid	Corning
VitriCol	Human	Neonatal cells	I	n	3 (mg/mL)	0.01 M HCl	CellSystems
Type II	Bovine	Tracheal cartilage	II	n	3 (mg/mL)	0.02 M acetic acid	Sigma Aldrich

Table 1: Table S1: Overview of the collagen sources used in the experiments.
Specification of the animal source, tissue origin, collagen type (either type I or type II), presence of telopeptide end regions that mediate intrafibrillar crosslinking, stock concentration, stock buffer conditions, and the supplier.

Collagen type	γ_c	**z**	**F**	Φ	$\tilde{\kappa} * 10^4$
Telo 0.5 (Bovine telo 37°C 0.5 mg/mL)	0.19±0.02	3.16	0.74	2.1	2.25±0.85
Human (Human atelo 37°C 1 mg/mL)	0.045±0.006	3.7	0.83	2	0.4±0.08
Rat 37 (Rat tail telo 37°C 1 mg/mL)	0.47±0.007	2.9	0.77	2.2	1.7±0.15
Type II (Bovine atelo type II 37°C 1 mg/mL)	0.1±0.001	3.56	0.81	2	0.33±0.07
Rat 27 (Rat tail telo 27°C 1 mg/mL)	0.21±0.01	3.2	0.75	2.1	0.95±0.05
Rat 34 (Rat tail telo 34°C 1 mg/mL)	0.48±0.05	2.9	0.77	2.2	1.6±0.15
Rat 30 (Rat tail telo 30°C 1 mg/mL)	0.28±0.01	3	0.7	2.2	1.05±0.06
Telo 37 (Bovine telo 37°C 1 mg/mL)	0.12±0.003	3.42	0.77	2.1	1.4±0.1
Atelo (Bovine atelo 37°C 1 mg/mL)	0.15±0.01	3.36	0.77	2.1	0.37±0.02
Telo 30 (Bovine telo 30°C 1 mg/mL)	0.068±0.006	3.62	0.82	2	~1

Table 2: Table S2: Overview of parameters quantifying the strain-stiffening response of the entire range of collagen networks. Collagen networks were assembled from different collagen types (I or II) and tissue and animal sources (Supplementary Table S1), at different temperatures (27, 30, 34, or 37°C) and at different concentrations (1 mg/ml if unspecified, otherwise 0.5 mg/ml). First, the average connectivity z was determined by calibrating the critical strain γ_c against 2D network simulations. Next, the corresponding critical exponents f and Φ were determined from the best-matching simulations. Finally, the dimensionless bending rigidity $\tilde{\kappa}$ was determined by fitting the constitutive equation for fibrous networks (Eq. 1 in the Materials and Methods section of the main text) to the experimentally measured strain-stiffening curves of collagen networks (see Supplementary Figure S8a) using $\tilde{\kappa}$ as the only adjustable parameter. Data are averages over 3 independent measurements.

3

Stress management in composite biopolymer networks

Living tissues show an extraordinary adaptiveness to strain, which is crucial for their proper biological functioning. The physical origin of this mechanical behaviour has been widely investigated using reconstituted networks of collagen fibres, the principal load-bearing component of tissues. However, collagen fibres in tissues are embedded in a soft hydrated polysaccharide matrix, which generates substantial internal stresses, and the effect of this on tissue mechanics is unknown. Here, by combining mechanical measurements and computer simulations, we show that networks composed of collagen fibres and a hyaluronan matrix exhibit synergistic mechanics characterized by an enhanced stiffness and delayed strain stiffening. We demonstrate that the polysaccharide matrix has a dual effect on the composite response involving both internal stress and elastic reinforcement. Our findings elucidate how tissues can tune their strain-sensitivity over a wide range and provide a novel design principle for synthetic materials with programmable mechanical properties.

Chapter based on: Burla, F.*, Tauber, J.*, Dussi, S., van der Gucht, J., Koenderink, G.H. *Stress management in composite biopolymer networks.* Nat. Phys. **15**, 249-263, 2019.

3.1 Introduction

The soft tissues in our body, such as the skin, muscles and arteries, have a striking ability to switch from being soft at small deformations to being stiff at high deformations [124]. This adaptive response to strain enables tissues to accommodate dynamic processes such as cell proliferation and migration [125], while preventing tissue rupture [45]. Recent biophysical studies have revealed that the main determinant of tissue strain-stiffening is collagen, a scaffolding protein that forms fibrillar networks [7, 45]. Collagen networks have the intrinsic ability to undergo a transition from soft to rigid when strained [126] because at the coarse-grained level of fibres they have a sub-isostatic architecture, meaning that the average number of fibres meeting at each junction (three for branches and four for crosslinked fibres) is below the Maxwell stability criterion of six for a network of springs [56]. Fibrous networks are soft at small strains because they respond primarily by fibre bending, but stiffen at large deformations as the fibres align along the principal direction of strain and start to stretch [40, 41, 58]. However, collagen networks within tissues are always embedded in a soft hydrated matrix composed of polysaccharides and glycosylated proteins whose mechanical role is unknown [23]. Recent computational models suggest that these matrix polymers might elastically reinforce the fibrillar collagen matrix [62, 63]. However, the role of the matrix is probably more complex, because the constituent molecules carry large negative charges [69]. It has been shown that the matrix consequently generates substantial mechanical stresses, especially in cartilaginous tissues [127–129], which could have a large impact on tissue mechanics given the strong strain-sensitivity of collagen.

3.2 Materials and methods

3.2.1 Sample preparation

The tissue-mimetic composite system was prepared by mixing bovine dermal collagen type I atelocollagen (PureCol from CellSystems, supplied at 3.2 mg/ml in 0.01 M HCl) or telocollagen (TeloCol, from CellSystems, supplied at 3.1 mg/ml in 0.01 M HCl) and thiol-modified hyaluronan supplied as a lyophilized powder (Glycosil, 2B Scientific, 240 kDa) on ice. The networks were co-assembled in phosphate buffered saline (Sigma Aldrich) with the pH set to 7.4 using 0.1 M NaOH (Sigma Aldrich). Finally, the PEGDA crosslinker (Extralink PEGDA, 2B Scientific, 3.4 kDa) in a concentration (w/v) ratio of 1:4 with hyaluronan (molar ratio 20:1) was added just before inserting the sample in the rheometer or microscopy sample cells, to prevent premature crosslinking of the hyaluronan networks. The experiments were performed at a fixed concentration of 1 mg/ml collagen and at hyaluronan concentrations ranging from 0 to 7 mg/ml.

3.2.2 Hyaluronan labelling

Hyaluronan was fluorescently labelled by coupling fluorescein-labelled maleimide (BDP FL maleimide, from Lumiprobe) with the thiol groups on the hyaluronan chains. Briefly, we dissolved the hyaluronan to a concentration of 10 mg/ml. We then dissolved the dye in dimethylsulfoxide (Sigma Aldrich) to a concentration of 30 mg/ml and added it to the hyaluronan solution in a tenfold molar excess. The reaction was allowed to proceed overnight at 4 °C. The sample was finally gel-filtrated with a desalting column (PD-10, GE Healthcare) to remove the excess dye.

3.2.3 Rheology measurements

All the experiments were performed on an Anton Paar Physica MCR501 rheometer, equipped with a cone plate geometry with a diameter of 40 mm and cone angle of 1°. We verified that the measurements were independent of gap size by repeating the experiments with a parallel plate geometry with gaps of 200 and 400 μm (data not shown). The samples were allowed to polymerize for 2 h at a temperature of 37 °C, maintained by a Peltier plate, while monitoring the evolution of the linear shear moduli with a small-amplitude oscillatory strain (0.5% strain, 0.5 Hz). The steady-state values of the linear viscoelastic moduli were calculated as an average over the last ten data points of the polymerization curve, and the average reported is representative of at least three independent measurements. After polymerization, the nonlinear elastic response was measured using a well-established prestress protocol [107]. Briefly, a constant stress σ was applied for 30 s to probe for network creep, and then an oscillatory stress $\delta\sigma$ was superposed with an amplitude of 1/10 σ. The resulting differential strain $\delta\gamma$ was then used to calculate the differential (or tangent) modulus K'= $\delta\sigma/\delta\gamma$.

3.2.4 Determination of linear mechanical enhancement, onset and critical strain

The linear mechanical enhancement was determined by dividing the elastic modulus G_0 measured at the end of polymerization of the composite network (G_{meas}) by the sum (G_{sum}) of the elastic moduli G_0 of the two individual components. The errors for the linear mechanical enhancement are calculated from error propagation.

The rheology data in the nonlinear regime were evaluated using a custom-written Python routine. Consistent with a definition that was previously introduced in the context of fibrillar network mechanics [60], for the onset strain determination we first considered the curve K'/σ versus σ. Subsequently, we performed a cubic spline interpolation and determined the minimum of the resulting curve (Supplementary Fig. 21a). The associated stress was characterized as the onset stress σ_o, and the corresponding strain was taken to be the onset strain γ_o. To determine the critical strain, we calculated the cubic spline derivative of the curve log K' as a function of

log γ. The strain at which this function attained its maximum was taken to be the critical strain γ_c (Supplementary Fig. 21b). All the characteristic strain values are shown as averages with a standard error of the mean of at least three measurements.

3.2.5 Delayed gelation experiments

Delayed gelation experiments were performed by polymerizing collagen in the presence of hyaluronan in the rheometer for 40 min, before adding the PEGDA crosslinker around the trap. The crosslinker was then allowed to diffuse into the gel for 300 min before performing prestress measurements. To speed up the diffusion process, measurements were performed using a smaller cone plate geometry compared to the bulk of the measurements, with a diameter of 20 mm. We verified that the shear moduli of hyaluronan gels with the crosslinker mixed in before polymerization or added after polymerization were comparable, indicating that the crosslinker was indeed able to enter the gels (Supplementary Fig. 5).

3.2.6 Microscopy experiments and image analysis

The composite networks were imaged with an inverted Eclipse Ti microscope (Nikon) using a 100x oil immersion objective with a numerical aperture (NA) of 1.49 (Nikon). The collagen networks were imaged in confocal reflectance microscopy mode, while hyaluronan was imaged by confocal fluorescence detection, and both components were imaged using a 488 nm argon laser for illumination (Melles Griot). Images were acquired 10 μm above the bottom surface, over a depth of 30 μm and with a step size of 0.2 μm, and are shown as maximum intensity projections obtained with ImageJ [108]. Before imaging, the networks were allowed to polymerize for at least 2 h in a sample holder composed of two coverslips (Menzel Microscope Coverslips 2460 mm, 1, Thermo Scientific) separated by a silicon chamber (Grace Bio-Labs CultureWell chambered coverglass, Sigma Aldrich). The sample holder was subsequently placed in a Petri dish with humid tissue and closed by parafilm to ensure constant humidity, and then placed in a warm room (37°C) before observation. Time-lapse movies of network formation were obtained by polymerizing the networks directly on the microscope in a similar geometry as described above, with the help of a custom-built temperature-controlled chamber. To determine the mesh size of the networks, we applied an algorithm [109] implemented in a custom-written Python routine. Briefly, images were background-subtracted and binarized with an Otsu threshold algorithm. Afterwards, the distance between white and dark pixels was counted along the rows and columns. Histograms of the distance distribution were then fitted with an exponential probability distribution and the mean value (converted from pixels to μm) was taken to be the average mesh size.

3.2.7 Particle tracking

Particle tracking was performed using latex fluorescent beads with a diameter of 0.4 μm (Reagent microspheres, green visible fluorescent carboxylate modified, Duke Scientific). The beads were surface-functionalized with pluronic (Pluronic F-127, Sigma Aldrich) to avoid interaction with the biopolymers, following a published procedure [130]. The beads were added to the samples before polymerization and, after 2 h, networks were imaged with the same microscope and chamber as described above, at a distance of at least 10 μm above the bottom glass coverslip (1 f.p.s. acquisition, 100 ms exposure time). The particles' displacements in the x-y plane were determined with subpixel accuracy by analysing the movies with a custom-written Python code based on Trackpy [131].

3.2.8 Spin down assay

To check whether we could detect any association between hyaluronan and collagen, we performed a spin-down assay. Briefly, we co-polymerized collagen and hyaluronan (without PEGDA crosslinks) in an Eppendorf tube at 37°C for 2 h. Afterwards, the collagen network was precipitated by centrifugation for 90 min at 8,000g and the supernatant was collected. The presence of hyaluronan in the supernatant was assessed by measuring an UV-vis absorption spectrum with a spectrophotometer (Thermo Scientific, Nanodrop 2000) and comparing this with the spectra for supernatants obtained from pure collagen and pure hyaluronan after a similar spin-down procedure.

3.2.9 Determination of collagen bending rigidity

To determine the bending rigidity of collagen fibres prepared from either atelocollagen or telocollagen, we measured the nonlinear elastic response of pure collagen networks prepared at 1 mg/ml using the prestress protocol described above. The dimensionless bending rigidity was extracted from the strain-stiffening curves by comparing them to curves obtained with the following analytical expression valid for sub-marginal fibrous networks, described in ref. [41]:

$$\frac{\tilde{\kappa}}{|\Delta\gamma|^{\Phi}} = \frac{K'}{|\Delta\gamma|^{f}} \left(\pm 1 + \frac{K'^{\frac{1}{f}}}{\Delta\gamma} \right)^{(\phi - f)} \tag{3.1}$$

where $\tilde{\kappa}$ is a free parameter corresponding to the dimensionless bending rigidity, K'is the measured value of the differential modulus, $|\Delta\gamma|$ is the distance between the considered γ and the critical strain, and f and Φ are critical exponents set by the network architecture, here taken to be 0.77 and 2.2 by comparing the measured values of the onset and critical strain with published results [60].

3.2.10 Laser ablation assay

Laser ablation experiments were performed on a Nikon Ti Eclipse inverted microscope. The collagen network was imaged with confocal reflectance microscopy with the previously described set-up. Next, the hyaluronan meshwork in the vicinity of a collagen fibre was ablated by 30 s illumination with a circular spot of roughly 1-5 μm diameter using a pulsed infrared laser (Mai Tai, DeepSee, SpectraPhysics) operated at a wavelength of λ = 700 nm and a nominal power of 1,400 mW. The collagen network was subsequently imaged again to check for the recoil of collagen fibres in the vicinity of the ablation spot. Images are shown using an ImageJ hyperstack projection, such that fibres that remain immobile show up in white.

3.2.11 Composite network simulations

We model the tissue-like composite networks as an athermal and sub-marginal fibre network that represents the collagen network, embedded in a homogeneous (not diluted) matrix of linear elastic springs that represents the linearly elastic hyaluronan matrix [57, 132]. All simulations are performed on a lattice of LxL nodes, where L=50, with initial lattice spacing d=1. The fibre network is modelled on a triangular lattice, using a dilution procedure to achieve a maximum local connectivity z of four bonds per node. As shown previously with similar models [41, 60], it is possible to quantitatively describe the nonlinear elastic properties of reconstituted collagen networks, provided that model-dependent parameters, such as connectivity and number of crosslinks per fibre, are properly matched. For these simulations we consider networks with an average connectivity z=3.4. The total energy of the system is:

$$E = E^{fiber}_{stretch} + E^{fibre}_{bend} + E^{matrix}_{stretch} = \sum_{<ij>} \frac{1}{2}\frac{\mu_1}{l_{0,1}}\left(l - l_{0,1}\right)^2 + \sum_{<ijk>} \frac{1}{2}\frac{\kappa_1}{l_{0,1}}\left(\theta - \theta_{0,1}\right)^2 + \sum_{<ij>} \frac{1}{2}\frac{\mu_2}{l_{0,2}}\left(l - l_{0,2}\right)^2 \quad (3.2)$$

where μ_1 and κ_1 are the stretching and bending constant for the fibre segments, respectively, and μ_2 is the stretching constant for the matrix segments. Nearest-neighbour nodes are indicated with indices ij, and l is the distance between the two nodes (spring length). Bending contributions are associated only to segments belonging to the same straight fibre, that are indicated with the triplet ijk, θ denotes the angle between the triplet and $\theta_{0,1}$ the rest angle. The rest lengths $l_{0,1}$ and $l_{0,2}$ of the fibre and matrix segments are expressed in terms of the initial lattice spacing d (we use $l_{0,1}$ =d in all simulations), and we use the reduced quantities $\tilde{\mu}_2 = \mu_2/\mu_1$ and $\tilde{\kappa} = \kappa d^2/\mu_1$. We vary the matrix properties $\tilde{\mu}_2$ from 10^{-5} to 10^{-3} while the fibre bending rigidity $\tilde{\kappa}$ is either 10^{-4} or 10^{-5}, corresponding to the measured values for atelocollagen and telocollagen networks (see Supplementary Figure 10). The mechanical behaviour of the composite networks is obtained in three steps. First,

to simulate the compressive stress exerted by the hyaluronan matrix, we reduce $l_{0,2}$, which we vary from 0.50 to 1.00. Secondly, we allow the system to achieve an internal balance between the fibre network and the matrix via (isotropic) bulk compression in steps of 0.1% strain, with each step followed by energy minimization, until a minimum in the total energy as a function of bulk strain is reached. Thirdly, we perform a quasistatic shear simulation in steps of 0.1% strain. The stress is obtained as $\sigma = frac1Afracd E d\gamma$ and the elastic shear modulus as $K' = 1/A\ (d^2E)/(d\gamma^2)$, where A is the area of the system. We indicate the linear modulus (calculated for strains γ<2%) with G_0. We obtain the onset strain γ_o and critical strain γ_c that characterize the strain-stiffening response from the dependence of K'/σ on σ. The first minimum corresponds to (γ_o, σ_o), where σ_o is the onset stress where stiffening sets in. The maximum corresponds to (γ_c, σ_c), where σ_c is the critical stress.

3.2.12 Simulations of an effective single-component network

To achieve a quantitative comparison with the experimental system, we develop an effective single-component model. In this case, we use a phantom fibre network with an average connectivity z=3.2. The presence of the hyaluronan matrix is implicitly implemented as follows. The effect of the matrix stiffness is captured by an increase of the fibre bending stiffness $\tilde{\kappa}$ to $\tilde{\kappa}_{eff}$,similar to recent simulations of the linear elastic properties of two-component composites [62]. To account for the local compression of the collagen network by the hyaluronan matrix, we isotropically compress the system in steps of 0.1% strain, followed by energy minimization. Subsequently, all the rest angles θ_0 of the fibres are reset to their value after compression to ensure mechanical equilibrium, meaning that the system retains its shape even if the boundaries are removed. To obtain the network mechanical response, a quasistatic shear simulation is performed in the same manner as described above.

3.3 Results

To understand the interplay between elastic effects and internal stress in the mechanical response of tissues, we reconstituted biomimetic composites from two paradigmatic biopolymers: collagen and hyaluronan (Fig. 1a). Collagen type I is the most ubiquitous member of the collagen family [7], and hyaluronan is abundant in healthy tissues and upregulated in solid tumours [133]. Rheology measurements show that collagen and hyaluronan individually respond rather differently to an applied shear strain (Fig. 1b). Collagen networks stiffen with strain above a threshold of about 5-10%, as expected from their sub-isostatic fibrous architecture. By contrast, crosslinked hyaluronan networks exhibit a mechanical response that to a good approximation is linear in the range of strains that we consider (Fig. 1b). Unlike collagen, hyaluronan polymers are flexible, with a persistence length of only

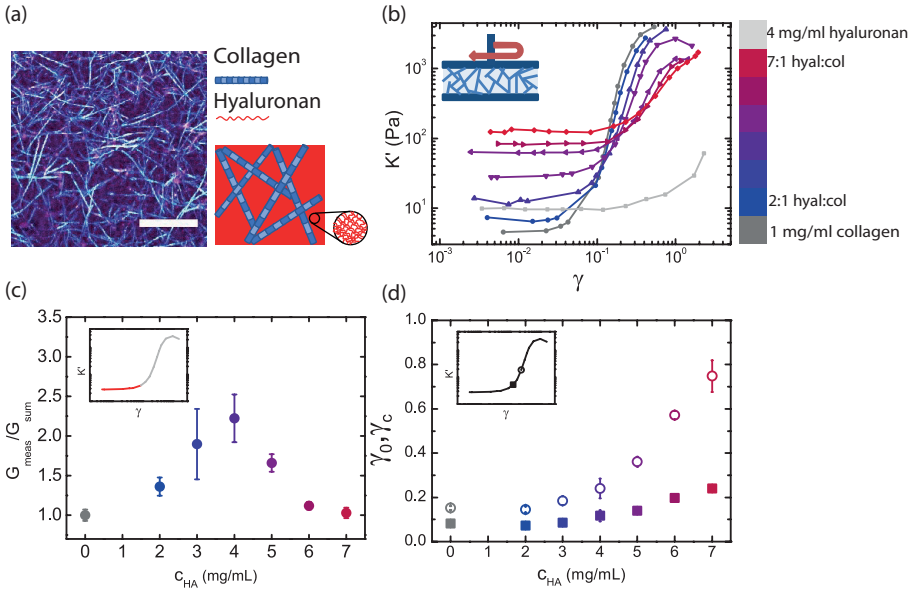

Figure 1: Composite collagen-hyaluronan networks as a minimal tissue-mimetic model system. (a) Confocal image and a schematic of a composite network composed of a fibrous scaffold of collagen mixed with a soft hyaluronan gel. (b) Differential elastic modulus, K'=$\delta\sigma/\delta\gamma$ as a function of applied strain for composites with a fixed concentration of collagen (1 mg/mL) and varying hyaluronan concentrations (coloured curves). For comparison, pure collagen is shown in dark grey and hyaluronan (4 mg/mL) in light grey. Inset: the network is probed by shearing between two parallel plates. (c) Linear mechanical enhancement and (d) onset strain (γ_o, solid symbols) and critical strain (γ_c, open symbols) as a function of hyaluronan concentration (d), plotted with the same colour code as in (b). Data represent average values. Error bars in (c) were obtained by propagating the standard deviation of the measured moduli of at least three independent measurements. Error bars in (d) represent standard error of the mean for at least three independent measurements.

5-10 nm [31]. Their elastic properties are therefore determined by chain entropy, and the network response is linear until the long chains are pulled taut.

Having established the individual networks' response, we generated composites by polymerizing collagen monomers in the presence of a mixture of hyaluronan chains and poly(ethylene glycol) diacrylate (PEGDA) crosslinkers. Collagen polymerization and hyaluronan crosslinking occur concurrently, resulting in an interpenetrating double network. The final collagen network looks almost identical to its pure collagen counterpart (Supplementary Fig. 1) and hyaluronan forms a background that is uniform over length scales much smaller than the collagen network mesh size (Supplementary Fig. 2), suggesting that the two networks do not interact, as confirmed by biochemical assays (Supplementary Fig. 3).

To test the impact of hyaluronan on the strain-stiffening response of collagen, we performed rheology measurements on composites with a fixed 1 mg/ml collagen concentration and hyaluronan concentrations (c_{HA}) ranging from 0 to 7 mg/ml. The composites strain-stiffen, but with a strong dependence on the hyaluronan content (Fig. 1b). The addition of hyaluronan results in a striking enhancement of the linear elastic modulus G_0 beyond the sum of the moduli of the individual components (Fig. 1c). This synergistic enhancement appears to be at a maximum around 4 mg/ml, beyond the concentration at which hyaluronan first forms a percolating network (Supplementary Fig. 4). In the nonlinear regime, the composite networks have a strongly delayed stiffening response compared to pure collagen (Fig. 1d). Both the onset strain γ_o, where nonlinearity first sets in, and the critical strain γ_c, where collagen fibres complete the transition from a bending- to stretching-dominated mode of deformation, shift upwards with increasing hyaluronan concentration (Fig. 1d). In pure collagen networks, one important factor influencing the onset of strain-stiffening is the network connectivity [41, 60]. To test whether hyaluronan impacts the connectivity of collagen networks, we performed delayed crosslinking experiments, adding PEGDA crosslinks only after collagen polymerization was complete. As the mechanics of the composite networks is very similar irrespective of whether hyaluronan is crosslinked during or after collagen polymerization (Supplementary Fig. 5), we conclude that the delayed strain-stiffening of composites is not caused by changes in the collagen network connectivity.

Another important determinant of the onset of strain-stiffening in collagen networks is mechanical stress [40, 48, 134]. To test whether hyaluronan causes any build-up of stresses during network formation, we measure the time-dependence of the normal stress σ_N that the composite system exerts on the top rheometer plate as it assembles (Fig. 2a,b). Initially (t=0), collagen monomers and hyaluronan chains form a viscous solution. As collagen starts to assemble in fibres (Fig. 2a) and hyaluronan starts to crosslink (t=20 min), G_0 and σ_N increase simultaneously (Fig. 2b). The positive sign of the normal stress indicates swelling of the polymerizing gel. As hyaluronan continues crosslinking and collagen continues polymerizing (t=60 min), the normal force reverses and decreases, eventually reaching negative values, indicating gel contraction. A similar normal stress evolution is observed for hyaluronan alone, whereas collagen develops no observable normal stress (Supplementary Fig. 6). We interpret the normal force build-up as a competition between the electrostatic repulsion of the charged hyaluronan polymers and the intrinsic tendency of polymer chains to contract to maximize their configurational entropy. At the beginning of the crosslinking process, the electrostatic interactions dominate, causing the system to swell. As crosslinking progresses, the fraction of crosslinked hyaluronan chains increases and the associated contractile forces eventually take over. To investigate whether the contractile stresses that develop in the hyaluronan gel are transmitted to the collagen network, we performed localized laser ablation experiments, using a high-intensity laser to disrupt the

hyaluronan meshwork in the interstices of the collagen network. Localized removal of hyaluronan caused an immediate recoil of neighbouring collagen fibres, indicating the release of mechanical stress (Fig. 2d,e and Supplementary Fig. 7). Altogether, our observations seem to suggest that the hyaluronan matrix indeed exerts compressive stresses on the collagen fibres, as sketched in Fig. 2f.

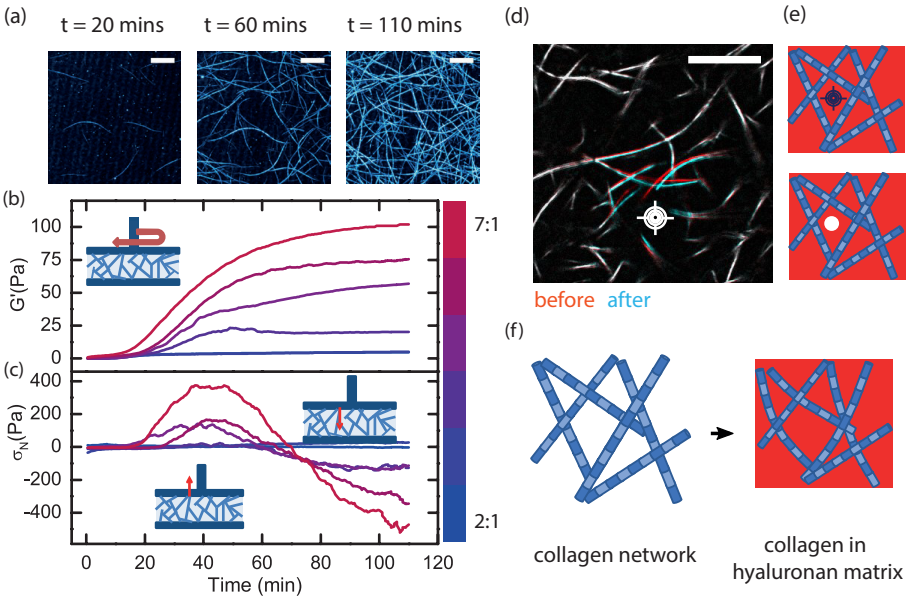

Figure 2: The hyaluronan gel prestresses the collagen network during gelation (a) Z-projected confocal reflectance images of a composite network during the gelation process at three different time points, showing the formation of collagen fibres. Scale bars indicate 10 μm. (b) Evolution of the linear elastic modulus and (c) the corresponding normal force during network gelation for samples with a fixed collagen concentration (1 mg/mL) and different hyaluronan concentrations (from 2 mg/mL to 7 mg/mL). Note that the normal stress first increases, indicative of a swelling pressure, but afterwards decreases and reaches negative values, indicative of contractile stress. (d) Superposed confocal images taken before (red) and after (blue) localized ablation of the hyaluronan matrix (target) with a strong laser, schematically shown in (e). The collagen fibres are everywhere immobile (visible as white) except in the vicinity of the laser spot, where they recoil. Scale bar is 5 μm. (f) Our data suggest that hyaluronan forms a contractile matrix that causes the collagen fibres to bend.

To test whether the internal stress generated by hyaluronan can explain the altered strain-stiffening response of composite networks, we use two-component network simulations. We model collagen as a sub-isostatic network of fibre segments of length $l_{0,1}$ with bending and stretching energy proportional to the constants κ and μ_1, respectively, while hyaluronan is modelled as a homogeneous mesh of springs of length $l_{0,2}$ and stretching energy proportional to μ_2 (Figure 3a). To assess the effect of increasing hyaluronan concentration, we first vary the matrix stiffness

μ_2. We observe an increase of the linear modulus of the composite networks with increasing μ_2, but no changes in the non-linear behaviour (see Supplementary Figure 8). Therefore, we include the contractile tendency of hyaluronan by reducing the rest length of the matrix springs $l_{0,2}$. Subsequently, we allow the entire system to establish a mechanical equilibrium between the contracting stresses in the hyaluronan matrix and the resisting bending forces of the collagen network by allowing the system to compress (Figure 3a). Inducing compression by lowering $l_{0,2}$ while keeping the matrix stiffness μ_2 fixed has little effect on the linear regime, but delays the onset of strain stiffening (see Supplementary Figure 8). When we simultaneously increase μ_2 to account for elastic reinforcement and lower $l_{0,2}$ to account for internal stress build-up, we recover both the linear mechanical enhancement and the delay in strain-stiffening (Figure 3b and Supplementary Figure 9).

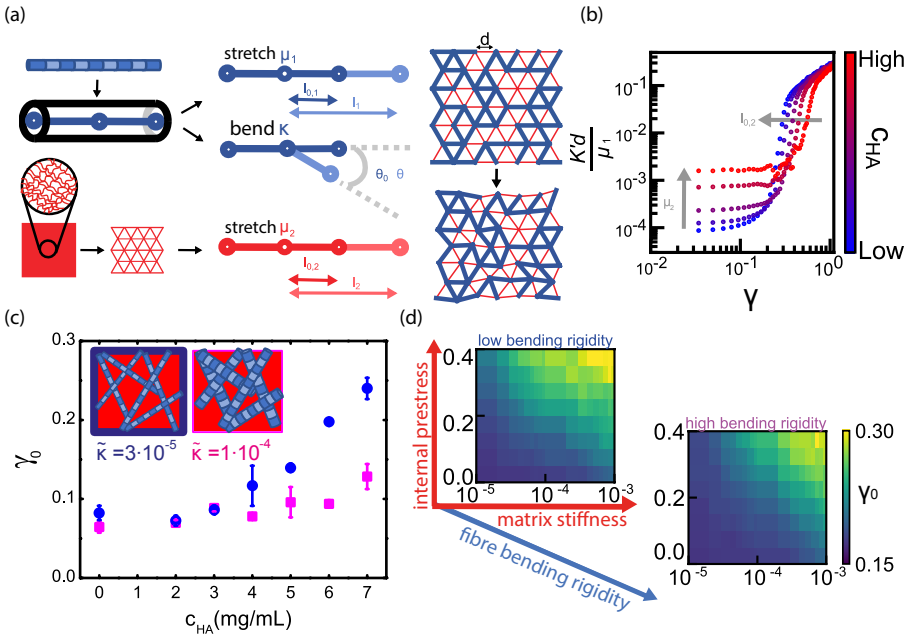

Figure 3: Computational modelling of two-component networks reveals that the composite mechanics depends on a balance between collagen bending and hyaluronan contraction. (a) The initial configuration is a sub-marginal fibre network (blue segments with stretching and bending resistance) embedded in a homogeneous flexible matrix (red segments, resistance to stretching only). To mimic the effect of hyaluronan contraction, we decrease the rest length $l_{0,2}$ of the matrix springs and reach mechanical equilibrium by allowing the network to compress. (b) Shear modulus as a function of strain for composite networks with varying matrix stiffness μ_2 and varying internal prestress $l_{0,2}$. We qualitatively recover the experimentally observed dependence on hyaluronan concentration when we allow for a simultaneous increase in matrix stiffness and in compressive force. In this set of simulations, the average connectivity z=3.4 and the (rescaled) fibre bending stiffness $\tilde{\kappa} = 3x10^{-5}$ are kept fixed to the corresponding experimental values of the collagen network. (c) Experimentally measured onset strain for telocollagen (magenta squares) and atelocollagen (blue circles) networks as a function of hyaluronan concentration. (d) In simulations, γ_o can be tuned by varying the collagen fibre rigidity and by independently varying the stiffness and internal stress of the hyaluronan gel, whereas experimentally the two matrix-related effects are inherently coupled when we vary hyaluronan concentration.

Our model suggests that hyaluronan tunes the mechanics of collagen networks through a combination of elastic reinforcement and internal prestress. This implies that the synergistic mechanics of the composites should be highly dependent on the fibre rigidity $\tilde{\kappa}$ (the ratio between κ and μ_1). Specifically, fibres more resistant to bending (larger $\tilde{\kappa}$) should be less sensitive to stresses arising from the background matrix. Furthermore, they should be less sensitive to the elastic reinforcement, given their already large bending rigidity. To test this prediction, we use a different

type of collagen that forms stiffer fibres thanks to molecular crosslinking mediated by non-helical peptide extensions of the triple helix known as telopeptides [111]. By fitting the mechanical response curves to an analytical expression for fibrous networks [41], we indeed find the fibre rigidity for the telocollagen to be $\tilde{\kappa} = 1x10^{-4}$ larger than for the atelocollagen considered so far, where $\tilde{\kappa} = 3x10^{-5}$(Supplementary Fig. 10). The strain-stiffening behaviour of networks formed by telocollagen is indeed less affected by hyaluronan, as compared to the atelocollagen, with smaller changes in the onset and critical strain, as well as smaller changes in the linear mechanical enhancement in the linear regime (Fig. 3c and Supplementary Figs. 11 and 12). Therefore, the mechanical properties of the composite system exhibit a phase space governed by a balance between the bending rigidity of collagen and the dual effect of the hyaluronan matrix on linear elasticity and internal stress (Fig. 3d).

Finally, we test whether the mechanical response of the double networks can be mapped onto an effective single-component model, as recently proposed for the linear elastic regime [62]. Our experiments suggest that this mapping should extend to the nonlinear elastic regime, as we can rescale the strain-stiffening curves of composites onto the curve for pure collagen by normalizing the nonlinear modulus with G_0 and the shear stress with an effective stress σ_{eff} (Figure 4a, see Supplementary Figure 13), which is manually computed and allows to overlap the curves. To capture the elastic reinforcement of collagen by the surrounding hyaluronan matrix in a single-component model, we assign an enhanced bending rigidity $\tilde{\kappa}_{eff}$ to the fibres, which accounts for the hindrance of fibre bending by the matrix [62]. Internal stresses are implemented by compressing the network and resetting the bending rest angles (Figure 4b). This simple model allows us to quantitatively map all experimental data for both atelocollagen and telocollagen networks onto a mechanical phase space controlled by $\tilde{\kappa}_{eff}$ and the level of collagen compression (Figure 4c). The mapping reveals that the compression is significantly higher for atelocollagen compared to telocollagen, consistent with the more elaborate double network model (Figure 3d). We furthermore find that the parameters controlling the linear and the non-linear regime are decoupled, with the linear modulus G_0 depending on $\tilde{\kappa}_{eff}$ and the critical strain γ_c on the extent of compression.

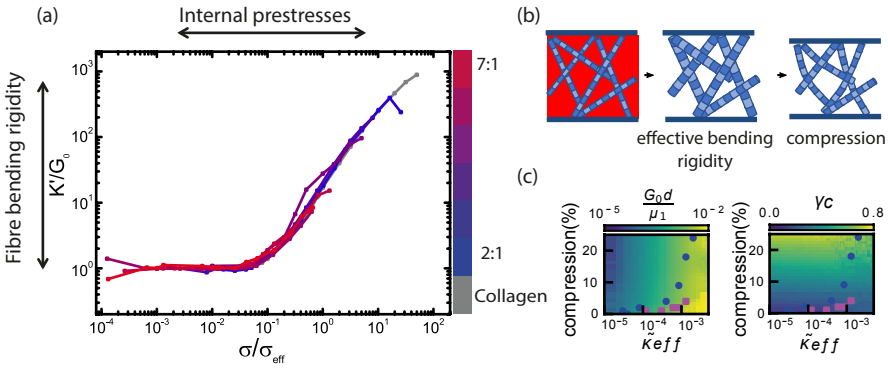

Figure 4: The mechanical response of composite networks can be mapped onto an effective single-component model. (a) The strain-stiffening curves of composite networks with varying hyaluronan concentration can be rescaled on top of the stiffening curve of a pure collagen network (grey) by normalizing the shear stress by an effective stress σ_{eff} and the nonlinear modulus by G_0. σ_{eff} is manually determined in order to be able to overlap the curves of the composites with the ones for collagen (see Supplementary Figure 13). The collagen concentration is fixed at 1 mg/mL. (b) The matrix effects can be incorporated in a single-component system by changing two properties of the collagen network: replacing the bending rigidity with an effective bending rigidity and compressing the network. (c) Map of G_0 and σ_c as a function of $\tilde{\kappa}_{eff}$ and compression. The symbols (magenta squares for telocollagen and blue circles for atelocollagen) indicate the quantitative mapping of the experimental results on the single-component model.

3.4 Conclusions

We have shown, by experiments on tissue-mimetic composites, that the combination of fibrous collagen networks with a soft polysaccharide hydrogel results in highly tunable nonlinear mechanics. The soft gel tunes the mechanics by introducing both elastic reinforcement and internal stresses. The stress-induced stiffening we observe is reminiscent of the active stiffening of cytoskeletal and extracellular matrix networks by contractile molecular motors or cells [52, 135, 136], but with the distinction that here energy consumption is not required. The minimal computational model we developed can be applied also to other soft tissues such as the plant cell wall, where a rigid cellulose network is combined with a soft pectin matrix [137]. Our findings not only elucidate how biology combines biopolymers with complementary properties to finely tune the mechanics of living tissues, but also provide a new avenue for the design of synthetic elastic materials. The bioinspired concept of combining semiflexible and flexible polymer networks to improve mechanical properties has been recently translated into material science [138]. Here, we show that internal stress generation introduces a powerful control knob to tune the mechanical response of a material. This principle is irrespective of the nature of the stress source, and can therefore also be implemented in synthetic materials by using pH- or temperature-

responsive components.

Acknowledgments

This work results from a close collaboration with J. Tauber, S. Dussi, J. van der Gucht (WUR), who developed and performed all of the simulations shown in this chapter. We thank F. C. MacKintosh (Rice University, Texas), E. Pelan (University of Birmingham), K. Jansen (UMC, Utrecht) and S. Stoyanov (Unilever B.V., the Netherlands) for many useful discussions, A. Sharma (Leibniz Institute for Polymer Research, Dresden) for the MatLab script for determining the bending rigidity of collagen fibres from rheology data, D. Nedrelow (University of Minnesota) for suggestions regarding the sample preparation, K. Miura (EMBL, Heidelberg, Germany) for the Temporal Colour Code ImageJ plugin and J. T. B. Overvelde (AMOLF, Amsterdam) for a critical reading of the manuscript. The work of F.B. and G.H.K. is part of the Industrial Partnership Programme Hybrid Soft Materials, which is carried out under an agreement between Unilever Research and Development B.V. and the Netherlands Organisation for Scientific Research (NWO). The work of J.T., S.D. and J.v.d.G. is part of the SOFTBREAK project funded by the European Research Council (ERC Consolidator Grant).

3.5 Supplementary Figures

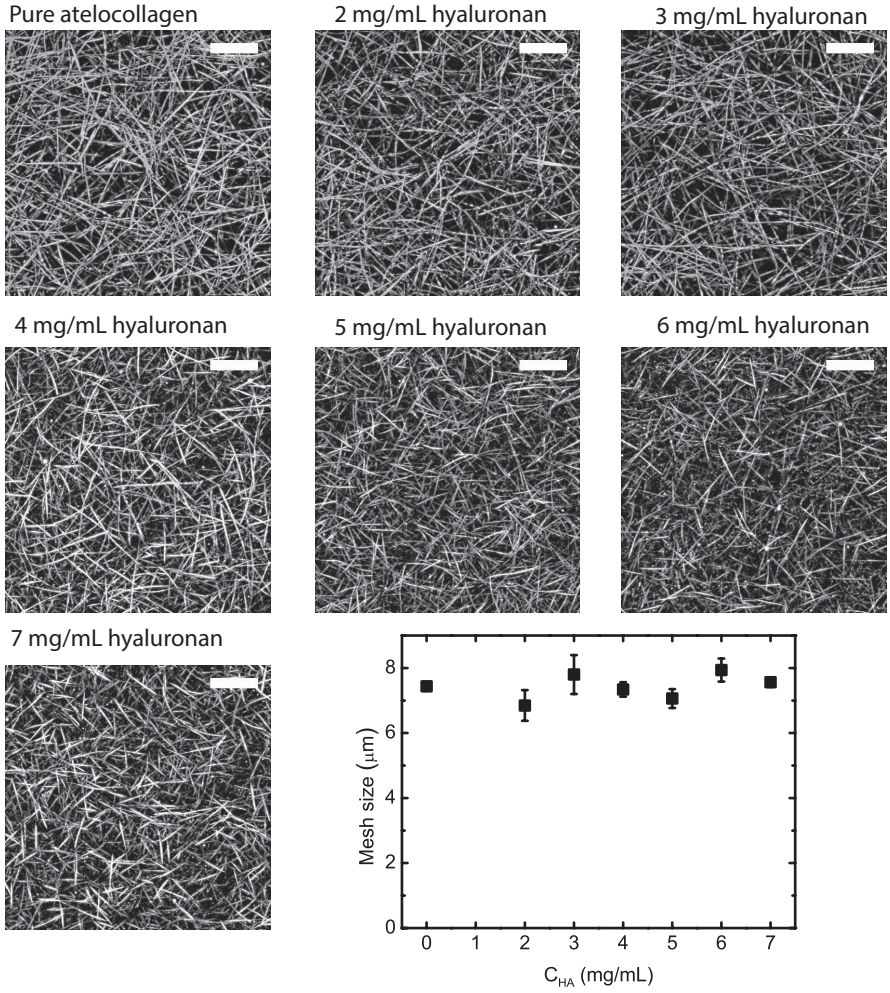

Supplementary Figure 1: Hyaluronan does not alter collagen network architecture. Confocal reflectance images of collagen in the presence of hyaluronan at concentrations varying from 0 to 7 mg/mL, together with a quantitative analysis of the average mesh size, reveal no substantial architectural changes in the collagen architecture. Scale bar indicates 10 μm.

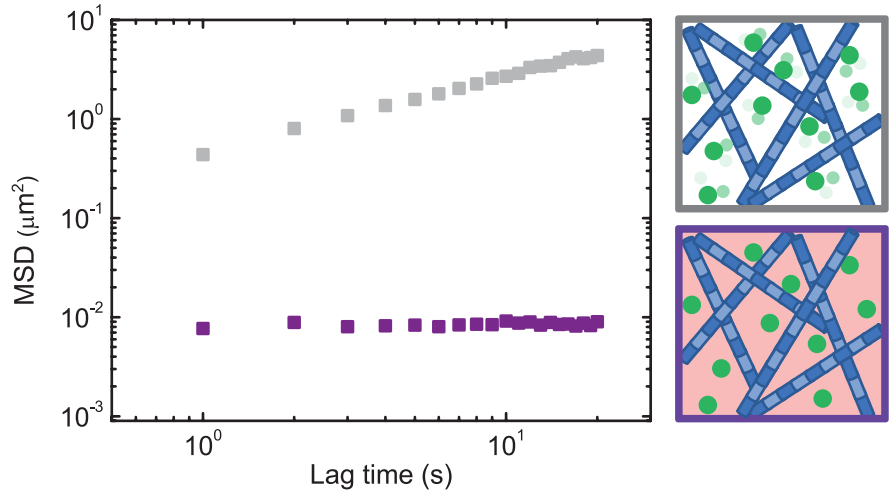

Supplementary Figure 2: Particle tracking measurements reveal that the hyaluronan matrix is uniform. Mean square displacement (MSD) of particles (shown in green in the schematics) embedded in pure collagen networks versus a composite system (1 mg/mL collagen and 4 mg/mL hyaluronan). The particles freely move in the solvent phase between the collagen pores in pure collagen networks (grey symbols), whereas they are immobilized in the hyaluronan mesh in the composite system (purple symbols).

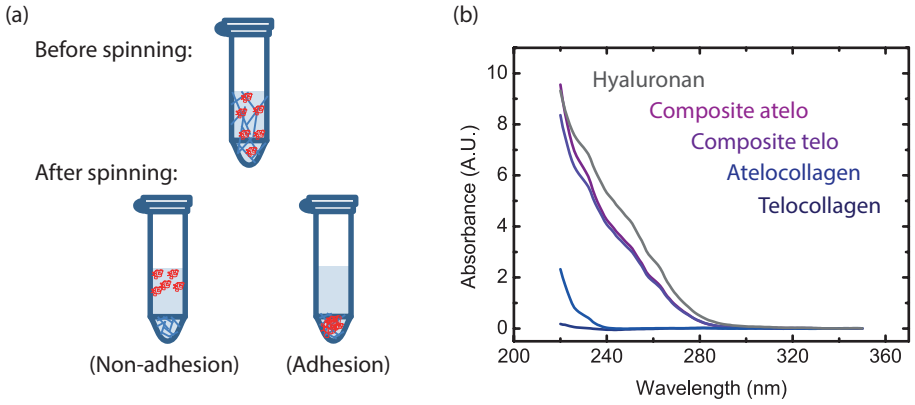

Supplementary Figure 3: Hyaluronan does not associate with collagen.(a) Schematic of the co-sedimentation assay, showing the composite network before centrifugation (upper panel) and after centrifugation (lower panel). Hyaluronan remains in the supernatant in case it does not bind collagen, and ends up in the pellet together with collagen in case it does bind. (b) Light absorbance as a function of wavelength for the supernatant obtained after centrifugation of a composite network with either atelocollagen or telocollagen (1 mg/mL collagen, 4 mg/mL hyaluronan), compared to the absorbance of pure solutions of hyaluronan (4 mg/mL), atelocollagen (1 mg/mL), and telocollagen (1 mg/mL). Since the absorbance spectrum of the supernatant resembles that of hyaluronan, it can be concluded that hyaluronan does not exhibit appreciable binding to collagen.

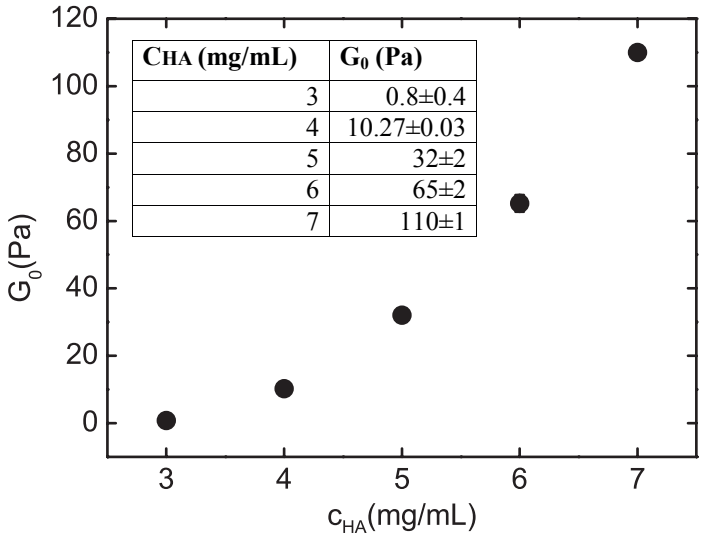

c_{HA} (mg/mL)	G_0 (Pa)
3	0.8±0.4
4	10.27±0.03
5	32±2
6	65±2
7	110±1

Supplementary Figure 4: Hyaluronan forms crosslinked networks at concentrations of 3 mg/mL and above.(a) Linear elastic modulus (and standard error of the mean based on 3 repeats) of crosslinked hyaluronan networks as a function of hyaluronan concentration, over the range examined in the main text. At concentrations below 3 mg/mL, we were not able to robustly measure the linear modulus, due to sensitivity limitations of the instrument. The molar ratio between the PEGDA crosslinker and the hyaluronan polymer is kept constant.

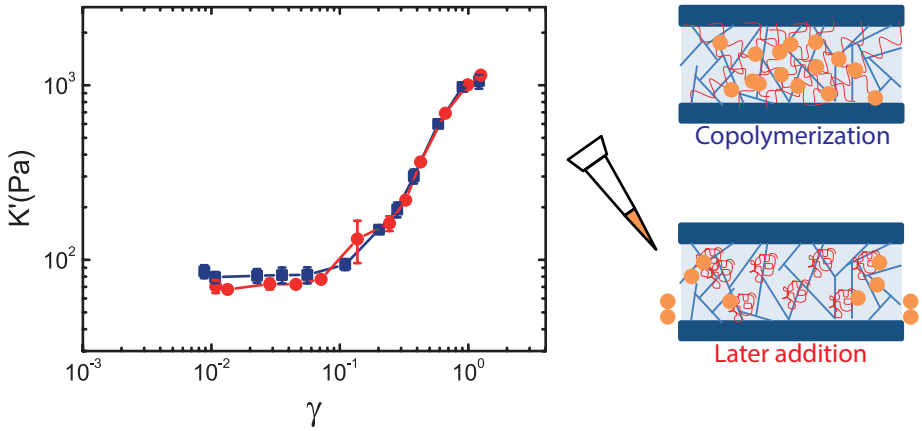

Supplementary Figure 5: Effect of delayed hyaluronan crosslinking on the mechanics of the composite. Strain-stiffening curves of a composite network (1 mg/mL collagen and 5 mg/mL hyaluronan) where the PEGDA crosslinker is included before collagen polymerisation (blue symbols, see schematic on the right, where the crosslinkers are indicated in orange) or after collagen polymerisation (red) are nearly identical. The average values on the basis of three independent repeats are $G_0 = 90 \pm 7$ Pa, $\gamma_o = 0.22 \pm 0.02$, and $\gamma_c = 0.43 \pm 0.10$ for co-gelation, compared to $G_0 = 80 \pm 10$ Pa, $\gamma_o = 0.2 \pm 0.01$, and $\gamma_c = 0.44 \pm 0.12$ for later crosslinker addition. Note that the moduli are slightly different from the data shown in the main text due to the use of a smaller cone plate geometry (20 mm instead of 40 mm) and a longer polymerisation time (6 hours instead of 2).

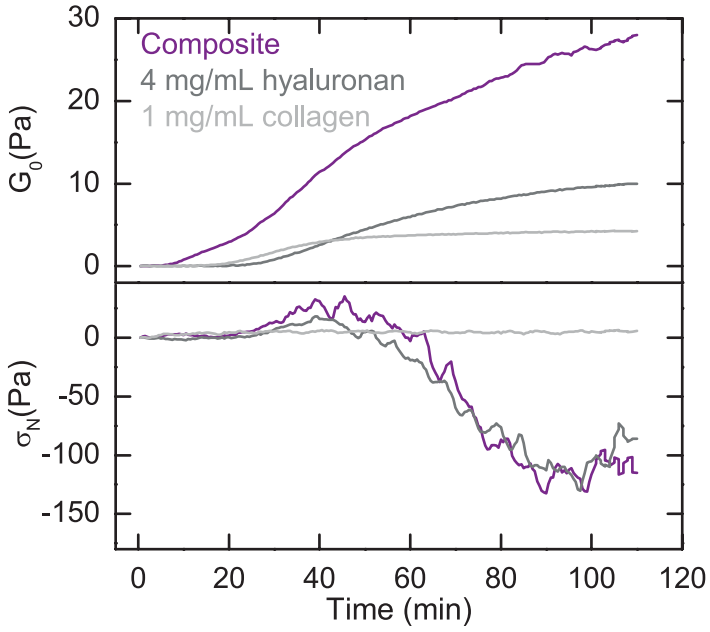

Supplementary Figure 6: Polymerisation curves and normal stress evolution for pure collagen, pure hyaluronan, and composite system. Top panel: Time evolution of the linear elastic shear modulus during polymerisation for a composite system composed of 1 mg/mL collagen and 4 mg/mL hyaluronan (purple, top-most curve), pure collagen at 1 mg/mL (light gray), and pure hyaluronan 4 mg/mL (dark grey). Bottom panel: Corresponding time evolution of the normal stress as a function of polymerisation time. Note that no measurable normal stress is observed in the pure collagen system. By contrast, the normal stress for the pure hyaluronan network and the collagen-hyaluronan composite first increases and then decreases, finally reaching a negative value indicative of contractile prestress.

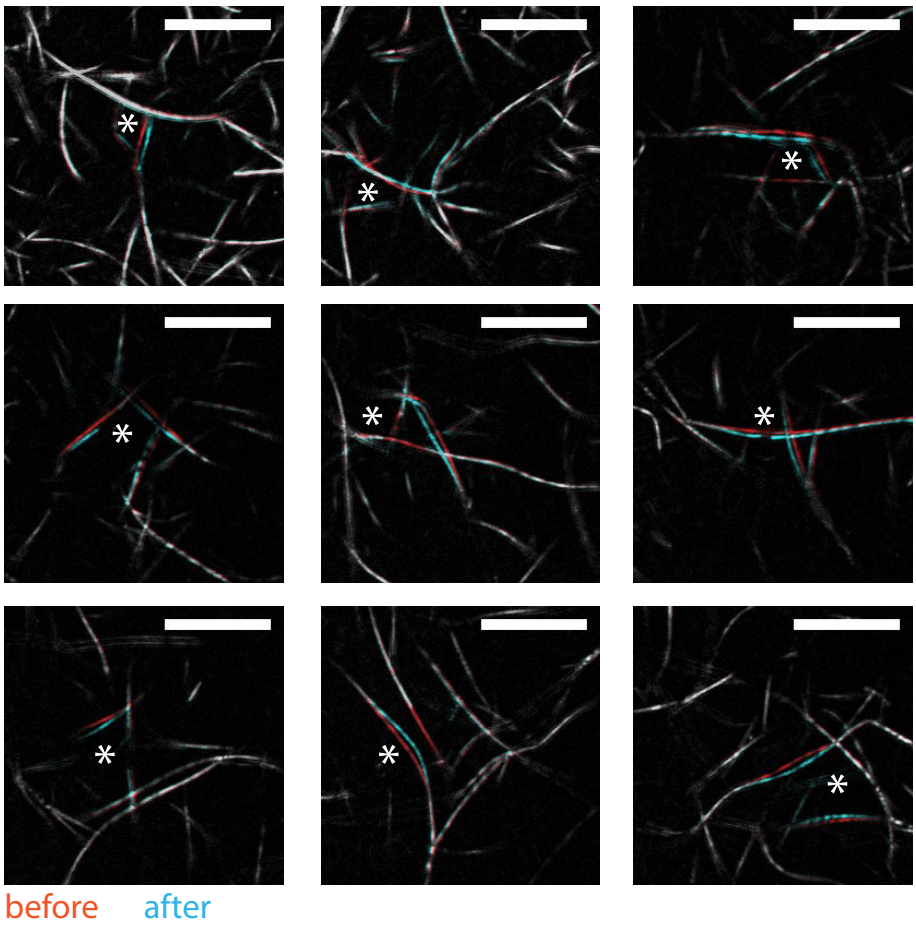

Supplementary Figure 7: Ablation experiments show how the surrounding stressed hyaluronan matrix affects the recoil of collagen fibres. Time projections of composite networks, showing only the collagen network imaged with label-free confocal reflectance microscopy, before and after localized ablation of the background hyaluronan network. The networks are composed of 1 mg/mL collagen and 4 mg/mL hyaluronan. Scale bars indicate 10 μm and asterisks represent the approximate location of the ablation spot.

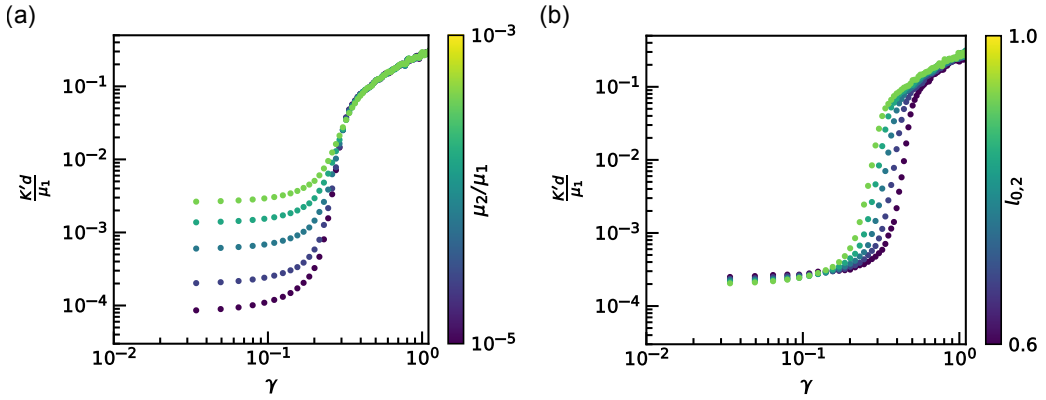

Supplementary Figure 8: Simulated two-component stiffening response when varying independently matrix stiffness and matrix prestress. Modulus versus strain curves for (a) varying matrix stiffness at fixed $l_{0,2} = 0.75d$ and (b) varying matrix rest length at fixed $\mu_2/\mu_1 = 1x10^{-4}$. Results obtained using diluted triangular networks with z=3.4, L=50, $N_{config} = 20$, $\tilde{\kappa} = 3x10^{-5}$ and $\tilde{\mu}_2 = 3x10^{-5}$.

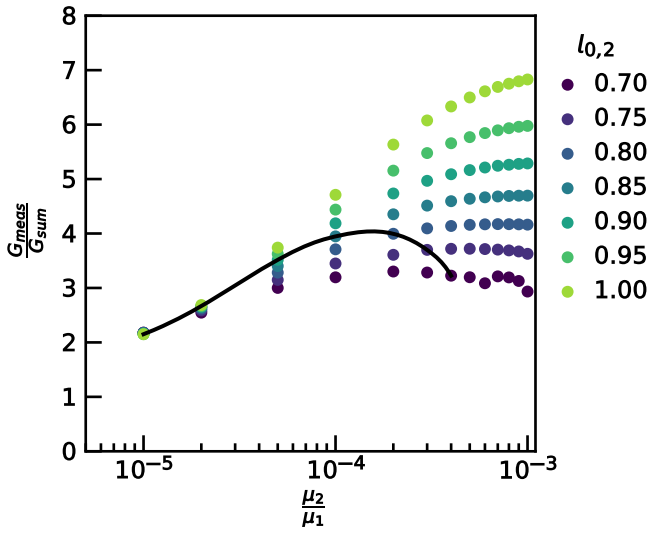

Supplementary Figure 9: Linear mechanical enhancement in the double network simulations. The linear mechanical enhancement is calculated for the double network simulations as G_{meas}/G_{sum}, with G_{meas} the modulus obtained in the double network simulations, and G_{sum} obtained as the sum of the modulus of the fibre network (z=3.4, $\tilde{\kappa} = 3x10^{-5}$) and that of the matrix (homogeneous triangular lattice with stiffness $\tilde{\mu_2}$). Without internal stress ($l_{0,2} = 1.00$), the linear mechanical enhancement is proportional to the matrix stiffness. For small μ_2, the linear mechanical enhancement depends weakly on the matrix rest length $l_{0,2}$. However, for large μ_2 there is a strong dependence on $l_{0,2}$. Experimentally, a peak is observed in the linear mechanical enhancement as a function of c_{HA}, as shown in Figure 1c. Qualitatively, we observe a similar trend in the simulation data. We start with the notion that the mechanical response as a function of hyaluronan concentration matches qualitatively with a simultaneous increase of matrix stiffness and decrease of rest length in the experiment (see figure 3b). We can estimate that the stiffness of the matrix ranges from $1x10^{-5}$ to $1x10^{-3}$ (data not shown). In addition, the quantitative mapping predicts a compression of 10% at a hyaluronan concentration of 5 mg/mL. In the double network simulations, this corresponds to l0 values between 1.00 and 0.70 (data not shown). The black line shows that, if the rest length decreases with increasing stiffness roughly following these ranges, a peak in the mechanical enhancement is present.

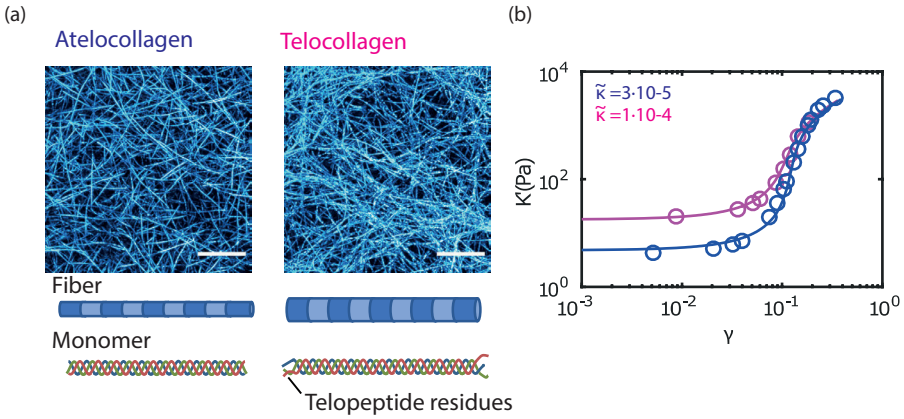

Supplementary Figure 10: Changing the fibre rigidity by including or removing the telopeptide regions of collagen. (a) Z-stack projections of atelo and telocollagen networks (1 mg/mL) imaged with confocal reflectance microscopy, together with schematics showing the difference between the two at the fibre level (different fibre diameter) and molecular level (absence or presence of telopeptides that mediate crosslinking between adjacent collagen monomers). (b) Fits (lines) of the athermal fibrous network model [41] to the measured strain-stiffening curves of the two types of networks (circles) reveal a different dimensionless fibre rigidity for collagen and atelocollagen (inset).

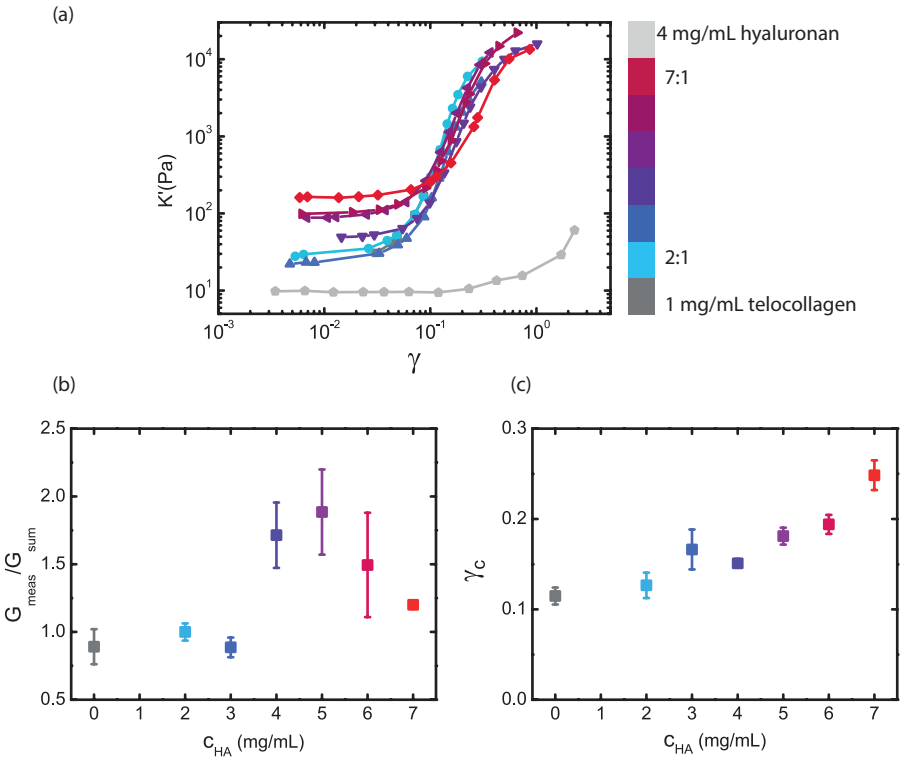

Supplementary Figure 11: Effect of hyaluronan on telocollagen network mechanics.(a) Strain stiffening curves of a pure telocollagen network (1 mg/mL) and composites with increasing hyaluronan concentration (see colour bar on the right). (b) Linear mechanical enhancement and (c) critical strain measured as a function of hyaluronan concentration. Error bars in (b) represent the error obtained with error propagation, while for (c) they are obtained by considering the standard error on the mean of at least three independent measurements

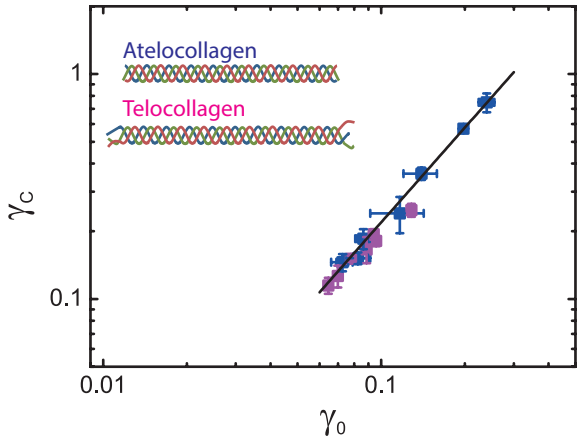

Supplementary Figure 12: Power law relationship between onset and critical strain for composite systems with varying hyaluronan concentration. The relationship between onset and critical strain follows a power law, consistent with prior observations for pure collagen systems [60]. Solid black line indicates a power-law with exponent 1.4.

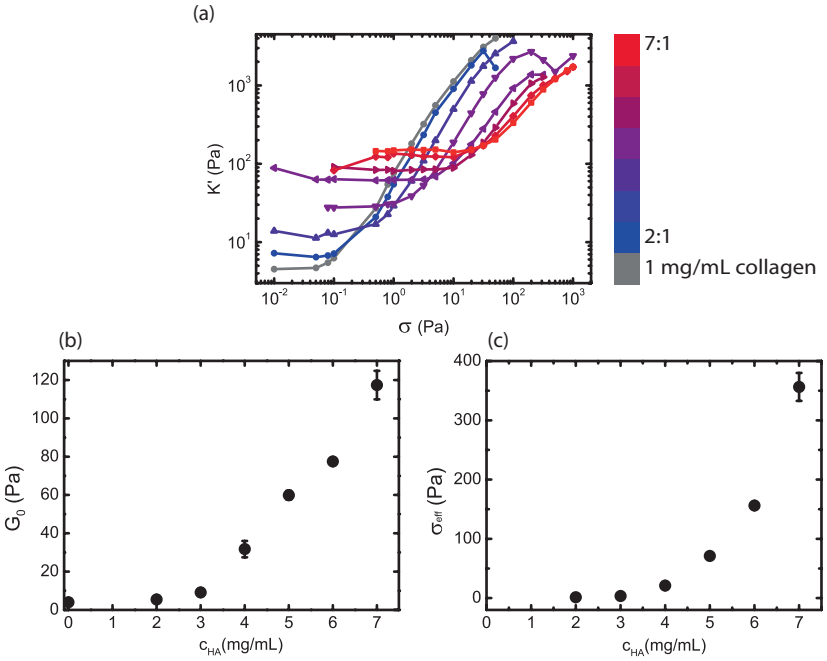

Supplementary Figure 13: Rescaling stress-stiffening curves onto a master curve.(a) Stress-stiffening curves of composite networks composed of 1 mg/ml atelocollagen and various concentrations of hyaluronan, which were used for obtaining the master curve in Figure 4. (b) Values of G_0 used to rescale curves on the y-axis, and (c) values of effective stress σ_{eff} used to rescale curves on the x-axis, both shown as a function of hyaluronan concentration. Error bars represent standard error on the mean of at least three independent measurements.

4

Particle diffusion in extracellular hydrogels

Hyaluronic acid is an abundant polyelectrolyte in the human body that forms extracellular hydrogels in connective tissues. It is essential for regulating tissue biomechanics and cell-cell communication, yet hyaluronan overexpression is associated with pathological situations such as cancer and multiple sclerosis. Due to its enormous molecular weight (in the range of millions of Daltons), accumulation of hyaluronan hinders transport of macromolecules including nutrients and growth factors through tissues and also hampers drug delivery. However, the exact contribution of hyaluronan to tissue penetrability is poorly understood due to the complex structure and molecular composition of tissues. Here we reconstitute biomimetic hyaluronan gels and systematically investigate the effects of gel composition and crosslinking on the diffusion of microscopic tracer particles. We combine ensemble-averaged measurements via differential dynamic microscopy with single-particle tracking. We show that the particle diffusivity depends on the particle size relative to the network pore size and also on the stress relaxation dynamics of the network. We furthermore show that addition of collagen, the other major biopolymer in tissues, causes the emergence of caged particle dynamics. Our findings are useful for understanding macromolecular transport in tissues and for designing biomimetic extracellular matrix hydrogels for drug delivery and tissue regeneration.

Chapter based on: Burla, F., Sentjabrskaja, T., Pletikapic, G., van Beugen, J., Koenderink, G.H. *Particle diffusion in extracellular hydrogels*, Soft Matter 16, 1366-1376, 2020.

4.1 Introduction

Hyaluronan is a charged linear polysaccharide that is widely present in the human body, where it forms extracellular hydrogels [10]. Together with bottlebrush proteoglycans and polysialic acid, it forms a dense layer around cells known as the glycocalix, which protects cells against damage and virus infections. This slimy coating also modulates cell-cell and cell-matrix communication by affecting the mobility and accessibility of receptor proteins in the cell membrane [11, 139]. Cancer cells have greatly upregulated levels of hyaluronan in their glycocalyx, which is thought to promote a tumor phenotype by increasing integrin adhesion and signalling [12, 140, 141]. In the cumulus cells that surround oocytes [142], hyaluronan forms a specialized jelly-like structure that is crosslinked by accessory proteins and is critical for fertilization [143, 144].

In soft connective tissues, hyaluronan is not grafted to cells but organized in entangled or crosslinked hydrogels with the help of accessory proteins. In cartilage and in the vitreous humor, hyaluronan is for instance found together with collagen fibrils and aggrecans. The molecular weight, concentration, and network structure of hyaluronan in these extracellular hydrogels vary with tissue type and change during tissue development and with age [10, 145]. These variations help tailor the biomechanical behavior of each tissue for its specific function and strongly influence cell physiology through mechanochemical signalling [146, 147]. In addition, variations in the physical properties of hyaluronan hydrogels influence the ability of macromolecules (growth factors, nutrients, and signaling factors), virus particles and cells to diffuse or migrate through the tissue [148]. Many pathological situations are associated with excessive deposition of hyaluronan and changes in its molecular weight, with deleterious consequences for tissue penetrability [149]. For instance, excessive deposition of hyaluronan in demyelinated lesions during multiple sclerosis inhibits regrowth of nerves [26], and changes in hyaluronan content in malignant tissues hampers the transport and delivery of cancer therapeutics [133, 150]. It is therefore important to understand how normal and pathological variations in hyaluronan molecular weight, concentration, and interactions with other matrix components impact the penetrability of the extracellular matrix. However, it is challenging to dissect the contribution of hyaluronan due to the complex composition and structure of living tissues. A way to overcome this difficulty is to reconstitute extracellular hydrogels from purified hyaluronan. Several previous studies have indeed reported measurements of particle mobility in reconstituted hyaluronan gels based on either passive microrheology (using video tracking or light scattering to detect the thermal motions of tracer particles [151–153]) or active microrheology (using optical tweezer manipulation of tracer particles [154]). With few exceptions [155, 156], the focus of these studies was on single-component networks of hyaluronan networks that interact solely through excluded volume and electrostatic interactions.

Here, we investigate the dynamics of both semidilute solutions and crosslinked gels of high molecular weight hyaluronan using a variant of passive microrheology known as differential dynamic microscopy (DDM) [157]. Rather than tracking the trajectories of individual tracer particles, this method probes the ensemble-averaged dynamics of many particles at once using a Fourier-space analysis of time-lapse movies. DDM analysis thus yields information comparable to data obtained by dynamic light scattering. DDM has a number of advantages over conventional particle tracking: it can be performed over a wider particle size range, can work with fluorescence, bright field and dark field microscopy data, and does not need complex tracking algorithms nor a costly setup [157, 158]. For these reasons, DDM was recently introduced as a new method for performing microrheology on soft matter systems [159–161]. We complement the ensemble-averaged information obtained from DDM with single particle tracking, using the same time-lapse imaging data as input, in order to test for the presence of spatial and temporal heterogeneities in particle dynamics that typically arise in heterogeneous systems such as polymer gels [162–165]. In order to understand how the dynamics of hyaluronan networks are modulated by accessory extracellular molecules that introduce crosslinks, we probe single-component gels with three different crosslink configurations: semidilute solutions, transiently crosslinked gels obtained by pH-triggered gelation [166], and chemically crosslinked gels. We show that semidilute solutions and transiently crosslinked hyaluronan networks simply hinder particle transport through enhanced viscous drag, whereas permanently crosslinked gels hamper particle diffusion by size exclusion. We also study two-component gels combining hyaluronan with a fibrillar collagen network, and show that the composite polymer gels exhibit caged dynamics. Our data reveal a rich phase-space for control over particle diffusion in the crowded extracellular space of tissue, both through variations in the physical properties of hyaluronan itself and through interactions with other matrix constituents. Our results can be useful in interpreting the impact of hyaluronan on cell-cell signaling [148] and on drug penetration through the interstitial matrix of tissues to solid tumours [133], as well as for the design of hyaluronan-based hydrogels for regenerative medicine and controlled drug release [167].

4.2 Materials and methods

4.2.1 Bead passivation protocol

Polystyrene tracer particles with diameters of 0.6 μm as specified by the supplier were purchased from Sigma Aldrich. Red fluorescent particles of 0.2 or 0.1 μm diameter as specified by the supplier were purchased from ThermoFischer Scientific (FluoroMax Dyed Red Aqueous Fluorescent Particles). To prevent non-specific interactions of the particles with the hyaluronan polymers, the particles were passivated with

poly(ethylene glycol) chains following an established protocol [130]. Briefly, 45 μL of a stock solution of particles was pipetted in an Eppendorf tube and sonicated for 5 minutes to disperse any aggregates. Next, 300 μL Pluronics F-128 (10% w/v, Sigma Aldrich) was added and incubated with the particles for 10 minutes. Subsequently, 120 μL toluene (99.5%, Sigma Aldrich) was added and the samples were incubated on a rotating wheel (18 rpm) for three hours. Toluene swells the particles, allowing for the hydrophobic blocks of the Pluronic chains to insert into the particle surface. Afterwards, toluene was removed by heating the Eppendorf tubes under the fume hood at 95°C for 15 minutes. The particles were centrifuged 5 times (10 minutes at 5000 rpm each time) with replacement of the supernatant by MilliQ water between each centrifugation step. This washing procedure deswells the particles, so the Pluronic chains become firmly anchored to the particle surface. The passivated particles were stored in the fridge for a maximum of 1 month. Before use, the particles were sonicated for 15 minutes to remove any aggregates. The hydrodynamic diameters of the particles, as determined from DDM measurements on dilute particle suspensions in water, were 0.15 μm, 0.22 μm and 0.66 μm, which is larger than the nominal radii likely due to the combined presence of the Pluronic layer and a solvation shell.

4.2.2 Image acquisition

Time-lapse videos used in both single particle tracking and differential dynamic microscopy analysis were acquired on an inverted Ti-Eclipse microscope (Nikon) with a 100x oil or 60x water immersion objective (Nikon) with numerical apertures of 1.49 and 1.27, respectively, and with a digital CMOS camera (Hamamatsu, Orca-Flash 4.0). For the larger 0.6 μm particles, we imaged with bright field mode using illumination with white Halogen light (Nikon). The smaller 0.2 and 0.1 μm particles were imaged with fluorescence microscopy, using a 532 nm laser (Lumencor LED) for illumination. The exposure time of the camera was set to 10 ms, giving access to a 100 fps acquisition rate. The delay time between each frame was varied from 0 to 100 ms depending on the sample viscosity, in order to obtain a full relaxation of the intermediate scattering function (or at least a partial relaxation in the case of chemically crosslinked networks). Each video consisted of 5000 frames and for each condition reported, videos were recorded from at least three different regions of the same sample and in at least three independently prepared samples. Collagen-hyaluronan composites were imaged in confocal reflectance mode, a method which allows label-free imaging, using a 488 nm Argon laser (Melles Griot) for illumination. Images were taken from 10 μm above the surface over a depth of 30 μm, with a step size of 0.5 μm, and are shown as maximum projection intensity.

4.2.3 DDM analysis

DDM analysis of the time lapse videos was performed using a custom written MatLab program based on principles explained in prior studies[157]. The thermal motions of the tracer particles in the viscoelastic medium provided by the hyaluronan hydrogels cause temporal fluctuations of the intensity in each image pixel with coordinates (x,y). Fourier transformation of the intensity time traces I(x,y,t) and correlation of the difference images at different lag times Δt produces the image structure function D (q,Δt):

$$D(\mathbf{q}, \Delta t) = < |i(\mathbf{q}, t + \Delta t) - i(\mathbf{q}, t)|^2 > \tag{4.1}$$

where q = 2π/l is the wavevector and l represents a characteristic distance in real space. The intermediate scattering function f(q,Δt) is obtained from the image structure function through the formula:

$$D(\mathbf{q}, \Delta t) = A(\mathbf{q})[1 - f(\mathbf{q}, \Delta t)] + B(\mathbf{q}) \tag{4.2}$$

where A(q) is a proportionality factor and B(q) represents the noise of the camera. By fitting f(q,Δt) to a phenomenological stretched exponential decay, $exp{-}(\Delta t/\tau(q))^n$ with stretching exponent n, one retrieves the diffusion coefficient of the tracer particles, D=1/($\tau(q)q^2$). In a Newtonian fluid of viscosity η, the diffusion coefficient of particle of radius r is inversely proportional to the viscosity according to the Stokes-Einstein relation:

$$D_m = \frac{k_B T}{6\pi\eta r} \tag{4.3}$$

Under certain conditions, this relation can be generalized to complex fluids that are viscoelastic:

$$\tilde{G}(s) = \frac{k_B T}{\pi a s < \tilde{r}^2(s) >} \tag{4.4}$$

where $\tilde{G}(s)$ and $< \tilde{r}^2(s) >$ represent the Laplace transforms of, respectively, the complex viscoelastic modulus of the fluid and the mean-squared displacement of the particles. This generalization is the basis for passive microrheology, a technique that since its inception [168] has been widely applied to study polymers, including biopolymers such as hyaluronan [151, 154]. One important condition for the generalized Stokes-Einstein relation to hold is that the tracer particles are large enough compared to the correlation length of the polymer network such that they perceive the network as a viscoelastic continuum [169]. In entangled polymer solutions, the tracer particle motions will then reflect the bulk solution viscosity. In order to extract the frequency-dependent storage modulus G'and loss modulus G", we first transformed the ISF at q = 4.5 μm^{-1} to obtain the mean-squared displacement according to the following relation[160] valid for displacements in 2D:

$$< \Delta r^2(\Delta t) >= -\frac{4}{q^2} ln(f(q, \Delta t)) \tag{4.5}$$

We subsequently employed the fitting routine implemented in [170] that is based on the Evans-Tassieri method[171].

4.2.4 Particle tracking

Single particle centroid tracking was performed with TrackPy [131], an algorithm based on the Crocker-Weeks tracking algorithm [172]. This algorithm allows to track and drift-subtract individual particle trajectories and to retrieve the corresponding meanâsquared-displacements. We next reloaded the trajectories to a custom-written Python program to calculate the ensemble-averaged van Hove distribution functions of particle displacements and to perform curve fitting with Gaussian and exponential functions, as well as calculation of the non-Gaussian parameter. For each video, we analyzed a total of at least 10000 trajectories, and for each sample we analyzed at least three independently prepared samples. We restricted the analysis to lag times Δt corresponding to at most 10% of the total length of the video, in order to avoid artefacts deriving from low statistics.

4.2.5 Sample preparation

Semidilute solutions of hyaluronic acid were prepared by dissolving sodium hyaluronate obtained by fermentation of Streptococcus Equii bacteria with a nominal molecular weight between 1.1-1.6 MDa (Sigma Aldrich) at a concentration of 1,2 or 4 mg/mL in phosphate buffered saline (PBS: pH 7.4, 138 mM NaCl; 2.7 mM KCl) obtained in tablet form from Sigma Aldrich. The samples were vigorously vortexed for several minutes or placed on a spinning wheel at room temperature for several hours to ensure full solubilisation. Transiently crosslinked hyaluronan gels at pH 2.5 were obtained by adding varying amounts of an aqueous solution of HCl to the semidilute solutions of hyaluronan. Chemically (i.e. permanently) crosslinked hyaluronan solutions were obtained by combining commercially available thiolated hyaluronic acid (Glycosil, 2B Scientific, 240 kDa) in powder form (2B Scientific) with a poly(ethylene glycol) diacrylate crosslink (Extralink PEGDA, 2B Scientific, 3.4 kDa) in PBS buffer. Composite hyaluronan-collagen samples were prepared by neutralizing type I collagen with intact telopeptide end-sequences from bovine dermis (TeloCol, CellSystems, supplied at 3.0 mg/mL in hydrochloric acid) by the addition of 1 M NaOH and PBS from a 10x stock concentration for buffering and quickly mixing this on ice with 2 mg/ml hyaluronan before collagen started to polymerize. Collagen was allowed to polymerize at 37°C for two hours before imaging. Passivated tracer particles were added directly before the measurements in a ratio of 1:100 with the final sample volume, and the solution was homogenized by

vigorous vortexing. In the case of crosslinked hyaluronan and composite collagen-hyaluronan samples, the particles were added prior to hyaluronan crosslinking or collagen polymerization, in order to ensure a homogeneous distribution across the sample.

4.2.6 Shear rheology

The linear viscoelastic moduli of semidilute and crosslinked hyaluronan networks were measured by small amplitude oscillatory shear rheology on a stress-controlled rheometer (Anton Paar MCR 501) equipped with a cone-plate geometry with a diameter of 40 mm, cone angle of 1°. The experiments were performed at a temperature of 22°C set by a Peltier system. Semidilute hyaluronan solutions were loaded onto the bottom plate with a pipette, putty samples were loaded with a spatula, and permanently crosslinked samples were quickly loaded with a pipette before crosslinking set in. The samples were allowed to thermally equilibrate for 10 minutes in the case of the semidilute and putty solutions, while the crosslinked gels were allowed to polymerize for two hours between the rheometer plates before measuring. After equilibration, we determined the linear viscoelastic moduli by applying an oscillatory shear strain at different oscillation frequencies, logarithmically spaced between 0.1 and 10 Hz, and a small strain amplitude of 0.5%. To determine the viscosity, we furthermore measured flow curves by applying a rotational shear with the strain rate increasing logarithmically from 0.01 to 100 s^{-1}. The reported results are averages of at least three independent measurements for each sample condition. The measurements on collagen and collagen-hyaluronan composites were performed after allowing for in situ collagen polymerization for two hours.

4.2.7 Mesh size determination

We inferred the mesh size of the crosslinked hyaluronan gels from the measured linear elastic shear modulus G' by referring to rubber elasticity theory[32, 173], which predicts:

$$G' = \rho_{el} k_B T \tag{4.6}$$

where $k_B T$ is the thermal energy and ρ_{el} represents the number density of elastically active network strands, related to the mesh size ϕ_{el} by:

$$\phi_{el} = \rho_{el}^{-1/3} \tag{4.7}$$

We thus estimate a mesh size ϕ_{el} = 200 nm for the 4 mg/mL crosslinked hyaluronan gels, for which we measured G'= 4 Pa. For the calculation of the mesh size of uncrosslinked hyaluronan, we employed the fact that the mesh size of a solution of worm-like chains polymer interacting through excluded volume only should scale according to [35]:

$$\phi = \sqrt{\frac{3}{\nu L}} \tag{4.8}$$

where L is the polymer length, and ν is the number of polymers per unit volume. We find values around 200 nm for the 4 mg/mL solution, comparable to the mesh size of the crosslinked network. This observation indicates that the network remains homogeneous in the presence of crosslinking.

To determine the mesh size of the 1 mg/ml collagen networks, we used a previously reported image analysis algorithm [109]. Briefly, we binarized a 3D-confocal image stack and measured the distances between on and off pixels. The distance distribution was well-fitted by an exponential decay, and the decay exponent was taken as the average mesh size after conversion from pixels to μm (121 nm/pixel). For 2 mg/ml collagen networks, we calculated the mesh size assuming that it scales with concentration according to $c^{-1/2}$. We obtained average mesh size values of 3 μm for 1 mg/mL collagen and 2 μm for 2 mg/mL collagen networks.

The mesh size of the composite networks was calculated as a geometrical average of the mesh sizes of the hyaluronan and collagen networks [174]:

$$\phi_c^{-3} = (\phi_{HA}^{-3} + \phi_{coll}^{-3}) \tag{4.9}$$

where ϕ_c is the composite mesh size, ϕ_{HA} is the hyaluronan mesh size, ϕ_{coll} is the collagen mesh size. We obtained a mesh size of 300 nm for a composite network composed of 1 mg/mL collagen and 2 mg/mL hyaluronan, almost identical to the mesh size of the hyaluronan-only network, consistent with the large mismatch between the hyaluronan and collagen mesh sizes.

4.3 Results

4.3.1 Effect of crosslinking on particle diffusivity in hyaluronan networks

We first measured particle diffusion in hyaluronan networks at different concentrations ranging from 1 to 4 mg/mL as a function of the state of chain crosslinking (Figure 1(a-c)). The overlap concentration $c*$ for hyaluronan with a molecular weight of 1 MDa is around 2 mg/mL [151, 152]. Given that entanglements typically set in at an entanglement concentration c_e that is at least 5 times larger than $c*$, the solutions should fall in the semidilute unentangled regime [175]. We verified this by measuring the concentration-dependence of the viscosity, which in the semidilute unentangled regime [176] scales with a power law of around 1.3 (see Supplementary Figure S1). Semidilute solutions were obtained by dissolving hyaluronan in physiological salt buffer (PBS) at neutral pH, where the electrostatic charges are screened and the polymers behave as random coils that interact mainly

via excluded volume and hydrodynamic interactions [177]. Transiently crosslinked networks were obtained by lowering the pH to 2.5, which reduces electrostatic repulsions among hyaluronan chains due to the proximity to its isoelectric point of 2.5 [178] and enhances chain associations through hydrogen bonds between amide and carboxylate residues [166]. This pH-induced gel state is traditionally referred to in the hyaluronan literature as the putty state [179]. Finally, permanently crosslinked networks were obtained by reacting thiol-modified hyaluronic acid with a diacrylate (PEGDA) crosslinker. We note that the measurements reported with the chemically crosslinked hyaluronan refer to a lower molecular weight than the entangled and transiently crosslinked hyaluronan samples. As shown in Supplementary Figure S2, DDM reveals similar dynamics for particles in solutions of the low (240 kDa) and high (1.5 MDa) molecular weight semidilute hyaluronan, but with a higher particle mobility, reflecting the lower solution viscosity associated with the lower molecular weight.

We seeded the hyaluronan networks with tracer particles with a diameter of 0.6 μm and measured the ensemble-averaged dynamics of these particles by recording time-lapse movies and performing DDM analysis. As shown in Figure 1, the dynamics of the particles as quantified through the intermediate scattering function (ISF) strongly varied with crosslinking conditions. Note that the scattering functions are shown for a q-value of 4.65 μm $^{-1}$, which is an intermediate value where the ISF is not affected by the drifting of the particles out of the field of view at high q (see [180] and Supplementary Figure S3). Particles in semidilute solutions of hyaluronan (Fig. 1a) exhibited simple diffusive behavior characterized by a single-exponential decay of the intermediate scattering function in the concentration range here investigated (Fig. 1d). A similar decay was observed in different regions of interest in a given sample, indicating that the material was homogeneous over length scales of hundreds of micrometers (the size of the field of view of the microscope) (see Supplementary Figure S4). Also, we observed comparable decays for different samples. The observations of simple diffusion and negligible spatial heterogeneity are consistent with the macroscopic rheology of the hyaluronan solutions, which behaved as viscous solutions with negligible elasticity (see Supplementary Figure S5a). Particles in the transiently crosslinked network obtained by pH-induced gelation (Fig. 1b) showed slower dynamics, although the intermediate scattering function still exhibited a single-exponential decay (Fig. 1e). This behavior is again qualitatively consistent with the macroscopic rheology of the gels, which behaved as viscoelastic Maxwell fluids (see Supplementary Figure S5b).

By contrast, particles in the permanently crosslinked network (Fig. 1c) showed different dynamics, depending on the concentration (Fig. 1f). Particles in gels made of 1 mg/mL hyaluronan showed simple diffusion with a diffusion coefficient slightly lower than in water. Particles in 2 mg/mL hyaluronan gels showed incomplete relaxation of the intermediate scattering function and particles in 4 mg/mL gels did

not measurably diffuse at all. Indeed, the 4 mg/mL gels behaved rheologically as elastic solids with a frequency-independent elastic modulus that was much larger than the loss modulus (see Supplementary Figure S5c). At concentrations lower than 3 mg/mL, as we previously reported[70], the samples were too soft to reliably measure an elastic modulus. We note that the ISFs for 4 mg/mL and 1 mg/mL hyaluronan networks were homogeneous across different fields of view, whereas the ISFs at 2 mg/mL showed substantial heterogeneity (see Supplementary Figure S4).

To quantify the particle dynamics, we fitted each intermediate scattering function to a stretched exponential decay

$$e^{-(\frac{\Delta t}{\tau(q)})^n} \tag{4.10}$$

allowing us to extract the transport coefficient $D = 1/(\tau(q)q^2)$ and the stretching exponent n. We furthermore compared the exponents n with the subdiffusive exponent α obtained from fitting the decay of $\tau(q)$ (over the range q = 1-10 μm^{-1}) to the form:

$$\tau(q) = (Kq^2)^{-1/\alpha} \tag{4.11}$$

to recover the transport coefficient K and subdiffusive exponent α. For the

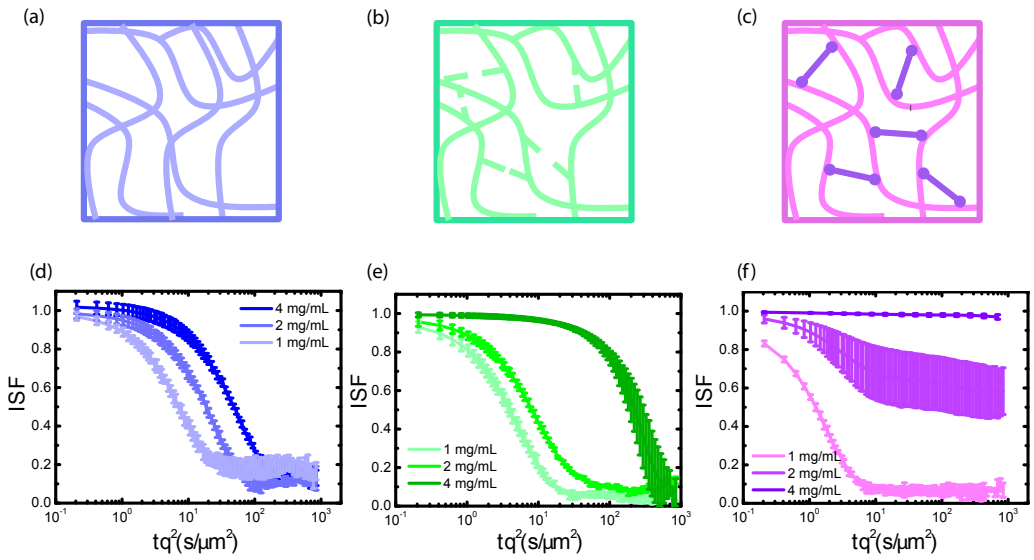

Figure 1: Diffusion of 0.6 μm tracer particles in hyaluronan networks with various degree of crosslinking. (a-c) Schematic overview of the different configurations of hyaluronan that were investigated: semidiluted (a), transiently crosslinked by pH-induced hydrogen-bonding ('putty', b), and chemically crosslinked by short PEGDA polymer links ('crosslinked ', c). (d-f) Corresponding intermediate scattering functions (ISF) at different concentrations of hyaluronan (see legends), averaged over at least three measurements per condition. Time on the x-axis is multiplied by q^2, where q = 4.65 μm^{-1}.

semidilute solutions and the transiently crosslinked networks obtained by pH-induced gelation, we found stretching exponents n close to 1 (see Supplementary Figure S6), consistent with simple diffusion. Consistent with this, also the subdiffusive exponent α from fitting the decay of $\tau(q)$ was close to 1 (see Supplementary Figure S6 and S7). The subdiffusive exponent for the mean-squared displacement $< \Delta r^2 >= 2K(\Delta t)^\alpha$ measured by particle tracking analysis was also close to 1, although we notice that the temporal range of the MSD was more limited than that of the DDM data due to low statistics at long lag times and limitations posed by the tracking accuracy at short lag times [160]. For the chemically crosslinked gels, we could only reliably determine α for 1 mg/ml, which was equal to one, because of the incomplete relaxation of the ISF at 2 and 4 mg/mL networks. The incomplete relaxation of the ISF suggests that for these two cases the particle motion is subdiffusive. In case of the 2 mg/mL system, this is accompanied by high spatial heterogeneity of the DDM correlation functions, as mentioned earlier. Similar behavior was recently reported for actin-microtubule composite networks, where subdiffusion was also accompanied by large heterogeneity[181].

The ensemble-averaged DDM analysis suggests that semidilute hyaluronan solutions and transient gels formed by acid-induced gelation behave as simple viscous media. Microrheology analysis of the data for entangled and transient hyaluronan networks confirm that these samples behave as viscoelastic fluids and furthermore show that the apparent viscosity experienced by the probe particles is about one order of magnitude lower than the macroscopic viscosity measured by rheology (see Supplementary Figure S8). This discrepancy is consistent with other microrheology data on polymer solutions, where this effect has been ascribed to polymer depletion from near the probe particles[169]. By contrast, the ensemble-averaged DDM analysis suggests that particles in chemically crosslinked hyaluronan networks are hindered by size exclusion since particles get increasingly immobilized with increasing polymer concentration (and hence decreasing pore size).

To test the dependence of particle mobility on the ratio between particle size and pore size, we measured the diffusivity of smaller tracer particles with diameters of 0.1 and 0.2 μm in permanently crosslinked networks. At 1 mg/mL, the particles experienced little hindrance from the network, irrespective of their size (Fig. 2a). The diffusion coefficient was in fact close to that in pure solvent and the stretching exponent n was close to 1. Furthermore, the ISFs collapsed onto a single master curve upon rescaling the time axis with the tracer diameter, consistent with the Stokes-Einstein relation (see Supplementary Figure S9). By contrast, at 2 mg/mL, the behavior did depend on the tracer size: the smallest (0.1 μm) tracers still diffused freely, while both 0.2 μm and 0.6 μm particles moved subdiffusively, as evidenced from incomplete relaxation of the ISF (Fig. 2b) and from subdiffusive exponents α smaller than 1 in case of the 0.2 μm particles (see Supplementary Figure S10). The ISFs did not collapse onto a single curve upon rescaling the time axis with

the tracer size. This observation demonstrates that the generalized Stokes-Einstein (GSE) relation, which would predict an inverse dependence of the relaxation time on particle size, does not hold. We indeed expect a breakdown of the GSE relation, because the dependence of particle mobility on the ratio between probe size and network mesh size indicates that size exclusion governs the mobility rather than the macroscopic viscosity (see Supplementary Figure S9b). In 4 mg/mL hyaluronan gels, the smallest (0.1 μm) particles still showed limited mobility, while the two larger particles (0.2 μm and 0.6 μm) were immobilized. Again, the ISFs did not collapse onto a single curve upon rescaling the time axis with the tracer size (see Supplementary Figure S8c), demonstrating a breakdown of the GSE relation.

The onset of immobilization which we observe here is consistent with independent estimates of the ratio between particle radius and mesh size. For the 4 mg/mL crosslinked networks, we estimate an average mesh size of 200 nm from the network elastic modulus. This value is consistent with the observation that the particles of diameter 0.2 μm are stuck in the network, while the 0.1 μm particles can move albeit being slowed down. At 2 mg/mL, we estimate from the scaling of mesh size with concentration an average mesh size of around 300 nm. However, in this case previous macroscopic rheology data indicated that the network is not fully percolated[70]. This likely explains why we observe heterogeneous dynamics for the 0.6 μm particles with large differences among ISFs measured in different sample regions (see Supplementary Figure S4). Finally, at 1 mg/mL, previously reported rheology data indicated that the network is not percolated[70], and indeed the particles experience free diffusion, governed by an apparent viscosity only slightly smaller than the solvent viscosity (see Supplementary Information S10).

A microrheology analysis for the 4 mg/mL permanently crosslinked gel shows that particles of 0.6 μm size report an elastic plateau modulus comparable with the modulus measured by rheology, suggesting that the particles feel the elastic response of the networks (see Supplementary Figure S8). We notice a dependence on the size of the particles used for microrheology analysis, consistent with the presence of structures in the network with characteristic sizes larger than the particles'size[182].

To test whether the densest (4 mg/mL) hyaluronan networks featured any spatial or temporal heterogeneities at the level of single-particle trajectories, we complemented the ensemble-averaged DDM analysis with an analysis of the individual particle trajectories in real space. We focused on the van Hove distribution, which yields the probability of finding a particle at a distance Δx or Δy after a time interval Δt and has been shown to provide insight in heterogeneities[164, 183–185]. We note that the probability of displacements in the x and y directions were isotropic (See Supplementary Figure S11). For a simple fluid, the van Hove probability distribution should be Gaussian, whereas for complex fluids with spatial and/or temporal heterogeneities it has non-Gaussian tails that are generally exponential[185, 186] . The distributions for all of the hyaluronan networks looked in first instance

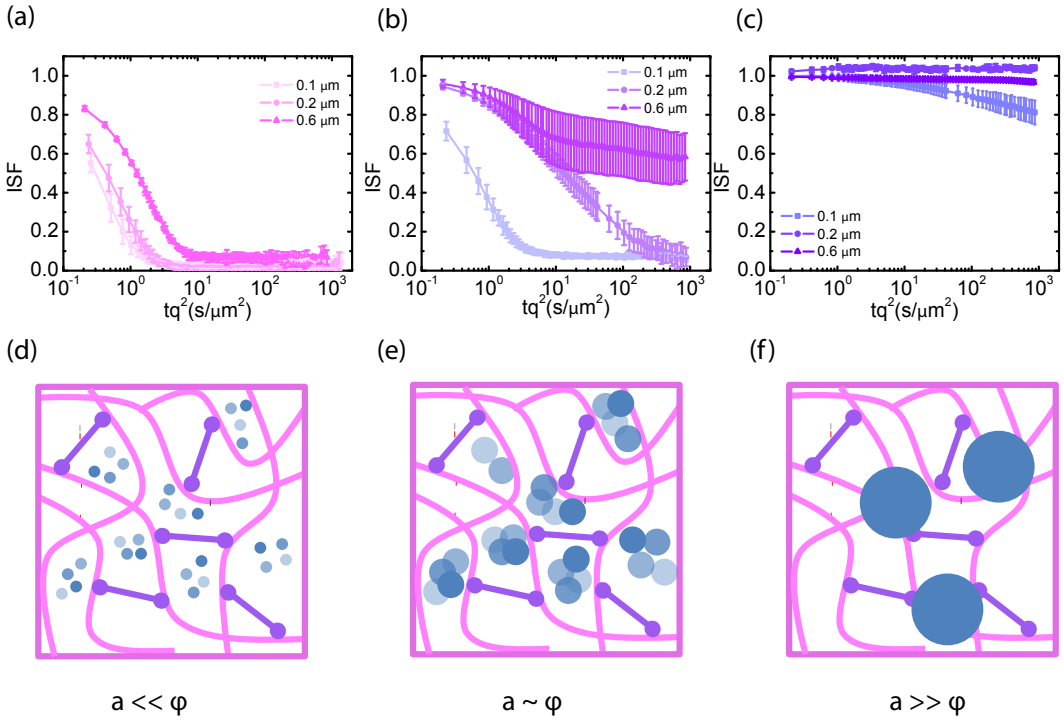

Figure 2: Mesh size effects on tracer particle mobility in chemically crosslinked hyaluronan networks. (a-c) ISF for three different tracer particle sizes (legends) in crosslinked gels with hyaluronan concentrations of 1 mg/mL (a), 2 mg/mL (b) and 4 mg/mL (c). (d-f) Schematic interpretation. When particle size a is much smaller than the network mesh size, they effectively experience the solvent viscosity with little hindrance from the network (d). (e) Particles with size a comparable to the mesh size experience hindered diffusion. (f) Particles with size a larger than the mesh size are immobilized.

Gaussian, with a width σ that increased with time due to diffusion (see Figure 3). However, the rate at which the van Hove functions broadened was lower for the transiently and permanently crosslinked networks than for the semidilute solution (see Supplementary Figure S12), consistent with the macroscopic rheology of the crosslinked samples being characteristic of an elastic solid rather than a fluid. We notice also that the distribution presents tails, which deviate from a Gaussian distribution. To quantify this deviation, we use the non-Gaussian parameter[187, 188]:

$$\xi = \frac{<\Delta x(\tau)^4>}{3<\Delta x(\tau)^2>^2} - 1 \tag{4.12}$$

This parameter is 0 for a Gaussian distribution and 2 for an exponential distribution, but it can assume larger values when the distribution function has heavy tails [189]. We found that ξ, for lag times where the particle displacement was larger than the tracking accuracy, was around 1 for all three types of hyaluronan

samples (see Supplementary Figure S12). This value, intermediate between that of a Gaussian and that of an exponential distribution, suggests indeed the presence of spatial heterogeneities. Although the reproducibility of the DDM measurements for different regions of interest indicated little evidence of inhomogeneity over length scales of hundreds of microns, the non-Gaussianity of the van Hove distribution shows that the material is heterogeneous at the micron scale.

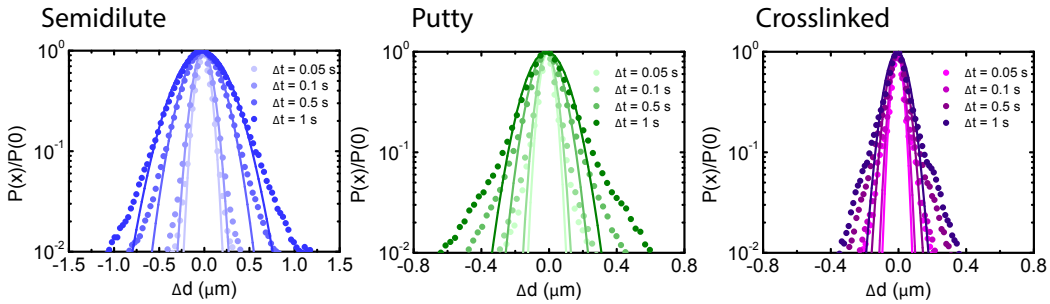

Figure 3: Real-space analysis of the individual particle trajectories in hyaluronan networks for different states of crosslinking. Gaussian fits (solid lines) to the Van Hove distributions of particle displacements (symbols) at different lag times, ranging from 0.05 to 1 s (legends), for semidilute hyaluronan solutions (blue, left), transiently crosslinked (putty) networks at pH 2.5 (green, middle) and permanently crosslinked networks (purple, right). The time-dependence of the width of the van Hove functions and the non-Gaussian parameter are shown in Supplementary Figure S12.

4.3.2 Composite hydrogels of hyaluronan and collagen

Since hyaluronan in many connective tissues is found in conjunction with fibrillar collagen, we then investigated the effect of interactions between hyaluronan and collagen on particle transport using DDM. We started from fibrillar collagen networks polymerized at 1 mg/mL and measured how the particle dynamics changed when hyaluronic acid was included, prior to polymerization, at a concentration of 2 mg/mL. As shown in Figure 4a, the intermediate scattering function for embedded 0.6 μm tracer particles revealed full relaxation in the two single-component cases of pure collagen (black) and pure hyaluronan (blue). Particle diffusion in collagen networks was only slightly slower than in pure solvent, likely because the mesh size of the network (~3 μm, Fig. 4b) was much larger than the particle size (see microrheology analysis in Supplementary Figure S13). The slightly enhanced drag on the particles could reflect the presence of a small fraction of non-polymerized collagen[111] or hydrodynamic drag imposed by the collagen fibrils. Surprisingly, particles in composite networks (orange) showed relaxation dynamics that were qualitatively different from the single-network responses: after a partial initial decay, the intermediate scattering function developed a plateau indicative of caged particle

motions. The subdiffusive exponent α for the composite network as determined from fitting $\tau(q)$ was ~0.5 (see Supplementary Figure S14), indicating subdiffusive motion[184, 190]. Through confocal imaging, we verified that the collagen network architecture was not affected by the presence of hyaluronan during polymerization (Fig. 4b-c). Qualitatively, neither the mesh size of the network nor the spatial organization of the fibers was significantly affected by the presence of hyaluronan. We quantitatively verified this by determining the mesh size of the collagen network within the composite network through image analysis. We found an average mesh size of 3.00 ± 0.05 μm in the presence of hyaluronan, which is indeed comparable to the mesh size of 3.1 ± 0.2 μm for the collagen-only network.

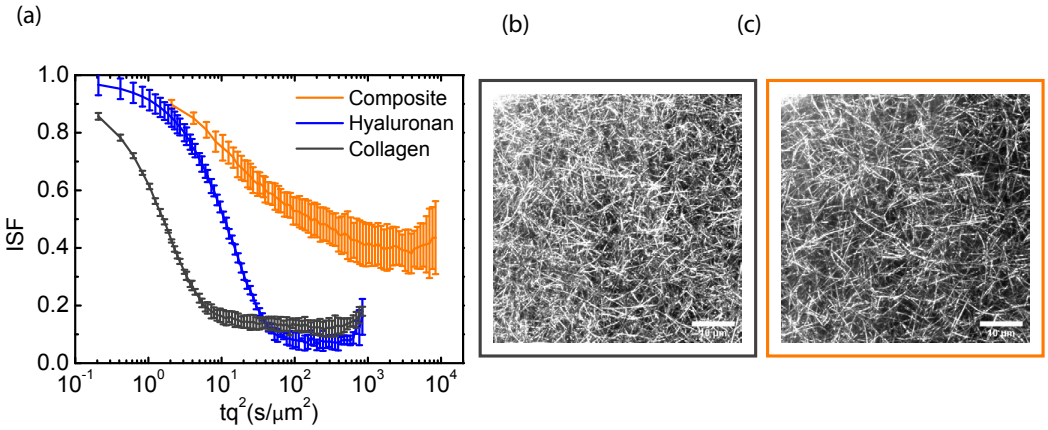

Figure 4: Particle dynamics in composite collagen-hyaluronan networks. (a) Intermediate scattering function (ISF) for 0.6 μm particles in networks of 1 mg/mL collagen (black curve), 2 mg/mL hyaluronan (blue) and composite collagen-hyaluronan (orange). (b-c) Confocal images of the fibrillar collagen network for a 1 mg/mL pure collagen network (b) and for a composite where the collagen fibrils are embedded in a hyaluronan background network that is not visible in the image (c). Scale bar indicates 10 μm.

To further test for caged dynamics in the composite networks, we analyzed the shape of the van Hove distribution functions constructed from the individual particle trajectories (see Figure 5). Similar to the pure hyaluronan systems, also the van Hove functions for the collagen network and the composite networks showed exponential tails, indicating microscale heterogeneities. A previous study[191] predicted that the exponential tails of the heterogeneous van Hove distribution should show a power-law scaling with time $\lambda = at^b$, with an exponent b of approximately 0.5, which results mathematically from a superposition of multiple Gaussians with different width (mirroring the heterogeneity of the sample). We observed values of b close to 0.5 for the pure hyaluronan gels at 2 mg/mL and a lower value of 0.3 for the collagen sample and the composite network (see Supplementary Information S15), similar to a previous report on heterogeneous networks[183]. The non-Gaussian parameter ξ

characterizing the deviation of the van Hove distributions from a Gaussian reached values of 1 for 2 mg/mL collagen, 0.8 for 1 mg/mL collagen and 0.4 for hyaluronan at long lag times. For the composite networks, ξ reached a value of 2 at long lag times, suggesting a higher degree of heterogeneity (see Supplementary Figure S16).

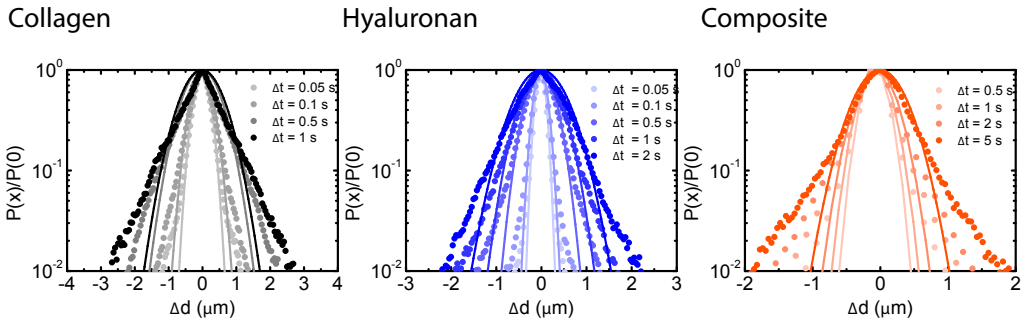

Figure 5: Single particle analysis of tracer particle dynamics in collagen-hyaluronan composite networks. Gaussian fits (solid line) to Van Hove distributions (squares) at different lag times, ranging from 0.05 to 1 s, for collagen (gray, left), 2 mg/mL semidilute hyaluronan (blue, middle), and ranging from 0.5 to 5 s for the composite networks (orange, right).

To test whether subdiffusion results from polymer interactions or simply from an increased overall polymer density, we also performed measurements on collagen-only networks with a higher concentration of 2 mg/mL. In this case we observed incomplete relaxation of the ISF (see Supplementary information S17-S18), similar to the composite. The decay of $\tau(q)$ was characterized at small q by a subdiffusive exponent α of 1, but showed deviations from this simple decay at larger values of q (see Supplementary Information S14). Thus, subdiffusion was also observed for the collagen-only network upon raising the concentration, but to a lesser extent than in the collagen/hyaluronan composite. Since the mesh size of the 2 mg/mL collagen network is around 2 μm, much larger than the particle size, the caged dynamics we observe likely originates from the rigidity of the network and this can potentially also contribute to the caged dynamics in the composite network containing 1 mg/ml collagen. To test the effect of collagen on the rigidity of the composite system, we performed macroscopic rheology measurements. As shown in Supplementary Figure S19, the elastic modulus of the composite network was identical to that of a collagen-only network (1 mg/mL) network showing that collagen dominates the elastic response. This observation can be rationalized with the fact that hyaluronan by itself behaves as a viscous fluid with a negligible elastic response (see also Supplementary Figure S5). By contrast, the collagen network has a finite elasticity, consistent with predictions for crosslinked networks of athermal filaments[40, 41].

4.4 Discussion

Hyaluronan is a polyelectrolyte widely present in the extracellular matrix of connective tissues, where it regulates tissue biomechanics and cell physiology. In this study, we investigated how different degrees of hyaluronan crosslinking and combination with collagen fibrils, which are also an abundant component of tissues, influence the diffusion of tracer particles. To this end, we employed differential dynamic microscopy (DDM) and real space particle tracking. We first focused on the effect of the state of crosslinking by comparing particle dynamics in semidilute solutions and in transiently and permanently crosslinked networks. In semidilute solutions and transiently crosslinked networks of hyaluronan, the tracer particles exhibited simple diffusion characterized by a single exponential decay of the intermediate scattering function measured with DDM and by Gaussian statistics for the individual particle displacements. By contrast, in permanently crosslinked networks, the particle dynamics was strongly dependent on the particle size relative to the network pore size, with large particles being immobilized and small particles experiencing free diffusion. This size exclusion effect is reminiscent of similar effects observed in other gels in which diffusion was shown to be dominated by physical obstruction [192, 193]. Particle motion in this case is strongly dominated by the ratio between the particle size and the characteristic pore size of the matrix. This finding is interesting when considering cases in which hyaluronan is cross-linked by binding proteins, as in the case of an anti-inflammatory response [194, 195]. The induced crosslinking could, by modulating the network pore size, restrict the access of pathogenic factors by size-exclusion. The concept of size-filtering from the extracellular matrix was previously reported to be one of the main mechanisms by which the ECM acts as a diffusion barrier [196]. We emphasize, however, that here we focused on the diffusion of uncharged, sterically stabilized particles that do not interact with the matrix. More complex additional hindrance effects can arise when considering the diffusion of charged particles that interact with the extracellular matrix through electrostatic attraction or repulsion [197–199].

After exploring how hyaluronan behaved as a single-component system, we proceeded to analyze the diffusive behavior emerging from the interaction of hyaluronan with collagen fibrils, the main component of the extracellular matrix in cartilage and many other connective tissues. Previous studies suggested that collagen pose a major hindrance with respect to diffusion [200, 201], although these studies were executed with nanosized tracer particles, much smaller than the ones we investigated. Here, we discovered a non-trivial interplay between the two extracellular matrix components. While particles in both of the one-component networks exhibited simple diffusive dynamics, where the intermediate scattering function measured with DDM relaxed as a single exponential, they exhibited caged dynamics in the composite networks, as evidenced by a plateau in the ISF and by subdiffusive exponents lower than 1. While the overall structure of the collagen matrix was not visibly affected by

the presence of hyaluronan, we cannot exclude that electrostatic interactions might induce spatial heterogeneities in hyaluronan[197, 202] which are too small to be detected by light microscopy. We notice that we do see subdiffusive behavior when we increase the collagen concentration from 1 to 2 mg/mL. At this higher collagen concentration, the ISF does not fully relax and the decay of $\tau(q)$ deviates from purely diffusive behavior. At high collagen concentration, the large rigidity of the collagen fibers likely contributes a caging effect, consistent with a previous study on composite networks of semiflexible actin and rigid microtubules[174]. In the composite network, the confining agent (hyaluronan) is much softer than collagen, but the mesh size is much smaller. Interestingly, we do not observe subdiffusive motion in a pure hyaluronan system at 4 mg/mL, suggesting the need of an elastically active element to induce subdiffusion. A further possible reason for the emergence of caged dynamics in the composite system is an effective interaction between the components, possibly related to the high negative charge of the hyaluronan and positive charges on collagen[203], which can induce spatial heterogeneities in the hyaluronan network.

4.5 Conclusion

We have shown that, depending on the degree of crosslinking and on the interaction with other components of the extracellular matrix, the diffusion of tracer particles in hyaluronan networks can change drastically. This is interesting when considering physiological situations where physical[204] or chemical[195] crosslinking occurs, as crosslinking is likely to influence the diffusion of nutrients, growth factors and other signaling macromolecules through tissues. While semidilute solutions and transiently crosslinked networks of hyaluronan hinder particle transport through enhanced viscous drag, permanently crosslinked networks mainly exert a size exclusion effect whereby particle mobility is dependent on its size. We furthermore revealed that composite networks of hyaluronan and collagen more strongly restrict particle mobility than expected from the sum of the two parts. This effect is likely related to the large rigidity of collagen fibers, since measurements on collagen-only networks of enhanced density also show caged dynamics. These observations echo recent findings in composite networks of semiflexible actin filaments and more rigid microtubules, where subdiffusion was also observed in response to the presence of rigid filaments[174]. Our results are interesting for understanding how diffusion is affected in the extracellular matrix of tissues, with potential implications in targeting the tumor microenvironment[205] and in the design of hyaluronan-based gels for drug delivery[206] and tissue regeneration[207, 208].

Acknowledgments

This work was performed in collaboration with T. Sentjabrskaja (AMOLF) and G. Pletikapic (AMOLF), who performed part of the DDM experiments and J. van Beugen (AMOLF), who performed viscosity measurements and initial DDM experiments. We thank T. Sentjabrskaja for providing the DDM analysis script. We thank B. Mulder (AMOLF) for a critical reading of the manuscript, L. van Buren (AMOLF/TU Delft) for help with the microscopy setup, B.C. Ilochonwu and T. Vermonde (Utrecht University) for advise on chemically crosslinking hyaluronan. The work of F.B., G.P. and G.H.K. was part of the Industrial Partnership Programme Hybrid Soft Materials that is carried out under an agreement between Unilever Research and Development B.V. and the Netherlands Organisation for Scientific Research (NWO). T.S. was supported by a postdoctoral Research Fellowship of the Deutsche Forschungsgemeinschaft (DFG).

4.6 Supplementary Figures

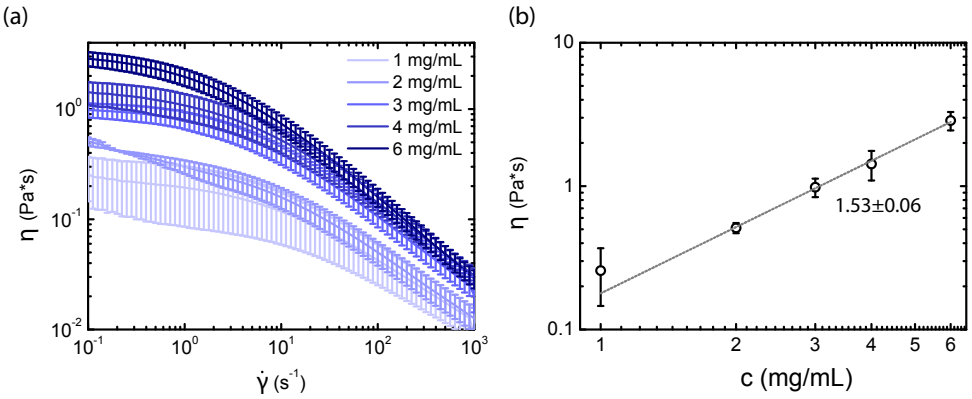

Supplementary Figure 1: Concentration dependence of the shear viscosity of semidilute hyaluronan solutions. (a) Shear viscosity as a function of shear rate for semidilute hyaluronan solutions with concentrations from 1 mg/mL to 6 mg/mL (see legend) determined with shear rheometry. (b) The low-shear viscosity (reported for $\dot{\gamma}$ =0.1 s^{-1}) scales with concentration c with a power law relationship $\eta = ac^b$, where b is 1.53±0.06. This exponent is roughly consistent with the expected b~1.3 scaling of semidilute polymer solutions. The data represents an average over three independent measurements and the error reported is the standard error of the mean.

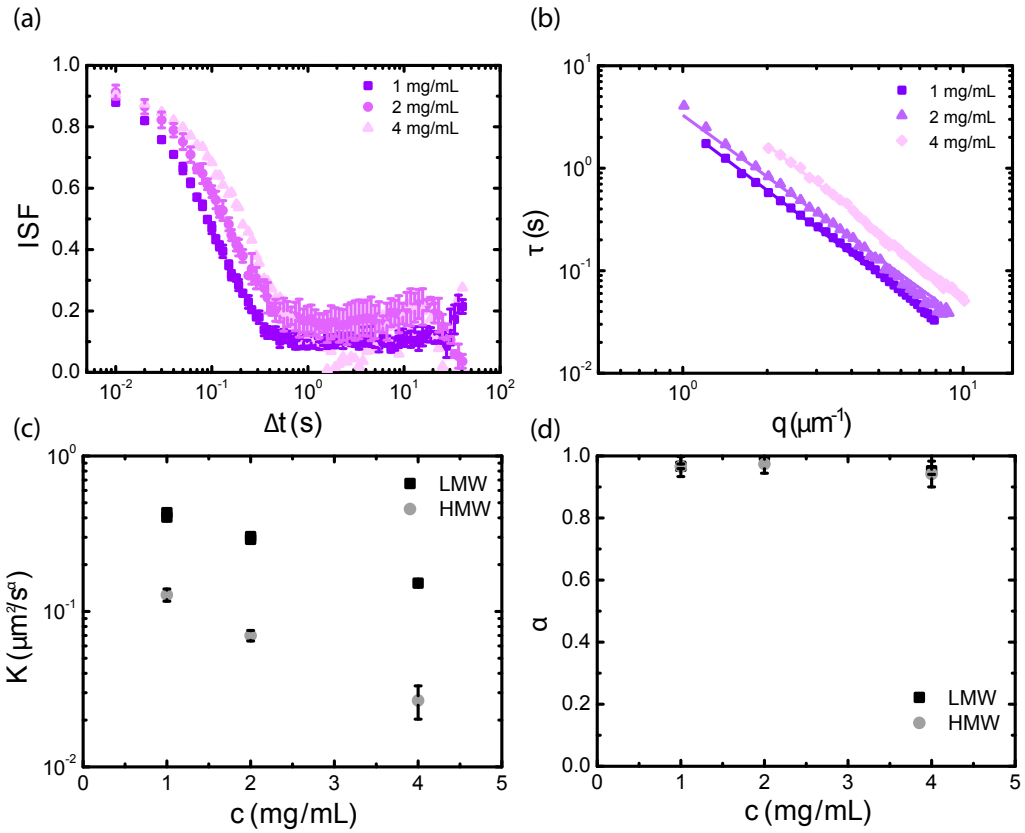

Supplementary Figure 2: DDM measurements of semidilute hyaluronan solutions, comparing high (240 kDa) and low (1.5 MDa) molecular weight samples for 0.6 μm particles. (a) ISF for hyaluronan of low molecular weight (240 kDa) at different concentrations, without chemical crosslinking. (b) τ(q) for the same samples. (c) Comparison of transport coefficient K and (d) subdiffusive exponent α for high molecular weight (HMW) and low molecular weight (LMW) samples.

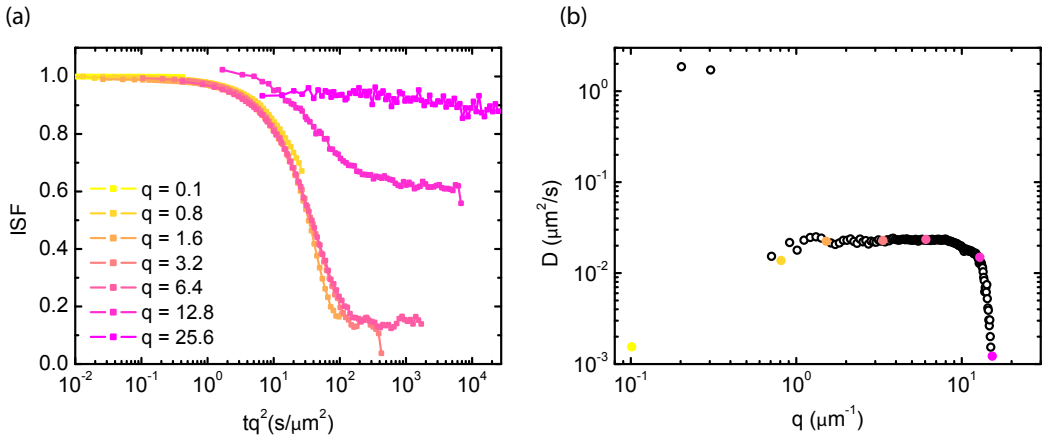

Supplementary Figure 3: Wavevector dependence of the intermediate scattering function (ISF). (a) ISF for 0.6 μm tracer particles embedded in 4 mg/mL (semidilute) hyaluronan solutions. Different colours indicate different q-values (expressed in the legend in units of μm^{-1}). For low q-values (0.1 μm^{-1}), the ISF does not fully decorrelate, because the measurement spans the whole field of view. At high q-values (>12.8 μm^{-1}), the measurement is dominated by noise because of the drifting of particles outside the field of view. (b) Apparent diffusion coefficient obtained from stretched exponential fits of the ISFs as a function of q, with colored symbols corresponding to the corresponding curves in panel a.

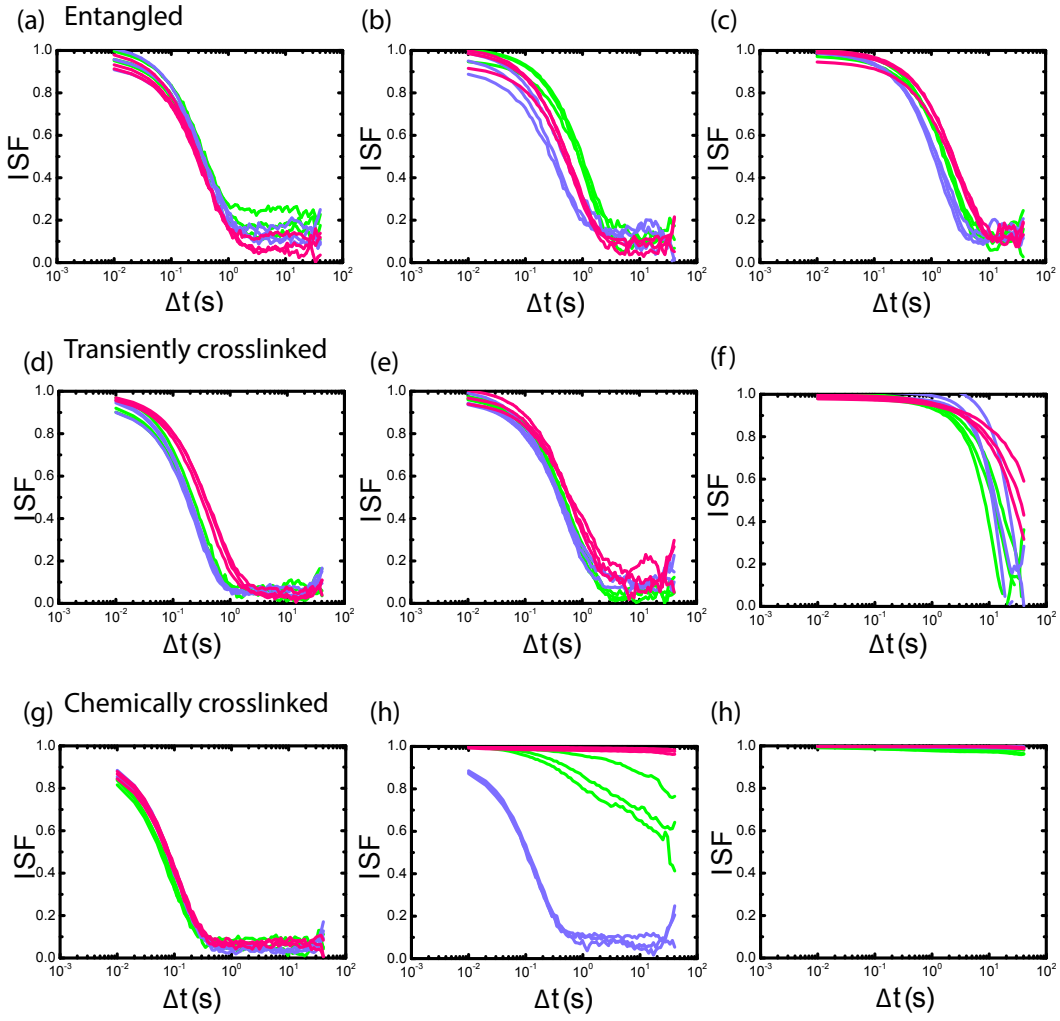

Supplementary Figure 4: Degree of heterogeneity in particle dynamics among ROIs for hyaluronan-only samples for different hyaluronan concentrations and crosslinking states (with 0.6 μm tracer particles). (a-b-c) ISF at q=4.5 μm^{-1} for semidilute samples, transiently crosslinked samples (d-e-f) and chemically crosslinked samples (g-h-i) at hyaluronan concentrations of 1 mg/mL (left column), 2 mg/mL (central column) and 4 mg/mL (right column). Each color represents an independently prepared sample, and each line represents data from one region of interest.

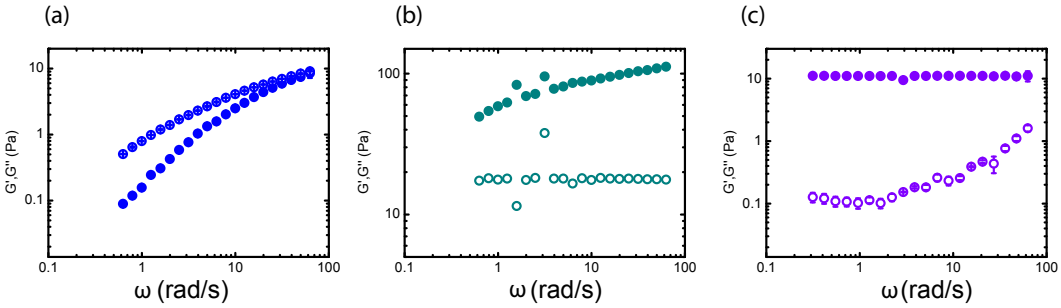

Supplementary Figure 5: Bulk rheology of the hyaluronan solutions and gels in the linear viscoelastic regime. (a) Frequency sweep of a semidilute hyaluronan solution at 4 mg/mL, which shows predominantly viscous behavior. (b) Frequency sweep of a transiently crosslinked hyaluronan gel (pH 2.5, putty state) at 4 mg/mL, which behaves as a transient gel. (c) Frequency sweep of a covalently crosslinked hyaluronan gel at 4 mg/mL, which behaves as a soft solid. The results are shown as an average of three repeats over independently prepared samples. The error bar represents the standard error of the mean. Full circles indicate elastic shear moduli G' and empty circles indicate viscous shear moduli G".

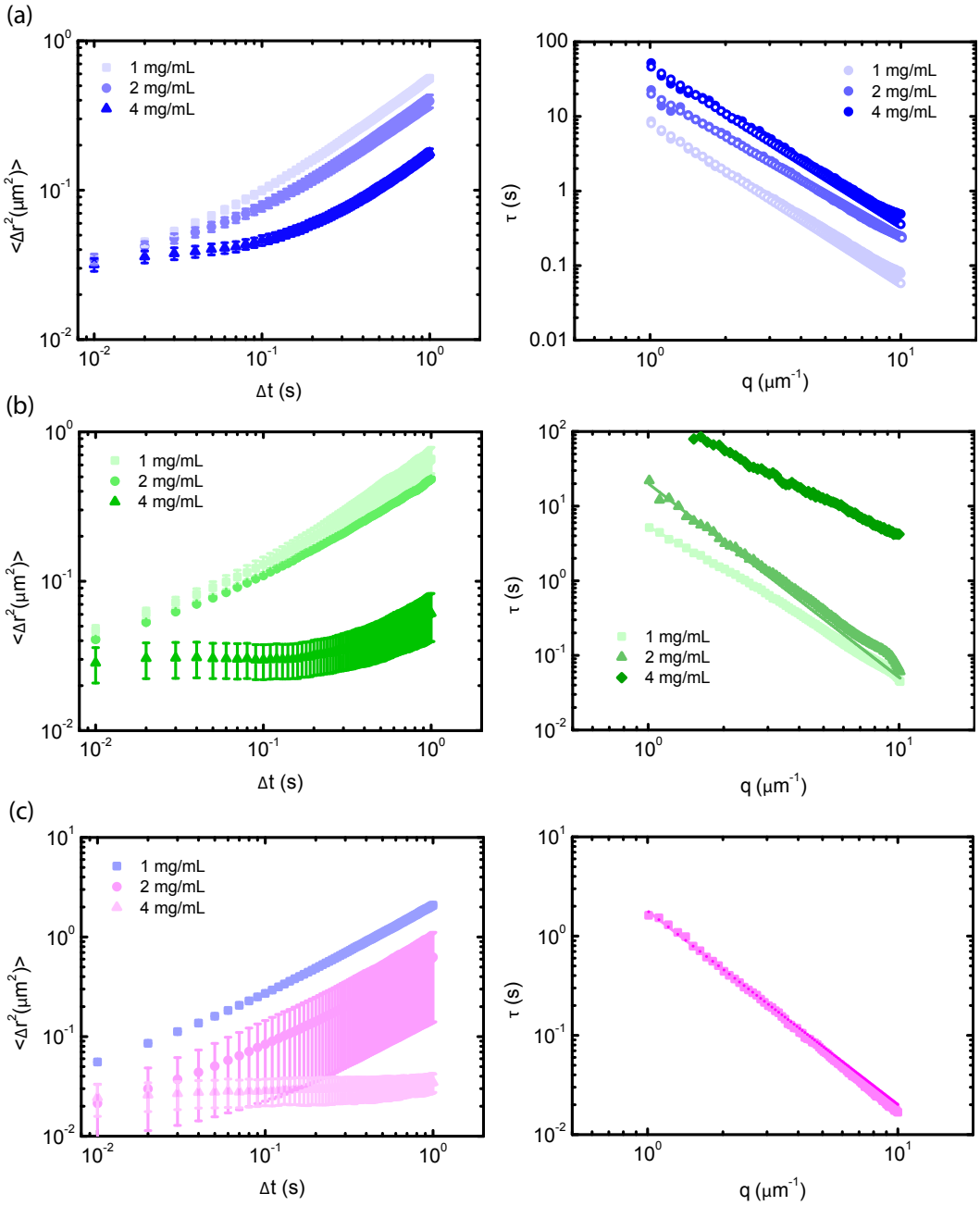

Supplementary Figure 6: MSD from single particle tracking and τ(q) from DDM for different hyaluronan concentrations and crosslinking states measured with 0.6 μm particles. Left panels: MSD determined from single-particle tracking for (a) entangled, (b) transiently crosslinked and (c) chemically crosslinked networks at concentrations between 1 and 4 mg/mL. Right panels: relaxation time τ obtained from fitting ISFs to a stretched exponential, for different values of q. In the crosslinked case, we show only the value of τ(q) at 1 mg/mL because the results at 2 mg/mL and 4 mg/mL do not show a full relaxation for the ISF.

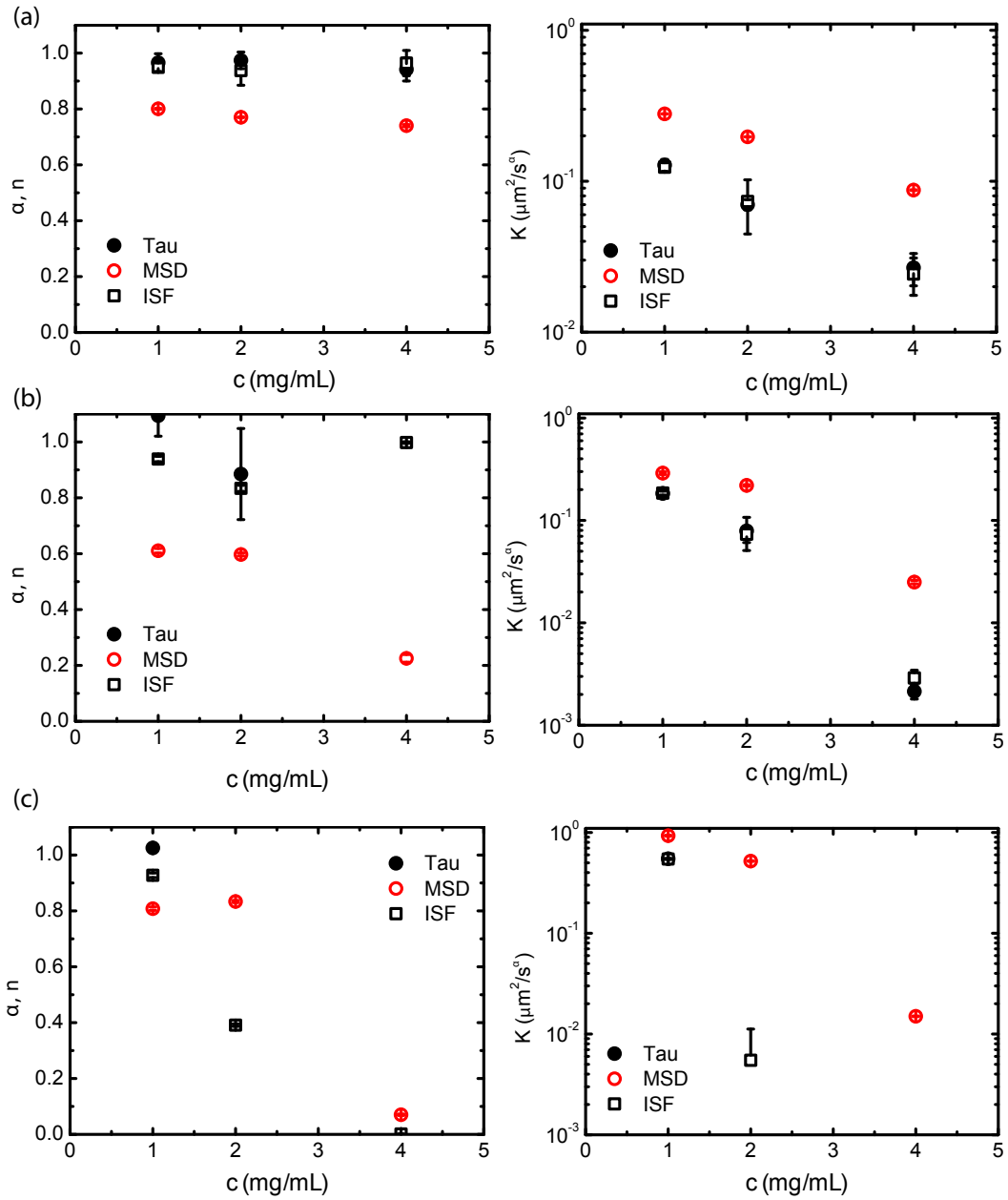

Supplementary Figure 7: Subdiffusive exponents α and transport coefficients K determined from fitting τ(q), the decay of the ISF, and the lag time dependence of the MSD from particle tracking, for different hyaluronan concentrations and crosslinking states and for 0.6 μm particles. Results show the subdiffusive exponent α or stretching exponent n (left panel) and transport coefficient K (right panel) for semidilute (a), transiently crosslinked (b) and chemically crosslinked (c) networks. In all cases, the subdiffusive exponents obtained from MSD are below the values obtained from DDM. This is likely related to the short time-interval over which the MSD traces could be obtained.

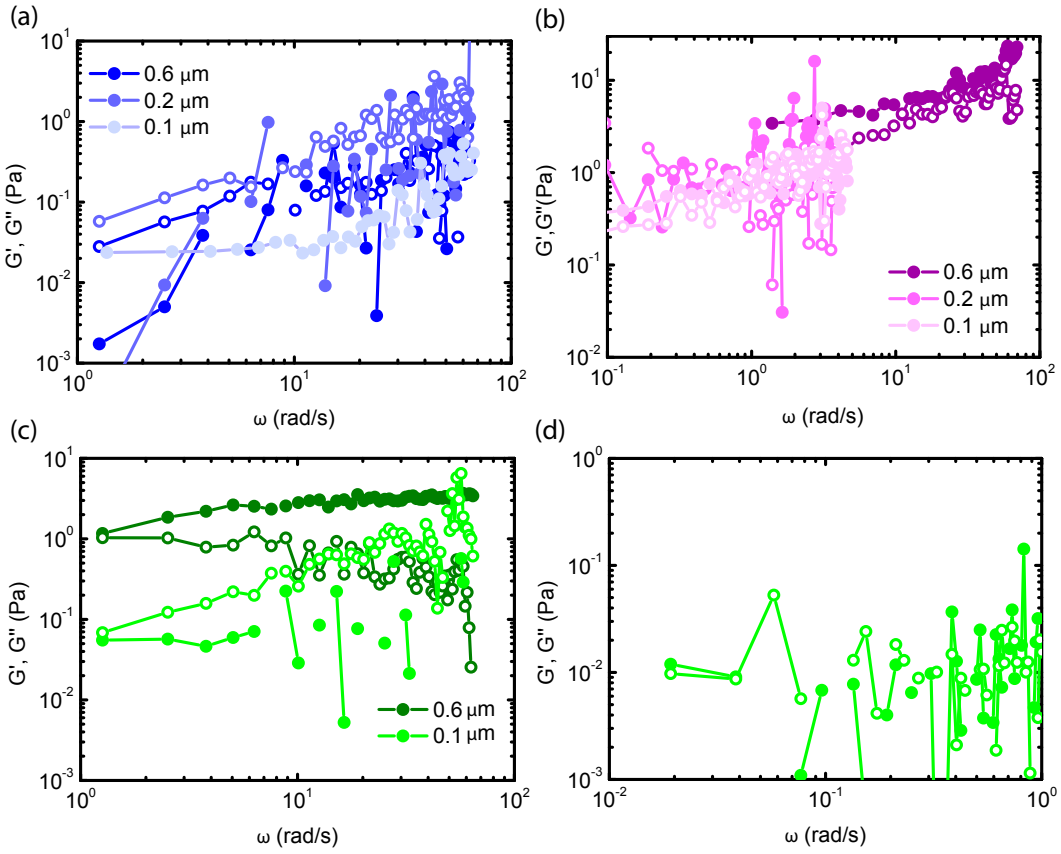

Supplementary Figure 8: Microrheology of hyaluronan gels at 4 mg/mL from DDM data probed with 0.1 μm, 0.2 μm and 0.6 μm particles. Microrheology storage and loss moduli for (a) semidilute, (b) permanently crosslinked and (c) transiently crosslinked hyaluronan networks obtained for different particle sizes, obtained from applying the Evans-Tassieri analysis method to the mean-squared-displacement obtained from DDM. Panel (d) represents microrheology of transiently crosslinked networks at a probe particle size of 0.2 μm. Solid circles represent the storage moduli G', and empty circles the loss moduli G".

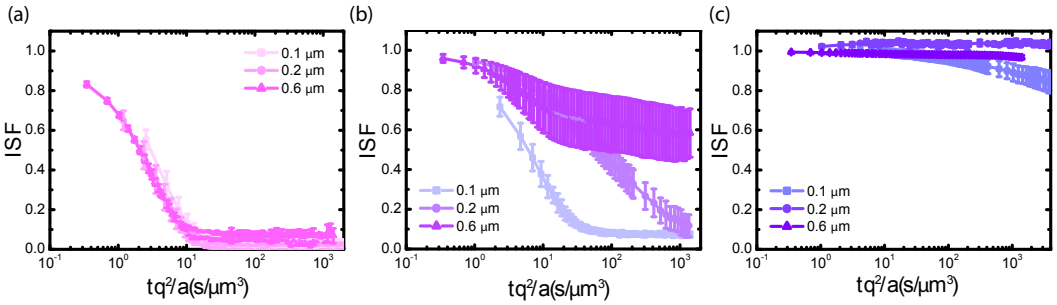

Supplementary Figure 9: Rescaling of the intermediate scattering function considering the particle size in crosslinked hyaluronan networks. (a) Collapse of the ISF of a 1 mg/mL crosslinked hyaluronan network for different particle sizes (see legend), obtained by dividing the x-axes for the particle diameter a. (b) Same rescaling for a 2 mg/mL and (c) a 4 mg/mL crosslinked hyaluronan network. Here, the size dependence of the diffusivity deviates from Stokes-Einstein behavior, consistent with diffusion being governed by size exclusion instead of an effective viscosity.

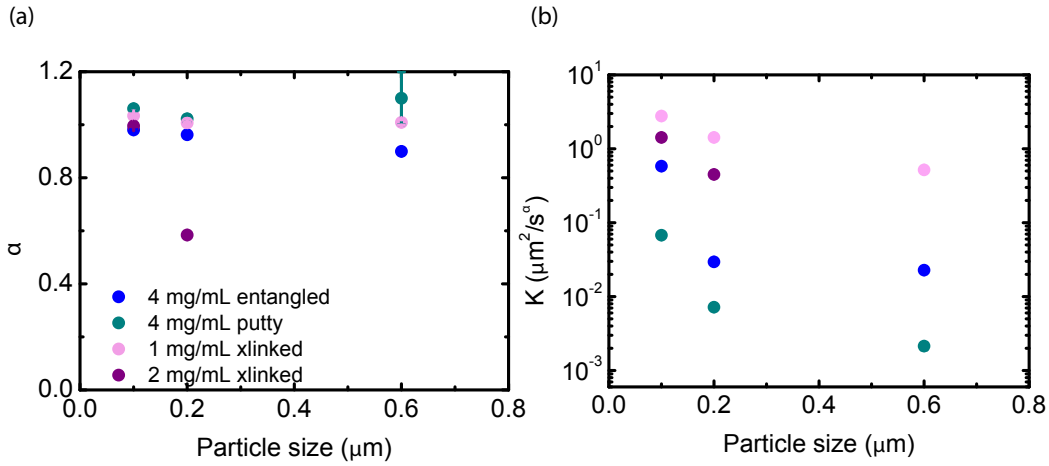

Supplementary Figure 10: Subdiffusive exponents α and transport coefficients K determined from DDM intermediate scattering functions for tracer particles of different sizes in variously crosslinked hyaluronan networks. (a) Subdiffusive exponent for different hyaluronan gels (see Legend) as a function of tracer particle diameter, obtained from fitting the decay of τ(q). (b) Transport coefficient for different hyaluronan gels as a function of tracer particle diameter. Values represent averages over at least 9 measurements obtained over three independently prepared samples, and the error shown is the standard error of the mean. For the crosslinked networks, we could not analyze data obtained at 4 mg/mL hyaluronan because of the incomplete decay of the ISF.

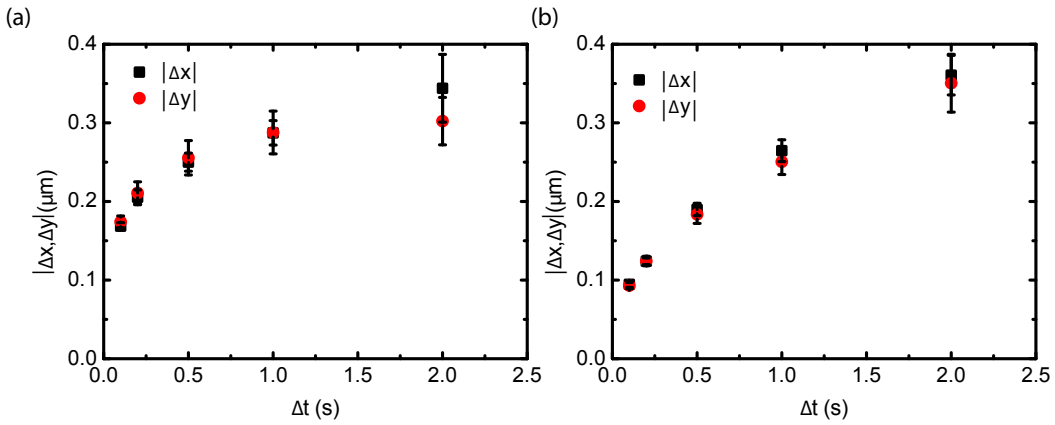

Supplementary Figure 11: Isotropy in x-y displacements for two representative examples of 4 mg/mL semidilute hyaluronan and 2 mg/mL collagen for 0.6 μm particles. . Representative examples are shown for a (a) collagen-only network at 2 mg/mL and (b) an entangled hyaluronan network at 4 mg/mL for different lag times.

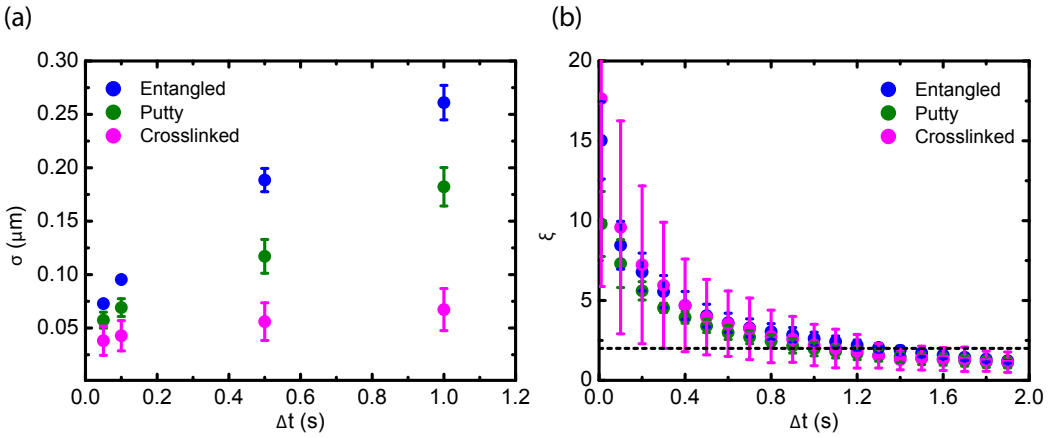

Supplementary Figure 12: Evolution of the width and the non-Gaussian parameter ξ of the van Hove distribution functions with lag time, measured for tracer particles (0.6 μm) in hyaluronan networks with varied crosslinking conditions. (a) The width was obtained from fitting the van Hove distributions to a Gaussian function for semidilute solutions (blue), putty gels (green), and crosslinked gels (purple) of hyaluronan gels (all at 4 mg/ml). Data represents an average over three independent measurements and the errors shown represent the standard error of the mean (b) Non-gaussian parameter calculated as a function of time for entangled (blue), putty (green) and crosslinked (pink) samples. The dotted line represents the expected value for an exponential distribution (ξ =2). The monotonic decrease of ξ with lag time reflects the fact that the displacement are initially smaller than the tracking accuracy [209, 210].

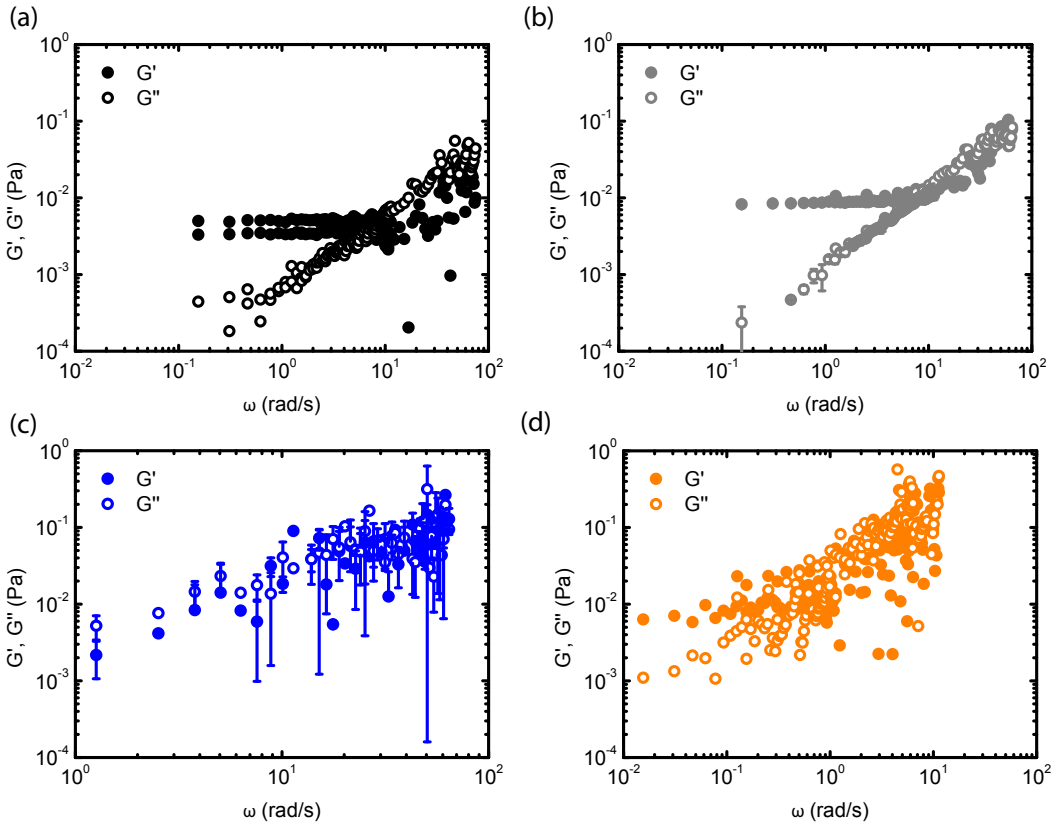

Supplementary Figure 13: Microrheology analysis of DDM data for collagen-only network at 1 and 2 mg/mL, semidilute hyaluronan at 2 mg/mL, and collagen (1 mg/mL)/hyaluronan (2 mg/mL) composite networks with 0.6 μm particles. (a) Microrheology for 1 mg/mL collagen, (b) 2 mg/mL collagen, (c) 2 mg/mL pure hyaluronan and (d) composite composed of 2 mg/mL hyaluronan and 1 mg/mL collagen.

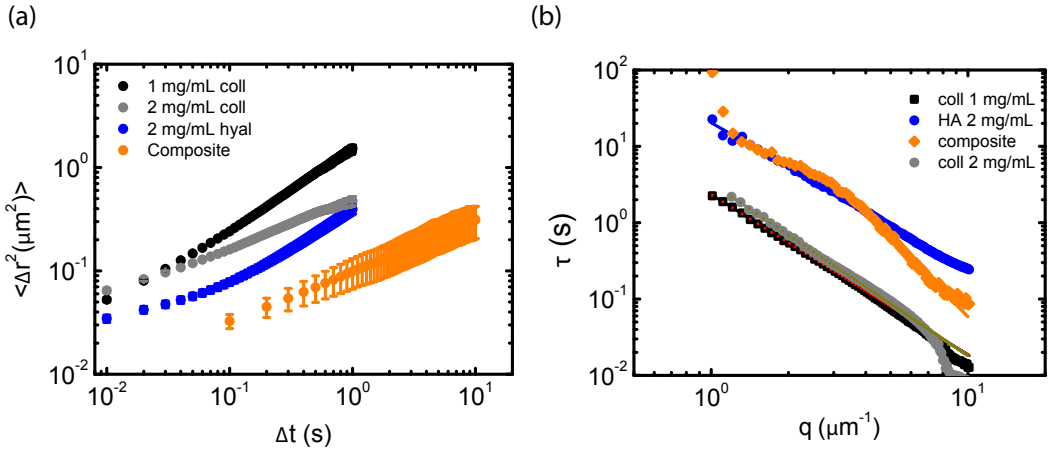

Supplementary Figure 14: Transport coefficients K and subdiffusion exponents α from DDM and from particle tracking for tracer particles (0.6 μm) in 1 mg/mL and 2 mg/mL collagen, 2 mg/mL semidiluted hyaluronan, and composite 1 mg/mL collagen-2 mg/mL hyaluronan networks. (a) MSD from particle tracking, (b) τ(q) from DDM for composite networks of 1 mg/mL collagen and 2 mg/mL hyaluronan, for collagen-only networks (either 1 or 2 mg/ml), and for 2 mg/mL hyaluronan networks,

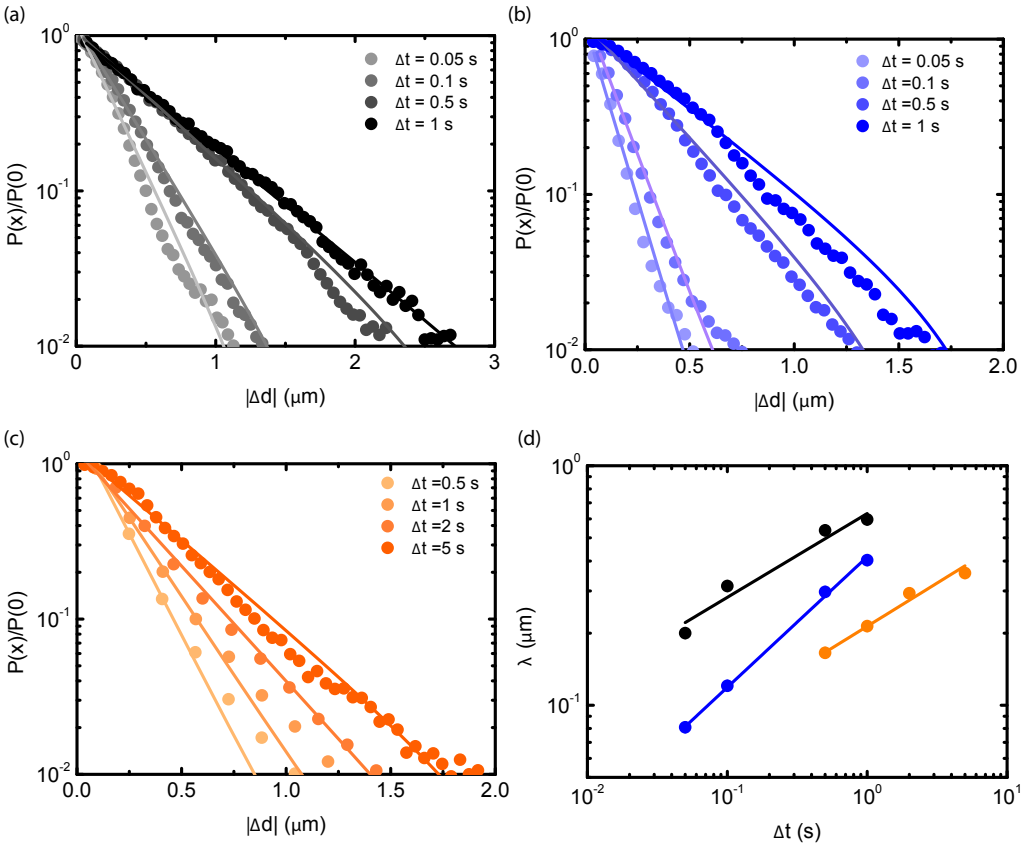

Supplementary Figure 15: Evolution of exponential tails of the van Hove distributions of collagen-only network at 1 mg/mL, semidiluted hyaluronan at 2 mg/mL and collagen-hyaluronan composite at 1 mg/mL collagen- 2 mg/mL hyaluronan with 0.6 μm particles probe size. Exponential decay for the van Hove distribution of (a) 1 mg/mL collagen networks, (b) 2 mg/mL hyaluronan solution and (c) 1 mg/mL collagen-2 mg/mL hyaluronan network. (d) Evolution of the decay exponent λ a as a function of lag time. Lines represent fits with power law slopes of: 0.35±0.05 (collagen, black), 0.54±0.01 (hyaluronan, blue), 0.36±0.03 (composite, orange). The error represents the error from the fit and the data points are obtained by pooling together all of the distributions of the data points for at least three different samples and over at least three different ROIs.

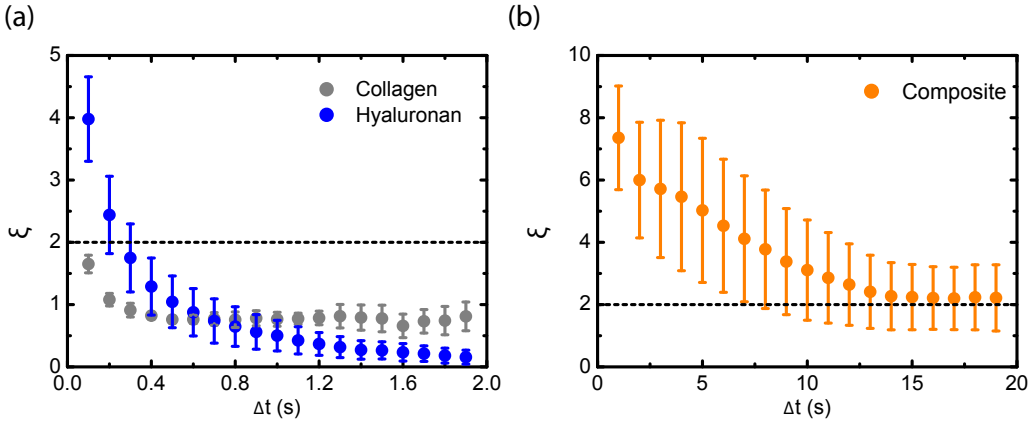

Supplementary Figure 16: Non-gaussian parameter ξ for pure collagen, pure hyaluronan and composite networks. Non-gaussian parameter calculated as a function of time for collagen (gray), hyaluronan (blue) and crosslinked (orange) samples. The dashed lines indicate the calculated value of ξ for an exponential distribution. The different timescales are related to the different acquisition times used for the samples.

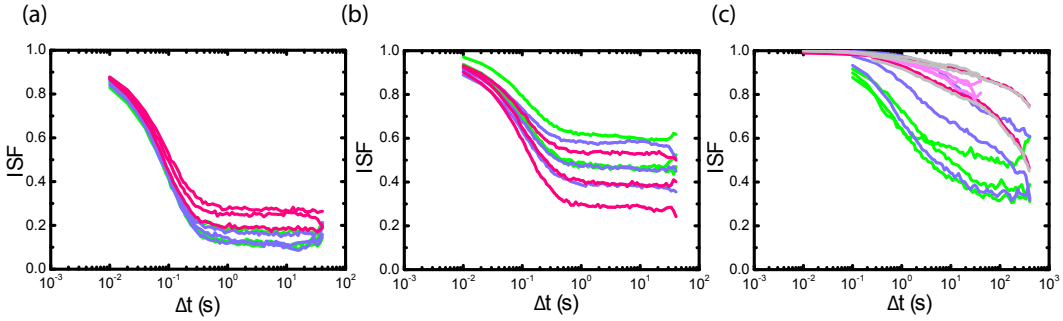

Supplementary Figure 17: Degree of heterogeneity in particle dynamics across ROIs for collagen-only networks and for collagen-hyaluronan composites. (a) ISF obtained for q = 4.5 μm^{-1} for (a) 1 mg/mL pure collagen network, (b) 2 mg/mL collagen-only network, and (c) a composite of 1 mg/mL collagen and 2 mg/mL hyaluronan. Each color represents an independently prepared sample, and each line represents one ROI.

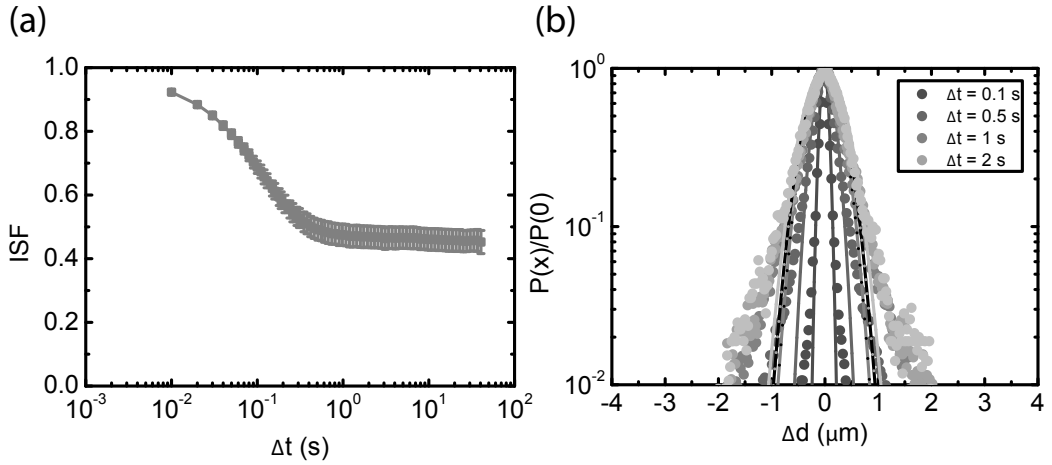

Supplementary Figure 18: ISF from DDM and van Hove distribution from particle tracking for a collagen-only network at a concentration of 2 mg/mL. (a) ISF at q= 4.5 μm^{-1} and (b) van Hove distribution at different lag times.

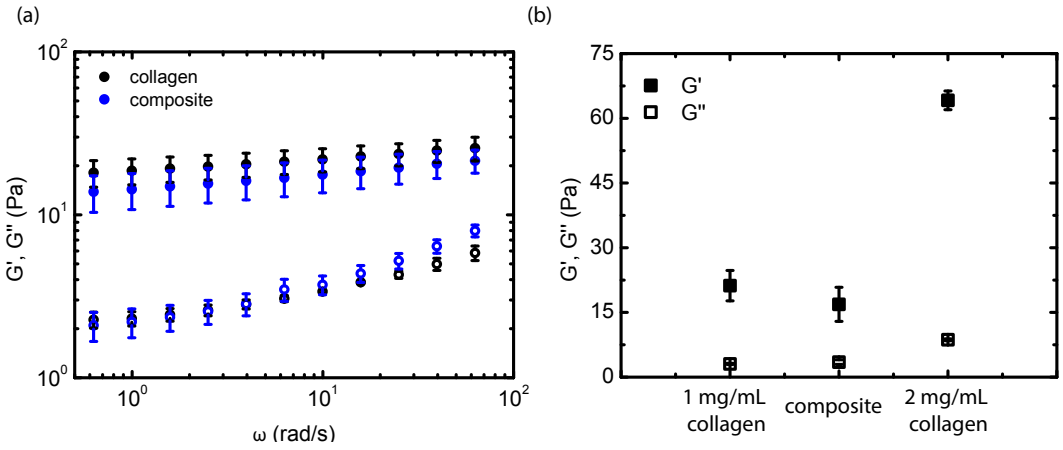

Supplementary Figure 19: Linear rheology of 1 and 2 mg/mL collagen-only and composite 1 mg/mL collagen-2 mg/mL hyaluronan networks. (a) Frequency sweep for a collagen network at 1 mg/mL (black symbols) and a composite collagen-hyaluronan network (1 and 2 mg/mL, respectively, blue symbols). The measurement represents an average over at least three different repeats, and the standard deviation represents the standard error of the mean. (b) Elastic (full symbols) and viscous (empty symbols) moduli for collagen networks at 1 and 2 mg/mL and composite networks with 1 mg/mL collagen and 2 mg/mL hyaluronan, measured at a frequency of 6.28 rad/s.

5

A nanoscale look at a biomimetic model of a healing tissue

When a blood vessel is injured, an enzymatic cascade triggers the rapid formation of a fibrin clot to stop the bleeding. During the subsequent wound healing process, this fibrin matrix is gradually replaced by a collagen matrix. Collagen and fibrin have remarkably different mechanical properties, dictated by their distinct structure and biological function. While fibrin is an elastomeric protein, optimized to withstand high shear deformations such as those exerted by blood flow, collagen is a rigid protein optimized to give strength to tissue but not extensibility. This raises the question how the mechanical properties of the two proteins combine in the evolving composite network during wound healing. Here, we compare and contrast the properties of reconstituted networks of collagen and fibrin by means of rheoSAXS, a technique that combines in situ small angle X-ray scattering (SAXS) with shear rheology. We first characterized the molecular packing structure of collagen and fibrin fibres and its development during polymerisation in the absence of shear. We then subjected the networks to shear deformation and found that both networks showed fibre alignment but neither network showed any measurable change in the axial packing periodicity of the fibres. However, the fibre packing density increased slightly for collagen while there was no significant change for fibrin. We furthermore show that in composite networks of collagen and fibrin, steric effects induce inhomogeneous polymerisation and bundling of the fibrin fibres, resulting in a lower elastic modulus and strength as compared to pure fibrin. Interestingly, we found that the mechanical response of the composite is dominated by collagen when it experiences shear for the first time, but is dominated by fibrin when the network is sheared a second time because the collagen ruptures while leaving the fibrin intact. Our results help in understanding the interplay of collagen and fibrin in a simplified, biomimetic model for wound-healing.

5.1 Introduction

Collagen is the most abundant protein in the extracellular matrix, where it forms a long-lived fibrous matrix optimized to provide tissues with a high resistance to shear and tensile stresses [23]. When tissues are injured, the wound is sealed by a temporary fibrous matrix that assembles from the plasma protein fibrinogen [211]. Fibrinogen forms fibrous networks that are optimized to withstand large shear and tensile strains such as those exerted by blood flow and contraction of platelets [103, 212]. Collagen and fibrinogen have remarkably different mechanical properties to satisfy these diverging physiological requirements. While collagen forms athermal fibrillar networks that strain-stiffen due to fibre alignment and that rupture at large stress but low (~40-80%) shear strain [41, 60] (see also Chapter 2 of this thesis), fibrin forms semiflexible polymer networks that can withstand large tensile strains of up to 300% due to their hierarchical structure [213, 214].

In many physiological situations, collagen and fibrin occur together in tissues. The paradigmatic example is wound healing, where a provisional fibrin matrix is progressively replaced by collagen fibres until the tissue is full restored [215]. The synergy between collagen and fibrin also plays a role in angiogenesis [216, 217], the process in which new blood vessels form from existing ones. This is also a key process in cancer regulation, because these new vessels are crucial to feed tumour cells [218].

Although the coexistence of fibrin and collagen is ubiquitous in the human body, little is known of the mechanical characteristics that emerge from combining rigid collagen fibres with elastomeric fibrin networks. While individual mechanical properties of fibrin and collagen networks have been well investigated, how the two components affect each other when present in a composite system has been, so far, the object of only few studies [219–222]. It was found that the hybrid composition induces structural changes of the two components during copolymerisation [219]. Specifically, a decrease in mean fibre diameter was reported for the composite networks [220]. Furthermore, the elastic response to a compressive deformation was measured to be intermediate between those of collagen and fibrin [219], which was ascribed to steric hindrance from the most abundant component, that prevents full percolation of the other one [223].

In this chapter, our goal is to explore the mechanical response of fibrin-collagen composites to shear deformation, as this deformation mode is relevant during wound healing, for example during blood flow, or stretching of the wounded skin during movement. Moreover, shear has the practical advantage over tensile and compressive deformations that the sample volume is constant, facilitating a quantitative interpretation of the nonlinear response to large strains. To probe the molecular response of the networks under shear, we use small angle X-ray

scattering (SAXS) in combination with a shear rheometer. Since SAXS operates in Fourier space, it is suitable for probing the nanoscale structure of materials presenting a certain degree of periodicity [224]. Even though fibrin and collagen networks are themselves disordered, the constituent fibres possess a characteristic crystalline structure along their long axis that arises from the self-assembly process. This crystallinity gives rise to Bragg peaks in the SAXS scattering pattern that constitute a fingerprint of strain-induced changes in fibre length and packing order. We first focussed on the molecular fingerprints of collagen, asking how they differ for different collagen types (sources and extraction method), how they develop during polymerisation, and how they change under shear deformation. We then investigated the same questions for fibrin. Finally, we examined the rheoSAXS response of the composites, where we systematically varied the concentrations of collagen and fibrin in order to mimic the evolution in composition that takes place during wound healing.

5.1.1 Background on SAXS

The basic principle of SAXS is to illuminate the sample of interest with an x-ray beam, which interacts with the structure of the sample and is scattered at various angles. If the sample shows a regular periodic structure, the scattering pattern will show well-defined Bragg peaks at a characteristic distance from the centre. This distance q, referred to as the wavevector, corresponds to the inverse of the diffraction length l:

$$q = \frac{2\pi}{l} \tag{5.1}$$

Thus, the closer the spacing of the grating (in our case, the smaller the axial packing periodicity of the fibres), the more distant will be the Bragg peak produced. The accessible wavevector range depends on the distance of the specimen to the detector d and on the angle with respect to the centre of the detector θ, through the relationship:

$$q = \frac{4\pi sin\theta}{d} \tag{5.2}$$

Fibrin and collagen fibres both possess a long-ranged periodic packing structure along their long axis with a periodicity that falls within the q-range accessible with SAXS [225–227]. Depending on the degree of crystalline order, multiple peaks corresponding to higher order reflections may occur, at distances nq, where n is an integer number.

Fibrin forms from fibrinogen precursor molecules (Figure 1a) that are converted into activated fibrin monomers by enzymatic cleavage of small peptides off the central region by thrombin. Fibrinopeptide cleavage triggers half-staggered self-assembly of the fibrin monomers into double-stranded protofibrils, which

subsequently bundle in-register with a 22.5 nm stagger [15]. Bundling is aided by the presence of long linker regions (known as αC-regions) that are flexible because they are unstructured along most of their length. We recently showed that shear deformations cause changes in the periodicity and crystalline order of the molecular packing structure of the fibres along the fibre axis, revealing changes in conformation of both the αC-regions and the folded core of the constituent molecules [214]. Collagen molecules are triple helical rods with short non-helical telopeptides on both ends (Figure 1b). Periodical distributions of alternating positive and negative electrostatic charges on the triple helical region together with specific telopeptide-helix interactions encode quarter-staggered self-assembly into fibrils with a packing periodicity of 67 nm [7, 228]. Previous SAXS measurements on collagenous tissues subject to tensile loading showed that their deformation is mediated by elongation of the molecules as well as intermonomer sliding [92, 229].

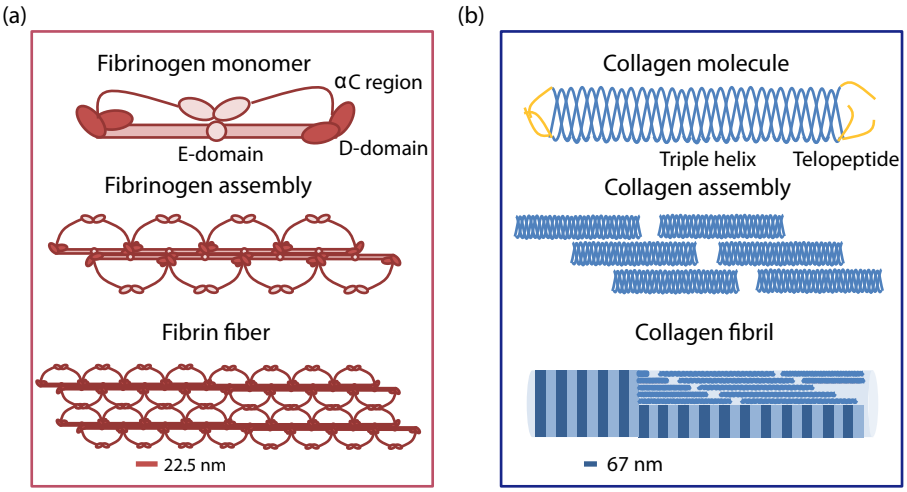

Figure 1: Ordered molecular packing structure of collagen and fibrin fibrils arising from hierarchical self-assembly.(a) Schematic showing the self-assembly of fibrinogen monomers (top) into double-stranded protofibrils (middle) and finally fibres (bottom). The half-staggered arrangement of the monomers gives rise to an axial periodicity of 22.5 nm. Note that the monomers are symmetric trinodular structures, where the central nodule (E-domain) is connected to the two terminal domains (D-domains) by alpha-helical coiled coils. From each D-domain, a long, largely unstructured peptide region emanates that is known as the αC-region. Thrombin-mediated conversion of fibrinogen to fibrin releases the αC-regions so they become available for lateral bonding of protofibrils [230]. (b) Triple-helical collagen molecules (top) assemble in a quarter-staggered manner (middle) into a fibril (bottom) with an axial periodicity of 67 nm referred to as the D-period. The fibrils are stabilized by helix-helix interactions and crosslinking of the non-helical short telopeptides (yellow disordered domains) with neighbouring helices.

In the absence of an applied shear, the fibrin and collagen networks studied in this chapter are isotropic. In this case, a convenient way of analysing the scattering

pattern is by radially integrating the intensity and plotting it as a function of q. In the presence of an applied shear, the fibres will align along the principal strain direction, which will show up in the form of an asymmetry between scattering in the vertical and horizontal quadrants [231]. A straightforward way to quantify the degree of alignment is by the following asymmetry parameter, defined as the normalized ratio in the intensity I_1 of a horizontal quadrant and the intensity I_2 of a vertical quadrant:

$$A_{asym} = \frac{|I_1 - I_2|}{I_1 + I_2} \tag{5.3}$$

In case of anisotropic samples, scattering profiles I(q) should be evaluated separately for the quadrants parallel and perpendicular to the orientation axis, as they provide different information. While the meridional scattering (with angle parallel to the strain direction) is sensitive to the staggered molecular packing along the axis, the equatorial scattering (with angles perpendicular to the strain direction) is sensitive to the packing structure of the fibrils transversely to the long axis(see Supplementary Figure S1).

The overall shape of I(q) scattering curves is determined by a superposition of the Bragg peaks characterizing the axial packing order on other scattering contributions originating from structures at different scales [232]. At low-q, the scattering is dominated by Porod scattering from the interface between fibrils and the solvent. Here, we expect a power-law decrease of the intensity I(q) with q with an exponent equal to minus the surface fractal dimension of the fibre, which ranges between 2 for sharp interfaces to 3 for a rough one. The lower limit q1 of the Porod regime is set by the inverse of the network mesh size while the upper limit q_2 is set by the inverse of the average fibre diameter d through the relationship: $q_2 = 2.2/d$ [225]. For $q > q_2$ (corresponding to smaller length scales), the q-dependence of the intensity is affected by the molecular packing structure of the fibres transverse to the fibre axis. Both collagen and fibrin fibres are bundles of rod-like monomers measuring at least ~100 monomers in cross-section, and are much less well-ordered along the transverse direction than along the long axis, although the exact manner and degree of order remains unclear. In case of collagen fibres, SAXS measurements on tendon tissue (which is comprised of unidirectionally aligned fibres) have revealed broad Bragg peaks whose position reflects the average spacing among molecules in a liquid-like arrangement [233]. Reconstituted collagen fibres formed by self-assembly may potentially be even less well-ordered than native fibres since they form in the absence of cells and auxiliary molecules. In case of fibrin fibres, some studies claimed that the lateral packing structure is fractal-like [234], while others found evidence of considerable crystalline order [226, 235]. To reconcile these conflicting findings, it has been proposed that fibrin fibres might be partially crystalline as a consequence of defects in the radial packing [225].

Since we were unable to observe distinct Bragg peaks that could be assigned to

radial crystallinity of the collagen and fibrin fibres in this study, we chose to quantify the radial packing structure of both fibre types in an effective manner by assuming a disordered arrangement characterized by a fractal dimension that is a proxy for the packing density. Specifically, we fitted the scattering curves for $q > q_2$ to the following relation:

$$I \sim q^{-D_f} \tag{5.4}$$

where D_f is the fractal dimension38. When D_f is low, it means that the fibres are loosely packed, while a higher D_f signifies a more efficient packing structure. The maximum fractal dimension in a 3D-system is 3 [236]. Although this description is simplified, the fractal dimension can serve as an effective parameter quantifying changes in packing density of the fibres during polymerisation and in response to an applied shear.

5.2 Materials and methods

5.2.1 Sample preparation

The samples were investigated at a protein concentration between 2-8 mg/mL. All of the collagen samples were mixed on ice and the preparation time was kept as short as possible in order to prevent premature collagen polymerisation. We tested three different sources of fibril-forming collagens. Type I collagen from rat tail (Corning) was purchased as an 8.34 mg/mL solution in acetic acid. This collagen species has intact telopeptides, which catalyse fibril assembly and mediate intrafibrillar crosslinking. Type II collagen (Sigma Aldrich) was purchased in a lyophilised form and dissolved in 0.01 M acetic acid. This collagen is extracted from chicken sternal cartilage and lacks the telopeptide ends. We reconstituted these two collagens in phosphate buffered saline (PBS) solution, by adding PBS 10x (Sigma Aldrich, tablet form: 0.01 M phosphate buffer, 0.0027 M potassium chloride and 0.137 M sodium chloride, pH 7.4), bringing the pH to a value of 7.4 through addition of NaOH (Sigma Aldrich), and then topping up to the final volume with MilliQ water. Finally, we employed also bovine dermal collagen type I (FibriCol from CellSystems), bought as a 10 mg/mL solution dissolved in 0.01 M HCl. This collagen lacks the telopeptides because it is purified by pepsin digestion. Since we used the bovine dermal collagen also in composite networks with fibrin, we changed the polymerisation buffer to 10x concentrated DMEM (Dulbecco's modified eagle medium) (Sigma Aldrich, with final salt concentrations of $CaCl_2$ 1.8 mM, KCl 5.36 mM, NaCl 109 mM) of pH 7.4 containing an additional 20 mM of HEPES.

Fibrin samples were prepared from human plasma fibrinogen (Plasminogen). We first dissolved the powder in milliQ water and then dialyzed to M-buffer (20 mM HEPES, 5.36 mM KCl, 109 mM NaCl, Sigma Aldrich) with three dialysis steps (10 kDa MWCO slide-A-lyzer cassette, ThermoScientific). The dialyzed

fibrinogen was brought to the desired concentration in a DMEM/20 mM HEPES buffer and polymerisation was triggered by adding human thrombin (Enzyme Research Laboratory) to a final concentration of 0.5 U/mL. For confocal imaging of fibrin and composite fibrin/collagen networks, fibrin was fluorescently labelled by including 10 mole % Alexa-488-labelled fibrinogen during polymerisation.

Collagen/fibrin composites were reconstituted by first preparing the collagen mix on ice, then rapidly adding fibrin at room temperature and adding thrombin right before polymerisation. We note that with our preparation, we have a lower concentration of $CaCl_2$ compared to what we have previously used [214] (1.8 mM instead of 5 mM). This could reduce the effectiveness of fibrin crosslinking by Factor XIII, which is co-purified with fibrinogen [237].

After mixing, the samples were rapidly inserted in borosilicate glass capillaries (10 μm wall thickness, Hilgenberg) and sealed with vaseline to prevent solvent evaporation, before being placed in an oven at 37°C for three hours to allow polymerisation. For rheology experiments, we pipetted the samples before polymerisation into the polycarbonate Couette cell of the rheometer, which was temperature-controlled with a rheometer Peltier temperature control. We allowed these samples to polymerise for two hours at 37°C before starting experiments. For confocal microscopy experiments, the samples were polymerised in a silicon chamber (Sigma Aldrich) sandwiched between two coverslips (MenzelGlaser). The samples for Scanning Transmission Electron Microscopy (STEM) were prepared by pipetting the samples in the cap of an Eppendorf tube that was subsequently closed and incubated for at least 2 hours at 37°C to allow for polymerisation. The gel surface was then peeled off with a carbon coated electron microscopy copper grid (Ted Pella, Redding, CA, USA). The grid was rinsed 5 times with milliQ water and blotted dry with the tip of a paper tissue.

5.2.2 SAXS experiments

We performed Small Angle X-ray Scattering experiments at the European Synchrotron Radiation Facility (ESRF) in Grenoble, France, on the DUBBLE BM26 beamline. The measurements were performed over four different beam time sessions, taking care to keep the experimental geometry fixed. The x-ray beam energy was 12 keV (10^{-10} m wavelength) and the beam dimensions were 300 x 300 μm. We employed a sample-to-detector distance of 3 m, which allows to access a q-range of 0.03 to 3 nm^{-1} matched to the relevant length scales in our measurements (ranging from 2 to 200 nm). SAXS scattering patterns were recorded with a Pilatus 1M detector [238]. The centre of the detector was protected by a beamstop, to prevent damage due to unscattered rays. To determine the centre of the scattering image used for radial integration and to calibrate the q-range, we referred to a calibration sample of silvere behenate (AgBe) powder, whose scattering peaks are sharp and well-defined (see Figure 2).

We determined the structural properties of the networks at rest by measuring networks polymerised inside glass capillaries. We performed rheoSAXS measurements on an MCR501 Anton Paar rheometer, with a custom-built polycarbonate Couette cell and a custom-built polycarbonate spindle attached to the motor via a custom shaft (D-CP/PP from Anton Paar). To assess changes in the network and fibre structure during shear, we first applied a strain ramp where the strain increased stepwise from 1% to 70%, then a ramp where the strain was decreased stepwise back to 0%, and finally another stepwise strain ramp all the way up to 300% in order to probe the rupture point (see also Figure 6c). Each step was held for 45 s, and in the last 30 s a SAXS image was acquired. The corresponding differential shear elastic modulus K'(γ) was determined by performing a cubic spline derivative of the stress-strain $\sigma(\gamma)$ curve at the end of sample relaxation.

We note that prior studies of fibrous networks have employed different ways to assess the non-linear mechanical response of the network to strain [107]. The first option is a prestress protocol, which is ideal for system that exhibit creep, as it probes the instantaneous mechanical response. The second option is a continuous strain ramp, which will measure a combination of elastic response and creep. The third option, used here, is a stepwise increase in strain, which is accompanied by stress relaxation during every step. We choose this protocol, because it has advantages for our purposes: (i) unlike the prestress protocol, which requires the adjustment of the applied stress values to the initial stiffness of the sample, this protocol employs strain as the input parameter so adjustment is independent on initial sample stiffness and (ii) unlike a linear strain ramp where the strain is increased continuously, the stepwise protocol allows us to keep the sample in the same state of strain deformation for several seconds, and record a scattering pattern over a period of 30 s, an integration time necessary for obtaining a SAXS image with sufficiently high signal-to-noise.

5.2.3 SAXS radial integration

We analysed the data with a custom Python routine written with the help of C. Martinez-Torres. The algorithm consisted of different steps, involving the loading and reading of the file from proprietary edf format. The scattering pattern was then background subtracted by subtracting the blank image of the buffer (contained either in a capillary or in the rheometer) in which the samples were prepared. The samples were then masked to remove the beam-stop as well as the bands between the panels (see Fig. 2a) by using a binary mask. We then used a .poni file, which is a calibration pattern obtained by using the known scattering pattern of AgBe, to determine the centre of the detector (Fig. 2a). We finally performed a radial integration of the intensity and plotted the integrated intensity as a function of q. For anisotropic samples, we performed integration over a single quadrant (meridional or equatorial) of the sample instead of the entire angle range.

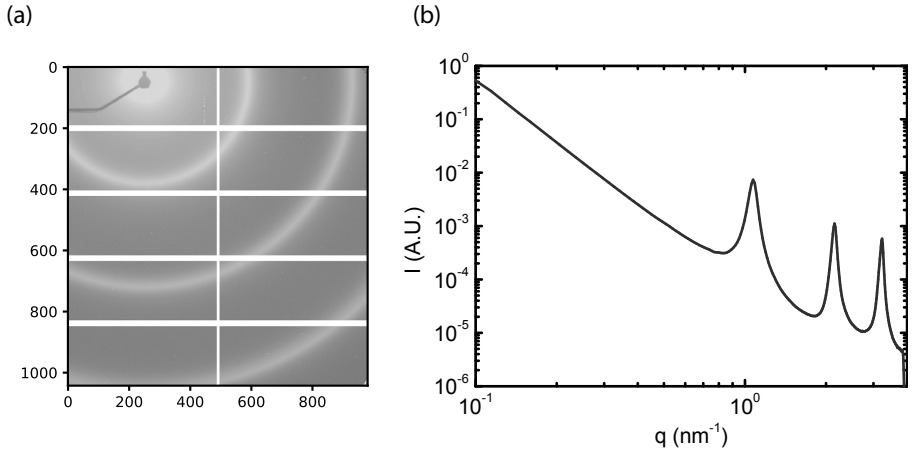

Figure 2: Example of a SAXS scattering pattern on a silver behenate powder.(a) Two-dimensional scattering pattern of a silver behenate (AgBe) powder after background subtraction. The sharp yellow (sections of) circles correspond to Bragg peaks that result from the periodic crystal structure of AgBe. The thread and dot in the upper-left corner are the beam stop, which protect the beam centre from excessive radiation, and a connecting wire. The white vertical and horizontal stripes correspond to the ten panels that make up the detector. (b) Radial integration of the scattering pattern gives rise to a scattering curve (scattering intensity as a function of wavevector q) with three sharp diffraction peaks, which are used as a reference for measuring the distance from the centre of the detector (around 1-2-3 nm^{-1}).

5.2.4 SAXS analysis of axial fibre packing order

The axial packing order was determined by plotting the data according to a Kratky plot [239], where the intensity I(q) is multiplied by q^2 and plotted as a function of q. This representation of the scattering data allowed us to single out the peaks arising from axial order. The Kratky plots were denoised by filtering the curves with a Savitzy-Golay filter, where a polynomial of n-th order is fitted to a set of adjacent data points to smooth the data. We usually used a polynomial of third order with a window of 5 consecutive points. We then applied the 'findpeaks' function from the package Scipy, where peaks are found by comparison with two neighbouring points. For noisy signals, as is the case here, this procedure can give rise to false peak detection, but the smoothing of the signal before searching for peaks helps mitigating this problem. Furthermore, we considered as real peaks only those appearing in at least two duplicate measurements of independently prepared samples under the same conditions.

5.2.5 SAXS analysis of radial fibre packing order

The radial packing structure of the fibres was characterized by performing power-law fits in defined q-ranges, between 0.2 and 1 nm^{-1}. We chose 0.2 nm^{-1} because it

corresponds to values smaller than the fibre diameter (about 100 nm, see electron microscopy images in Supplementary Figure S2), where scattering arises from the internal structure of the fibrils. We chose the highest end of the fitting range as 1 nm^{-1} because the scattering intensity hits the noise floor here.

5.2.6 Confocal microscopy

Confocal microscopy images were acquired with a Nikon Ti-eclipse microscope in confocal reflectance mode for collagen and in fluorescence mode for fibrin. In the composite networks, we specifically focussed on collagen-induced changes in fibrin structure, because the fluorescent labelling of fibrin allowed us to distinguish it from collagen. Both networks were illuminated with an Argon laser (488 nm, Albuquerque) through a 100x NA 1.49 oil immersion objective (Nikon). End-point measurements were taken on gels polymerised beforehand in a warm (37°C) room in a silicon chamber used to space two coverslips. We imaged a 3D portion of the network after polymerisation by performing a z-stack starting from a height of 10 μm above the bottom surface to avoid surface effects and taking images with a step size of 0.5 μm up to a total depth of 30 μm into the sample. The z-stack was then shown as a maximum intensity projection obtained with ImageJ [108]. Time-lapse image series on single confocal planes were acquired by polymerising networks inside a custom-built imaging chamber mounted on the microscope, where the temperature was controlled by flowing water from a water bath through channels surrounding the imaging chamber on the sides.

5.2.7 STEM microscopy

STEM images of fibres dried on an electron microscopy grid were obtained using High-Angle Annular Dark-Field mode (HAADF) on a Verios 460 electron microscope (FEI). To determine the axial packing periodicity of the fibrils, we drew a line along selected fibrils with the plugin 'Plot profile' in ImageJ, which retrieves the pixel intensity. We then used a custom-written Python script to filter the intensity profile data using a Savitzy-Golay filter, with a window length of 5 and a polynomial order of 3. We finally used the 'findpeaks' package from Scipy to obtain the local maxima and calculated the average distance between the peaks.

5.3 Results

5.3.1 Discerning structural differences between collagen types

We first investigated the SAXS scattering patterns arising from reconstituted collagen networks, exemplified in Figure 3. We compared different types of collagen, which were furthermore extracted from different tissue sources: type I collagen from rat tail

tendons, which retains the terminal telopeptide-end regions that mediate intrafibrillar crosslinking, and two collagens that lack the telopeptides, type II collagen from chicken sternal cartilage and type I atelocollagen from bovine dermis.

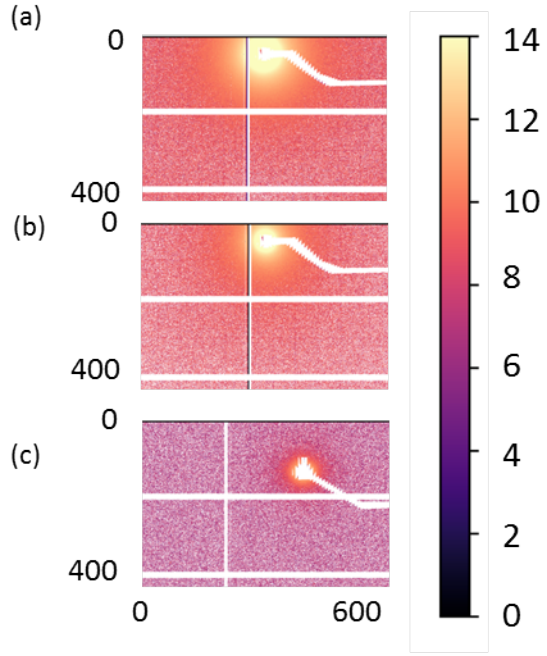

Figure 3: SAXS scattering patterns for reconstituted networks of collagen extracted from different tissue sources.(a) Scattering pattern of rat tail collagen at 8 mg/mL, (b) type II chicken sternal cartilage at 4 mg/mL and (c) atelocollagen at 6 mg/mL. The patterns are rather featureless, compared with the clear peaks observed for the AgBe powder (Fig. 2). The centre position of the beam is different for (a-b) compared to (c), because the images were acquired during different beam time sessions. The colour indicates the scattering intensity (colour bar on the right, expressed in arbitrary units). The x- and y-axes denote the pixel number.

Figure 4 shows the radially integrated scattering patterns (panel d) together with STEM images for the three different types of collagen (panels a-c). The STEM images reveal fibrils with a characteristic banded structure having an average repeat distance of around 67 nm (see extra STEM images and example line profile in Supplementary Figures S2-3). While for type II collagen (Fig. 4b) and bovine dermal collagen I (Fig. 4c) all of the imaged fibrils showed a clear D-banding with an average periodicity of 67±1 nm, only around 30 % of the imaged rat tail collagen I fibrils (Fig. 4a) showed the D-banding pattern, with an average periodicity of 65±1 nm. For all three collagens, however, the radially averaged SAXS data did not show any obvious Bragg peaks at first glance (Fig. 1d), but just an apparent smooth decrease in intensity with increasing wavevector q.

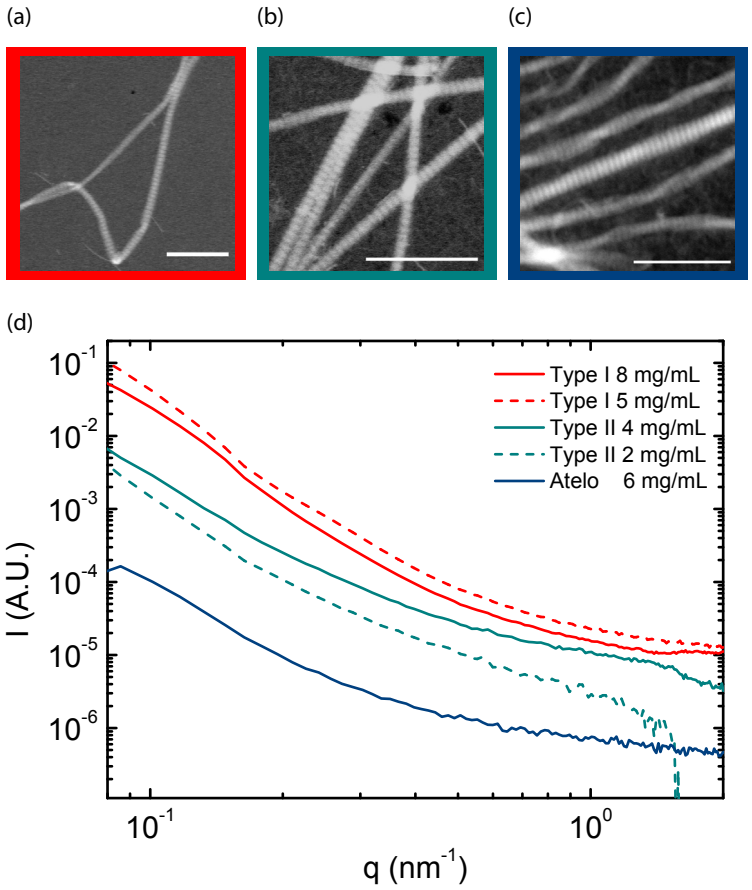

Figure 4: SAXS scattering patterns and STEM images of different collagen types. STEM images of (a) rat tail collagen type I at 1 mg/mL, (b) type II collagen at 1 mg/mL and (c) atelocollagen at 1 mg/mL. (d) Radially integrated scattering curves obtained for different collagen types and for different concentrations (see legend). Red lines represent scattering curves of rat tail type I collagen polymerised at 5 (dashed line) and 8 mg/mL (solid line), blue line represents atelocollagen I from bovine skin at 6 mg/mL, while green lines represent type II atelocollagen extracted from chicken sternal cartilage at 2 mg/mL (dashed line) and 4 mg/mL (solid line).

However, when we replotted the scattering data in the form of Kratky plots [112] by multiplying the intensity I(q) by q^2 and performed denoising with a Savitzky-Golay filter (see Supplementary Figure S4), we did observe Bragg peaks at positions consistent with the expected 67 nm-periodicity (see Figure 5; an overview of the unprocessed data can be found in Supplementary Figure S5). We detected multiple peaks with a peak-finding algorithm from the 5^{th} order onwards. We did not see the first order scattering peak, which should in principle be brightest. A possible reason might be that this peak is located relatively closely to the transmitted beam, in the centre of the detector: as our samples are mainly composed of water, there will be just a tiny fraction of light that is scattered while the majority of the incident photons

will be transmitted. We therefore decided to consider only a certain range for the q-integration, from 0.2-1 nm^{-1}, where we can first observe clear Bragg scattering peaks. The axial periodicity of the collagen fibres averaged over multiple peaks and over multiple SAXS scattering images per condition is summarized in Figure 5b. We observe periodicities varying between 66 and 69 nm, consistent with the 67 nm spacing observed in our STEM images and reported in prior SAXS studies [112, 122, 240]. The Bragg peaks are most pronounced for the type II atelocollagen fibres, consistent with the observations by STEM that these fibres are all banded and have a larger diameter than the type I collagen fibres.

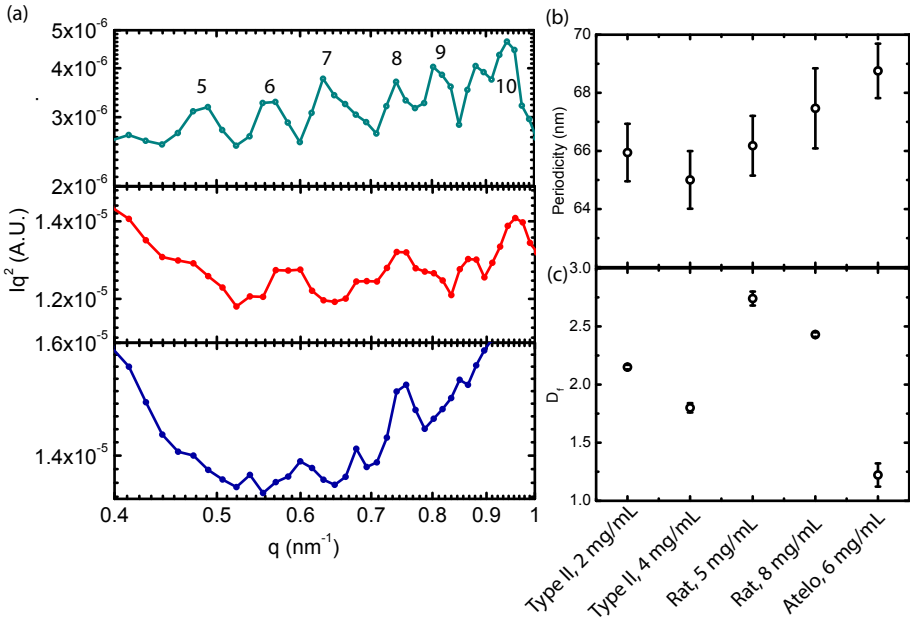

Figure 5: SAXS analysis of the axial and radial packing periodicity of collagen fibres. (a) Kratky plots obtained by multiplying the scattering intensity by the wavenumber squared and smoothing with a Savitzy-Golay filter. The plots represent different types of collagen, with the same colour coding as in figure 4. Type II atelocollagen (green) is shown at 2 mg/mL, rat tail collagen I (red) is shown at 5 mg/mL, and bovine dermal type I atelocollagen (blue) at 6 mg/mL. The numbers represent the expected positions of the n-th order reflections expected based on an axial periodicity of 67 nm. (b) Average axial periodicity extracted from the peak analysis of the three collagen samples at various concentrations (see legend). (c) Fractal dimension characterizing the radial packing order of the fibres, obtained by fitting the radially integrated intensity I(q) to a power-law in the q-range between 0.2 and 1 nm^{-1} where the scattering arises from the internal fibre structure.

To quantify the radial packing order of the fibres, we fitted the scattering profiles I(q) to a power law in the q-range 0.2-1 nm^{-1} where SAXS is sensitive to the internal structure of the fibres. Interestingly, the type I collagen having intact telopeptides had a higher fractal dimension (D_f =2.5 - 2.7) than the atelocollagen type I (D_f =1.2)

and type II (D_f =1.7-2.1), as shown in Fig. 5c, suggesting that telopeptide-mediated intrafibrillar crosslinking induces a more tightly packed internal fibre structure. This conclusion is consistent with our previous rheological comparisons of telo- and atelocollagen, where we showed that telocollagen fibres have a higher bending rigidity than atelocollagen fibres [70] (see Chapter 2 and 3). Further direct support comes from our recent mass-mapping study of different collagen types based on STEM, where we observed a higher mass-length ratio for telocollagen [241]. Both the type II collagen and the rat tail collagen furthermore exhibit a decrease of the fractal dimension with increasing collagen concentration.

5.3.2 Collagen under shear

By inserting a rheometer in the beam path (see Figure 6a-b), we were able to apply a controlled shear deformation on the samples and record the shear stress while at the same time measuring the resulting changes on the molecular level. We first monitored the development of structure during polymerisation while applying a small amplitude oscillatory shear to monitor the viscoelastic moduli, and subsequently measured the structural response under a stepwise strain ramp protocol with forward and backward strain sweeps to test reversibility (see Figure 6c).

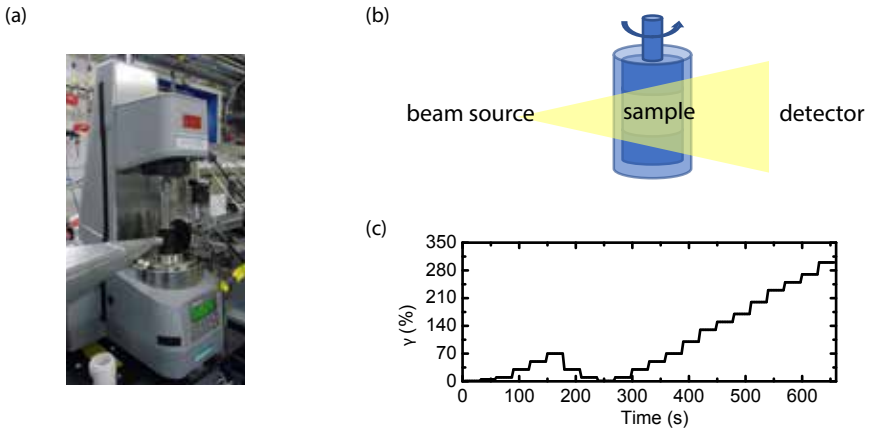

Figure 6: RheoSAXS setup. (a) Picture of the setup used for rheoSAXS measurements. The X-ray beam (left of the sample) hits the sample in the Couette cell from the side and is scattered by the network inside the Couette cell. The scattered intensity is collected on a detector (to the right of the sample). The picture was taken by B.Vos. (b) Schematic of the setup, where the Couette cell containing the network is placed between the beam source and the detector. (c) Strain ramp protocol used for shear rheology.

We first monitored the concurrent changes in network rheology and structure during collagen network polymerisation by applying a small shear oscillation (f = 0.5 Hz, γ= 0.5%) over a period of two hours (see Figure 7). The storage modulus G' and loss modulus G" display an initial lag time of ~40 min before there is a

discernible increase indicative of the formation of a space-spanning network (see Figure 7b). Next, they reach approximately constant values after a growth period of ~60 min. Confocal imaging showed that, although the moduli are close to zero in the first 60 min, there are nevertheless already fibrils present directly after initiating assembly at time ~0, which apparently do not yet form a percolating structure (see Supplementary Figure S6). The scattering profile reveals a Bragg peak denoting axial packing periodicity indicative of fibril formation (see Figure 7a and Supplementary Figure S7). The apparent fractal dimension of the fibre characteristic for the radial packing structure slightly increases during polymerisation (Fig. 7c), suggesting that the fibrils may potentially become more compact as they mature. Unfortunately, we only have one dataset, so we cannot test for statistical significance. The axial packing periodicity does not significantly change during polymerisation, staying around 67 nm (see Figure 7d). We calculated the periodicity from the peaks ranging from 7th-9th order (see Kratky plots in Supplementary Figure S7).

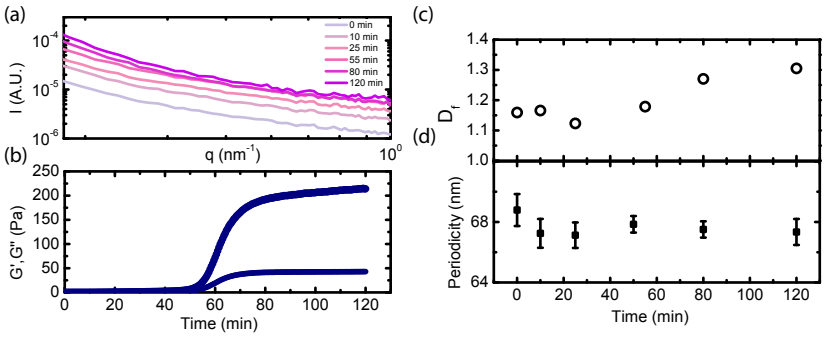

Figure 7: Time evolution of the scattering profile of a 6 mg/mL collagen network. (a) Scattering pattern for a polymerising bovine dermal atelocollagen network at 6 mg/mL, measured at different time points. The curves are shifted along the vertical axis for clarity. (b) Polymerisation curve obtained with shear rheology for the same network. Upper curve indicates G' and lower curve indicates G", consistent with the formation of a soft solid. (c) Fibre fractal dimension as a function of time for different times after the start of polymerisation, obtained by performing power-law fits to the scattering data for q between 0.2 and 1 nm^{-1} and (d) corresponding time evolution of the axial periodicity, where the error is calculated from the S.E.M. of multiple peaks.

Once the network was fully formed, we subjected it to increasing levels of strain (see Figure 6c), while allowing the stress to relax (see Supplementary Figure S8). Since the stress-strain curve contained too few data points to calculate the differential elastic modulus, Fig 8a shows prestress measurements (which we have reported in chapter 3 of this thesis and Ref. [70]) of the differential modulus, measured independently from the rheoSAXS measurements. The elastic response of the network is linear until the strain reaches ~10%, at which point the network starts to stiffen. At a strain of 15%, the modulus-strain curve shows an inflection. In previous work, it was shown by comparison of such strain-stiffening data with fibrous network

simulations that the strain where the inflection occurs demarcates the transition from a soft state dominated by fibre bending to a rigid state dominated by fibre stretching, as reviewed in Red. [242]. Around 40% strain, the elastic modulus decreases, indicating the onset of network rupture.

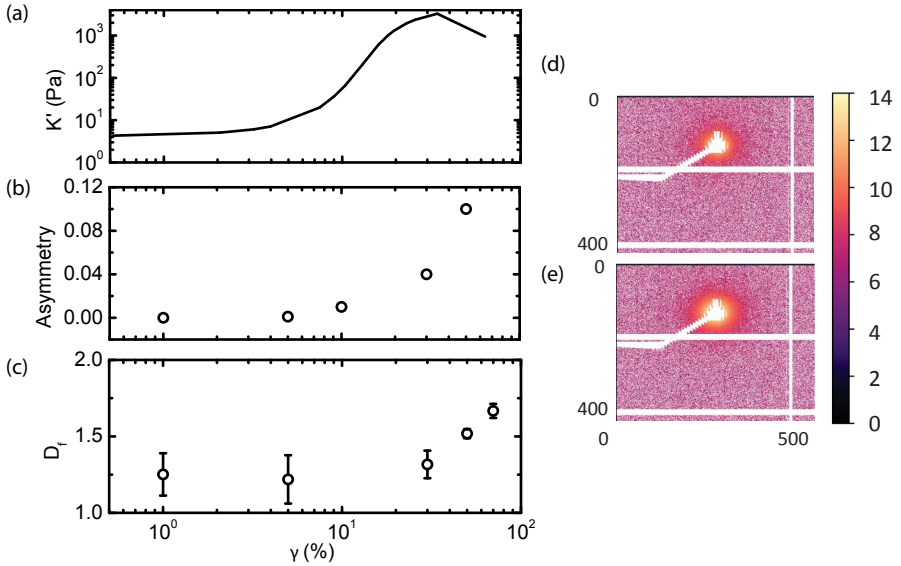

Figure 8: RheoSAXS response of a 6 mg/mL bovine dermal atelocollagen I network polymerised at 37°C. (a) Strain-stiffening response of a collagen network measured outside the X-ray beam, in terms of the differential elastic modulus as a function of strain measured using a prestress protocol. The rheology data acquired with rheoSAXS consisted of too few data points to fit the stress-strain response (shown in Supplementary Figure S8). (b) Asymmetry of the SAXS scattering pattern, quantified as a function of strain and (c) evolution of the fibre fractal dimension, obtained by radially integrating the equatorial scattering pattern and fitting a power-law to I(q) between 0.2 and 1 nm^{-1}. (d) Scattering pattern of the collagen network under strain shows initially (strain = 1%) an isotropic signal, while at higher strain (e) (strain = 70%) it shows alignment, through anisotropy between the horizontal and vertical quadrants. Numbers on the axes represent the pixels on the detector. Colour code represents the scattering intensity (see colour bar on the right).

Fig. 8b shows that the onset of strain-stiffening coincides with the development of an asymmetry in the scattering pattern (see also Fig. 8d-e). Surprisingly, even at strains beyond 40%, where the modulus decreases with strain, the asymmetry continues to increase, suggesting that network rupture is only partial. When we look at the fibre fractal dimension charactering the radial packing structure as a function of strain, we notice a number of interesting things (Fig. 8c). First, the fractal dimension is constant at low levels of strain, indicating that small strains do not cause fibre stretching. This is consistent with the fact that fibres are known [6] to predominantly experience bending deformations in the linear elastic regime. Second, the fractal dimension monotonically increases with increasing strain for strains above 10%.

In this strain regime, the fibres are indeed expected to be stretched, which likely makes the fibres more efficiently packed. A similar effect was observed also in a previous study on a whole tissue, the cornea [243]. In that study, the diameter of the collagen fibrils was shown to decrease with increasing tensile strain, indicating a more compact, tightly packed arrangement. Third, like the asymmetry, also D_f continues to increase even at strains beyond 40%, again suggesting that network rupture is only partial and a certain fraction of the fibrils still connects the rheometer plates so they experience a tensile load. This observation is consistent with our findings in Chapter 2, where we similarly observed by confocal microscopy that bonds persist at strains larger than the strain where K' peaks.

5.3.3 Fibrin under shear

We next investigated the rheological behaviour of a 6 mg/mL fibrin network. Again, we first monitored the evolution of the scattering pattern during network polymerisation (Fig. 9a), while simultaneously recording the increase of the elastic and viscous shear moduli (Fig. 9b). Polymerisation starts instantaneously, as shown by the rapid increase of the elastic modulus, but the elastic modulus does not reach saturation even after 2 hours (Fig. 9b). Similarly slow kinetics for equilibration of the elastic modulus were observed in prior studies, where it was shown that polymerisation is fast but subsequent crosslinking by Factor XIII is slow [244, 245]. The fibre fractal dimension, calculated by performing a power-law fit to the scattering curves for q-values between 0.2 and 1 nm^{-1}, shows a slight increase over time, which confirms earlier observations from light scattering of FXIII-crosslinking induced fibre compaction during polymerisation [245]. We note that the fibre fractal dimension is higher for fibrin than for collagen, while the change with time during polymerisation is smaller (note the different y-axis as compared to Figure 7). We refrain from an interpretation of the absolute magnitude of the fractal dimension of the two fibre types, because we regard it an effective number that provides a coarse-grained description of fibre packing. Unlike what we had observed previously [214] for fibrin networks, these curves are rather smooth, even with a similar processing algorithm as for collagen (see Supplementary Figure 9) and therefore we cannot report the axial periodicity here.

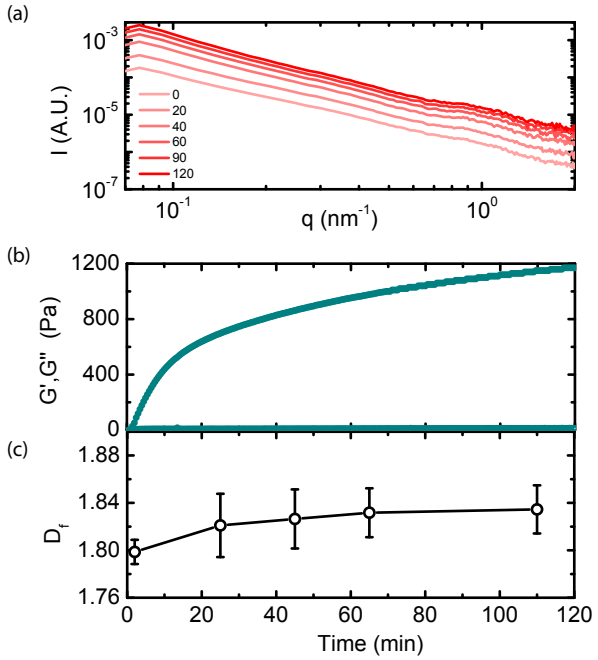

Figure 9: Time evolution of the SAXS scattering profile of a 6 mg/mL fibrin network correlated with the rheology. (a) Scattering pattern of the fibrin network at 6 mg/mL, for different times after the initiation of polymerisation. (b) Time evolution of the storage and loss shear moduli. Upper curve indicates G', lower curve G". (c) Fractal dimension of the fibrils during polymerisation, obtained by fitting a power-law decay to the radially integrated scattering curves in the q-range between 0.2 and 1 nm^{-1}.

We then subjected the fibrin network to shear deformation. We used a similar protocol as for collagen, with the main difference that we could apply much larger strains before network fracture thanks to the hierarchical structure of fibrin that provides multiple mechanisms to accommodate the strain [213] (see Figure 10a). We note that the maximum stiffness reached before rupture was much smaller when probed by the strain ramp protocol than by the prestress protocol reported in prior studies [213]. This difference is likely due to the stress relaxation that takes place after each stepwise increase in strain (Supplementary Figure S10). Stress relaxation is significant, probably because we polymerised the networks with a relatively low calcium concentration, which may reduce the level of crosslinking. Nevertheless, the elastic response of the sample is fully reversible when we first increase the strain to 70%, then back to zero, then back up. This observation indicates that there are no inelastic events such as rupture or remodelling. The network starts to stiffen at a strain of around 20%, but fibre alignment only becomes visible once the strain reaches ~30% (see Figure 10b and 10d-e). This observation is consistent with previous studies of alignment in fibrin network by optical birefringence [246], and with the notion that the initial stiffening response involves straightening out of the thermal bending undulations of the fibres [213]. Interestingly, while we observe a

softening of the network at high strain, consistent with partial breakage, we still observe continued fibre alignment, though with a small discontinuity around a strain of ~130%, which can be related to fracture and recoil of a portion of the network. We note that two consecutive stepwise strain ramps, one till 70% and the other till 300%, provide an identical response of the anisotropy, indicating that there are no irreversible changes in fibre orientation at least until strains of 70% (compare grey and black curve in Figure 10b). When measuring the evolution of fractal dimension with strain, we observed no significant changes (see Figure 10c).

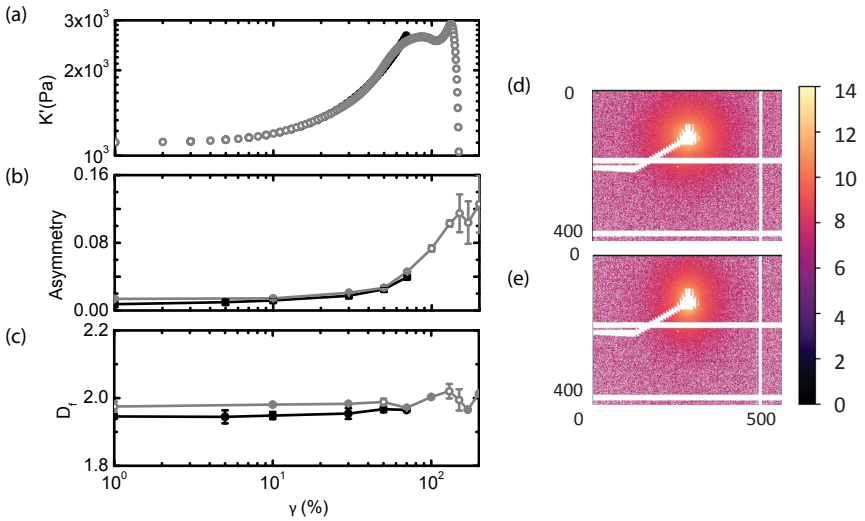

Figure 10: RheoSAXS response of a 6 mg/mL fibrin network polymerised at 37 °C. (a) The differential elastic modulus as a function of strain, evaluated from the stress-strain data in Supplementary Figure S10. (b) Asymmetry of the scattering pattern, quantified as a function of strain and (c) evolution of the fibre fractal dimension obtained by radially integrating the equatorial scattering pattern. In these graphs, the black squares represent the first loading phase, and the grey circles the second loading phase. In between the two loading phases, the network is unloaded. (d) Scattering pattern of the fibrin network shows initially (strain = 1%) an isotropic signal, while at higher strain (e) (strain = 130%) there is alignment. The numbers on the axes represent the pixels on the detector. Colour code represents the intensity of the scattered light (see colour bar on the right).

5.3.4 Composite networks under shear

After having assessed the response of each component individually, we examined the polymerisation process and ensuing structure of collagen-fibrin composites. When imaging the composite system at the end of the polymerisation process with confocal microscopy, we observe that both components form fully percolating networks that interpenetrate (Fig. 11a). The polymerisation curve recorded by shear rheology shows a biphasic increase of the shear moduli (Figure 11b). This response suggests that the polymerisation of each component within the composite is well-separated in time. Based on the polymerisation dynamics of the individual components, we

assume that the first phase is related to the polymerisation of fibrin, as it has no measurable lag time, while the second phase is related to collagen polymerisation, setting in around 40 minutes after mixing. The SAXS scattering patterns recorded during polymerisation faintly shows, at the end of polymerisation, a peak that corresponds to the 1st order Bragg peak expected from the 22.5 nm axial packing periodicity of fibrin (indicated by a star in Figure 11c). However, the interpretation of these peaks is complicated by the fact that the peaks corresponding to the axial packing periodicity of fibrin (q = 0.28 nm^{-1}*n) are close to the odd order peaks arising from the quarter-staggered arrangement of collagen (see also Kratky plots in Supplementary Figure S11). Similarly, the apparent fractal dimension for the composite system deduced from the power-law slope of I(q) is an intermediate value between that measured for collagen and fibrin fibres (see Figure 11d).

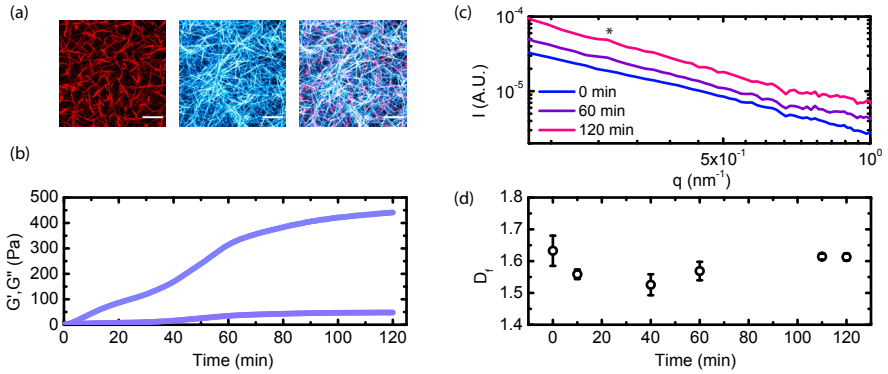

Figure 11: Time evolution of the scattering profile and rheology of a composite network made of 6 mg/mL fibrin and 4 mg/mL collagen. (a) Confocal images of the composite, with the fibrin channel (shown in red), collagen channel (shown in blue) and overlay of the two images. Both networks show full percolation. (b) Polymerisation process of the composite monitored by small amplitude oscillatory shear rheology. The moduli increase in a biphasic manner, presumably related to the sequential polymerisation of fibrin (first plateau) and collagen (second plateau). (c) Radially integrated scattering intensity shows a distinct though faint Bragg peak characteristic of fibrin's axial packing periodicity towards the end of the polymerisation process, indicated by a star. (d) Fibre fractal dimension obtained as the slope of a power-law fit to the radially integrated intensity in the range 0.2-1 nm^{-1}.

We then varied the relative concentrations of the two networks and quantified how this impacts the network structure. In Figure 12a, we show images of fibrin networks with increasing amounts of added collagen (only the fibrin network is shown). Upon addition of more collagen, the fibrin fibres become more clustered, giving rise to inhomogeneous clumps when the collagen concentration reaches 6 mg/mL. Strikingly, the radially integrated scattering intensity for composite networks shows a prominent Bragg peak (Fig. 12b), which becomes more apparent when more collagen is added (see also Supplementary Figure S12). We notice that here we can see the peak position more clearly than in Figure 11c, but we are also using a different

geometry: a capillary instead of a rheometer cell. For all the composite systems, the Bragg peak is centred at the same position of 0.28 nm^{-1}, consistent with the 22.5 nm periodicity of fibrin (see Figure 12d). The independence of the peak position on the collagen concentration indicates that the copolymerisation does not appreciably strain the fibrin fibres. The enhanced height of the peak is likely explained by the bundling of fibrin fibres observed with confocal microscopy, which increases the crystallite size. Meanwhile the average fractal dimension of the fibres decreases upon addition of collagen, likely because it represents a concentration-weighted average over the fractal dimensions of the collagen and fibrin fibres (see Figure 12c).

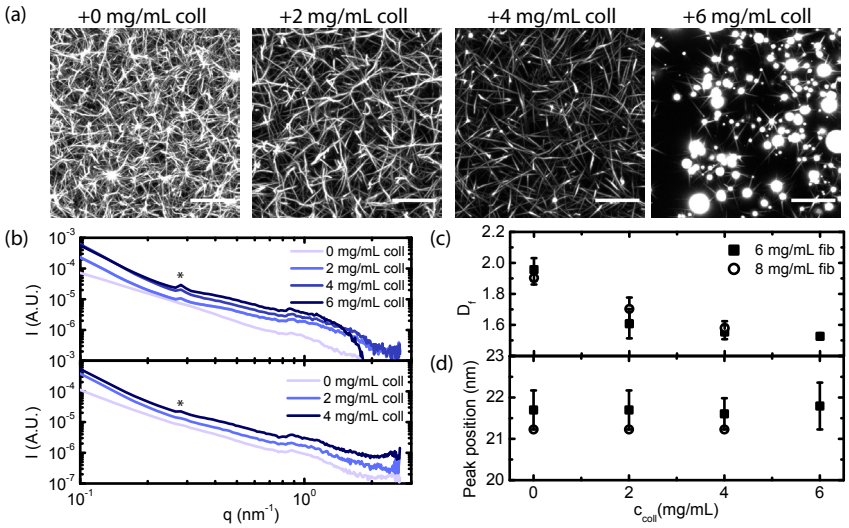

Figure 12: Effect of relative concentrations of fibrin and collagen on the composite properties. (a) Composite system imaged with confocal fluorescence microscopy, showing fibrin network structure for a fixed concentration of fibrin (6 mg/mL) and increasing concentrations of added collagen, as specified above each panel. Images are shown as a maximum intensity projection of a z-stack over a depth of 20 μm; scale bars indicate 10 μm. (b) Scattering pattern for a composite network after polymerisation, with a fixed amount of fibrin (6 mg/mL, upper panel, 8 mg/mL, lower panel) and increasing collagen concentration. (c) Average fibril fractal dimension as a function of collagen concentration in a composite network with a fixed concentration of fibrin (6 mg/mL, squares; 8 mg/mL, circles), obtained by fitting the radially integrated intensity between 0.2-1 nm^{-1}. (d) Position of the 1st order Bragg peak corresponding to the half-staggered packing order of fibrin as a function of collagen concentration (6 mg/mL, squares; 8 mg/mL, circles).

Interestingly, when considering the rheology of the composite system, we see that in the composite networks the moduli are lower than in the pure systems taken individually. Starting from a pure fibrin network, the moduli decrease monotonically as more collagen is added even though the total protein concentration increases (see Supplementary Figure S13). This observation could be explained by multiple effects, such as the bundling of the fibrin fibres induced by collagen addition, as well

as potentially incomplete polymerisation of one or both components due to steric hindrance.

We finally measured the structural and mechanical response of the composite to shear deformation. We chose to focus on a composite network formed by 4 mg/mL collagen and 6 mg/mL fibrin (see Supplementary Figure S14) to avoid the inhomogeneous clumps seen at higher collagen concentrations. The stiffening response, shown in Figure 13a, sets in very early (black line), but the modulus decreases at a strain of ~30% likely due to rupture of the collagen network. In the second loading ramp, the stiffening response is different compared to the first loading ramp, supporting the idea that the collagen network is damaged. An offline experiment carried out at 1 mg/mL collagen and 1 mg/mL fibrin showed that indeed collagen selectively breaks first, while the fibrin network retains its mechanical response (see Supplementary Figure S15). The scattering patterns again shows anisotropy developing at strains of around 30% (Fig. 13b), and, unlike the mechanical response, the anisotropy is fully reversible between the two loading ramps (compare black and grey curves). The final level of anisotropy reached is slightly lower than the one we reported for the single component fibrin systems. This could be due to the structural inhomogeneity introduced by co-polymerisation, which is expected to make the strain response of the system less affine. We observe that the packing structure shows a slight increase with strain (see Figure 13c), likely reflecting the increase in packing density of the collagen fibres we also observed for pure collagen networks.

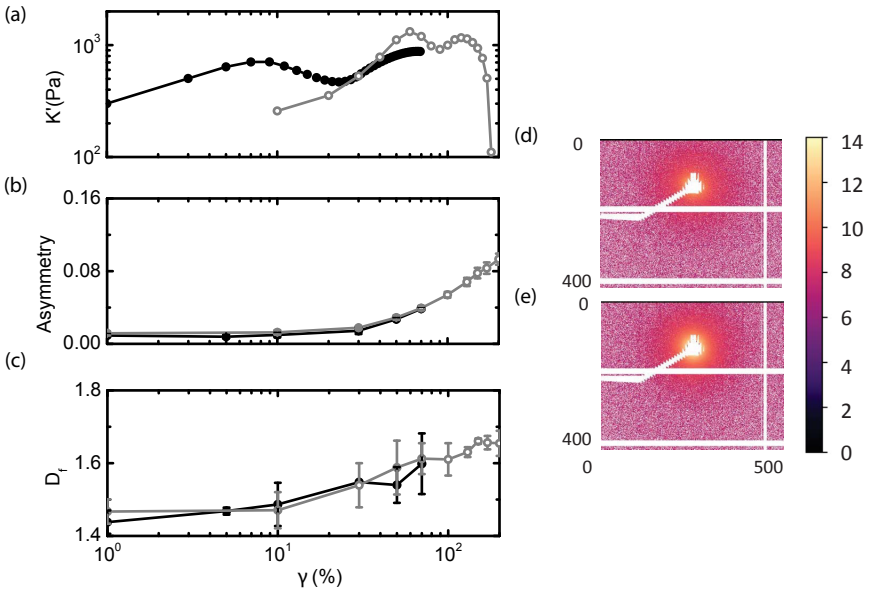

Figure 13: RheoSAXS response of a composite network made of 6 mg/mL fibrin and 4 mg/mL collagen, polymerised at 37°C. (a) Elastic response for a composite network, where the differential elastic modulus is shown as a function of strain (here the response is evaluated directly from the data in Supplementary Figure S13). (b) Asymmetry of the scattering pattern, quantified as a function of strain and (c) evolution of the fibre fractal dimension obtained by radially integrating the equatorial scattering pattern and taking the slope of a power-law fit to I(q). In these graphs, the black circles represent the first loading phase, and the grey circles the second loading. (d) Scattering pattern of the composite network is initially (strain = 1%) isotropic and becomes anisotropic at higher strain (e) (strain = 130%). Numbers on the axes represent pixel numbers. Colour bar on the right codes for the scattering intensity.

5.4 Discussion

We measured the nonlinear elastic response of composite networks of fibrin and collagen, two of the main components of the extracellular matrix. Both these proteins are present during wound healing, and understanding how the composite nature of the extracellular matrix in the wound bed affects the mechanical response can lead to the identification of better ways of engineering composite materials that can aid wound healing.

We first investigated the static scattering pattern of collagen I and II, extracted from different tissue sources. Prior SAXS experiments on collagen in whole tissue, such as the cornea [243] or tendon [92, 247], revealed a highly ordered molecular packing arrangement of the fibrils along the fibril axis, characterized by Bragg peaks. By contrast, the reconstituted collagen networks do not show pronounced Bragg peaks and the first and second order peaks are absent. We speculate that these two

peaks are masked by the fact that most of the X-rays are not scattered, but simply transmitted, thus preventing the observation of peaks at low q-values close to the beam centre. We showed, however, that it is nevertheless possible to identify the molecular fingerprint of collagen's quarter-staggered packing arrangement from higher order peaks that are visible in Kratky representations of the scattering curves. The axial packing periodicity was more marked for the type II atelocollagen from chicken cartilage and for type I atelocollagen from bovine dermis, which also showed a well-detectable periodicity when imaged with electron microscopy, while type I collagen extracted from rat tail only displayed partial D-banding in EM images. It would be interesting to check if this packing deficiency is characteristic of collagen lacking telopeptides or if it is tissue-dependent. A possible reason for the lack of a D-banding pattern in a large fraction of the rat tail collagen fibres could be that its assembly dynamics is much faster than for atelocollagen, which could lead to a more disorganized assembly. In fact, previous studies have shown that the presence of a lag time promotes the assembly of D-banded fibres from purified collagen [248, 249]. Another striking difference that we identified between the different types of collagen was the radial packing density of the fibres, as quantified through the power-law slope of the intensity decay with q that we interpret as the fractal dimension of the radial packing arrangement. Specifically, we found that the fibre fractal dimension for telocollagen was higher than for the atecollagens. This is consistent with our previous observations that telocollagen fibrils have a larger bending rigidity [70] and larger mass-per-length ratio [241], likely because crosslinking mediated by the telopeptide end regions of the molecule promotes a tighter packing.

We next investigated the development of fibre packing order during polymerisation of both fibrin and collagen. For both systems, we observed that the Bragg peaks characteristic of the axial packing periodicity were present already in the early stages of polymerisation. Apparently, there is a rapid formation of fibres in both cases, and their further maturation does not involve any change in the axial packing periodicity. We did observe a slight increase of the fibre fractal dimension as a function of polymerisation time, which is consistent with progressively tighter packing of the fibrils as they mature.

Next, we measured the elastic and structural response of the networks under shear deformation. We discovered that the fibre fractal dimension in case of collagen increased under shear, suggesting that fibres under tensile load get densified. This interpretation is consistent with proposed deformation mechanisms of collagen fibrils within whole tissues such as corneal tissues [243] and tendons [122, 247], where fibrils were proposed to stretch by a combination of monomer stretching and sliding of monomers past one another and where the fibre diameter was reported to decrease with strain. In our study, we employed collagen that lacks the telopeptide end regions and therefore lacks interfibrillar crosslinking necessary for hampering

monomer sliding. In the future, it would be interesting to compare the rheoSAXS response of atelocollagen with that of collagen with intact telopeptides. We did not observe any measurable changes in the position of the Bragg peaks characteristic of the axial packing periodicity of collagen upon application of strain. We note that our detection algorithm is only sensitive to changes in periodicity of at least 2 nm, while previous studies have shown that the changes in axial periodicity upon application of strain are of the order of only 0.5 nm [250]. We observed an increase in the anisotropy of the scattering patterns under shear, confirming earlier models proposing that collagen fibres align along the shear direction, which causes a strain-controlled transition from a soft state dominated by fibre bending to a rigid state dominated by fibre stretching.

For fibrin networks, we observed a markedly different structural response to shear compared to collagen networks. Unlike collagen, we observed no significant change in the transversal fractal dimension of the fibrils as a function of strain. Fibrils started to align at a shear strains of around 30%, consistent with a previous study [246], which is later than the onset strain for strain-stiffening around 10%. The delayed alignment is consistent with earlier models proposing that the initial strain-stiffening originates from the entropic force-extension response of the semiflexible fibrin fibres [251, 252]. We could not observe any clear Bragg peaks from the axial packing periodicity of fibrin, in contrast to previous studies, where we and others did observe Bragg peaks [214, 253]. The assembly conditions used in prior work promoted the assembly of fibrin in thick fibres, which give rise to a distinct peak arising from the 21.95 nm periodicity. Here, we used a different buffer and a lower calcium concentration. The lack of a marked Bragg peak could therefore be caused by the strong sensitivity of fibrin self-assembly to the buffer and ionic conditions used for polymerisation [254].

Finally, we investigated the mechanical and structural response of composite networks of collagen and fibrin to an applied shear strain. This is, to our knowledge, the first report of SAXS measurements on such a composite. The average fibril fractal dimension for the composites was intermediate between those of pure collagen and pure fibrin. We could recognize the Bragg peak from the half-staggered packing of fibrin and found that the peak position was not changed by the presence of collagen, indicating that strains introduced by copolymerisation - if any - are small. Interestingly, the presence of collagen increased the intensity of the Bragg peak for fibrin, likely due to collagen-induced bundling of fibrin fibres. Our results are different from previous reports for fibrin-collagen composites [219], where a decrease in the diameter of both fibres was observed by scanning electron microscopy; however, the concentrations used there were lower than the ones we used here. In our system, bundling caused an inhomogeneous network structure that resulted in a lower elastic modulus for the composites compared to the sum of the elastic moduli of the separate networks. The composite networks also displayed less alignment

with shear than the isolated networks, suggesting that the inhomogeneous network structure makes the deformation less affine.

5.5 Conclusions

In this chapter, we investigated the molecular structure of reconstituted fibrin and collagen networks and of their composite matrix, which occurs during wound healing. In case of collagen, the SAXS measurements showed a clear difference between the molecular packing structure of fibres formed from collagen with and without the telopeptide end regions. Atelocollagen assembled with a long lag time and formed fibrils with a banded structure, whereas telocollagen assembled more rapidly and the fibrils were only partially banded. During the polymerisation process, the axial packing periodicity remained constant but the fibre fractal dimension characterizing the fibre packing density increased, suggesting that the fibres become more compact as they mature. Fibrin networks by themselves did not show any clear Bragg peak in the scattering pattern. As for collagen, the fibre fractal dimension increased during the polymerisation process. Interestingly, in the composite system we observed an enhancement of the peak associated with fibrin, likely due to collagen-induced bundling of the fibrin fibres. When collagen and fibrin networks were sheared, they responded differently on the molecular scale. While collagen fibrils acquired a more compact packing structure under shear, likely due to fibre elongation by intramolecular sliding, fibrin fibres did not show a significant change. This is qualitatively consistent with the fact that collagen and fibrin obtain their extensibility from different deformation mechanisms [6]. It would be interesting, in the future, to investigate the role of telopeptide-mediated intrafibrillar crosslinking of collagen on the mechanical response, to see if the putative sliding mechanism can be switched off.

When investigating composite networks, we found that the presence of collagen induces bundling in fibrin, leading to reduced mechanical properties and earlier failure as compared to the pure fibrin system. It would be useful to complement our observations with other multiscale measurements, such as confocal rheology, which provides a real-space read-out of network remodelling and which can specifically distinguish collagen from fibrin by using different fluorescent labels (see Chapter 2). Our results can be useful in designing materials with enhanced extensibility inspired by the molecular design of fibrin and collagen, as well as in understanding the physiological role of the mechanical interplay between collagen and fibrin in processes such as wound healing and angiogenesis.

Acknowledgments

We thank C. Martinez-Torres (AMOLF, TU Delft), B. Vos (AMOLF) and L. Baldauf (AMOLF, TU Delft) for participating in the synchrotron experiments and for useful

discussion. We thank C. Martinez-Torres for help with the data analysis and with the STEM image acquisition. We thank A. Iyer for initial help with STEM images acquisition, H. Schoenmaker, N. Commandeur, D. Ursem and for technical help with the rheoSAXS setup. We thank D. Hermida-Merino and F. Ledrappier for assistance at the DUBBLE beamline. We thank M. Verweij for the design of the rheometer adaptation for SAXS microscopy and the mechanical workshop at AMOLF for realising it. We thank the design and mechanical workshop of AMOLF for constructing the temperature-controlled imaging chamber. Finally, we thank P. Kouwer (Radboud University Nijmegen) for help with the design of the rheoSAXS setup and for lending us a rheometer that was used to perform experiments not shown in this chapter.

5.6 Supplementary Figures

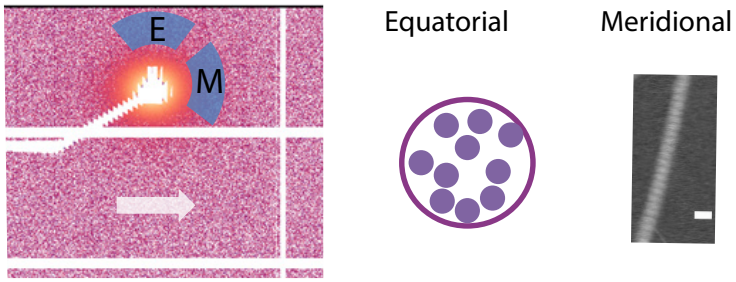

Supplementary Figure 1: Schematic of meridional and equatorial quadrants of the 2D SAXS scattering pattern used for discriminating effects of shear-induced fibre alignment on the fractal dimension. The meridional area of the scattering pattern (obtained by integrating between -30°and 30°with respect to the centre of the detector) provides information on the axial structure of the fibres, while the equatorial sector (obtained by integrating between 60°and 120°) provides information on the lateral structure of the fibres (transversal). The arrow indicates the direction of shear.

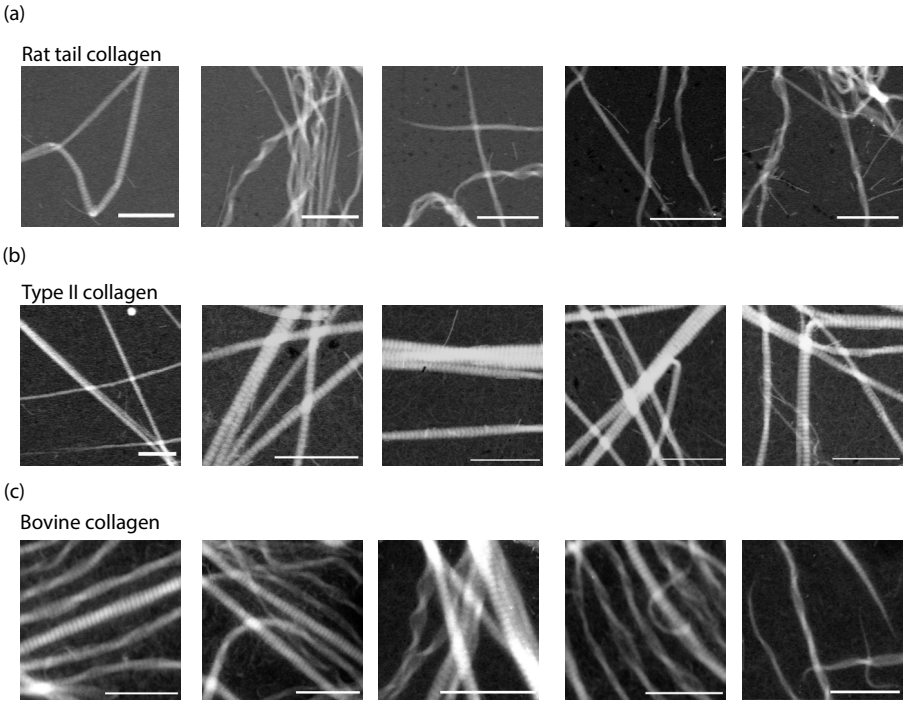

Supplementary Figure 2: Additional STEM images of collagen fibrils. (a) STEM images of rat tail collagen I. Not all of the imaged fibrils show the expected D-banding periodicity. (b) STEM images of type II atelocollagen from chicken sternal cartilage. The D-banding is obvious for all of the fibrils. (c) STEM images of type I atelocollagen from bovine skin. The images show a fraction of non-polymerised fibrils in the background, as well as thin straight filaments (Tobacco Mosaic Virus rods), that were included to enable quantitative mass-mapping. Scale bars: 1 μm. Part of these images are also shown in Ref. [241].

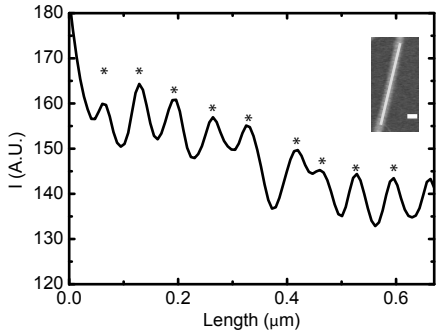

Supplementary Figure 3: Quantification of D-banding of collagen from STEM images. Example of an intensity line profile of a collagen fibril, after filtering with a Savitzky-Golay filter of 5 points width and a polynomial of order 3. The asterisks indicate the detected peak positions, which relate to the collagen overlap regions because the intensity is linearly proportional to the protein mass. The example shown here refers to rat tail collagen I at 1 mg/mL. Scale bar indicates 1 μm.

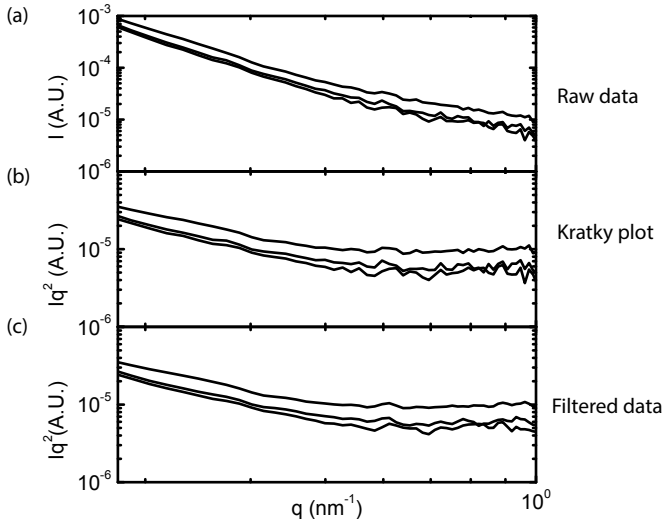

Supplementary Figure 4: Extraction of Bragg peaks from radially averaged scattering patterns for collagen. (a) Background-subtracted scattering intensity obtained from radial integration of the scattering pattern of a 5 mg/mL rat tail collagen network as a function of q. (b) The intensity is multiplied by q^2 to enhance the features corresponding to the collagen periodicity. This representation is known as a Kratky plot. (c) The Kratky plot is then filtered to remove noise by using a Savitky-Golay filter with a width of 5 points and a polynomial of order 3.

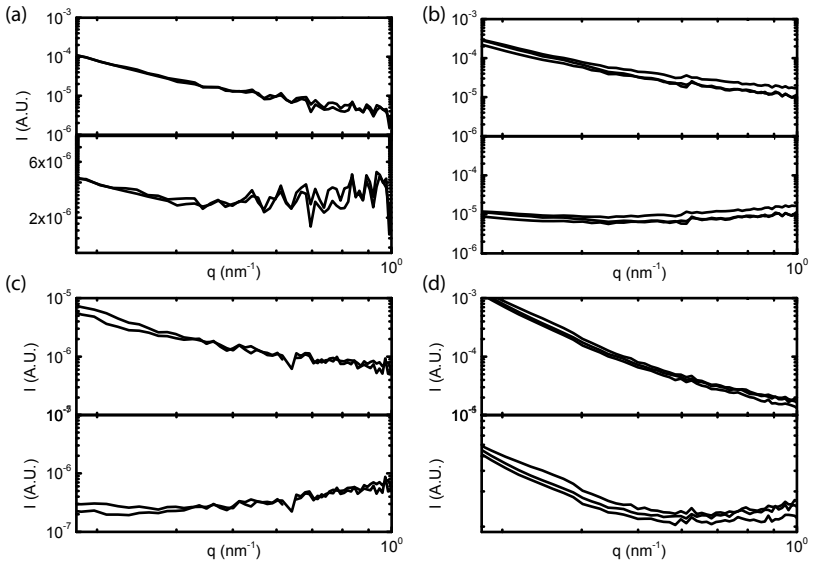

Supplementary Figure 5: Background-subtracted intensity profiles for the different collagens investigated in this work. Upper panels: scattering curve, lower panels: unfiltered Kratky plots. Data are shown for (a) 2 mg/mL type II collagen, (b) 4 mg/mL type II collagen (c) 6 mg/mL atelocollagen and (d) 8 mg/mL rat tail collagen. The Kratky plots are then filtered to finally obtain the data shown in Figure 5.

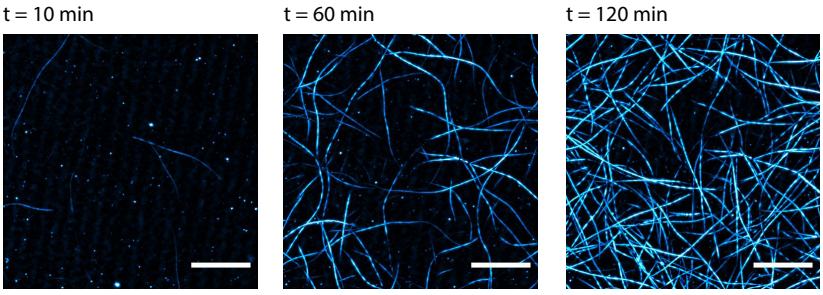

Supplementary Figure 6: Timelapse of a bovine dermal atelocollagen network at 1 mg/mL. Images show maximum intensity projections of a pure collagen network during polymerisation, over a depth of 20 μm. At early time-points, there is already evidence of fibrils, even if the elastic modulus is unmeasurably small.

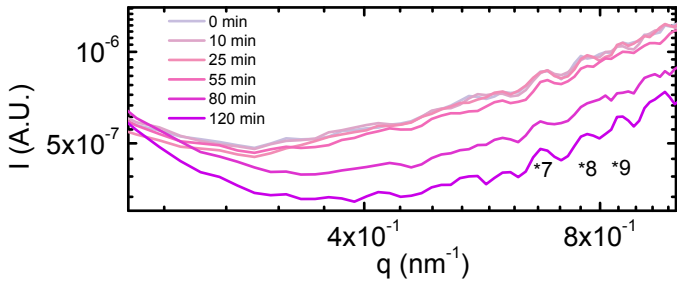

Supplementary Figure 7: Kratky plots measured during bovine dermal atelocollagen polymerisation at 6 mg/mL. Kratky plot as a function of q at different time points, as indicated in the legend. The numbers indicate the approximate position and the order of the scattering Bragg peaks expected for a periodicity of 67 nm.

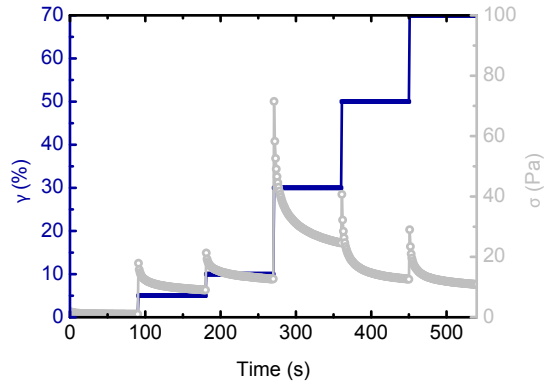

Supplementary Figure 8: Rheological response of a bovine dermal atelocollagen network at 6 mg/mL investigated with a stepwise strain protocol. The rheological response of the collagen network is probed by applying a stepwise strain ramp (blue curve, shown as a function of time), while monitoring the stress relaxation (pink curve). At strains of around 30%, the sample shows marked stress-relaxation, consistent with partial sample rupture. However, even at higher strains, the network still has a finite elastic modulus, which indicates that some fibres are still engaged.

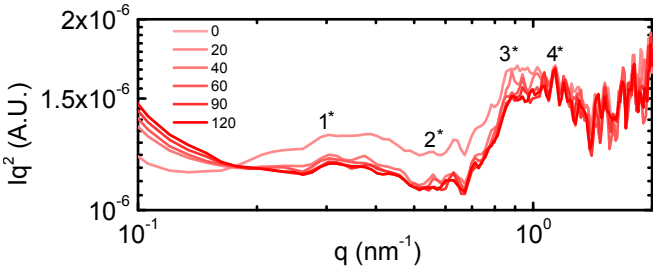

Supplementary Figure 9: Time-resolved Kratky plots of 6 mg/mL fibrin during polymerisation. The curves indicate the smoothened Kratky plots obtained at various time points (see legend). The numbers indicate the expected positions of the n-th peaks for the fibrin periodicity.

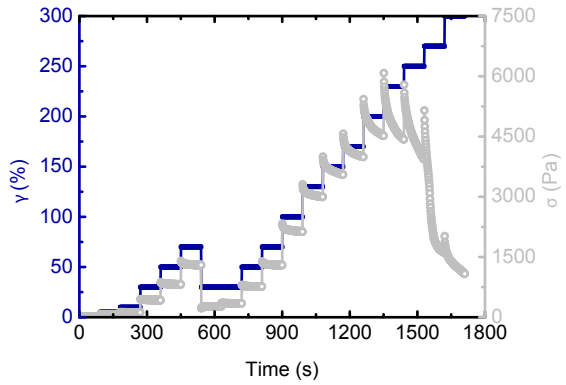

Supplementary Figure 10: Rheological response of a fibrin network at 6 mg/mL investigated with a stepwise strain protocol. The rheological response of the fibrin network is probed by applying a stepwise strain ramp (blue curve, shown as a function of time), while monitoring the stress relaxation (pink curve). The mechanical response of the network is rather reversible until strains of around 70%. While at low strains the network does not exhibit substantial stress relaxation, around 130% the sample begins to do so, consistent with partial sample rupture. However, the network still shows a finite elastic modulus up until strains of around 270%.

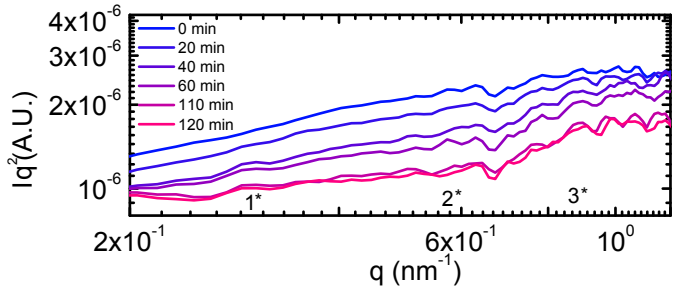

Supplementary Figure 11: Time-resolved Kratky plots for polymerising composite fibrin/collagen networks. Smoothened Kratky plots for various times after the start of polymerisation for a composite of 6 mg/mL fibrin and 4 mg/mL collagen. The numbers indicate expected peak positions and orders of the expected axial periodicity of 22.5 nm for fibrin.

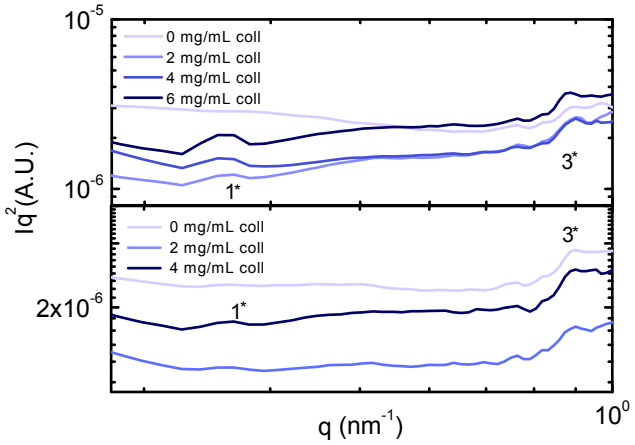

Supplementary Figure 12: Kratky plot for composite networks of fibrin and collagen as a function of network composition. Smoothened Kratky plots for a 6 mg/mL (upper panel) and 8 mg/mL (lower panel) fibrin network with various amounts of collagen added. The numbers indicate the expected peak positions and the corresponding orders calculated assuming an axial periodicity of 22.5 nm.

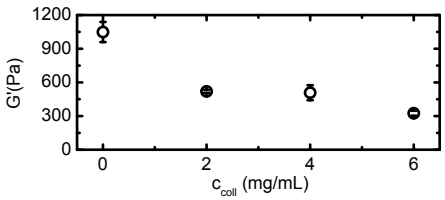

Supplementary Figure 13: Linear shear rheology of composite networks consisting of 6 mg/mL fibrin and increasing amounts of added collagen. The linear elastic modulus of the fibrin network (at a fixed concentration of 6 mg/mL) decreases with increasing amounts of collagen added. This counterintuitive effect could be due to the fibrin fibre bundling we observed with confocal imaging and/or to incomplete polymerisation due to steric hindrance.

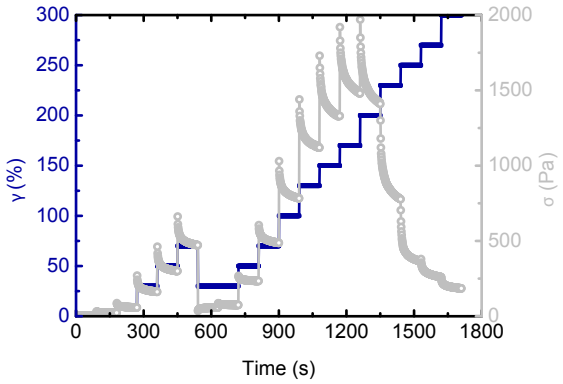

Supplementary Figure 14: Rheological response of a composite network of 6 mg/mL fibrin and 4 mg/mL collagen, investigated with a stepwise increase in strain. The rheological response of the composite network is probed by applying a stepwise strain ramp (blue curve, shown as a function of time), while monitoring the stress relaxation (pink curve). The mechanical response of the network is not reversible when strains of around 70% are applied, consistent with rupture of the collagen network. The network exhibits substantial stress relaxation already around strains of 70%, also consistent with partial sample rupture. The network appears to fail earlier than the pure fibrin network (Supplementary Figure S10), yielding at strains of around 200% compared to 250% for fibrin.

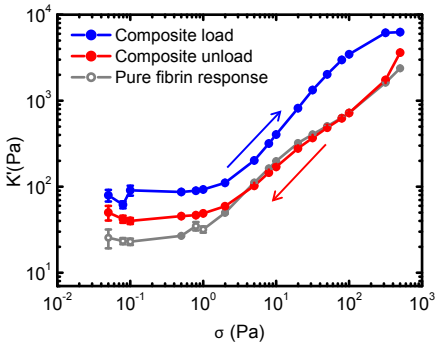

Supplementary Figure 15: Rheological response of a composite collagen-fibrin network. The response of a 1 mg/mL collagen and 1 mg/mL fibrin composite indicates that the composite responds initially as a collagen network (blue curve), but at high stresses the network breaks and the response (red curve) now follows that of pure fibrin (grey curve).

6

Role of pH-induced stickiness and chain length in hyaluronan hydrogel mechanics

Hyaluronan is an essential structural biopolymer in the extracellular matrix of connective tissues such as skin and cartilage. It is a linear polyelectrolyte with the ability to form viscoelastic hydrogels by chain entanglements and by physical crosslinks provided by hydrogen bonding interactions. Here, we investigate the roles of entanglements and transient crosslinks in hyaluronan hydrogel mechanics by performing shear rheology measurements on purified hyaluronan as a function of the chain molecular weight and the solution pH. We show that entanglements dominate the rheology at neutral pH, whereas physical crosslinking dominates when the pH is lowered to 2.5, a value close to the isoelectric point of hyaluronan. Time-temperature superposition measurements reveal that the flow activation energy of the hydrogels strongly increases when the pH is lowered to 2.5 and that it increases with hyaluronan molecular weight at low pH because longer chains carry more sticky groups. This behaviour is consistent with the sticky reptation model, where stress relaxation via polymer reptation is tuned by reversible binding and unbinding events. Further research on the mechanical properties of this peculiar hydrogel can help in designing materials for applications in regenerative medicine and drug delivery.

6.1 Introduction

Hyaluronan is an essential component of the extracellular matrix that forms the scaffold of mammalian tissues. It is ubiquitous in a wide range of tissues, from skin and cartilage to the brain [10, 167]. Hyaluronan is a linear polyelectrolyte composed of repeating disaccharide units that carry a large negative charge density at neutral pH due to the presence of carboxylate groups [31, 255, 256]. By virtue of its large molecular weight and charge, hyaluronan is able to form soft viscoelastic hydrogels [257]. In connective tissues such as skin and cartilage, hyaluronan hydrogels tune the transport properties and rigidity of the tissue and provide protection against compressive loads [127, 258, 259]. In joints, hyaluronan controls the viscosity of the synovial fluid and provides lubrication [260–262]. In addition to regulating physical properties of tissues, this polymer also regulates cell-matrix and cell-cell interactions and thereby contributes to physiological processes such as cell-cell communication [11], wound healing [263] and development [145]. Accordingly, abnormalities in the expression level or the molecular weight of hyaluronan contribute to various diseases, such as inflammation [264], multiple-sclerosis [26] and cancer [11, 129, 265, 266]. In the human body, hyaluronan normally has a large molecular weight of up to 10 MDa [10], corresponding to chain lengths of tens of micrometers. However, diseases such as cartilage degeneration are associated with a marked reduction of the hyaluronan molecular weight [260–262, 267].

Because of its central importance in human health and disease, there have been many studies of the material properties of isolated hyaluronic acid (reviewed in Ref. [167]). Like many other biopolymers, hyaluronic acid is responsive to external stimuli, such as temperature, solution pH, salt concentration and divalent counterions. Of these triggers, the solution pH has the most marked effect: in a narrow pH range centred around pH 2.5, hyaluronan solutions turn into soft solids that are stretchable [178, 268, 269]. This special gel state is commonly referred to as the putty state [179]. Recent vibrational spectroscopy measurements have revealed that the pH-induced gelation of hyaluronan is due to the formation of specific inter-chain hydrogen-bonds between the carboxyl and amide groups on its repeating disaccharide units [166] (see Figure 1a). So far, putty state formation has been observed for high molecular weight hyaluronan (> 1 million Daltons), but not for molecular weights below 100 kDa [179]. The molecular weight could influence putty state formation through various effects, e.g. by influencing the percolation threshold of hyaluronan chains, their ability to form topological entanglements, and the average number of hydrogen bond stickers per chain. So far, a quantitative experimental study that disentangles the effects of entanglements and transient crosslinking is lacking.

Here, we report rheological measurements on hyaluronan solutions, comparing high (>1.5 MDa) and low (100 kDa) molecular weight hyaluronan, at neutral pH

where the chains interact by excluded volume interactions only [152], and at pH 2.5 where the chains additionally interact by transient hydrogen-bond associations [166]. We show that switching the pH from 7.0 to 2.5 results in a marked increase in the viscoelastic shear moduli as well as in the stress relaxation time scale for both molecular weights. However, the viscoelastic state of the two polymers is different: while the high molecular weight (HMW) hyaluronan behaves as a soft solid with a plateau modulus of ~100 Pa, low molecular weight (LMW) hyaluronan solutions behave as viscoelastic fluids. Time-temperature superposition measurements reveal that the HMW hyaluronan exhibits a substantially higher activation energy for network flow in the putty state compared to its LMW counterpart. We interpret these findings in the context of the sticky reptation model [270, 271] previously applied to entangled synthetic polymers interacting by thermoreversible cross-linking [272, 273], which predicts that longer chains incur extra friction due to the increased number of stickers per chain.

6.2 Materials and methods

6.2.1 Sample preparation

We obtained low molecular weight (LMW, Mw 100 kDa) sodium hyaluronate from LifeCore biomedical, and high molecular weight (HMW, Mw 1.5-1.8 MDa) sodium hyaluronate from Sigma Aldrich. Both hyaluronan preparations were manufactured by microbial fermentation. Solutions of LMW hyaluronan at a concentration of 70 and 100 mg/mL and solutions of HMW hyaluronan between 5-20 mg/mL were prepared by dissolving weighed amounts of hyaluronic acid in an aqueous solution containing 0.15 M NaCl (Sigma Aldrich) and HCl (Sigma Aldrich) ranging from 0 to 206 mM. The solution pH was measured with a pH meter equipped with a microelectrode (Hanna Instruments, Germany). The polymer concentrations were chosen such that the concentration relative to the overlap concentration c* was comparable for both polymers. Based on the nominal molecular weights of the two hyaluronan preparations, we expect overlap concentrations of 11 mg/ml for LMW hyaluronan and 2 mg/ml for HMW hyaluronan [151]. At the hyaluronan concentrations used in this study, we operate in the entangled regime ($c > c_e$), given that the onset of entanglements for flexible polymers is expected at c_e~2-5 c* [186]. For the LMW hyaluronan we tested whether the molecular weight was large enough to generate entanglements by measuring the solution viscosity by applying a rotational shear with a strain rate increasing logarithmically from 0.01 to 100 s^{-1} using a stress-controlled MCR 501 rheometer (see below for details on the instrument).

6.2.2 Time-temperature superposition rheology experiments

Frequency spectra of the linear viscoelastic shear moduli as a function of temperature were measured with a stress-controlled MCR 501 rheometer (Anton Paar, Austria), using a plate-plate measuring geometry with a 40 mm diameter and 100 μm gap. The plate temperature was controlled by a Peltier plate connected to the lower plate and a hood controlling the temperature of the upper plate. Samples were loaded at room temperature (22°C) and equilibrated for 10 minutes before starting experiments. Small amplitude (0.5%) oscillatory shear tests were performed at 20 frequencies logarithmically spaced between 0.1 and 10 Hz, at different temperatures of 5, 10, 15, 22, 30 and 40°C. We started from 22°C and decreased the temperature to 15, 10, and 5°C, and then up to 30 and 40°C. The temperature was adjusted between each frequency sweep at the fastest rate allowed by the rheometer (around 2°C/s) and after reaching the desired temperature, we waited for equilibration by checking for saturation of the elastic and loss moduli, which always occurred within two minutes. We also verified that there was no hysteresis in the sample until a temperature of 65°C (data not shown), consistent with prior studies showing hyaluronan is stable up to 50°C and is hydrolysed above 90°C on a timescale of about 1 hour [274]. Time-temperature superposition analysis of the frequency (ω) spectra was performed by determining an appropriate shift factor $a_T(T)$ to overlap both the elastic modulus G'(ω) and the viscous shear modulus G"(ω) onto their respective reference curve measured at the reference temperature T_0 = 295 K (22°C). The temperature dependence of the shift factors was fitted to the Arrhenius equation to obtain the activation enthalpy E_a for stress relaxation:

$$log(a_T) = -\frac{E_a}{2.303R}\left(\frac{1}{T} - \frac{1}{T_0}\right) \tag{6.1}$$

where R is the universal gas constant. The activation energy in units of k_BT was obtained by dividing by Avogadro's number, where k_B is Boltzmann's constant and T is the absolute temperature. For each condition, experiments were performed on three independently prepared samples.

6.3 Results and discussion

6.3.1 pH and molecular weight dependence of hyaluronan hydrogel rheology

To study the impact of pH-dependent crosslinking on hyaluronan hydrogel rheology, we decided to compare solutions of hyaluronan polymers at two pH values (2.5 and 7.0) and at two molecular weights (100 kDa and 1.5 MDa) (see Figure 1a). The two pH values were chosen because they represent two distinct regimes of chain interactions. At pH 7.0, previous rheology and self-diffusion studies have indicated that hyaluronan chains interact by excluded volume interactions only, provided that

the ionic strength is sufficiently high such that electrostatic repulsions are screened [177, 275]. At pH 2.5, high molecular weight hyaluronan forms soft and stretchable gels that are referred to as putty [179, 276], due to hydrogen-bonding interactions [166]. The two molecular weights were chosen to be a factor 15 different, to probe the influence of the number of hydrogen-bond stickers per chain on the rheology. To ensure that we compared the two hyaluronan polymers in the same semidilute entangled concentration regime, we adjusted the polymer concentrations such that they were comparable, relative to the overlap concentration. The entangled regime sets in at the so-called entanglement concentration c_e, which is generally a factor 2-5 higher than the overlap concentration c* where the polymer coils first touch [151, 152]. We therefore chose to work at c = 10 mg/mL for HMW hyaluronan (c* = 2 mg/ml) and at c = 70 mg/mL for LMW hyaluronan (c* = 11 mg/ml). To verify that the LMW hyaluronan exceeded the critical molecular weight for entangling, we measured the steady-state viscosity of these solutions at pH 7.0 as a function of concentration. In the unentangled semidilute regime ($c^* < c < c_e$) the viscosity should scale approximately linearly in concentration, with an exponent of 1.3, while in the entangled regime ($c > c_e$), the viscosity should rise more steeply with concentration with a power-law exponent between 3 and 3.4 [186]. We observed approximate $c^{3.3}$-scaling for the viscosity between 40 and 100 mg/mL (Fig. S1 in the Supplementary Information), confirming that the solutions are in the entangled regime at 70 mg/mL.

We characterized the time-dependent rheology of the samples by performing frequency sweeps using strain oscillations with a small (0.5%) amplitude. As shown in Fig. 1b, the frequency spectra for HMW hyaluronan, independent of pH, show a transition from a solid response (G'>G") at high frequencies to a fluid response (G'<G") at low frequencies. The shape of the frequency spectrum is characteristic for entangled polymer solutions, which generally display a Maxwell-type behaviour with a rubber-like plateau that persists until a time t ~τ and a terminal ($\omega < 1/\tau$) regime where the moduli tend towards G"~ω^1 and G'~ω^2 scaling [33, 186], although here we do not yet see the full relaxation. The main effects of lowering the pH are a down-shift of the frequency for the crossover of G' and G", marking the transition from the rubber plateau to the terminal regime (from 5 rad/s at pH 7.0 to ~0.2 rad/s at pH 2.5), and an approximately 10-fold increase of the plateau modulus (from ~20 Pa at pH 7.0 to ~200 Pa at pH 2.5). These changes are in line with expectations for entangled polymers that experience transient crosslinking interactions as formulated by the sticky reptation model [270, 271]. Sticky interactions slow reptation by adding an additional friction on the chains that is proportional to the (effective) bond lifetime and quadratic in the number of stickers per chain. At the same time, transient crosslinks enhance the shear modulus G_0 in the rubbery plateau since, according to the theory of rubber elasticity [271], G' is the sum of the free energy of the strands in the material, G'= $\nu_x k_B T$, where ν_x= cN_A/M is the number density of elastically active network strands. The simplest assumption is that the number densities of

constraints provided by entanglements and crosslinks add up. Our data therefore suggest that reducing the pH from 7.0 to 2.5 creates a 10-fold increase in the density of elastic constraints.

As shown in Fig. 1c, changing the pH from 7.0 to 2.5 has a more drastic effect on the rheology of the LMW hyaluronan compared to the HMW variant. At pH 7.0, the LMW hyaluronan solutions behave as viscoelastic fluids, having a loss modulus G" larger than the elastic modulus G' over the probed frequency range (10-60 rad/s). Note that the frequency range is limited by the minimum detectable sample torque at small frequencies and by instrument inertia at high frequencies. The moduli scale with frequency as G"~ω^1 and G'~ω^2 as expected for entangled polymer solutions in the terminal (long-time) regime. Our data suggest that the entanglements must have a life time shorter than 100 ms (the highest frequency we can probe), since we do not observe any sign of a rubber plateau. Decreasing the pH to 2.5 causes a strong increase of the shear moduli (by nearly 100-fold for G' and nearly 10-fold for G"), such that they become comparable in magnitude. Strikingly, the storage and loss moduli now both show a frequency scaling consistent with the $\omega^{1/2}$ scaling expected in the Rouse regime [33, 277]. We verified that the viscosity of the solvent is negligible compared to the viscosity of the polymer, and the power-law trend is not affected [278] (see Supplementary Figure S2). The Rouse regime is the short-time ($t \ll \tau$) regime found at times much smaller than the entanglement time τ, where the polymers equilibrate their contour length [33]. If true, this observation therefore suggests that the sticky interactions that develop at pH 2.5 significantly delay relaxation of the polymer chains [279]. Since we do not observe any transition to another frequency regime, however, we cannot exclude that we instead observe the terminal relaxation regime, but with a much shallower frequency dependence than expected from the Maxwell model. Polydispersity is known to cause broadening of the frequency spectrum [186], especially in case of sticky polymers [273].

6.3.2 Temperature dependence of hyaluronan hydrogel rheology

Our findings suggest that a single time scale, which is modulated by pH-dependent chain interactions, may control the rheology of hyaluronan hydrogels. To test this idea, we performed measurements at different temperatures, since temperature is known to modulate the strength of hydrogen-bonds [166]. As shown in Figure 2, the shear moduli for both chain molecular weights and both solution pH values were indeed strongly dependent on temperature: increasing the temperature lowered the magnitude of the shear moduli. In case of the HMW hyaluronan, increasing the temperature in addition increased the characteristic frequency where the rubber plateau crosses over to the terminal regime, consistent with faster stress relaxation. By contrast, in case of the LMW hyaluronan, we observe a change in the frequency dependence from a monotonic $\omega^{1/2}$ dependence across the entire frequency range at lower temperatures (5-22°C) to one where the elastic modulus develops a

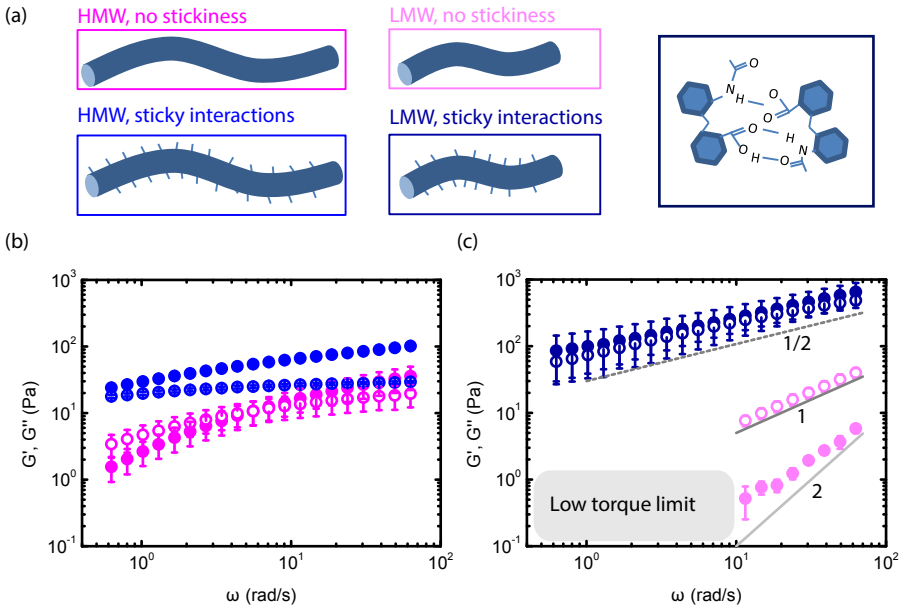

Figure 1: Linear viscoelastic shear moduli of hyaluronan hydrogels at room temperature (T=22°C). (a) Schematic of the experimental conditions: we compare high molecular weight (HMW, 1.5 MDa, left) and low molecular weight (LMW, 100 kDa, right) hyaluronan at pH 7.0 (pink) where the chains are entangled and pH 2.5 (blue). The chains transiently associate by hydrogen-bonding interactions between carboxyl and amide groups depicted in the molecular structure (schematic redrawn from Ref.[166]). (b) Frequency sweeps for HMW hyaluronan (c = 10 mg/mL) showing elastic (solid circles) and viscous (open circles) shear moduli at pH 7 (pink) and pH 2.5 (blue). (b) Corresponding frequency sweeps for LMW hyaluronan (c = 70 mg/mL). Note that the pH 7.0 data set is cut off below 10 rad/s, where the instrument torque was <50-fold above the noise. The measurements represent an average over three independent experiments, with error bars corresponding to the standard error of the mean. The grey lines represent power-laws with exponents 1 and 2 (terminal regime in Maxwell model) and 1/2 (high-frequency Rouse regime) indicated in the graph.

plateau at low frequency at higher temperatures (30-40°C). This observation lends support to our earlier hypothesis that the $\omega^{1/2}$ scaling regime may represent a high frequency Rouse regime, since the data suggest that the slowest Rouse relaxation time (crossover from Rouse to rubber plateau) shifts up with increasing temperature as expected in case of weaker crosslinking. We note that the hyaluronan hydrogels were thermoreversible: there was no hysteresis in the rheology when the temperature was shifted back up or back down (Fig. S3 in the Supplementary Information).

To test if a single interaction mechanism can account for the observed temperature dependence, we performed time-temperature superposition analysis using 22°C as the reference temperature. The idea behind this analysis is that the stress relaxation time according to the sticky reptation model is proportional to the (effective) bond

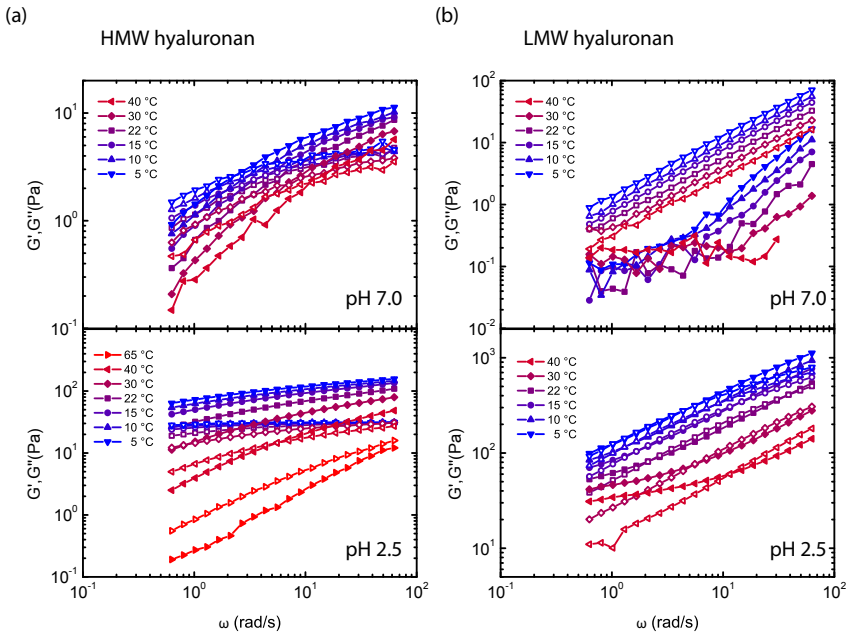

Figure 2: Temperature dependence of the frequency spectra of the shear moduli of hyaluronan solutions, comparing high versus low molecular weight chains and neutral versus acidic pH. (a) Upper panel: HMW hyaluronan (1.5 MDa, 10 mg/ml) at pH 7.0, lower panel: HMW hyaluronan at pH 2.5. (b) Upper panel: LMW hyaluronan (100 kDa, 70 mg/ml) at pH 7.0, lower panel: LMW hyaluronan at pH 2.5.

life time and should therefore be exponentially dependent on temperature [280]. As shown in Figure 3, we can indeed construct master curves for each data set by shifting the data along the frequency axis by a temperature-dependent shift factor a_T. The fact that the same horizontal shift factors apply for G' and G" indicates that hyaluronan gels are thermorheologically simple materials [281] for which a single temperature-dependent interaction scale sets the rheology.

Interestingly, the frequency spectra are rather different for the LMW and HMW samples, consistent with the trends observed in Figure 1. The HMW hyaluronan samples behave as Maxwell fluids with a rubbery plateau at the higher frequencies and a crossover to a terminal relaxation regime at lower frequencies (Fig 3a). At pH 7.0, we do not reach low enough frequencies to confirm whether the moduli at long times tend towards the G"~ω^1 and G'~ω^2 dependencies expected for a Maxwell fluid with a single relaxation time. At pH 2.5, we do reach lower normalized frequencies, but the low-frequency scaling of G' seems somewhat shallower than the G'~ω^2 scaling of the Maxwell model. A likely explanation is the size polydispersity of the hyaluronan [186].

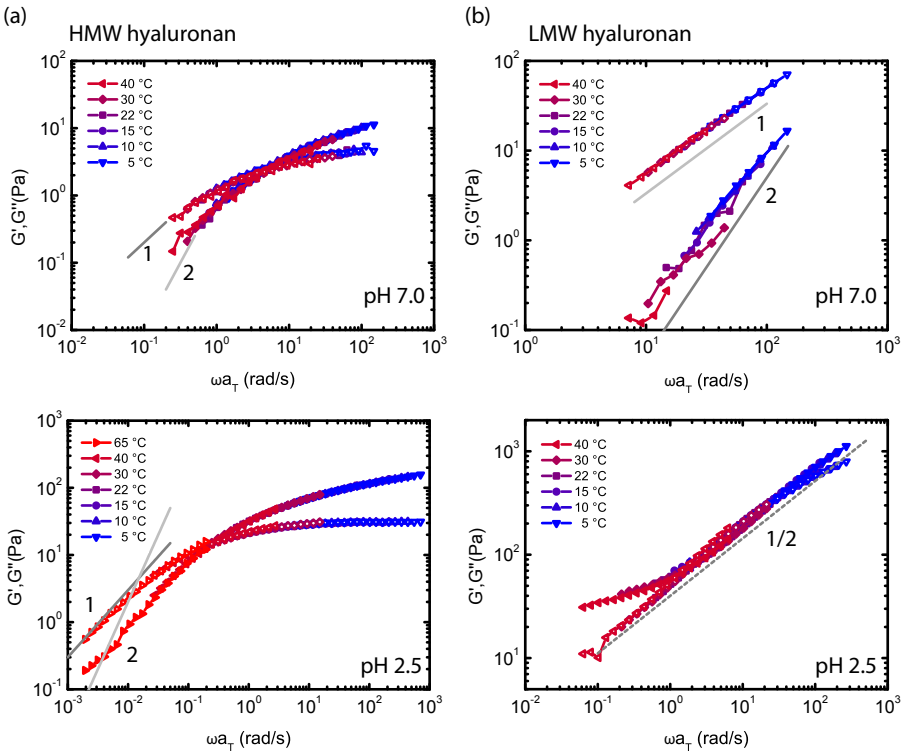

Figure 3: Temperature dependence of the frequency spectra of the shear moduli of hyaluronan solutions, comparing high versus low molecular weight chains and neutral versus acidic pH. (a) Upper panel: HMW hyaluronan (1.5 MDa, 10 mg/ml) at pH 7.0, lower panel: HMW hyaluronan at pH 2.5. (b) Upper panel: LMW hyaluronan (100 kDa, 70 mg/ml) at pH 7.0, lower panel: LMW hyaluronan at pH 2.5.

The LMW hyaluronan samples show a strikingly different behaviour. At pH 7.0, the moduli show the G"~ω^1 and G'~ω^2 power-law scaling with frequency typical of the terminal regime ($\omega < 1/\tau$) of a Maxwell fluid. We do not observe a crossover to a rubbery plateau even for normalized frequencies ωa_T up to 100 rad/s, indicating that entanglements are very short-lived. Compared to the 15-fold heavier HMW variant, the stress relaxation (reptation) time τ must therefore be at least 100 times faster. Qualitatively, the observed molecular weight dependence is consistent with predictions of the reptation model of Doi and Edwards [33], which predicts that the reptation time τ should increase as M^3, and with a wealth of empirical evidence (reviewed in [Ref.[186]) suggesting $\tau \sim M^{3.4}$. In the pH 2.5 condition, both the loss and the storage modulus for LMW hyaluronan instead scale approximately as $\omega^{1/2}$over a large frequency range (ωa_T= 1-100 rad/s). For low normalized frequencies (ωa_T< 1 rad/s), G' flattens, which suggests that we observe a transition from the high-frequency ($\omega \gg 1/\tau$) Rouse regime of entangled polymers to the rubbery plateau [33]. Apparently, turning on chain associations by lowering the pH from 7.0 to 2.5 strongly enhances the Rouse time for LMW

hyaluronan, indicating strongly enhanced friction on the chains. We see a similar trend at higher LMW concentrations, where we also see the onset of a rubber plateau at low frequencies (Supplementary Figure S4).

To retrieve the flow activation energy of the hyaluronan hydrogels [282], we constructed Arrhenius plots of the shift factors a_T as a function of the inverse temperature relative to the reference temperature T_0=22°C for each data set. As shown in Figure 4a, we obtained straight lines for all data sets, indicating that the relaxation time is controlled by the thermally activated dissociation of bonds between chains. As shown in Fig. 4b, the activation energy at pH 2.5 (taken from the slope of the Arrhenius plots) is higher than at pH 7.0 for both HMW and LMW hyaluronan, consistent with the expectation from the sticky reptation model that pH-induced hydrogen-bonding enhances the friction on the chains. Interestingly, the activation energy is strongly molecular weight dependent for the putty state at pH 2.5, whereas it shows little molecular weight dependence for the entangled state at pH 7.0.

In the entangled state at pH 7.0, the activation energy is around 12 k_BT, consistent with a prior report for high molecular weight hyaluronan[152, 283]. We note that this earlier study was carried out at 50 mg/mL, a much larger concentration than studied here (10 mg/mL), suggesting little effect of concentration on the activation energy. We indeed find little dependence of the activation energy on hyaluronan concentration at pH 7.0, both for HMW hyaluronan between 5 and 20 mg/mL and for LMW hyaluronan between 70 and 100 mg/mL (see Supplementary Figure S5a).

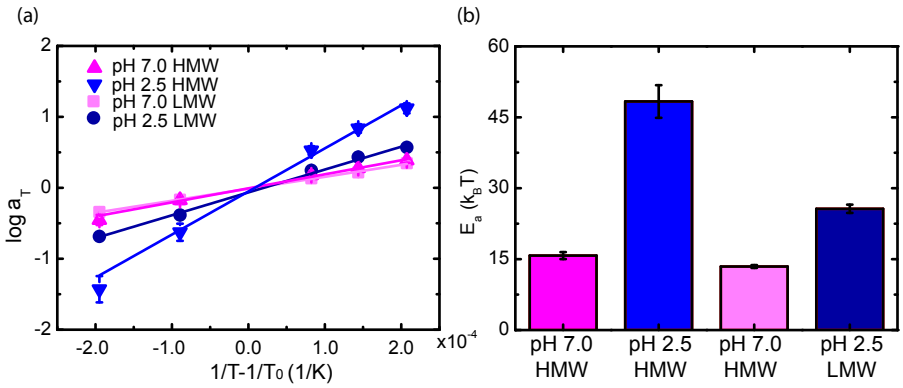

Figure 4: Flow activation energy of hyaluronan solutions, comparing high and low molecular weight chains and neutral and acidic pH.(a) Arrhenius plot showing the shift factors used for constructing the time-temperature superposition data in Fig. 3 as a function of the inverse of the temperature relative to the reference temperature T_0 = 22°C. LMW data were measured at 70 mg/mL, while HMW data were measured at 10 mg/mL. Lines show linear fits whose slopes represent the flow activation energy. (b) Activation energies retrieved from the Arrhenius fits, expressed in units of thermal energy k_BT.

For the putty state at pH 2.5, the activation energy is around 50 k_BT for HMW hyaluronan and 30 k_BT for LMW hyaluronan. We also measured activation energies at other hyaluronan concentrations, and observed that the activation energy was independent of concentration (see Supplementary Figure S5b). The enhanced flow activation energy at pH 2.5 compared to pH 7.0 is consistent with the additional presence of transient associations between the chains. In particular, the energy scale is consistent with typical association energies of hydrogen bonds, which span from a few to tens of k_BT [284]. The increase of the flow activation energy with increasing molecular weight is also consistent with the sticky reptation model, which predicts a higher friction for higher molecular weight chains because these carry more stickers [285]. The stickers are formed by the amide and carboxyl residues on the repeating disaccharide units of hyaluronan [166] (Figure 1a). The HMW hyaluronan chains contain about 3750 disaccharides, while the LMW hyaluronan chains contain only 250 disaccharides (considering that the molecular weight of a disaccharide is 400 Da [286]). The average number of stickers per chain is therefore ~15 times higher for the HMW hyaluronan compared to the LMW hyaluronan.

6.3.3 Universal master-curve for hyaluronan hydrogel rheology

Until now, we rescaled data sets for different molecular weights and pH values onto separate master curves. To test if a single constitutive law describes all data, independent of molecular weight, pH and temperature, we finally rescaled all curves onto a single master curve. This idea was inspired by recent studies showing that time-temperature superposition can be extended to other environmental parameters that control the relaxation times of noncovalent gels such as ionic strength [287, 288]. To rescale the curves, we now needed not only a horizontal shift factor a_T for the frequency axis, but also a vertical shift factor b_T to collapse G' and G". This finding indicates that variations in pH, molecular weight and temperature not only change the stress relaxation time scale of the system, but also the density of entanglements and/or crosslinks. With the same shift factors a_T and b_T (Supplementary Figure S6), we could collapse both G' and G" for all conditions onto a single master curve (Fig. 5) that exhibits three distinct frequency regimes that are characteristic for entangled polymer solutions:

1. Terminal relaxation ($\omega < 1/\tau$): low-frequency regime corresponding to time scales t>τ longer than the reptation time τ.

2. Rubber plateau ($1/\tau < \omega < 1/\tau_{Rouse}$): elastic regime where chain entanglements act as transient crosslinks.

3. Rouse regime ($\omega > 1/\tau_{Rouse}$): high-frequency regime corresponding to time scales t < τ_{Rouse} that are short compared to the Rouse time τ_{Rouse}, where stress is relaxed by chain contour length fluctuations.

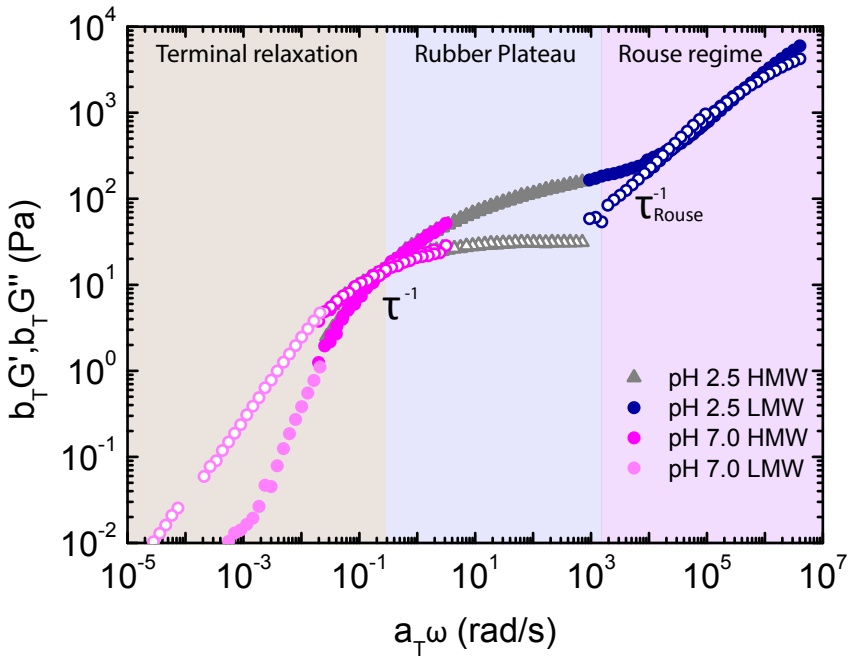

Figure 5: Universal mastercurve for hyaluronan hydrogel rheology obtained by rescaling frequency sweeps both along the frequency and the modulus axis, using shift factors a_T and b_T, respectively. Data include frequency sweeps gathered at temperatures between 5 and 40°C (not color-coded) and at hyaluronan concentrations of 70 mg/ml (LMW) and 10 mg/ml (HMW). The data are shifted onto a reference set measured for HMW hyaluronan at pH 2.5 and at 22°C (grey triangles). We first shifted the horizontal axis, then the vertical axis to obtain overlap. The colors correspond to either LMW or HMW and either pH 2.5 or pH 7.0, as specified in the legend.

The apparent collapse onto a single mastercurve strongly suggests that the physical interactions that control the rheology are the same, regardless of molecular weight, temperature and pH. However, we caution that the frequency range accessible with macroscopic rheometry is limited, so none of the experimental conditions individually spans all three regimes. It would therefore be interesting to test the validity of the universal scaling by augmenting the rheological measurements with optical microrheology measurements, which can access much larger frequencies because the probe inertia is smaller [152], and with creep tests, which can access lower frequencies [171].

6.4 Conclusions

In the present study, we investigated the formation of a pH-dependent elastic state of hyaluronan as a function of its molecular weight. We compared hyaluronan of two

different chain lengths (HMW of 1.5 MDa and LMW of 100 kDa) at concentrations that were chosen to be comparable when normalized by the overlap concentration c*. The rationale for this choice was that we could compare the two hyaluronan variants in the same concentration regime, namely the semidilute entangled regime where the chains are loosely entangled. At neutral pH, both hyaluronan polymers formed entangled solutions with a Maxwell-type response where the stress relaxation time strongly dependent on molecular weight. In the frequency range accessible by macroscopic rheometry (0.1-100 rad/s), the frequency spectrum for the LMW variant covered only the terminal regime ($\omega < 1/\tau$) whereas the frequency spectrum for the HMW variant covered both the terminal regime ($\omega < 1/\tau$) and the rubber plateau ($\omega > 1/\tau$). The stress relaxation (reptation) time τ at neutral pH was at least 100-fold faster for the LMW variant compared to the HMW variant, consistent with the strong (M^3) molecular weight dependence predicted by the reptation model [33]. By performing measurements over an extended temperature range (5-40°C), we could show that the stress relaxation time displayed an Arrhenius-type dependence on temperature with a flow activation energy of 12 k_BT at pH 7, where chain friction is only affected by excluded volume interactions and viscous drag. By lowering the pH to 2.5, we could switch on temperature-dependent interactions mediated by hydrogen-bonding. Stickiness caused a strong slow-down of the stress relaxation time and a strongly enhanced flow activation energy (30 k_BT for LMW hyaluronan and 50 k_BT for HMW hyaluronan), consistent with the sticky reptation model. Our findings show that hyaluronan forms thermoreversible gels whose macroscopic properties can be tuned by the molecular weight of the polymer and by environmental conditions such as pH and temperature.

In the context of human physiology, understanding how the mechanical properties of extracellular matrix polymers are affected by pH is relevant since many diseases, like cancer and inflammation, are associated with acidosis [289], a decrease of the extracellular pH. Even though the average pH values in this situation are reported to be of order 5.8 [290], potentially lower pH values might be reached locally and transiently, and in turn affect the dynamics of hyaluronan. In the context of materials science, it has become clear in recent years that noncovalently bonded hydrogels have many desirable properties such as stimuli-responsiveness, toughness, and an inherent capacity for self-healing and recovery after mechanical damage. Such materials have possible applications for shape memory, self-healing and adhesive materials [291]. Hyaluronan is biocompatible and already used for a broad range of biomedical applications, from drug delivery to tissue regeneration [167, 292–294]. It would therefore be interesting in the future to extend our study of the linear rheological properties of hyaluronan hydrogels to the non-linear regime of large deformations and to complex time-dependent effects such as plasticity and self-healing [295, 296].

Acknowledgments

We thank Fred MacKintosh (Rice University, Texas) for useful discussions on flexible polymer rheology and time-temperature superposition for the hyaluronan data, and Huib Bakker and Giulia Giubertoni (AMOLF) for useful discussions on the molecular mechanisms behind the pH-dependent interactions of hyaluronan.

6.5 Supplementary Figures

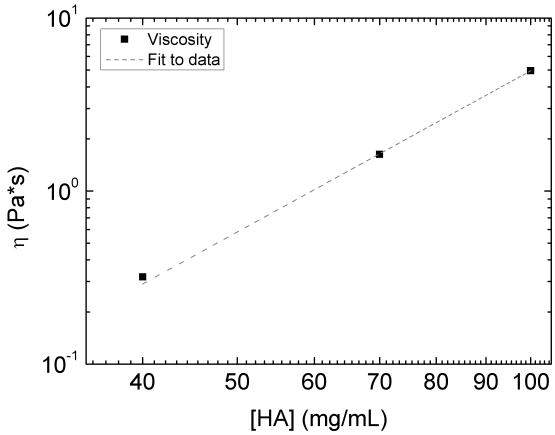

Supplementary Figure 1: Dependence of the steady-shear viscosity at low shear rates for LMW hyaluronan solutions on hyaluronan concentration.. Shear viscosities were determined for a strain rate of 0.1 s^{-1}. The viscosity scales with concentration according to a power law with best-fit exponent 3.3±0.4 (grey dashed line), consistent with the prediction of the reptation model for semidilute entangled solutions of flexible polymers. Data were obtained at 22°C, and indicate one repeat.

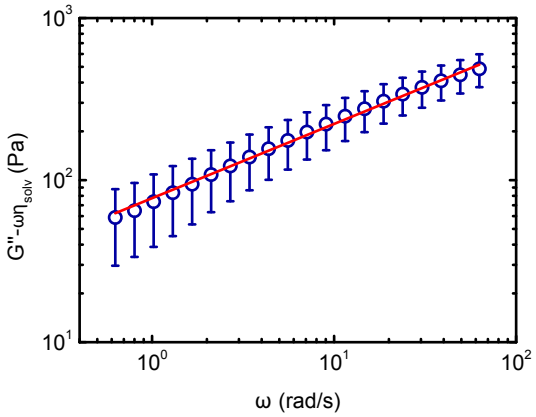

Supplementary Figure 2: Solvent contribution to the loss modulus is negligible for 70 mg/mL LMW solutions at pH 2.5 and 22°C. We verified that the solvent viscosity gives a negligible contribution to the power-law scaling of G"with frequency for the LMW solution at pH 2.5. The red line indicates a fit of the data to a power law, which yields an exponent of 0.46±0.01.

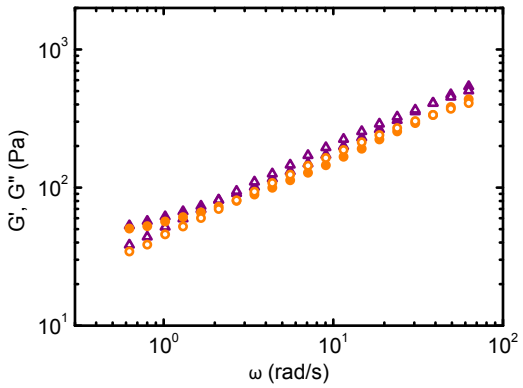

Supplementary Figure 3: Thermoreversibility of the rheology of hyaluronan solutions. Two measurements on LMW hyaluronan at pH 2.5, carried out at a temperature of 22°C before (purple) and after (orange) a complete temperature cycle where the temperature was changed stepwise from 22 down to 5°C and then up to 40°C. Both the elastic modulus G' (full circles) and the viscous modulus G" (empty circles) return back to the original moduli.

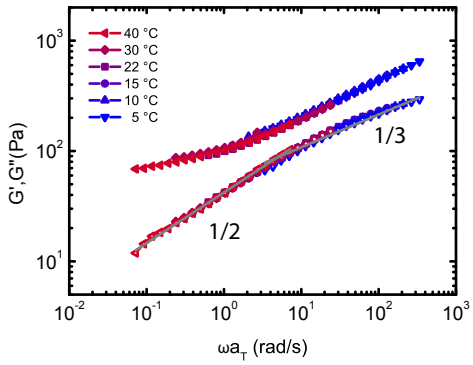

Supplementary Figure 4: Rheology of a 100 mg/mL hyaluronan solution at pH 2.5. For the 100 mg/ml sample at pH 2.5 we observe $\omega^{1/2}$ scaling of the shear moduli transitioning towards $\omega^{1/3}$ at high frequency, and a crossover to a rubber plateau at low frequency.

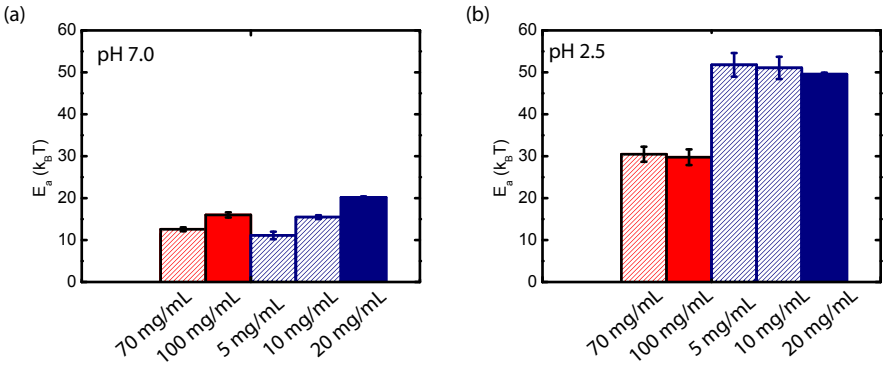

Supplementary Figure 5: Concentration dependence of the flow activation energies for high and low molecular weight hyaluronan solutions at neutral and acidic pH. (a) Activation energy for neutral solutions of LMW (red) and HMW (blue) hyaluronan. (b) Corresponding data for acidic solutions. The concentration was varied from 70 to 100 mg/ml in case of LMW hyaluronan and from 5 to 20 mg/mL in case of HMW hyaluronan (see labels).

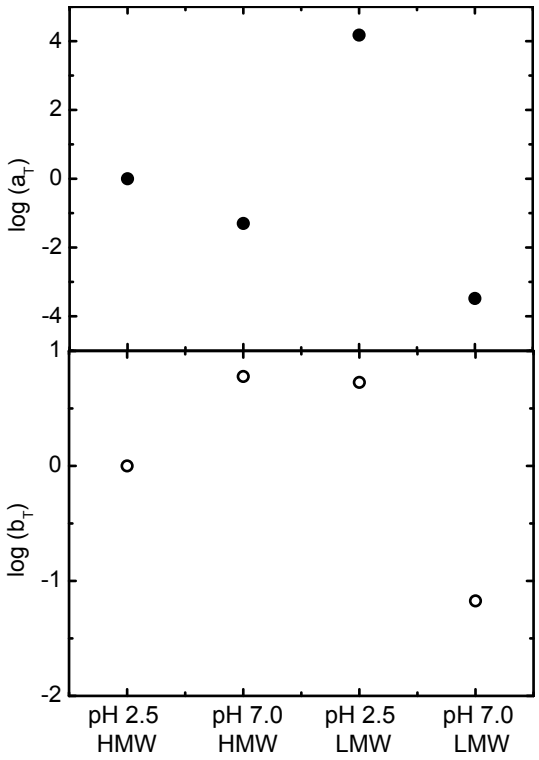

Supplementary Figure 6: Shift factors used to collapse the frequency spectra of hyaluronan solutions of low and high molecular weight for two pH values (2.5 and 7.0) and over an extended temperature range (5-22°C) onto a single (b_TG'($a_T\omega$) and b_TG"($a_T\omega$) mastercurve. Upper panel: horizontal shift factors to overlap the frequency axis. Lower panel: vertical shift factors to overlap the G'and G"axis. HMW hyaluronan at pH 2.5 and a temperature of 22°C was used as the reference.

7

Summary and conclusions

Our bodies are mechanically supported by tissues, which provide us with the ability to stand and move. Each tissue has different properties tailored to its function: bones are rather hard and undeformable, whereas skin can be easily stretched; tendons can withstand large loads, while fat tissue wraps us in a soft shell that comforts us during the winter months. Strikingly, all these different tissues are composed of the same set of building blocks: tiny filaments a thousand times thinner than a hair.

Cells produce the building blocks for these filaments and expel them into the extracellular space, where they spontaneously assemble, first into filaments and then into large web-like structures that are known as the extracellular matrix. Besides providing structural support to our bodies, the extracellular matrix also provides an environment where cells can thrive. In facts, cells actively probe the structure and mechanical properties of the matrix and use this information to make decisions whether or not to differentiate, migrate, grow, or die. It is for instance known that undifferentiated stem cells grown in an environment that is as soft as fat tissue will turn into fat cells, whereas cells grown in a stiff bone-like environment will turn into osteoblasts. It is therefore essential that the mechanical properties of the extracellular matrix are carefully regulated, such that it can simultaneously ensure the correct tissue deformability and mechanical integrity and the right mechanical cues to cells.

The strategy by which the human body can achieve such a wide range of mechanical properties is by juxtaposing different molecular building blocks and by arranging these building blocks in structurally different ways. Bones are rather ordered structures that are rigid due to a combination of collagen fibres and rigid minerals. Skin and cartilage are instead supported by isotropic networks of collagen fibres resembling three-dimensional spider webs, which can support loads from

multiple directions. Instead, tendons are highly aligned bundles of collagen fibrils, like electricity cables, that can support high tensile loads along one direction.

The goal of this thesis was to understand how a hybrid molecular composition together with the topology of the extracellular matrix contribute to the mechanical properties of mammalian tissues. To this end, we reconstituted biomimetic systems composed of either one or two purified extracellular matrix components, focusing on collagen, fibrin and hyaluronic acid. Collagen is the main constituent of connective tissues, forming a fibrillar scaffold that confers mechanical support to cells; hyaluronic acid is a highly charged, flexible molecule that maintains tissues hydration, and fibrin forms a provisionary fibrillar matrix that mediates the repair of wounded tissues. We chose these systems because of their physiological relevance and the importance of their interactions in many tissues and during wound healing.

We investigated the mechanical behavior of the biomimetic matrix systems by deforming them by shear rheology while at the same time probing the structural changes by either directly imaging the fibrils or performing small-angle-x-ray scattering (SAXS). In this way we could reveal how the network architecture and composition govern the elastic response and ultimate strength. In addition to the mechanical response, we also studied the permeability of the networks by probing the mobility of small particles seeded into the networks. The network permeability is an important parameter for tissues because it controls nutrient and growth factor transport to cells. Our reductionist experimental approach allowed us to investigate a simpler environment than a whole tissue, allowing us to quantitatively interpret our findings in the context of theoretical models for polymers. These models are often used for more familiar, non-living materials, ranging from plastic to textiles, paper, and food, but here we showed that they also apply to the biopolymers that shape tissues.

We first focused on the main component of the extracellular matrix, collagen, in chapter 2. Recent studies revealed that the network connectivity, i.e. the number of fibers meeting at a junction, is the main parameter that determines the elastic response of collagen networks. Collagen networks are comprised of branches, which have a connectivity of 3, and fibre crossovers, which have a connectivity of 4. It is possible to tune the average connectivity of reconstituted collagen networks between 3 and 4, by using different types of collagen and varying the self-assembly conditions (salts and temperature). Here we compared the mechanical strength of a wide spectrum of reconstituted collagen networks and thereby discovered that the maximum shear strain (deformation) that the networks can sustain without breaking is also determined by their connectivity. Surprisingly, this means that collagen network breakage is governed by the same set of rules governing the fracture of simpler fibrous materials. However, to fully describe our measurements, we also had to consider the ability of collagen fibres to undergo irreversible changes in length

by monomer sliding at large deformations (plasticity) in case the fibres are only weakly crosslinked internally. We furthermore found that networks connected by branches can stretch further than networks connected by 4-fold crosslinks, because the branches can accommodate extra strain by opening up. Our findings reveal that simple mathematical descriptions of fibrous networks can be very insightful in describing the bulk behaviour of collagen networks, but if we want a more accurate prediction of the strength of these polymers we need to resort to more detailed descriptions. We furthermore learn from collagenous tissues that a disordered network architecture with low connectivity and additional plastic deformations mechanisms are powerful design principles for engineering stretchable materials.

We then explored in chapter 3 how tissues achieve another essential mechanical feature, namely strain-stiffening. Strain-stiffening is the process where tissues increase their stiffness when they are pulled. This feature is of crucial importance for the integrity of tissues, as you can experience for yourself when you pull on your ear lobe. Strain-stiffening is rather well-understood in single-component collagen systems, where it has been explained in terms of a transition from a floppy state at small strain to a rigid state at high strain, in analogy to the response of the net around your oranges when you stretch it. However, it is not clear how tissue stiffening is impacted by the combination of collagen fibres with other extracellular matrix components. We investigated networks made of collagen fibres and hyaluronan, mimicking the composite matrix present in tissues such as cartilage, skin, and the intervertebral disks. We observed that adding hyaluronan to a collagen network delays the onset strain where strain-stiffening sets in, and increases the elastic modulus to a value that is more than the sum of the parts. By comparing our experiments with simulations of fibrous networks, we could show that hyaluronan modulates collagen network mechanics by two mechanisms, namely by providing an elastic background that limits collagen fibre bending and by generating a compressive stress that delays collagen network stiffening. Despite the simplified nature of our in vitro and in silico model systems, we believe that our findings provide insight in the mechanics of tissues since there is indeed evidence of large hyaluronan-dependent internal stress. Moreover, our findings provide inspiration for engineering bio-based or synthetic materials for tissue repair or replacement and for developing fibrous composites with a well-controlled non-linear mechanical response.

After investigating the mechanical properties of composite collagen-hyaluronan matrices, we explored in chapter 4 how diffusion occurs within such networks. We inserted small particles with sizes similar to those of natural macromolecules such as virus particles that cause infections, and nanoparticles for drug delivery during cancer therapies. We followed the spontaneous, thermally driven displacements of the particles in the reconstituted extracellular matrix gels to obtain information about the local viscosity and pore structure. By using different particle sizes, we first

verified that dilute solutions of hyaluronan polymers hinder particle transport by increasing the viscosity, while hyaluronan crosslinking, which for instance occurs during inflammation, causes hyaluronan networks to act as a size exclusion filter. In crosslinked gels, particle diffusion is dictated by the ratio between the pore size of the network and the size of the particles. In fibrillar collagen networks, the particles could move almost unhindered through the solvent in the large pores between fibers. However, when collagen and hyaluronan were combined in a composite network, the particles suddenly exhibited caged dynamics: they were confined to a tight space, which they could only escape from after a certain waiting time. We speculate that the enhanced hindrance of particle motion might be due to interactions between collagen and hyaluronan, which potentially cause pockets of increased hyaluronan density.

In chapter 5, we moved on to the mechanical properties of another composite system that is also important in the human body, made of collagen and fibrin. This composite is essential during wound healing, where a provisionary matrix of fibrin is progressively replaced by collagen. The initial fibrin matrix needs to withstand the large shear strain imposed by blood flow so it can prevent bleeding, whereas the collagen matrix that is formed after wound repair should form a permanent matrix that can withstand large stresses. Therefore, fibrin and collagen have contrasting mechanical properties, even though they both form random fibrillar networks and the fibers have a similar shape and diameter. Molecularly, the origin of the contrasting mechanics is thought to be that fibrin is an elastomeric protein that can stretch by several times its length, whereas collagen is a rigid protein that breaks at small deformations. To test this model and to measure the effective response when the two proteins are combined in composite networks, we performed X-ray scattering measurements on networks under shear. Here we used the fact that when the networks are illuminated with an X-ray beam, they scatter light in a particular angular pattern that reflects the fibre orientations and the internal molecular structure of the fibres. By combining X-ray scattering with rheology we could thus take molecular snapshots as a function of strain. We found that collagen and fibrin fibres both align under shear. We furthermore observed that the aligned fibres increase their packing density in case of collagen, whereas they do not notably change in case of fibrin. Finally, we show that composite networks of collagen and fibrin are softer and weaker than the two networks by themselves because collagen causes fibrin fibre bundling, resulting in inhomogeneous networks.

Finally, in chapter 6 we investigated a peculiar physical transition of hyaluronan that takes place when the solution is acidified. It is thought that acidification introduces sticky interactions between the hyaluronan polymer chains through enhanced hydrogen-bonding. Using rheology, we could show that switching the pH from neutral (pH 7) to acidic (pH 2.5) indeed switches the system from a viscous fluid to an elastic gel. We could modulate the adhesion strength by changing the

temperature, which allowed us to measure the flow activation energy that depends on the ability of the polymer chains to slide past one another. We found that the flow activation energy was higher at low pH than at high pH, consistent with the idea that sticky interactions create enhanced friction between polymer chains. We also found that the activation energy at low pH was higher for longer hyaluronan polymers than for shorter ones, probably because longer chains carry more sticky groups. In spite of the variety of hyaluronan molecular weights, solution pH values and temperatures, the flow properties of the hyaluronan hydrogels appear to be governed by the same molecular process, namely crosslink dissociation. The acidic condition studied here may potentially appear transiently in diseased tissues, for instance during cancer, where cells acidity the extracellular environment. Moreover, it will be interesting to find out if pH-induced gelation can be used to engineer hydrogels based on hyaluronan or other polysaccharides, like alginate, for tissue repair.

The findings of this thesis are useful for elucidating the physical mechanisms that contribute to tissue dysfunctions such as vascular rupture in aneurysms or skin fragility in patients suffering from genetic disorders such as Ehlers-Danlos. Our findings are also useful for aiding the rational design of materials that can be used for tissue replacement or drug delivery. As the systems we studied here can be generally well described by minimal computational models, we can also extend some of the physical principles highlighted here to describe fibrous networks and hydrogels outside the biological realm. Strikingly, the interplay of just two polymeric components with contrasting mechanical properties already results in composite materials with a quite rich range of behaviours. It would be interesting, in the future, to increase the molecular and structural complexity of the experimental model systems by adding additional extracellular matrix components. Potential candidates would be proteoglycans, as they are widely present in the brain extracellular matrix, or elastin, as it is an elastomeric protein conferring stretchability to tissues. It would furthermore be interesting to include cells, which are known to strongly influence the mechanical behaviour of tissues by exerting pulling forces and modifying the chemical composition through matrix synthesis and degradation. Finally, it would be insightful to connect the findings obtained in simplified systems to the mechanics of real tissues where the amounts of collagen and hyaluronan are modulated, for instance by inducing overexpression of enzymes such as metalloproteinases, hyaluron synthase, or hyaluronidase.

List of publications

Publications covered in this thesis

1. **Burla, F.***, Mulla, Y.*, Vos, B., Aufderhorst-Roberts, A., Koenderink, G.H. *From mechanical resilience to active material properties in biopolymer networks.* Nat. Rev. Phys. 1, 249-263, 2019 (chapter 1).

2. **Burla, F.***, Dussi, S.*, Martinez-Torres, C., Tauber, G., van der Gucht, J., Koenderink, G.H., *Connectivity and plasticity determine collagen network fracture.* PNAS 117 (15), 2020 (chapter 2).

3. **Burla, F.***, Tauber, J.*, Dussi, S., van der Gucht, J., Koenderink, G.H. *Stress management in composite biopolymer networks.* Nat. Phys. 15 (6), 2019 (chapter 3).

4. **Burla, F.**, Sentjabrskaja, T., Pletikapic, G., van Beugen, J., Koenderink, G.H. *Particle diffusion in extracellular hydrogels.* Soft Matter 16, 1366-1376, 2020 (chapter 4).

Other publications

1. Staneva, R.*, **Burla, F.***, Koenderink, G.H., Descroix, S., Vignjevic, D.M., Attieh, Y., Verhulsel, M. *A new biomimetic assay reveals the temporal role of matrix stiffening in cancer cell invasion.* Molecular biology of the cell, 29 (25), 2979-2988, 2018.

2. King, G.A., **Burla, F.**, Peterman, E.J.G.*,Wuite, G.J.L.* *Supercoiling DNA optically.* PNAS, 116 (52), 26534-26539, 2019.

3. Fanalista, F.*, Birnie, A.*, Maan, R., **Burla, F.**, Charles, K., Pawlik, G., Deshpande, S., Koenderink, G.H., Dogterom, M., Dekker, C. *Shape and Size Control of Artificial Cells for Bottom-Up Biology.* ACS Nano, 13(5) 5439-5450 2019.

4. Giubertoni, G., **Burla, F.**, Martinez-Torres, C., Dutta, B., Pletikapic, G., Pelan, E., Rezus, Y.L.A., Koenderink, G.H., Bakker, H.J. *Molecular Origin of the Elastic State of Aqueous Hyaluronic Acid.* Journal of Physical Chemistry B, 123 (14), 3043-3049 2019.

5. Visscher, D.O., Gleadall, A., Buskermolen, J.K., **Burla, F.**, Segal, J., Koenderink, G.H., Helder, M.N., van Zuijlen, P.P.M. *Design and fabrication of a hybrid alginate hydrogel/poly (η-caprolactone) mold for auricular cartilage reconstruction.* Journal of Biomedical Materials Research Part B, 107 (5), 2019.

6. Martinez-Torres, C., **Burla, F.**, Alkemade, C., Koenderink, G.H. *Revealing the Assembly of Filamentous Proteins with Scanning Transmission Electron Microscopy.* Plos One 14(12): e0226277, 2019.

7. Vos, B.E., Martinez-Torres, C., **Burla, F.**, Weisel, J.W., Koenderink, G.H. *Revealing the molecular origins of fibrin's elastomeric properties by in situ X-ray scattering.* Acta Biomaterialia 104, 39-52, 2020.

8. van Dam, E., Giubertoni, G., **Burla, F.**, Koenderink, G.H., Bakker, H.J. *Hyaluronan Biopolymers Release Water Upon pH-induced Gelation.* Phys. Chem. Chem. Phys., accepted manuscript, 2020.

About the author

Federica Burla was born in Como, Italy, in 1990. She got her Bachelor degree in Physics at the University of Milan and, after spending two months in China, continued her education at the University of Milan, with a Master in Soft Matter and Statistical Physics. During her Master, Federica carried out a ten-months research internship in the group of Physics of Living Systems of Prof. G.J.L. Wuite and Prof. E.J.G. Peterman at the VU, Amsterdam, where she conducted research on structural and mechanical properties of supercoiled DNA, by means of optical tweezers and fluorescence microscopy.

After obtaining her Master in Physics cum laude, Federica started a PhD at AMOLF, in the group of Biological Soft Matter led by Prof. G.H. Koenderink, where she investigated the mechanics of composite extracellular matrix system which led to this thesis. In her PhD, Federica had the chance of collaborating with many research groups, both in the Netherlands and abroad, which resulted in several publications. For one of these publications, *Stress management in composite biopolymer networks*, written together with the group of Prof. J. van der Gucht at the University of Wageningen, Federica was awarded the Minerva prize from NWO for the best physics publication over the course of two years authored by a female scientist.

During her PhD, Federica was a member of the editorial board of Amsterdam Science, a magazine issued by the UvA to communicate scientific findings to a broad audience. In her free time, Federica loves traveling, learning languages, reading books and practicing sports outdoor such as rowing, running, long-distance hiking, diving and yoga.

Acknowledgments

During this whole time, from the beginning of the first experiments until now, I've been daydreaming of writing this last and most important chapter. I've been extremely lucky in having by my side people old and new that supported me through the journey, challenged my way of thinking and shared many happy moments, shaping the way I experienced these years, and I'm deeply thankful to all of them.

The first of them is of course my supervisor, Gijsje. You are a fantastic mentor, and from the start your trust helped me enormously in developing new ways of thinking independently and taking my first steps as a real scientist. In spite of the freedom you gave me, I have always felt you were always ready to discuss the meaning of the data and providing encouragement when they did not seem to make sense. I am amazed at how efficiently you can deliver help and always make sure that everyone of us can meet their deadlines. I will never forget the feedback tour-de-force before handing in the thesis! Thanks for teaching me that the most fruitful way of doing Science is by being driven by the pure curiosity of understanding, and the best way to grasp it is by engaging in constant discussion with other people. I am proud of having you as a mentor, as you are a really good person before being a really good scientist, and I'm certainly going to miss you.

Erwin, Martin, Paul, Tina and Wouter, thanks a lot for accepting to be in my reading committee: I look forward to our scientific discussion. Erwin, it's fun that you were there both at the beginning of my master project and at the end of my PhD!

Simone, Justin and Jasper, I feel extremely lucky at having shared so much of this work with you. Together, two chapters of these thesis were conceived and developed over many meetings and countless cups of coffee until they took their final shape. I learned a lot from you and greatly enjoyed our collaboration. You are extremely talented scientists. Thanks to Giulia, Eliane, Heleen and Huib for sharing frustrations and joys of the 'putty 'project, and thanks to Blessing and Tina for precious advice on how to work with hyaluronan and how to think of it from a chemical perspective. Dafydd, working with a plastic surgeon was a wonderful chance of seeing real application of extracellular gels. Fede and Tony, thanks for introducing me to the magic world of microfluidics. Fred, thanks for many discussions and your sharp insights both in network mechanics and Mediterranean cuisine. Thanks also Eddie

and Simeon for your help and interest through the whole project. Rali, Danijela, Marine, Youmna and Stephanie, being a part of your work on cancer cell invasion was a special experience.

One of the highlights of the PhD were definitely the trips to the synchrotron. Thanks to Daniel for the support and thanks to the SAXS team, Bart, Cristina and Lucy for sharing wine tasting, nights of endless measurements, chocolate bars and questionable TV shows. Bart, thanks for your enthusiasm about rheology, tea, and classical music, which unexpectedly turned to German metal in the wee hours. Cristina, I am deeply impressed by your coding skills and your ability of delivering high quality work as well as deadpan jokes. Thanks for your enormous help during the PhD and for allowing my Spanish street jargon. Lucy, I'm glad to have found someone with the same fear of walking behind slow people, and I am very fascinated by your keen sense of observation and curiosity for many aspects of life.

It was a pleasure working with all the other members of the Biosoft group! Celine, you radiate calm and kindess, and I really cherish our memories together, from the summer swims to many parties. Agata, the energy you put in your many interests is inspiring and contagious! Thanks for all the fun times together and your advice in holiday planning, for which I carefully followed your steps. Lennard, you are a great person to have around, with your positive attitude, funny jokes and your incredible determination. I am sure you will win the fight against the liposomes, don't give up. Yuval, thanks for being one of the few people who appreciate my jokes and for introducing me to the weirdest sports, in the name of the Yuval's angels. Adi, thanks for sharing your pure love for science and for STEM sessions. Tatjana, thanks for all of your help with the DDM. Galja, thanks for our work together and for your croatian proverbs. Thanks Marjolein for your help in the lab as well as your reading advices. Jeff, it's great to see your enthusiasm in the lab and the effort you put in helping everyone. Irene, even if it was just for a few weeks, working with you was real fun, I am looking forward to all the mojitos to come! Karin, thanks for sharing collagen wisdom even when you had already left the group. Rosalie, I'm glad we were in the office together and we could become friends, sharing many walks outside and even a failed attempt on a theatre career. Gerard, good luck with alien drawings in the septin fields! Anders, it was nice working with you on the review. Viktoria, thanks for your insights during group meetings. Thanks to my students: Ruben, it was very brave of you to take such a leap for your internship project, and we can't say it was a boring adventure! Ilva, you've done great work and I'm confident you will keep up your determination during your own PhD. Joey, thanks for kickstarting the DDM work with your relaxed but efficient attitude. Thanks also to the Ganzinger's gang for joining in our last year of meetings. Bela, thank you for adopting me when the group left, and thanks to Sander, Pieter-Rein, Jeroen, Kristina and Tom for all the input during Biomeeting.

Much of this work has been facilitated by the fantastic help provided by the support team at AMOLF. Thanks Marnix, Hinco, Neils, Dion for all the help in designing and mounting instruments. Thanks Marko for always helping out, even

when I just could not press the on button on the computer. Thanks to Andre, Tatiana, Angela, Juliette, Clyde, Wiebe, Henk-Jan, Ricardo, Teresa, Petra, Ernie, the workshop and all of the support team for your precious help and chats at the coffee machine.

Besides being a great place for work, AMOLF was also hiding true gems in terms of friendships. Giulia, our friendship stretches way before the AMOLF times and I feel we can truly share everything. Thanks for taking care of me through all this time. I am grateful for having you as such great friend and I am sure we will continue walking together through many journeys, as we did in the Italian countryside or along the Amstel. Marco, thanks for always being there, whether for sharing an ice cream, coffees, sportive attempts or deep conversations and gossiping. Your calm attitude at the end of our PhDs has been an enormous help in maintaining a healthy mindset. Keep a spot free on the swedish couch!

Mario and Mathijs, my fantastic office mates. We started and finished our PhD at similar times, and it felt like we have grown up together in this adventure. I cherish all the playful and more serious moments we have spent together in the office, especially those involving birds' documentaries. Mario, the first memory I have of you is an argument on the value of contemporary art, and since then we have been arguing a lot, but also shared a true friendship. Thanks for your honest and meaningful advice, which very often helped me navigating through complicated situations. I am sure that your sharp insights and natural curiosity will drive you very far in you scientific career. Mathijs, I am glad to have witnessed the energy you put in everything that you do, from coding brain worms, to speaking about politics, to eating leverworst sandwiches. Thanks for our walks and lunches in the sun even in the middle of the winter, always punctuated by good conversations and loads of mutual moral support. I will miss you guys a lot.

Olga, you have been a precious friends from the start of our internship at the VU all the way until now. It was a privilege to be by your side in these years and witness the growth of your family. Even though you will miss your plants more than me, I will miss you a lot when you will move away. Jenny, thanks for your high energy and your ability to see the sunny side of life, delivered during our romantic yearly outings. Cristina, you are a sweetheart and I deeply enjoy our activities together, from yoga in the park to getting stuck on a motor boat with no motor anymore. Vanda, thanks for always been up for our conversation in the lab, always steered towards trips in exotic places. Nicola, even if you left long ago, your kindness and party spirit left a very long legacy here in Amsterdam. Giorgio, Ale, Vane, Lorenzo, Giulia M., thanks for keeping up the italian spirit in this cold country! I cherish many good memories of the time spent with Parisa, Anne-Bart, Florian, Roberto, Caro, Moritz, Laura, Giada, Kevin, Michele, Jacopo, Harmen, Mareike, Marloes, Lukas, Steffen, Simone K., Martijn, Joris, Yvonne, Simone B., Melle, Xuan. Thank you for that!

I wish to thank also Heleen and Michael for the nice and constructive experience at Amsterdam Science.

Some people were not directly related to AMOLF but contributed to my happiness

and well-being, and sometimes we even engaged in academic discussions. Den, thanks for being our unofficial roommate, for your hearty laughter as well as the many open-heart conversations we've had. Seeing you leaving was painful, but distance has only strengthened our special friendship. Jordi, thanks for the many ways we understand each other. You are a precious friends and I admire your multi-talented personality. Megghi, thanks for your way of always being able to ask the right questions and provide the right advice, as well as a good dose of madness.

Berry, thank you for all of our dinners and karaoke together, and mostly for your enthusiasm for life. It was a special honor to be standing next to you when you were handed out your title, even though you are not really a scientist :). Rosa, thanks for your kindness, empathy and great ability in understanding people. Even though we do rather different things on a day-to-day basis, you are such a good listener that I feel no distance between your artistic and my scientific world. Jas, thanks for your light-heartedness, chilled attitude and witty sense of humor which are always refreshing, and have been the start of many deeper conversations accompanied by white wine. Felix, thanks for being such a good sailor and the initiator of so many parties! Fede F., it was fun to swap our roles of country-girl and city-boy in the past years. It seems that our paths keep crossing each others', and I hope this tradition will continue during the years. The way in which you can see the magic in the ordinary is really special. Paolo, I hope you will soon move back here, so that we can resume our shawarma diet. Chiara A., thanks for adopting me everytime I visited Leuven in these past years. Judith J., thanks for all the fun moments we've had while painting your house and flower pots and for taking care of Giulia, with you she's in very good hands. Chiara L., I am so happy you were at hand's reach in Leiden and we could still share so much in these years. Your academic enthusiasm is contagious, to the point I am now also passionate about Sanskrit poems. Judith v.S., I am happy we sticked together through these years and I am excited for your new life in the US. Thanks for your constant encouragement and sweetness. Jules and Karsta, thanks for the amazing weekends in the sun of France, which we could only reciprocate with cold and rainy times in Amsterdam. Giulia B., witnessing your passion for science and yours and Marilia 's energy is special. Jerom, thanks for making such a splendid work of art for the cover of the thesis! Graeme, I'm very happy to see how you finally got your own lab!

Thanks also to Agata M., Joost, Steffie, Rosa L., Sheila, Michael, Lucy, Dian, Luca, Fabio, Nataliya, Mateja, Blaz, Sevgi, Bram, Guido, Oz, Chris, Freddy, Lukas, Sita, Hessel, Sol, Chris, Liselotte, Dieter, Liza, Kumayl and Saliha for the fun memories together. I am very happy to have met you all.

Thanks to Lies, Chris, Peter, Anneke, Jaap and Bas for making me feel welcome and for introducing me to interesting Dutch traditions!

Marta, thanks for putting up with me through the distance, many things have changed since we are apart, but I feel we can always reconnect as if these years have stood still. Isa, I am glad that we are finally in the same time-zone. Noe, Vane, Luci, Fede I hope you will come back to visit me in spite of the adventures I put

you through! Fil, Giorgio, Teo, Buz, thanks for sticking with me through the years and always making me feel as if I had never left. I cervelli, Ragu, Beppe, Carlo, Davide, Giac, Buccio, Fabio, it's always good to share impressions of our scientific lives abroad on our yearly wedding and Christmas lunch.

Franci, in spite of your constant teasing, I know you will be always there for me, just like a sister can do. Mamma, papa', thanks for all the unconditional love that I've felt from you through my whole life and all the opportunities you've given me. Thank you for your support in this adventure, even if it's always painful to be separated. Thank you Edo and Bigia for always giving me a warm welcome back.

Douwe, I can't imagine what this PhD would have been without you. Particularly in the last phase of it, you always helped me putting things in perspective with your rational mind. I am amazed at how you could give so much balance to my life, while at the same time always pushing me out of my comfort zone. I am sure we will keep fostering each other's sense of adventure. Our years together have been filled up with love and incredible adventures and I'm looking forward to everything that awaits us.

Bibliography

[1] A. Seireg, “Leonardo da Vinci â The Bio-mechanician BT - Biomechanics,” (New York, NY), pp. 65–74, Springer US, 1969.

[2] I. Md Rian and M. Sassone, “Tree-inspired dendriforms and fractal-like branching structures in architecture: A brief historical overview,” *Frontiers of Architectural Research*, vol. 3, pp. 298–323, sep 2014.

[3] L. M. Giulia and F. Mauro, “Art & Mathematics in Antonio Gaudí’s Architecture: "La Sagrada Familia",” *Journal of Applied Mathematics*, vol. 1, no. I, 2010.

[4] D. E. Discher, P. Janmey, and Y.-l. Wang, “Tissue Cells Feel and Respond to the Stiffness of Their Substrate,” *Science*, vol. 310, pp. 1139 LP – 1143, nov 2005.

[5] J. M. Muncie and V. M. Weaver, “The Physical and Biochemical Properties of the Extracellular Matrix Regulate Cell Fate,” *Current Topics in Developmental Biology*, vol. 130, pp. 1–37, jan 2018.

[6] F. Burla, Y. Mulla, B. E. Vos, A. Aufderhorst-Roberts, and G. H. Koenderink, “From mechanical resilience to active material properties in biopolymer networks,” *Nature Reviews Physics*, vol. 1, no. 4, pp. 249–263, 2019.

[7] K. Holmes, D.F., Lu, Y., Starborg, T., Kadler, “Collagen Fibril Assembly and Function.”

[8] J. R. Couchman and C. A. Pataki, “An introduction to proteoglycans and their localization,” *The journal of histochemistry and cytochemistry : official journal of the Histochemistry Society*, vol. 60, pp. 885–897, dec 2012.

[9] N. Maeda, “Proteoglycans and neuronal migration in the cerebral cortex during development and disease,” *Frontiers in neuroscience*, vol. 9, p. 98, mar 2015.

[10] M. K. Cowman, T. A. Schmidt, P. Raghavan, and A. Stecco, "Viscoelastic Properties of Hyaluronan in Physiological Conditions," *F1000Research*, vol. 4, no. May, p. 622, 2015.

[11] J. C. H. Kuo, J. G. Gandhi, R. N. Zia, and M. J. Paszek, "Physical biology of the cancer cell glycocalyx," *Nature Physics*, vol. 14, no. 7, pp. 658–669, 2018.

[12] M. J. Paszek, C. C. Dufort, O. Rossier, R. Bainer, J. K. Mouw, K. Godula, J. E. Hudak, J. N. Lakins, A. C. Wijekoon, L. Cassereau, M. G. Rubashkin, M. J. Magbanua, K. S. Thorn, M. W. Davidson, H. S. Rugo, J. W. Park, D. A. Hammer, G. Giannone, C. R. Bertozzi, and V. M. Weaver, "The cancer glycocalyx mechanically primes integrin-mediated growth and survival," *Nature*, vol. 511, no. 7509, pp. 319–325, 2014.

[13] R. E. Shadwick, "Mechanical design in arteries," *Journal of Experimental Biology*, vol. 202, no. 23, pp. 3305–3313, 1999.

[14] P. Singh, C. Carraher, and J. E. Schwarzbauer, "Assembly of Fibronectin Extracellular Matrix," *Annual Review of Cell and Developmental Biology*, vol. 26, pp. 397–419, oct 2010.

[15] M. Pieters and A. S. Wolberg, "Fibrinogen and fibrin: An illustrated review," *Research and Practice in Thrombosis and Haemostasis*, vol. 3, pp. 161–172, apr 2019.

[16] U. G. Wegst, H. Bai, E. Saiz, A. P. Tomsia, and R. O. Ritchie, "Bioinspired structural materials," *Nature Materials*, vol. 14, no. 1, pp. 23–36, 2015.

[17] J. D. Currey, "Tensile yield in compact bone is determined by strain, post-yield behaviour by mineral content," *Journal of Biomechanics*, vol. 37, pp. 549–556, apr 2004.

[18] M. Franchi, A. Trirè, M. Quaranta, E. Orsini, and V. Ottani, "Collagen structure of tendon relates to function," *TheScientificWorldJournal*, vol. 7, pp. 404–420, 2007.

[19] A. Masic, L. Bertinetti, R. Schuetz, S. W. Chang, T. H. Metzger, M. J. Buehler, and P. Fratzl, "Osmotic pressure induced tensile forces in tendon collagen," *Nature Communications*, vol. 6, pp. 1–8, 2015.

[20] B. T. Käsdorf, F. Arends, and O. Lieleg, "Diffusion Regulation in the Vitreous Humor," *Biophysical Journal*, vol. 109, no. 10, pp. 2171–2181, 2015.

[21] L. W. Lau, R. Cua, M. B. Keough, S. Haylock-Jacobs, and V. W. Yong, "Pathophysiology of the brain extracellular matrix: A new target for remyelination," *Nature Reviews Neuroscience*, vol. 14, no. 10, pp. 722–729, 2013.

[22] E. Ruoslahti, "Brain extracellular matrix," *Glycobiology*, vol. 6, no. 5, pp. 489–492, 1996.

[23] J. Mouw, G. Ou, and V. Weaver, "Extracellular matrix assembly: a multiscale deconstruction," *Nature Reviews Molecular Cell Biology*, vol. 15, no. 12, pp. 771–785, 2014.

[24] P. Tranquilli Leali, C. Doria, A. Zachos, A. Ruggiu, F. Milia, and F. Barca, "Bone fragility: current reviews and clinical features," *Clinical cases in mineral and bone metabolism : the official journal of the Italian Society of Osteoporosis, Mineral Metabolism, and Skeletal Diseases*, vol. 6, pp. 109–113, may 2009.

[25] Y. Xu and G. A. C. Murrell, "The basic science of tendinopathy," *Clinical orthopaedics and related research*, vol. 466, pp. 1528–1538, jul 2008.

[26] S. A. Back, T. M. F. Tuohy, H. Chen, N. Wallingford, A. Craig, J. Struve, N. L. Luo, F. Banine, Y. Liu, A. Chang, B. D. Trapp, B. F. Bebo, M. S. Rao, and L. S. Sherman, "Hyaluronan accumulates in demyelinated lesions and inhibits oligodendrocyte progenitor maturation," vol. 11, no. 9, pp. 966–972, 2005.

[27] D. M. Chari, "Remyelination In Multiple Sclerosis," *International Review of Neurobiology*, vol. 79, pp. 589–620, jan 2007.

[28] J. van Mameren, K. C. Vermeulen, F. Gittes, and C. F. Schmidt, "Leveraging Single Protein Polymers To Measure Flexural Rigidity," *The Journal of Physical Chemistry B*, vol. 113, pp. 3837–3844, mar 2009.

[29] J. Block, H. Witt, A. Candelli, E. J. Peterman, G. J. Wuite, A. Janshoff, and S. Köster, "Nonlinear Loading-Rate-Dependent Force Response of Individual Vimentin Intermediate Filaments to Applied Strain," *Physical Review Letters*, vol. 118, p. 48101, jan 2017.

[30] T. F. Bartsch, M. D. Kochanczyk, E. N. Lissek, J. R. Lange, and E.-L. Florin, "Nanoscopic imaging of thick heterogeneous soft-matter structures in aqueous solution," *Nature Communications*, vol. 7, no. 1, p. 12729, 2016.

[31] J. P. Berezney and O. A. Saleh, "Electrostatic Effects on the Conformation and Elasticity of Hyaluronic Acid, a Moderately Flexible Polyelectrolyte," *Macromolecules*, vol. 50, pp. 1085–1089, feb 2017.

[32] P. G. de Gennes, "Reptation of a Polymer Chain in the Presence of Fixed Obstacles," *The Journal of Chemical Physics*, vol. 55, pp. 572–579, jul 1971.

[33] M. Doi and S. F. Edwards, "Dynamics of concentrated polymer systems. Part 1.âBrownian motion in the equilibrium state," *Journal of the Chemical Society,*

Faraday Transactions 2: Molecular and Chemical Physics, vol. 74, no. 0, pp. 1789–1801, 1978.

[34] J. Käs, H. Strey, and E. Sackmann, "Direct imaging of reptation for semiflexible actin filaments," *Nature*, vol. 368, no. 6468, pp. 226–229, 1994.

[35] P. Lang and E. Frey, "Disentangling entanglements in biopolymer solutions," *Nature Communications*, vol. 9, no. 1, p. 494, 2018.

[36] L. Blanchoin, R. Boujemaa-Paterski, C. Sykes, and J. Plastino, "Actin Dynamics, Architecture, and Mechanics in Cell Motility," *Physiological Reviews*, vol. 94, pp. 235–263, jan 2014.

[37] N. Basnet, H. Nedozralova, A. H. Crevenna, S. Bodakuntla, T. Schlichthaerle, M. Taschner, G. Cardone, C. Janke, R. Jungmann, M. M. Magiera, C. Biertümpfel, and N. Mizuno, "Direct induction of microtubule branching by microtubule nucleation factor SSNA1," *Nature Cell Biology*, vol. 20, no. 10, pp. 1172–1180, 2018.

[38] Y.-C. Lin, C. P. Broedersz, A. C. Rowat, T. Wedig, H. Herrmann, F. C. MacKintosh, and D. A. Weitz, "Divalent Cations Crosslink Vimentin Intermediate Filament Tail Domains to Regulate Network Mechanics," *Journal of Molecular Biology*, vol. 399, pp. 637–644, jun 2010.

[39] H. M. Kagan and W. Li, "Lysyl oxidase: Properties, specificity, and biological roles inside and outside of the cell," *Journal of Cellular Biochemistry*, vol. 88, pp. 660–672, mar 2003.

[40] A. J. Licup, S. Münster, A. Sharma, M. Sheinman, L. M. Jawerth, B. Fabry, D. A. Weitz, and F. C. MacKintosh, "Stress controls the mechanics of collagen networks," *Proceedings of the National Academy of Sciences*, vol. 112, no. 31, pp. 9573–9578, 2015.

[41] A. Sharma, A. J. Licup, K. A. Jansen, R. Rens, M. Sheinman, G. H. Koenderink, and F. C. Mackintosh, "Strain-controlled criticality governs the nonlinear mechanics of fibre networks," *Nature Physics*, vol. 12, no. 6, pp. 584–587, 2016.

[42] N. Gostynska, G. Shankar Krishnakumar, E. Campodoni, S. Panseri, M. Montesi, S. Sprio, E. Kon, M. Marcacci, A. Tampieri, and M. Sandri, "3D porous collagen scaffolds reinforced by glycation with ribose for tissue engineering application," *Biomedical Materials*, vol. 12, p. 055002, aug 2017.

[43] R. Staneva, F. Burla, G. H. Koenderink, S. Descroix, D. M. Vignjevic, Y. Attieh, and M. Verhulsel, "A new biomimetic assay reveals the temporal role of matrix stiffening in cancer cell invasion," *Molecular Biology of the Cell*, vol. 29, pp. 2979–2988, oct 2018.

[44] C. Valero, H. Amaveda, M. Mora, and J. M. García-Aznar, "Combined experimental and computational characterization of crosslinked collagen-based hydrogels," *PLoS ONE*, vol. 13, no. 4, pp. 1–16, 2018.

[45] C. Storm, J. J. Pastore, F. C. MacKintosh, T. C. Lubensky, and P. A. Janmey, "Nonlinear elasticity in biological gels," *Nature*, vol. 435, no. 7039, pp. 191–194, 2005.

[46] O. Chaudhuri, S. H. Parekh, and D. A. Fletcher, "Reversible stress softening of actin networks," *Nature*, vol. 445, no. 7125, pp. 295–298, 2007.

[47] B. E. Vos, L. C. Liebrand, M. Vahabi, A. Biebricher, G. J. L. Wuite, E. J. G. Peterman, N. A. Kurniawan, F. C. MacKintosh, and G. H. Koenderink, "Programming the mechanics of cohesive fiber networks by compression," *Soft Matter*, vol. 13, no. 47, pp. 8886–8893, 2017.

[48] A. S. G. van Oosten, M. Vahabi, A. J. Licup, A. Sharma, P. A. Galie, F. C. MacKintosh, and P. A. Janmey, "Uncoupling shear and uniaxial elastic moduli of semiflexible biopolymer networks: compression-softening and stretch-stiffening," *Scientific Reports*, vol. 6, p. 19270, jan 2016.

[49] F. C. MacKintosh, J. Käs, and P. A. Janmey, "Elasticity of Semiflexible Biopolymer Networks," *Physical Review Letters*, vol. 75, pp. 4425–4428, dec 1995.

[50] J. Liu, G. H. Koenderink, K. E. Kasza, F. C. MacKintosh, and D. A. Weitz, "Visualizing the Strain Field in Semiflexible Polymer Networks: Strain Fluctuations and Nonlinear Rheology of F-Actin Gels," *Physical Review Letters*, vol. 98, p. 198304, may 2007.

[51] M. L. Gardel, J. H. Shin, F. C. MacKintosh, L. Mahadevan, P. Matsudaira, and D. A. Weitz, "Elastic Behavior of Cross-Linked and Bundled Actin Networks," *Science*, vol. 304, pp. 1301 LP – 1305, may 2004.

[52] G. H. Koenderink, Z. Dogic, F. Nakamura, P. M. Bendix, F. C. MacKintosh, J. H. Hartwig, T. P. Stossel, and D. A. Weitz, "An active biopolymer network controlled by molecular motors," *Proceedings of the National Academy of Sciences*, vol. 106, pp. 15192 LP – 15197, sep 2009.

[53] P. H. J. Kouwer, M. Koepf, V. A. A. Le Sage, M. Jaspers, A. M. van Buul, Z. H. Eksteen-Akeroyd, T. Woltinge, E. Schwartz, H. J. Kitto, R. Hoogenboom, S. J. Picken, R. J. M. Nolte, E. Mendes, and A. E. Rowan, "Responsive biomimetic networks from polyisocyanopeptide hydrogels," *Nature*, vol. 493, p. 651, jan 2013.

[54] M. Fernandez-CastanoâRomera, R. P. M. Lafleur, C. Guibert, I. K. Voets, C. Storm, and R. P. Sijbesma, "Strain Stiffening Hydrogels through Self-Assembly and Covalent Fixation of Semi-Flexible Fibers," *Angewandte Chemie International Edition*, vol. 56, pp. 8771–8775, jul 2017.

[55] B. Yan, J. Huang, L. Han, L. Gong, L. Li, J. N. Israelachvili, and H. Zeng, "Duplicating Dynamic Strain-Stiffening Behavior and Nanomechanics of Biological Tissues in a Synthetic Self-Healing Flexible Network Hydrogel," *ACS Nano*, vol. 11, pp. 11074–11081, nov 2017.

[56] J. C. Maxwell, "On the calculation of the equilibrium and stiffness of frames," *The London, Edinburgh, and Dublin Philosophical Magazine and Journal of Science*, vol. 27, pp. 294–299, apr 1864.

[57] C. P. Broedersz, X. Mao, T. C. Lubensky, and F. C. MacKintosh, "Criticality and isostaticity in fibre networks," *Nature Physics*, vol. 7, no. 12, pp. 983–988, 2011.

[58] P. R. Onck, T. Koeman, T. van Dillen, and E. van der Giessen, "Alternative Explanation of Stiffening in Cross-Linked Semiflexible Networks," *Physical Review Letters*, vol. 95, p. 178102, oct 2005.

[59] A. J. Licup, S. Münster, A. Sharma, M. Sheinman, L. M. Jawerth, B. Fabry, D. A. Weitz, and F. C. MacKintosh, "Stress controls the mechanics of collagen networks," *Proceedings of the National Academy of Sciences*, vol. 112, no. 31, pp. 9573–9578, 2015.

[60] K. A. Jansen, A. J. Licup, A. Sharma, R. Rens, F. C. MacKintosh, and G. H. Koenderink, "The Role of Network Architecture in Collagen Mechanics," *Biophysical Journal*, vol. 114, no. 11, pp. 2665–2678, 2018.

[61] Y. L. Han, P. Ronceray, G. Xu, A. Malandrino, R. D. Kamm, M. Lenz, C. P. Broedersz, and M. Guo, "Cell contraction induces long-ranged stress stiffening in the extracellular matrix," *Proceedings of the National Academy of Sciences*, vol. 115, pp. 4075 LP – 4080, apr 2018.

[62] J. M. van Doorn, L. Lageschaar, J. Sprakel, and J. van der Gucht, "Criticality and mechanical enhancement in composite fiber networks," *Physical Review E*, vol. 95, p. 42503, apr 2017.

[63] A. S. Shahsavari and R. C. Picu, "Exceptional stiffening in composite fiber networks," *Physical Review E*, vol. 92, p. 12401, jul 2015.

[64] M. Das and F. C. MacKintosh, "Poisson's Ratio in Composite Elastic Media with Rigid Rods," *Physical Review Letters*, vol. 105, p. 138102, sep 2010.

[65] C. P. Brangwynne, F. C. MacKintosh, S. Kumar, N. A. Geisse, J. Talbot, L. Mahadevan, K. K. Parker, D. E. Ingber, and D. A. Weitz, "Microtubules can bear enhanced compressive loads in living cells because of lateral reinforcement," *Journal of Cell Biology*, vol. 173, no. 5, pp. 733–741, 2006.

[66] B. P. Bouchet, I. Noordstra, M. van Amersfoort, E. A. Katrukha, Y.-C. Ammon, N. D. Ter Hoeve, L. Hodgson, M. Dogterom, P. W. B. Derksen, and A. Akhmanova, "Mesenchymal Cell Invasion Requires Cooperative Regulation of Persistent Microtubule Growth by SLAIN2 and CLASP1," *Developmental cell*, vol. 39, pp. 708–723, dec 2016.

[67] E. Latorre, S. Kale, L. Casares, M. Gómez-González, M. Uroz, L. Valon, R. V. Nair, E. Garreta, N. Montserrat, A. del Campo, B. Ladoux, M. Arroyo, and X. Trepat, "Active superelasticity in three-dimensional epithelia of controlled shape," *Nature*, vol. 563, no. 7730, pp. 203–208, 2018.

[68] S. T. Kreger and S. L. Voytik-Harbin, "Hyaluronan concentration within a 3D collagen matrix modulates matrix viscoelasticity, but not fibroblast response," *Matrix biology : journal of the International Society for Matrix Biology*, vol. 28, pp. 336–346, jul 2009.

[69] V. K. Lai, D. S. Nedrelow, S. P. Lake, B. Kim, E. M. Weiss, R. T. Tranquillo, and V. H. Barocas, "Swelling of Collagen-Hyaluronic Acid Co-Gels: An In Vitro Residual Stress Model," *Annals of biomedical engineering*, vol. 44, pp. 2984–2993, oct 2016.

[70] F. Burla, J. Tauber, S. Dussi, J. van der Gucht, and G. H. Koenderink, "Stress management in composite biopolymer networks," 2019.

[71] E. M. Huisman, C. Heussinger, C. Storm, and G. T. Barkema, "Semiflexible Filamentous Composites," *Physical Review Letters*, vol. 105, p. 118101, sep 2010.

[72] H. Wada and Y. Tanaka, "Mechanics and size-dependent elasticity of composite networks," *EPL (Europhysics Letters)*, vol. 95, no. 2, p. 29901, 2011.

[73] M. Bai, A. R. Missel, W. S. Klug, and A. J. Levine, "The mechanics and affineânonaffine transition in polydisperse semiflexible networks," *Soft Matter*, vol. 7, no. 3, pp. 907–914, 2011.

[74] Y.-C. Lin, G. H. Koenderink, F. C. MacKintosh, and D. A. Weitz, "Control of non-linear elasticity in F-actin networks with microtubules," *Soft Matter*, vol. 7, no. 3, pp. 902–906, 2011.

[75] S. N. Ricketts, J. L. Ross, and R. M. Robertson-Anderson, "Co-Entangled Actin-Microtubule Composites Exhibit Tunable Stiffness and Power-Law Stress Relaxation," *Biophysical Journal*, vol. 115, no. 6, pp. 1055–1067, 2018.

[76] M. Das and F. C. MacKintosh, "Mechanics of soft composites of rods in elastic gels," *Physical Review E*, vol. 84, p. 61906, dec 2011.

[77] V. Pelletier, N. Gal, P. Fournier, and M. L. Kilfoil, "Microrheology of Microtubule Solutions and Actin-Microtubule Composite Networks," *Physical Review Letters*, vol. 102, p. 188303, may 2009.

[78] M. H. Jensen, E. J. Morris, R. D. Goldman, and D. A. Weitz, "Emergent properties of composite semiflexible biopolymer networks," *Bioarchitecture*, vol. 4, no. 4-5, pp. 138–143, 2014.

[79] Y.-l. Yang, C. Sun, M. E. Wilhelm, L. J. Fox, J. Zhu, and L. J. Kaufman, "Influence of chondroitin sulfate and hyaluronic acid on structure, mechanical properties, and glioma invasion of collagen I gels," *Biomaterials*, vol. 32, no. 31, pp. 7932–7940, 2011.

[80] A. S. LaCroix, S. E. Duenwald-Kuehl, R. S. Lakes, and R. Vanderby, "Relationship between tendon stiffness and failure: A metaanalysis," *Journal of Applied Physiology*, vol. 115, no. 1, pp. 43–51, 2013.

[81] M. I. Converse, R. G. Walther, J. T. Ingram, Y. Li, S. M. Yu, and K. L. Monson, "Detection and characterization of molecular-level collagen damage in overstretched cerebral arteries," *Acta Biomaterialia*, vol. 67, pp. 307–318, feb 2018.

[82] Anne M. Robertson, Xinjie Duan, Khaled M. Aziz, Michael R. Hill, Simon C. Watkins and J. R. Cebral, "Diversity in the Strength and Structure of Unruptured Cerebral Aneurysms," *Ann Biomed Eng.*, vol. 25, no. 3, pp. 289–313, 2016.

[83] S. Sugita and T. Matsumoto, "Local distribution of collagen fibers determines crack initiation site and its propagation direction during aortic rupture," *Biomechanics and Modeling in Mechanobiology*, vol. 17, no. 2, pp. 577–587, 2018.

[84] Q. D. Tran, Marcos, and D. Gonzalez-Rodriguez, "Permeability and viscoelastic fracture of a model tumor under interstitial flow," *Soft Matter*, vol. 14, no. 30, pp. 6386–6392, 2018.

[85] M. Arroyo and X. Trepat, "Hydraulic fracturing in cells and tissues: fracking meets cell biology," *Current Opinion in Cell Biology*, vol. 44, pp. 1–6, feb 2017.

[86] S. P. Veres, J. M. Harrison, and J. M. Lee, "Repeated subrupture overload causes progression of nanoscaled discrete plasticity damage in tendon collagen fibrils," *Journal of Orthopaedic Research*, vol. 31, no. 5, pp. 731–737, 2013.

[87] T. W. Herod, N. C. Chambers, and S. P. Veres, "Collagen fibrils in functionally distinct tendons have differing structural responses to tendon rupture and fatigue loading Acta Biomaterialia Collagen fibrils in functionally distinct tendons have differing structural responses to tendon rupture and fati," *Acta Biomaterialia*, vol. 42, no. June, pp. 296–307, 2016.

[88] P. Fratzl and R. Weinkamer, "Nature's hierarchical materials," *Progress in Materials Science*, vol. 52, no. 8, pp. 1263–1334, 2007.

[89] M. J. Buehler and Y. C. Yung, "Deformation and failure of protein materials in physiologically extreme conditions and disease," *Nature Materials*, vol. 8, no. february, pp. 175–188, 2009.

[90] R. B. Svensson, H. Mulder, V. Kovanen, and S. P. Magnusson, "Fracture mechanics of collagen fibrils: Influence of natural cross-links," *Biophysical Journal*, vol. 104, no. 11, pp. 2476–2484, 2013.

[91] R. B. Svensson, S. T. Smith, P. J. Moyer, and S. P. Magnusson, "Acta Biomaterialia Effects of maturation and advanced glycation on tensile mechanics of collagen fibrils from rat tail and Achilles tendons," *Acta Biomaterialia*, vol. 70, pp. 270–280, 2018.

[92] K. Misof, G. Rapp, and P. Fratzl, "A new molecular model for collagen elasticity based on synchrotron x- ray scattering evidence," *Biophysical Journal*, vol. 72, no. 3, pp. 1376–1381, 1997.

[93] J. F. Ribeiro, E. Heber, M. L. S. Mello, and B. D. C. Vidal, "Skin Collagen Fiber Molecular Order : A Pattern of Distributional Fiber Orientation as Assessed by Optical Anisotropy and Image Analysis," vol. 8, no. 1, pp. 5–7, 2013.

[94] Q. Meng, S. An, R. A. Damion, Z. Jin, R. Wilcox, J. Fisher, and A. Jones, "Journal of the Mechanical Behavior of Biomedical Materials The effect of collagen fi bril orientation on the biphasic mechanics of articular cartilage," *Journal of the Mechanical Behavior of Biomedical Materials*, vol. 65, pp. 439–453, 2017.

[95] K. J. Bos, D. F. Holmes, R. S. Meadows, K. E. Kadler, D. Mcleod, and P. N. Bishop, "Collagen fibril organisation in mammalian vitreous by freeze etch / rotary shadowing electron microscopy," vol. 32, pp. 301–306, 2001.

[96] J. H. Lindeman, B. A. Ashcroft, J. W. M. Beenakker, M. Van Es, N. B. Koekkoek, F. A. Prins, J. F. Tielemans, H. Abdul-Hussien, R. A. Bank, and T. H. Oosterkamp, "Distinct defects in collagen microarchitecture underlie vessel-wall failure in advanced abdominal aneurysms and aneurysms in Marfan syndrome," *Proceedings of the National Academy of Sciences of the United States of America*, vol. 107, no. 2, pp. 862–865, 2010.

[97] S. M. Vanderheiden, M. F. Hadi, and V. H. Barocas, "Crack Propagation Versus Fiber Alignment in Collagen Gels: Experiments and Multiscale Simulation," *Journal of Biomechanical Engineering*, vol. 137, oct 2015.

[98] M. F. Hadi and V. H. Barocas, "Microscale Fiber Network Alignment Affects Macroscale Failure Behavior in Simulated Collagen Tissue Analogs," *Journal of Biomechanical Engineering*, vol. 135, no. 2, p. 021026, 2013.

[99] R. Y. Dhume, E. D. Shih, and V. H. Barocas, "Multiscale model of fatigue of collagen gels," *Biomechanics and Modeling in Mechanobiology*, vol. 18, no. 1, pp. 175–187, 2019.

[100] K. Bircher, M. Zündel, M. Pensalfini, A. E. Ehret, and E. Mazza, "Tear resistance of soft collagenous tissues," *Nature Communications*, vol. 10, no. 1, pp. 1–13, 2019.

[101] S. Leikin, D. C. Rau, and V. A. Parsegian, "Temperature-favoured assembly of collagen is driven by hydrophilic not hydrophobic interactions," *Nature Structural Biology*, vol. 2, no. 3, pp. 205–210, 1995.

[102] W. Traub, "Molecular assembly in collagen," *FEBS Letters*, vol. 92, no. 1, pp. 114–120, 1978.

[103] M. Guthold, W. Liu, E. A. Sparks, L. M. Jawerth, L. Peng, M. Falvo, R. Superfine, R. R. Hantgan, and S. T. Lord, "A comparison of the mechanical and structural properties of fibrin fibers with other protein fibers," *Cell Biochemistry and Biophysics*, vol. 49, no. 3, pp. 165–181, 2007.

[104] S. Asif Iqbal, D. Deska-gauthier, and L. Kreplak, "Assessing collagen fibrils molecular damage after a single stretchârelease cycle," *Soft Matter*, 2019.

[105] S. Ricard-Blum, "The Collagen Family," *Cold Spring Harbor Perspectives in Biology*, vol. 3, no. 1, pp. 1–19, 2011.

[106] S. J. Aper, A. C. Van Spreeuwel, M. C. Van Turnhout, A. J. Van Der Linden, P. A. Pieters, N. L. Van Der Zon, S. L. De La Rambelje, C. V. Bouten, and M. Merkx, "Colorful protein-based fluorescent probes for collagen imaging," *PLoS ONE*, vol. 9, no. 12, pp. 1–21, 2014.

[107] C. P. Broedersz, M. Depken, N. Y. Yao, M. R. Pollak, D. A. Weitz, and F. C. MacKintosh, "Cross-link-governed dynamics of biopolymer networks," *Physical Review Letters*, vol. 105, no. 23, pp. 2–5, 2010.

[108] J. Schindelin, I. Arganda-Carreras, E. Frise, V. Kaynig, M. Longair, T. Pietzsch, S. Preibisch, C. Rueden, S. Saalfeld, B. Schmid, J.-Y. Tinevez, D. J. White, V. Hartenstein, K. Eliceiri, P. Tomancak, and A. Cardona, "Fiji: an open-source platform for biological-image analysis," *Nature Methods*, vol. 9, p. 676, jun 2012.

[109] L. J. Kaufman, C. P. Brangwynne, K. E. Kasza, E. Filippidi, V. D. Gordon, T. S. Deisboeck, and D. A. Weitz, "Glioma Expansion in Collagen I Matrices : Analyzing Collagen Concentration-Dependent Growth and Motility Patterns," *Biophysical Journal*, vol. 89, no. 1, pp. 635–650, 2005.

[110] T. C. Baradet, J. C. Haselgrove, and J. W. Weisel, "Three-dimensional reconstruction of fibrin clot networks from stereoscopic intermediate voltage electron microscope images and analysis of branching," *Biophysical Journal*, vol. 68, no. 4, pp. 1551–1560, 1995.

[111] M. Shayegan, T. Altindal, E. Kiefl, and N. R. Forde, "Intact Telopeptides Enhance Interactions between Collagens," *Biophysj*, vol. 111, no. 11, pp. 2404–2416, 2016.

[112] L. Zhang, D. Z. Rocklin, L. M. Sander, and X. Mao, "Fiber networks below the isostatic point: Fracture without stress concentration," *Physical Review Materials*, vol. 1, no. 5, pp. 1–5, 2017.

[113] M. M. Driscoll, B. G.-g. Chen, T. H. Beuman, S. Ulrich, and S. R. Nagel, "The role of rigidity in controlling material failure," *PNAS*, vol. 113, no. 39, pp. 10813–10817, 2016.

[114] E. Berthier, J. E. Kollmer, S. E. Henkes, K. Liu, J. M. Schwarz, and K. E. Daniels, "Rigidity percolation control of the brittle-ductile transition in disordered networks," *Physical Review Materials*, vol. 075602, no. 3, pp. 1–9, 2019.

[115] S. Dussi, J. Tauber, and J. van der Gucht, "Athermal Fracture of Elastic Networks: How Rigidity Challenges the Unavoidable Size-Induced Brittleness," pp. 1–13, 2019.

[116] R. C. Arevalo, J. S. Urbach, and D. L. Blair, "Size-dependent rheology of type-I collagen networks," *Biophysical Journal*, vol. 99, no. 8, pp. 8–11, 2010.

[117] S. Munster, L. M. Jawerth, B. A. Leslie, J. I. Weitz, B. Fabry, and D. A. Weitz, "Strain history dependence of the nonlinear stress response of fibrin

and collagen networks," *Proceedings of the National Academy of Sciences*, vol. 110, no. 30, pp. 12197–12202, 2013.

[118] E. Ban, J. M. Franklin, S. Nam, L. R. Smith, H. Wang, R. G. Wells, O. Chaudhuri, J. T. Liphardt, and V. B. Shenoy, "Mechanisms of Plastic Deformation in Collagen Networks Induced by Cellular Forces," *Biophysical Journal*, vol. 114, no. 2, pp. 450–461, 2018.

[119] J. Liu, D. Das, F. Yang, A. G. Schwartz, G. M. Genin, S. Thomopoulos, and I. Chasiotis, "Energy dissipation in mammalian collagen fibrils: Cyclic strain-induced damping, toughening, and strengthening," *Acta Biomaterialia*, vol. 80, pp. 217–227, oct 2018.

[120] B. Depalle, Z. Qin, S. J. Shefelbine, and M. J. Buehler, "In fl uence of cross-link structure , density and mechanical properties in the mesoscale deformation mechanisms of collagen fi brils," vol. 52, pp. 1–13, 2015.

[121] P. Fratzl, K. Misof, I. Zizak, G. Rapp, and S. Bernstorff, "Fibrillar Structure and Mechanical Properties of Collagen," vol. 122, pp. 119–122, 1997.

[122] R. Puxkandl, I. Zizak, O. Paris, J. Keckes, W. Tesch, S. Bernstorff, P. Purslow, and P. Fratzl, "Viscoelastic properties of collagen: Synchrotron radiation investigations and structural model," *Philosophical Transactions of the Royal Society B: Biological Sciences*, vol. 357, no. 1418, pp. 191–197, 2002.

[123] E. Prince and E. Kumacheva, "Design and applications of man-made biomimetic fibrillar hydrogels," *Nature Reviews Materials*, vol. 4, no. 2, pp. 99–115, 2019.

[124] Y. Lanir, "Multi-scale Structural Modeling of Soft Tissues Mechanics and Mechanobiology," *Journal of Elasticity*, vol. 129, no. 1, pp. 7–48, 2017.

[125] S. van Helvert, C. Storm, and P. Friedl, "Mechanoreciprocity in cell migration," *Nature Cell Biology*, vol. 20, no. 1, pp. 8–20, 2018.

[126] C. Broedersz and F. MacKintosh, "Modeling semiflexible polymer networks," *Reviews of Modern Physics*, vol. 86, pp. 995–1036, jul 2014.

[127] D. A. Narmoneva, J. Y. Wang, and L. A. Setton, "Nonuniform swelling-induced residual strains in articular cartilage," *Journal of Biomechanics*, vol. 32, no. 4, pp. 401–408, 1999.

[128] A. J. Michalek, M. G. Gardner-Morse, and J. C. Iatridis, "Large residual strains are present in the intervertebral disc annulus fibrosus in the unloaded state," *Journal of biomechanics*, vol. 45, pp. 1227–1231, apr 2012.

[129] C. Voutouri and T. Stylianopoulos, "Accumulation of mechanical forces in tumors is related to hyaluronan content and tissue stiffness," *PLoS ONE*, vol. 13, no. 3, pp. 1–14, 2018.

[130] A. J. Kim, V. N. Manoharan, and J. C. Crocker, "Swelling-based method for preparing stable, functionalized polymer colloids," *Journal of the American Chemical Society*, vol. 127, no. 6, pp. 1592–1593, 2005.

[131] D. Allan, T. Caswell, N. Keim, and C. van der Wel, "trackpy: Trackpy v0.3.2," aug 2016.

[132] S. B. Lindström, D. A. Vader, A. Kulachenko, and D. A. Weitz, "Biopolymer network geometries: Characterization, regeneration, and elastic properties," *Physical Review E*, vol. 82, p. 51905, nov 2010.

[133] K. S. Rankin and D. Frankel, "Hyaluronan in cancer-from the naked mole rat to nanoparticle therapy," *Soft Matter*, vol. 12, no. 17, pp. 3841–3848, 2016.

[134] M. Vahabi, A. Sharma, A. J. Licup, A. S. G. van Oosten, P. A. Galie, P. A. Janmey, and F. C. MacKintosh, "Elasticity of fibrous networks under uniaxial prestress," *Soft Matter*, vol. 12, no. 22, pp. 5050–5060, 2016.

[135] D. Mizuno, C. Tardin, C. F. Schmidt, and F. C. MacKintosh, "Nonequilibrium Mechanics of Active Cytoskeletal Networks," *Science*, vol. 315, pp. 370 LP – 373, jan 2007.

[136] K. A. Jansen, R. G. Bacabac, I. K. Piechocka, and G. H. Koenderink, "Cells actively stiffen fibrin networks by generating contractile stress," *Biophysical journal*, vol. 105, pp. 2240–2251, nov 2013.

[137] D. J. Cosgrove, "Growth of the plant cell wall," *Nature Reviews Molecular Cell Biology*, vol. 6, no. 11, pp. 850–861, 2005.

[138] M. Jaspers, *Mechanics and Structure of Strain Stiffening Biomimetic Hydrogels*. 2017.

[139] A. Chopra, M. E. Murray, F. Byfield, M. Mendez, R. Halleluyan, D. Restle, D. R.-B. Aroush, P. A. Galie, K. Pogoda, R. Bucki, C. Marcinkiewicz, G. D. Prestwich, T. Zarembinski, and P. A. Janmey, "Augmentation of integrin-mediated mechanotransduction by hyaluronic acid," *Biomaterials*, vol. 35, no. 1, pp. 71–82, 2014.

[140] N. N. Pavlova and C. B. Thompson, "The Emerging Hallmarks of Cancer Metabolism," 2016.

[141] E. A. Turley, D. K. Wood, and J. B. McCarthy, "Carcinoma cell hyaluronan as a "portable" cancerized prometastatic microenvironment," *Cancer Research*, vol. 76, no. 9, pp. 2507–2512, 2016.

[142] M. Yokoo and E. Sato, "Physiological function of hyaluronan in mammalian oocyte maturation," 2011.

[143] A. Salustri, L. Campagnolo, F. G. Klinger, and A. Camaioni, "Molecular organization and mechanical properties of the hyaluronan matrix surrounding the mammalian oocyte," *Matrix Biology*, vol. 78-79, pp. 11–23, may 2019.

[144] X. Chen, R. Bonfiglio, S. Banerji, D. G. Jackson, A. Salustri, and R. P. Richter, "Micromechanical Analysis of the Hyaluronan-Rich Matrix Surrounding the Oocyte Reveals a Uniquely Soft and Elastic Composition," *Biophysical Journal*, vol. 110, no. 12, pp. 2779–2789, 2016.

[145] P. Rooney and S. Kumar, "Inverse relationship between hyaluronan and collagens in development and angiogenesis," *Differentiation*, vol. 54, pp. 1–9, oct 1993.

[146] K. Pogoda, R. Bucki, F. J. Byfield, K. Cruz, T. Lee, C. Marcinkiewicz, and P. A. Janmey, "Soft Substrates Containing Hyaluronan Mimic the Effects of Increased Stiffness on Morphology, Motility, and Proliferation of Glioma Cells," *Biomacromolecules*, vol. 18, no. 10, pp. 3040–3051, 2017.

[147] F. Rehfeldt, A. E. X. Brown, M. Raab, S. Cai, A. L. Zajac, A. Zemel, and D. E. Discher, "Hyaluronic acid matrices show matrix stiffness in 2D and 3D dictates cytoskeletal order and myosin-II phosphorylation within stem cells," *Integrative Biology*, vol. 4, no. 4, pp. 422–430, 2012.

[148] R. G. Thorne and C. Nicholson, "In vivo diffusion analysis with quantum dots and dextrans predicts the width of brain extracellular space," *Proceedings of the National Academy of Sciences of the United States of America*, vol. 103, no. 14, pp. 5567–5572, 2006.

[149] T. Ji, J. Lang, J. Wang, R. Cai, Y. Zhang, F. Qi, L. Zhang, X. Zhao, W. Wu, J. Hao, Z. Qin, Y. Zhao, and G. Nie, "Designing Liposomes to Suppress Extracellular Matrix Expression to Enhance Drug Penetration and Pancreatic Tumor Therapy," *ACS Nano*, vol. 11, no. 9, pp. 8668–8678, 2017.

[150] R. Burgos-Panadero, F. Lucantoni, E. Gamero-Sandemetrio, L. de la Cruz-Merino, T. Álvaro, and R. Noguera, "The tumour microenvironment as an integrated framework to understand cancer biology," *Cancer Letters*, vol. 461, no. May, pp. 112–122, 2019.

[151] A. Dodero, R. Williams, S. Gagliardi, S. Vicini, M. Alloisio, and M. Castellano, "A micro-rheological and rheological study of biopolymers solutions: Hyaluronic acid," *Carbohydrate Polymers*, vol. 203, no. September 2018, pp. 349–355, 2019.

[152] C. Oelschlaeger, M. Cota Pinto Coelho, and N. Willenbacher, "Chain flexibility and dynamics of polysaccharide hyaluronan in entangled solutions: A high frequency rheology and diffusing wave spectroscopy study," *Biomacromolecules*, vol. 14, no. 10, pp. 3689–3696, 2013.

[153] J. Cribb, L. D. Osborne, J. P.-L. Hsiao, L. Vicci, A. Meshram, E. T. O'Brien, R. C. Spero, R. Taylor, and R. Superfine, "A high throughput array microscope for the mechanical characterization of biomaterials," *Review of Scientific Instruments*, vol. 86, p. 023711, feb 2015.

[154] N. Nijenhuis, D. Mizuno, C. F. Schmidt, H. Vink, and J. A. Spaan, "Microrheology of hyaluronan solutions: Implications for the endothelial glycocalyx," *Biomacromolecules*, vol. 9, no. 9, pp. 2390–2398, 2008.

[155] C. Oelschlaeger, F. Bossler, and N. Willenbacher, "Synthesis, Structural and Micromechanical Properties of 3D Hyaluronic Acid-Based Cryogel Scaffolds," *Biomacromolecules*, vol. 17, no. 2, pp. 580–589, 2016.

[156] I. M. Hansen, M. F. Ebbesen, L. Kaspersen, T. Thomsen, K. Bienk, Y. Cai, B. M. Malle, and K. A. Howard, "Hyaluronic Acid Molecular Weight-Dependent Modulation of Mucin Nanostructure for Potential Mucosal Therapeutic Applications," *Molecular Pharmaceutics*, vol. 14, no. 7, pp. 2359–2367, 2017.

[157] R. Cerbino and V. Trappe, "Differential dynamic microscopy: Probing wave vector dependent dynamics with a microscope," *Physical Review Letters*, vol. 100, no. 18, pp. 1–4, 2008.

[158] R. Cerbino and P. Cicuta, "Perspective: Differential dynamic microscopy extracts multi-scale activity in complex fluids and biological systems," *Journal of Chemical Physics*, vol. 147, no. 11, 2017.

[159] A. V. Bayles, T. M. Squires, and M. E. Helgeson, "Probe microrheology without particle tracking by differential dynamic microscopy," *Rheologica Acta*, vol. 56, no. 11, pp. 863–869, 2017.

[160] P. Edera, D. Bergamini, V. Trappe, F. Giavazzi, and R. Cerbino, "Differential dynamic microscopy microrheology of soft materials: A tracking-free determination of the frequency-dependent loss and storage moduli," *Physical Review Materials*, vol. 1, no. 7, pp. 1–11, 2017.

[161] M. A. Escobedo-Sánchez, J. P. Segovia-Gutiérrez, A. B. Zuccolotto-Bernez, J. Hansen, C. C. Marciniak, K. Sachowsky, F. Platten, and S. U. Egelhaaf, "Microliter viscometry using a bright-field microscope: η -DDM," *Soft Matter*, vol. 14, no. 34, pp. 7016–7025, 2018.

[162] B. R. Dasgupta and D. A. Weitz, "Microrheology of cross-linked polyacrylamide networks," *Physical Review E - Statistical, Nonlinear, and Soft Matter Physics*, vol. 71, no. 2, pp. 1–9, 2005.

[163] L. Vaccari, M. Molaei, R. L. Leheny, and K. J. Stebe, "Cargo carrying bacteria at interfaces," *Soft Matter*, vol. 14, no. 27, pp. 5643–5653, 2018.

[164] M. T. Valentine, P. D. Kaplan, D. Thota, J. C. Crocker, T. Gisler, R. K. Prud'homme, M. Beck, and D. A. Weitz, "Investigating the microenvironments of inhomogeneous soft materials with multiple particle tracking," *Physical Review E - Statistical Physics, Plasmas, Fluids, and Related Interdisciplinary Topics*, vol. 64, no. 6, p. 9, 2001.

[165] J. Mellnik, P. A. Vasquez, S. A. McKinley, J. Witten, D. B. Hill, and M. G. Forest, "Micro-heterogeneity metrics for diffusion in soft matter," *Soft Matter*, vol. 10, no. 39, pp. 7781–7796, 2014.

[166] G. Giubertoni, F. Burla, C. Martinez-Torres, B. Dutta, G. Pletikapić, E. G. Pelan, Y. L. A. Rezus, G. H. Koenderink, and H. J. Bakker, "Molecular Origin of the Elastic State of Aqueous Hyaluronic Acid," *The Journal of Physical Chemistry B*, p. acs.jpcb.9b00982, mar 2019.

[167] K. J. Wolf and S. Kumar, "Hyaluronic Acid: Incorporating the Bio into the Material," *ACS Biomaterials Science and Engineering*, vol. 5, pp. 3753–3765, 2019.

[168] T. G. Mason and D. A. Weitz, "Optical measurements of frequency-dependent linear viscoelastic moduli of complex fluids," *Physical Review Letters*, vol. 74, no. 7, pp. 1250–1253, 1995.

[169] D. T. Chen, E. R. Weeks, J. C. Crocker, M. F. Islam, R. Verma, J. Gruber, A. J. Levine, T. C. Lubensky, and A. G. Yodh, "Rheological Microscopy: Local Mechanical Properties from Microrheology," *Physical Review Letters*, vol. 90, no. 10, p. 4, 2003.

[170] T. Maier and T. Haraszti, "Python algorithms in particle tracking microrheology," *Chemistry Central Journal*, vol. 6, no. 1, p. 144, 2012.

[171] R. M. L. Evans, M. Tassieri, D. Auhl, and T. A. Waigh, "Direct conversion of rheological compliance measurements into storage and loss moduli," *Physical Review E*, vol. 80, p. 12501, jul 2009.

[172] J. C. Crocker and D. G. Grier, "Methods of digital video microscopy for colloidal studies," *Journal of Colloid and Interface Science*, vol. 179, no. 1, pp. 298–310, 1996.

[173] P. Pincus, "Excluded volume effects and stretched polymer chains," *Macromolecules*, vol. 9, no. 3, pp. 386–388, 1976.

[174] S. J. Anderson, C. Matsuda, J. Garamella, K. R. Peddireddy, R. M. Robertson-Anderson, and R. McGorty, "Filament rigidity vies with mesh size in determining anomalous diffusion in cytoskeleton," *Biomacromolecules*, vol. 20, no. 12, pp. 4380–4388, 2019.

[175] T. P. Lodge, N. A. Rotstein, and S. Prager, "Dynamics of Entangled Polymer Liquids: Do Linear Chains Reptate?," in *Advances in Chemical Physics*, Advances in Chemical Physics, pp. 1–132, jan 2007.

[176] A. V. Dobrynin, R. H. Colby, and M. Rubinstein, "Scaling Theory of Polyelectrolyte Solutions," *Macromolecules*, vol. 28, pp. 1859–1871, mar 1995.

[177] W. E. Krause, E. G. Bellomo, and R. H. Colby, "Rheology of sodium hyaluronate under physiological conditions," *Biomacromolecules*, vol. 2, no. 1, pp. 65–69, 2001.

[178] I. Gatej, M. Popa, and M. Rinaudo, "Role of the pH on hyaluronan behavior in aqueous solution," *Biomacromolecules*, vol. 6, no. 1, pp. 61–67, 2005.

[179] E. A. Balazs and J. Cui, "The story of hyaluronan putty," *Bioactive Carbohydrates and Dietary Fibre*, vol. 2, no. 2, pp. 143–151, 2013.

[180] F. Giavazzi, P. Edera, P. J. Lu, and R. Cerbino, "Image windowing mitigates edge effects in Differential Dynamic Microscopy," *European Physical Journal E*, vol. 40, no. 11, 2017.

[181] K. Regan, D. Wulstein, H. Rasmussen, R. McGorty, and R. M. Robertson-Anderson, "Bridging the spatiotemporal scales of macromolecular transport in crowded biomimetic systems," *Soft Matter*, vol. 15, no. 6, pp. 1200–1209, 2019.

[182] C. D. Chapman, K. Lee, D. Henze, D. E. Smith, and R. M. Robertson-anderson, "Onset of Non-Continuum E ff ects in Microrheology of Entangled Polymer Solutions," 2014.

[183] C. H. Lee, A. J. Crosby, T. Emrick, and R. C. Hayward, "Characterization of heterogeneous polyacrylamide hydrogels by tracking of single quantum dots," 2014.

[184] K. He, F. Babaye Khorasani, S. T. Retterer, D. K. Thomas, J. C. Conrad, and R. Krishnamoorti, "Diffusive dynamics of nanoparticles in arrays of nanoposts," *ACS Nano*, vol. 7, no. 6, pp. 5122–5130, 2013.

[185] G. Tarjus, "Breakdown of the Stokes-Einstein relation in supercooled liquids," *The Journal of Chemical Physics*, vol. 103, p. 3071, 1995.

[186] T. P. Lodge, N. A. Rotstein, and S. Prager, "Dynamics of Entangled Polymer Liquids: Do Linear Chains Reptate?," jan 1990.

[187] B. Stuhrmann, M. Soares e Silva, M. Depken, F. C. MacKintosh, and G. H. Koenderink, "Nonequilibrium fluctuations of a remodeling in vitro cytoskeleton," *Phys. Rev. E*, vol. 86, p. 020901, Aug 2012.

[188] T. Toyota, D. A. Head, C. F. Schmidt, and D. Mizuno, "Non-gaussian athermal fluctuations in active gels," *Soft Matter*, vol. 7, pp. 3234–3239, 2011.

[189] M. G. Bulmer, *Principles of statistics*. Courier Corporation, 1979.

[190] J. D. C. Jacob, K. He, S. T. Retterer, R. Krishnamoorti, and J. C. Conrad, "Diffusive dynamics of nanoparticles in ultra-confined media," *Soft Matter*, vol. 11, no. 38, pp. 7515–7524, 2015.

[191] B. Wang, S. M. Anthony, C. B. Sung, and S. Granick, "Anomalous yet Brownian," *Proceedings of the National Academy of Sciences of the United States of America*, vol. 106, no. 36, pp. 15160–15164, 2009.

[192] S. S. Olmsted, J. L. Padgett, A. I. Yudin, K. J. Whaley, T. R. Moench, and R. A. Cone, "Diffusion of macromolecules and virus-like particles in human cervical mucus," *Biophysical Journal*, vol. 81, no. 4, pp. 1930–1937, 2001.

[193] B. Amsden, "An Obstruction-Scaling Model for Diffusion in Homogeneous Hydrogels," *Macromolecules*, vol. 32, no. 3, pp. 874–879, 1999.

[194] A. J. Day and C. M. Milner, "TSG-6: A multifunctional protein with anti-inflammatory and tissue-protective properties," *Matrix Biology*, vol. 78-79, pp. 60–83, may 2019.

[195] A. J. Day and C. A. de la Motte, "Hyaluronan cross-linking: a protective mechanism in inflammation?," *Trends in Immunology*, vol. 26, pp. 637–643, dec 2005.

[196] J. Zámečník, L. Vargová, A. Homola, R. Kodet, and E. Syková, "Extracellular matrix glycoproteins and diffusion barriers in human astrocytic tumours," *Neuropathology and Applied Neurobiology*, vol. 30, no. 4, pp. 338–350, 2004.

[197] T. Stylianopoulos, M. Z. Poh, N. Insin, M. G. Bawendi, D. Fukumura, L. L. Munn, and R. K. Jain, "Diffusion of particles in the extracellular matrix: The effect of repulsive electrostatic interactions," *Biophysical Journal*, vol. 99, no. 5, pp. 1342–1349, 2010.

[198] J. Witten and K. Ribbeck, "The particle in the spider's web: transport through biological hydrogels," *Nanoscale*, vol. 9, no. 24, pp. 8080–8095, 2017.

[199] O. Lieleg and K. Ribbeck, "Biological hydrogels as selective diffusion barriers," *Trends in Cell Biology*, vol. 21, no. 9, pp. 543–551, 2011.

[200] S. Ramanujan, A. Pluen, T. D. McKee, E. B. Brown, Y. Boucher, and R. K. Jain, "Diffusion and convection in collagen gels: Implications for transport in the tumor interstitium," *Biophysical Journal*, vol. 83, no. 3, pp. 1650–1660, 2002.

[201] C. d. L. D. Arne Erikson, Hilde Nortvedt Andersen, Stine Nalum Naess, Pawel Sikorski, "Physical and chemical modifications of collagen gels: impact on diffusion.," *Biopolymers.*, vol. 89, no. 2, pp. 135–143, 2008.

[202] V. P. Chauhan, R. M. Lanning, B. Diop-Frimpong, W. Mok, E. B. Brown, T. P. Padera, Y. Boucher, and R. K. Jain, "Multiscale measurements distinguish cellular and interstitial hindrances to diffusion in vivo," *Biophysical Journal*, vol. 97, no. 1, pp. 330–336, 2009.

[203] E. J. Chung, A. E. Jakus, and R. N. Shah, "In situ forming collagen-hyaluronic acid membrane structures: Mechanism of self-Assembly and applications in regenerative medicine," *Acta Biomaterialia*, vol. 9, no. 2, pp. 5153–5161, 2013.

[204] P. Bełdowski, P. Weber, A. Dėdinaitė, P. M. Claesson, and A. Gadomski, "Physical crosslinking of hyaluronic acid in the presence of phospholipids in an aqueous nano-environment," *Soft matter*, vol. 14, no. 44, pp. 8997–9004, 2018.

[205] J. M. Fleming, S. T. Yeyeodu, A. McLaughlin, D. Schuman, and D. K. Taylor, "In Situ Drug Delivery to Breast Cancer-Associated Extracellular Matrix," *ACS Chemical Biology*, vol. 13, no. 10, pp. 2825–2840, 2018.

[206] A. C. Anselmo, Y. Gokarn, and S. Mitragotri, "Non-invasive delivery strategies for biologics," *Nature Reviews Drug Discovery*, vol. 18, no. 1, pp. 19–40, 2018.

[207] J. Li and D. J. Mooney, "Designing hydrogels for controlled drug delivery," *Nature Reviews Materials*, vol. 1, no. 12, pp. 1–18, 2016.

[208] R. Narayanaswamy and V. P. Torchilin, "Hydrogels and their applications in targeted drug delivery," *Molecules*, vol. 24, no. 3, 2019.

[209] L. L. Josephson, E. M. Furst, and W. J. Galush, "Particle tracking microrheology of protein solutions," *Journal of Rheology*, vol. 60, no. 4, pp. 531–540, 2016.

[210] E. M. Furst and T. M. Squires, *Microrheology*. Oxford University Press, 2017.

[211] M. W. Mosesson, K. R. Siebenlist, and D. A. Meh, "The Structure and Biological Features of Fibrinogen and Fibrin," *Annals of the New York Academy of Sciences*, vol. 936, no. 1, pp. 11–30, 2006.

[212] R. I. Litvinov and J. W. Weisel, "Fibrin mechanical properties and their structural origins," *Matrix Biology*, vol. 60-61, pp. 110–123, jul 2017.

[213] I. K. Piechocka, K. A. Jansen, C. P. Broedersz, N. A. Kurniawan, F. C. MacKintosh, and G. H. Koenderink, "Multi-scale strain-stiffening of semiflexible bundle networks," *Soft Matter*, vol. 12, no. 7, pp. 2145–2156, 2016.

[214] B. E. Vos, C. Martinez-Torres, F. Burla, J. W. Weisel, and G. H. Koendernik, "Revealing the molecular origins of fibrin's elastomeric properties by in situ X-ray scattering," *bioRxiv*, p. 797464, jan 2019.

[215] J. M. Reinke and H. Sorg, "Wound repair and regeneration," *European Surgical Research*, vol. 49, no. 1, pp. 35–43, 2012.

[216] M. G. Tonnesen, X. Feng, and R. A. Clark, "Angiogenesis in wound healing," *Journal of Investigative Dermatology Symposium Proceedings*, vol. 5, no. 1, pp. 40–46, 2000.

[217] X. Feng, M. G. Tonnesen, S. A. Mousa, and R. A. Clark, "Fibrin and collagen differentially but synergistically regulate sprout angiogenesis of human dermal microvascular endothelial cells in 3-dimensional matrix," *International Journal of Cell Biology*, no. May 2014, 2013.

[218] H. F. Dvorak, "Tumors: Wounds That Do Not Heal," *Cancer Immunol Res*, vol. 3, no. 1, pp. 1–11, 2015.

[219] V. K. Lai, S. P. Lake, C. R. Frey, R. T. Tranquillo, and V. H. Barocas, "Mechanical Behavior of Collagen-Fibrin Co-Gels Reflects Transition From Series to Parallel Interactions With Increasing Collagen Content," *Journal of Biomechanical Engineering*, vol. 134, feb 2012.

[220] V. K. Lai, C. R. Frey, A. M. Kerandi, S. P. Lake, R. T. Tranquillo, and V. H. Barocas, "Acta Biomaterialia Microstructural and mechanical differences between digested collagen â fibrin co-gels and pure collagen and fibrin gels," *Acta Biomaterialia*, vol. 8, no. 11, pp. 4031–4042, 2012.

[221] R. R. Rao, A. W. Peterson, J. Ceccarelli, A. J. Putnam, and J. P. Stegemann, "Matrix composition regulates three-dimensional network formation by endothelial cells and mesenchymal stem cells in collagen/fibrin materials," *Angiogenesis*, vol. 15, pp. 253–264, jun 2012.

[222] O. V. Kim, R. I. Litvinov, J. Chen, D. Z. Chen, J. W. Weisel, and M. S. Alber, "Compression-induced structural and mechanical changes of fibrin-collagen composites," *Matrix Biology*, vol. 60-61, pp. 141–156, 2017.

[223] D. S. Nedrelow, D. Bankwala, J. D. Hyypio, V. K. Lai, and V. H. Barocas, "Mechanics of a two-fiber model with one nested fiber network, as applied to the collagen-fibrin system," *Acta Biomaterialia*, vol. 72, pp. 306–315, may 2018.

[224] C. E. Blanchet and D. I. Svergun, "Small-Angle X-Ray Scattering on Biological Macromolecules and Nanocomposites in Solution," *Annual Review of Physical Chemistry*, vol. 64, no. 1, pp. 37–54, 2013.

[225] C. Yeromonahos, B. Polack, and F. Caton, "Nanostructure of the fibrin clot," *Biophysical Journal*, vol. 99, no. 7, pp. 2018–2027, 2010.

[226] J. Torbet, J. M. Freyssinet, and G. Hudry-Clergeon, "Oriented fibrin gels formed by polymerization in strong magnetic fields," *Nature*, vol. 289, no. 5793, pp. 91–93, 1981.

[227] L. Stryer, C. Cohen, and R. Langridge, "Axial period of fibrinogen and fibrin," *Nature*, vol. 197, no. 4869, pp. 793–794, 1963.

[228] N. Kuznetsova and S. Leikin, "Does the triple helical domain of type I collagen encode molecular recognition and fiber assembly while telopeptides serve as catalytic domains? Effect of proteolytic cleavage on fibrillogenesis and on collagen-collagen interaction in fibers," *Journal of Biological Chemistry*, vol. 274, no. 51, pp. 36083–36088, 1999.

[229] N. Sasaki and S. Odajimat, "TECHNICAL / X-Ray," vol. 29, no. 5, pp. 655–658, 1996.

[230] A. D. Protopopova, N. A. Barinov, E. G. Zavyalova, A. M. Kopylov, V. I. Sergienko, and D. V. Klinov, "Visualization of fibrinogen αC regions and their arrangement during fibrin network formation by high-resolution AFM," *Journal of Thrombosis and Haemostasis*, vol. 13, no. 4, pp. 570–579, 2015.

[231] K. M. Meek and A. J. Quantock, "The Use of X-ray Scattering Techniques to Determine Corneal Ultrastructure," vol. 20, no. 1, 2001.

[232] F. Ferri, M. Greco, G. Arcòvito, M. De Spirito, and M. Rocco, "Structure of fibrin gels studied by elastic light scattering techniques: Dependence of fractal dimension, gel crossover length, fiber diameter, and fiber density on monomer concentration," *Physical review. E, Statistical, nonlinear, and soft matter physics*, vol. 66, no. 1, p. 11913, 2002.

[233] D. J. Hulmes, "Building collagen molecules, fibrils, and suprafibrillar structures," *Journal of Structural Biology*, vol. 137, no. 1-2, pp. 2–10, 2002.

[234] W. A. Voter, C. Lucaveche, A. E. Blaurock, and H. P. Erickson, "Lateral packing of protofibrils in fibrin fibers and fibrinogen polymers," *Biopolymers*, vol. 25, no. 12, pp. 2359–2373, 1986.

[235] M. Missori, M. Papi, G. Maulucci, G. Arcovito, G. Boumis, A. Bellelli, G. Amiconi, and M. De Spirito, "Cl- and F- anions regulate the architecture of protofibrils in fibrin gel," *European Biophysics Journal*, vol. 39, no. 6, pp. 1001–1006, 2010.

[236] B. Sapoval, *Universalités et fractales: jeux d'enfant ou délits d'initié?* Flammarion, 1997.

[237] P. H. Kopper, "Role of Calcium in Fibrin Formation," *Nature*, vol. 198, no. 4879, pp. 493–494, 1963.

[238] C. Broennimann, E. F. Eikenberry, B. Henrich, R. Horisberger, G. Huelsen, E. Pohl, B. Schmitt, C. Schulze-Briese, M. Suzuki, T. Tomizaki, H. Toyokawa, and A. Wagner, "The PILATUS 1M detector," *Journal of Synchrotron Radiation*, vol. 13, no. 2, pp. 120–130, 2006.

[239] O. Glatter and O. Kratky, "Small angle x-ray scattering.," *London: Academic Press Inc. Ltd.*, 1982.

[240] P. Fratzl, N. Fratzl-Zelman, and K. Klaushofer, "Collagen packing and mineralization. An x-ray scattering investigation of turkey leg tendon," *Biophysical Journal*, vol. 64, no. 1, pp. 260–266, 1993.

[241] C. Martinez-Torres, F. Burla, C. Alkemade, and G. H. Koenderink, "Revealing the Assembly of Filamentous Proteins with Scanning Transmission Electron Microscopy," pp. 1–30, 2019.

[242] F. Burla, Y. Mulla, B. E. Vos, A. Aufderhorst-Roberts, and G. H. Koenderink, "From mechanical resilience to active material properties in biopolymer networks," *Nature Reviews Physics*, vol. 1, no. 4, pp. 249–263, 2019.

[243] J. S. Bell, S. Hayes, C. Whitford, J. Sanchez-weatherby, O. Shebanova, C. Vergari, C. P. Winlove, N. Terrill, T. Sorensen, A. Elsheikh, and K. M. Meek, "Acta Biomaterialia The hierarchical response of human corneal collagen to load," *Acta Biomaterialia*, vol. 65, pp. 216–225, 2018.

[244] I. K. Piechocka, N. A. Kurniawan, J. Grimbergen, J. Koopman, and G. H. Koenderink, "Recombinant fibrinogen reveals the differential roles of α- and γ-chain cross-linking and molecular heterogeneity in fibrin clot strain-stiffening," *Journal of Thrombosis and Haemostasis*, vol. 15, pp. 938–949, may 2017.

[245] N. A. Kurniawan, J. Grimbergen, J. Koopman, and G. H. Koenderink, "FactorÂ XIII stiffens fibrin clots by causing fiber compaction," *Journal of Thrombosis and Haemostasis*, vol. 12, pp. 1687–1696, oct 2014.

[246] H. Kang, Q. Wen, P. A. Janmey, J. X. Tang, E. Conti, and F. C. MacKintosh, "Nonlinear elasticity of stiff filament networks: strain stiffening, negative normal stress, and filament alignment in fibrin gels," *The journal of physical chemistry. B*, vol. 113, pp. 3799–3805, mar 2009.

[247] D. J. S. Hulmes, T. J. Wess, and P. Fratzl, "Radial Packing , Order , and Disorder in Collagen Fibrils," *Biophysical Journal*, vol. 68, no. 5, pp. 1661–1670, 1995.

[248] G. C. Wood and M. K. Keech, "The formation of fibrils from collagen solutions. 1. The effect of experimental conditions: kinetic and electron-microscope studies," *The Biochemical journal*, vol. 75, pp. 588–598, jun 1960.

[249] F. Silver and R. Trelstad, "Linear aggregation and the turbidimetric lag phase: Type I collagen fibrillogenesis in vitro," *Journal of Theoretical Biology*, vol. 81, pp. 515–526, dec 1979.

[250] M. Ovaska, Z. Bertalan, A. Miksic, M. Sugni, M. J. Alava, C. A. M. La, and S. Zapperi, "Deformation and fracture of echinoderm collagen networks," *Journal of the Mechanical Behavior of Biomedical Materials*, vol. 65, pp. 42–52, 2017.

[251] I. K. Piechocka, R. G. Bacabac, M. Potters, F. C. Mackintosh, and G. H. Koenderink, "Structural hierarchy governs fibrin gel mechanics," *Biophysical journal*, vol. 98, pp. 2281–2289, may 2010.

[252] K. M. Weigandt, D. C. Pozzo, and L. Porcar, "Structure of high density fibrin networks probed with neutron scattering and rheology," *Soft Matter*, vol. 5, no. 21, pp. 4321–4330, 2009.

[253] A. E. X. Brown, R. I. Litvinov, D. E. Discher, P. K. Purohit, and J. W. Weisel, "Multiscale mechanics of fibrin polymer: Gel stretching with protein unfolding and loss of water," *Science*, vol. 325, no. 5941, pp. 741–744, 2009.

[254] N. A. Kurniawan, T. H. Van Kempen, S. Sonneveld, T. T. Rosalina, B. E. Vos, K. A. Jansen, G. W. Peters, F. N. Van De Vosse, and G. H. Koenderink, "Buffers Strongly Modulate Fibrin Self-Assembly into Fibrous Networks," *Langmuir*, vol. 33, no. 25, pp. 6342–6352, 2017.

[255] E. Geissler, A. M. Hecht, and F. Horkay, "Scaling equations for a biopolymer in salt solution," *Physical Review Letters*, vol. 99, no. 26, pp. 18–21, 2007.

[256] F. Horkay, J. Magda, M. Alcoutlabi, S. Atzet, and T. Zarembinski, "Structural , mechanical and osmotic properties of injectable hyaluronan-based composite hydrogels," *Polymer*, vol. 51, no. 19, pp. 4424–4430, 2010.

[257] M. K. Cowman, H. G. Lee, K. L. Schwertfeger, J. B. McCarthy, and E. A. Turley, "The content and size of hyaluronan in biological fluids and tissues," 2015.

[258] V. Shenoy and J. Rosenblatt, "Diffusion of Macromolecules in Collagen and Hyaluronic Acid, Rigid-Rod-Flexible Polymer, Composite Matrices," *Macromolecules*, vol. 28, no. 26, pp. 8751–8758, 1995.

[259] E. V. Maytin, "Hyaluronan: More than just a wrinkle filler," *Glycobiology*, vol. 26, no. 6, pp. 553–559, 2016.

[260] T. E. Ludwig, M. M. Hunter, and T. A. Schmidt, "Cartilage boundary lubrication synergism is mediated by hyaluronan concentration and PRG4 concentration and structure," *BMC Musculoskeletal Disorders*, vol. 16, p. 386, dec 2015.

[261] Y. Zhu and S. Granick, "Biolubrication: Hyaluronic acid and the influence on its interfacial viscosity of an antiinflammatory drug," *Macromolecules*, vol. 36, no. 4, pp. 973–976, 2003.

[262] T. A. Schmidt, N. S. Gastelum, Q. T. Nguyen, B. L. Schumacher, and R. L. Sah, "Boundary lubrication of articular cartilage: Role of synovial fluid constituents," *Arthritis & Rheumatism*, vol. 56, pp. 882–891, mar 2007.

[263] M. G. Neuman, R. M. Nanau, L. Oruña-Sanchez, and G. Coto, "Hyaluronic acid and wound healing," *Journal of Pharmacy and Pharmaceutical Sciences*, vol. 18, no. 1, pp. 53–60, 2015.

[264] A. C. Petrey and C. A. de la Motte, "Hyaluronan, a crucial regulator of inflammation," *Frontiers in immunology*, vol. 5, p. 101, mar 2014.

[265] B. P. Toole, "Hyaluronan: From extracellular glue to pericellular cue," jul 2004.

[266] M. Liu, C. Tolg, and E. Turley, "Dissecting the Dual Nature of Hyaluronan in the Tumor Microenvironment," *Frontiers in immunology*, vol. 10, p. 947, may 2019.

[267] M. M. Temple-Wong, S. Ren, P. Quach, B. C. Hansen, A. C. Chen, A. Hasegawa, D. D. D'Lima, J. Koziol, K. Masuda, M. K. Lotz, and R. L. Sah, "Hyaluronan concentration and size distribution in human knee synovial fluid: variations with age and cartilage degeneration.," *Arthritis research & therapy*, vol. 18, p. 18, jan 2016.

[268] D. A. Gibbs, E. W. Merrill, K. A. Smith, and E. A. Balazs, "Rheology of hyaluronic acid," *Biopolymers*, vol. 6, pp. 777–791, jun 1968.

[269] S. Wu, L. Ai, J. Chen, J. Kang, and S. Cui, "Study of the mechanism of formation of hyaluronan putty at pH 2.5: Part I. Experimental measurements," *Carbohydrate polymers*, vol. 98, pp. 1677–1682, nov 2013.

[270] L. Leibler, M. Rubinstein, and R. H. Colby, "Dynamics of reversible networks," *Macromolecules*, vol. 24, pp. 4701–4707, aug 1991.

[271] M. Rubinstein and A. N. Semenov, "Dynamics of entangled solutions of associating polymers," *Macromolecules*, vol. 34, no. 4, pp. 1058–1068, 2001.

[272] M. Ahmadi, L. G. D. Hawke, H. Goldansaz, and E. van Ruymbeke, "Dynamics of Entangled Linear Supramolecular Chains with Sticky Side Groups: Influence of Hindered Fluctuations," *Macromolecules*, vol. 48, pp. 7300–7310, oct 2015.

[273] S. Hackelbusch, T. Rossow, P. van Assenbergh, and S. Seiffert, "Chain Dynamics in Supramolecular Polymer Networks," *Macromolecules*, vol. 46, pp. 6273–6286, aug 2013.

[274] K. M. Lowry and E. M. Beavers, "Thermal stability of sodium hyaluronate in aqueous solution.," *Journal of biomedical materials research*, vol. 28, pp. 1239–1244, oct 1994.

[275] P. Gribbon, B. C. Heng, and T. E. Hardingham, "The molecular basis of the solution properties of hyaluronan investigated by confocal fluorescence recovery after photobleaching," *Biophysical Journal*, vol. 77, no. 4, pp. 2210–2216, 1999.

[276] I. C. M. Dea, R. Moorhouse, D. A. Rees, S. Arnott, J. M. Guss, and E. A. Balazs, "Hyaluronic Acid: A Novel, Double Helical Molecule," *Science*, vol. 179, pp. 560 LP – 562, feb 1973.

[277] B. A. Krajina, C. Tropini, A. Zhu, P. DiGiacomo, J. L. Sonnenburg, S. C. Heilshorn, and A. J. Spakowitz, "Dynamic Light Scattering Microrheology Reveals Multiscale Viscoelasticity of Polymer Gels and Precious Biological Materials," *ACS Central Science*, vol. 3, pp. 1294–1303, dec 2017.

[278] G. H. Koenderink, M. Atakhorrami, F. C. MacKintosh, and C. F. Schmidt, "High-Frequency Stress Relaxation in Semiflexible Polymer Solutions and Networks," *Physical Review Letters*, vol. 96, p. 138307, apr 2006.

[279] M. Rubinstein and A. N. Semenov, "Thermoreversible Gelation in Solutions of Associating Polymers. 2. Linear Dynamics," *Macromolecules*, vol. 31, pp. 1386–1397, feb 1998.

[280] F. Tanaka and S. Edwards, "Viscoelastic properties of physically crosslinked networks: Part 2. Dynamic mechanical moduli," *Journal of Non-Newtonian Fluid Mechanics*, vol. 43, pp. 273–288, jul 1992.

[281] L. de Lucca Freitas and R. Stadler, "Influence of hydrogen bonding on the temperature dependence of the viscoelastic properties," 1988.

[282] J. D. Ferry, "Viscoelastic properties of polymers," 1980.

[283] A. Charlot and R. Auzély-Velty, "Novel hyaluronic acid based supramolecular assemblies stabilized by multivalent specific interactions: Rheological behavior in aqueous solution," *Macromolecules*, vol. 40, no. 26, pp. 9555–9563, 2007.

[284] D. W. Bolen and G. D. Rose, "Structure and energetics of the hydrogen-bonded backbone in protein folding.," *Annual review of biochemistry*, vol. 77, pp. 339–362, 2008.

[285] Z. Zhang, C. Liu, X. Cao, L. Gao, and Q. Chen, "Linear Viscoelastic and Dielectric Properties of Strongly Hydrogen-Bonded Polymers near the Sol-Gel Transition," *Macromolecules*, vol. 49, no. 23, pp. 9192–9202, 2016.

[286] J. M. Cyphert, C. S. Trempus, and S. Garantziotis, "Size Matters: Molecular Weight Specificity of Hyaluronan Effects in Cell Biology," *International Journal of Cell Biology*, vol. 2015, 2015.

[287] R. F. Shamoun, H. H. Hariri, R. A. Ghostine, and J. B. Schlenoff, "Thermal transformations in extruded saloplastic polyelectrolyte complexes," *Macromolecules*, vol. 45, no. 24, pp. 9759–9767, 2012.

[288] E. Spruijt, J. Sprakel, M. Lemmers, M. A. Stuart, and J. Van Der Gucht, "Relaxation dynamics at different time scales in electrostatic complexes: Time-salt superposition," *Physical Review Letters*, vol. 105, no. 20, pp. 1–4, 2010.

[289] C. Corbet and O. Feron, "Tumour acidosis: from the passenger to the driver's seat," *Nature Reviews Cancer*, vol. 17, p. 577, sep 2017.

[290] F. Erra Díaz, E. Dantas, and J. Geffner, "Unravelling the interplay between extracellular acidosis and immune cells," *Mediators of Inflammation*, vol. 2018, 2018.

[291] M. A. C. Stuart, W. T. S. Huck, J. Genzer, M. Müller, C. Ober, M. Stamm, G. B. Sukhorukov, I. Szleifer, V. V. Tsukruk, M. Urban, F. Winnik, S. Zauscher, I. Luzinov, and S. Minko, "Emerging applications of stimuli-responsive polymer materials," *Nature Materials*, vol. 9, no. 2, pp. 101–113, 2010.

[292] G. Huang and H. Huang, "Application of hyaluronic acid as carriers in drug delivery," *Drug delivery*, vol. 25, pp. 766–772, nov 2018.

[293] S. Trombino, C. Servidio, F. Curcio, and R. Cassano, "Strategies for Hyaluronic Acid-Based Hydrogel Design in Drug Delivery," *Pharmaceutics*, vol. 11, p. 407, aug 2019.

[294] M. Hemshekhar, R. M. Thushara, S. Chandranayaka, L. S. Sherman, K. Kemparaju, and K. S. Girish, "Emerging roles of hyaluronic acid bioscaffolds in tissue engineering and regenerative medicine," *International Journal of Biological Macromolecules*, vol. 86, pp. 917–928, may 2016.

[295] F. Meng, R. H. Pritchard, and E. M. Terentjev, "Stress Relaxation, Dynamics, and Plasticity of Transient Polymer Networks," *Macromolecules*, vol. 49, no. 7, pp. 2843–2852, 2016.

[296] R. Long, K. Mayumi, C. Creton, T. Narita, and C. Y. Hui, "Time dependent behavior of a dual cross-link self-healing gel: Theory and experiments," *Macromolecules*, vol. 47, no. 20, pp. 7243–7250, 2014.